Deep Submillimetre Observations of Faint Dusty Galaxies

PROEFSCHRIFT

ter verkrijging van
de graad van Doctor aan de Universiteit Leiden,
op gezag van de Rector Magnificus Dr. D.D. Breimer,
hoogleraar in de faculteit der Wiskunde en
Natuurwetenschappen en die der Geneeskunde,
volgens besluit van het College voor Promoties
te verdedigen op woensdag 6 oktober 2004
klokke 14.15 uur

door

Kirsten Kraiberg Knudsen
geboren te Odder, Denemarken
in 1976

Promotiecomissie

Promotor :	Prof. dr. M. Franx
Co-promotor :	Dr. P. P. van der Werf
Referent :	Dr. T. M. A. Webb
Overige leden :	Dr. A. W. Blain (California Institute of Technology)
	Prof. dr. V. Icke
	Prof. dr. G. K. Miley
	Prof. dr. P. T. de Zeeuw

Front cover: The James Clerk Maxwell Telescope with the submillimetre sky in the background. The sky image has been constructed from submillimetre maps from the Leiden-SCUBA Lens Survey, which is the main part of this thesis. The picture of the JCMT is a rare photo, as the telescope can actually be seen. Under normal circumstances, when the dome is open, a large Goretex membrane is in front of the telescope (protecting the telescope, stabilizing the walls of the dome and filtering out the bright sunlight during daytime observations.)

Back cover: A true-colour image of a securely identified near-infrared counterpart of one of the SCUBA sources in the field MS1054$-$03. In the image, the red channel is the near-infrared data taken at wavelength 2.2 μm. The red galaxy in the middle is the underlying galaxy giving rise to the submillimetre emission detected with SCUBA. The galaxy is only seen in the near-infrared, not in the optical. The 'yellow' galaxies are members of the galaxy cluster MS1054$-$03. The size of the image is $50' \times 50'$.

Contents

Contents

Contents

Chapter 1

Introduction

The ubiquitous presence of dust throughout the Universe and its absorbing properties, which cause an obscuration of background sources, have a large influence on our understanding of the processes in the Universe. The detection of the far-infrared/submillimetre background radiation with *COsmic Background Explorer* (*COBE*; Puget et al., 1996; Fixsen et al., 1998; background radiation is shown in Figure 1.1) and the fact that it has an energy density comparable to that of the ultraviolet/optical background radiation (e.g., Bernstein et al., 2002a,2002b), indicates that approximately half of the activity in the Universe is or has been obscured by dust. Thus, unquestionably, observations in the infrared (IR) of the high redshift universe are indispensable for constraining models for galaxy formation and evolution. With the advent of the first submillimetre (submm) mapping instrument SCUBA (Submillimetre Common-User Bolometer Array; Holland et al., 1999), unbiased observations at submm wavelengths searching for high redshift populations became possible. Already the first observations yielded a number of submm bright galaxies (Smail et al., 1997; Hughes et al., 1998), which locally are rare objects (Soifer, Neugebauer & Houck, 1987; Sanders & Mirabel, 1996).

This thesis is about the Leiden-SCUBA Lens Survey, a submm mapping survey, studying the distant dusty galaxies. The observations were done on galaxy cluster fields, where the clusters have gravitational potentials deep enough to create a strong effect of gravitational lensing. Through these "nature's own telescopes" we study sources, which otherwise might not have been observable with the current observing techniques. Observations of the fainter submm galaxies are essential for more reasons, the two most important being (*i*) resolving the bulk of the far-IR background radiation and (*ii*) understanding of the submm galaxy population as a whole.

1.1 Galaxy formation and evolution

In the simple optical morphological classification of galaxies from Hubble (1926) there are two main types of galaxies, namely the ellipticals and the spirals. While the ellipticals typically are red, gas-poor and harbour an old evolved stellar population, the spiral galaxies are blue with a dominant population of young stars and contain large amounts of gas and dust. This suggests that the galaxies have different ages and likely have formed and evolved differently. The definition of the formation of a galaxy is not straightforward, but can be defined e.g. as the time of formation of the dominant stellar population or the assembly of the dark matter. Here we focus on the formation of the dominant stellar population in a galaxy. The expected time scale for the formation is related to the dynamical time scale
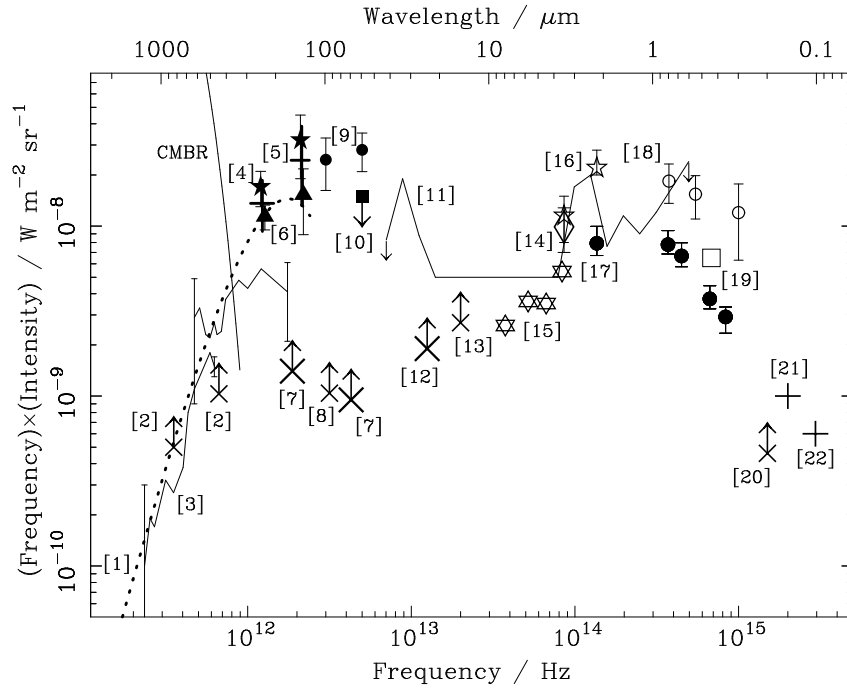
Figure 1.1: *The observed intensity of extragalactic background radiation from the ultraviolet to the submm spectral range, including the new measurements and limits from Spitzer. This figure shows the background energy density in the Universe from sources other than the Cosmic Microwave Background Radiation (CMBR; the CMBR is indicated at the long wavelength side of the figure). Most of the remaining background energy density is radiated at X-ray wavelengths, but contains significantly less energy. Though some significant uncertainty remains, the combination of measurements and limits indicates that a comparable amount of energy is received from the far-infrared background, which peaks at a wavelength of about 200 μm, and from the near-infrared/optical background, which peaks at a wavelength between 1 and 2 μm. The data originates from a wide range of sources: [1] Fixsen et al. (1998); [2] Puget et al. (1996); [3] Blain et al. (1999a); [4] Schlegel et al. (1998); [5] Hauser et al. (1998); [6] Lagache et al. (2000a) see also Kiss et al. (2001); [7] Dole et al. (2004); [8] Kawara et al. (1998); [9] Finkbeiner et al. (2000); [10] Dwek & Krennich, (2004); [11] Stanev and Franceschini (1998); [12] Papovich et al., (2004); [13] Altieri et al. (1999); [14] Dwek and Arendt (1998); [15] Fazio et al., (2004); [16] Wright and Johnson (2001); [17] Pozzetti et al. (1998); [18] Bernstein (1999) and Bernstein et al. (2002a); [19] Toller et al. (1987); [20] Armand et al. (1994); [21] Lampton et al. (1990); and [22] Murthy et al. (1999). For a detailed review of cosmic IR backgrounds see Hauser and Dwek (2001). Note that Lagache et al. (2000a,2000b) claim that the Finkbeiner et al. points ([9]) could be affected by diffuse zodiacal emission. Where multiple results are available in the literature the most sensitive result is quoted.*

of $t \sim 10^8$ yr. Spheroids harbour most of the matter locked up in stars (Fukugita et al., 1998), thus it is important to understand these objects. The most massive galaxies are elliptical galaxies, which have (stellar) masses $10^9 - 10^{12}\,M_\odot$. As ellipticals show no sign of significant star formation, the stars must have formed at earlier epochs, possibly at prodigious rates.

The currently most successful model for galaxy formation and evolution is the model of hierarchical structure formation (e.g., Press & Schechter, 1974), where galaxies are assembled through mergers and accretion of smaller galaxies. This type of models is often realised through N-body simulations and semi-analytical models (e.g., Kauffman et al., 1999; Guiderdoni et al., 1998). This model essentially replaces earlier scenarios, where galaxies form at high redshift through a collapse of a single object on a short time scale and undergo a single intense starburst after which the stellar populations evolve passively (Eggen, Lynden-Bell & Sandage, 1962).

In the hierarchical model the star formation rates are typically predicted to be moderate, of a few to few tens $M_\odot yr^{-1}$ (e.g., Baugh et al., 1998; Cole et al., 1994), which is consistent with the ultraviolet(UV)/optical observations. That is, however, not sufficient to form the most massive galaxies. The large number of spheroids and ellipticals harbouring evolved stellar populations at redshift $z \sim 1$ (e.g., Moriondo et al., 2000) suggests formation at much higher redshift and that at star formation rates larger than observed in the UV/optical.

1.2 The cosmic star formation history

An important observable for understanding galaxy formation and evolution is the star formation rate (henceforth SFR). The most obvious approach for studying the star formation rate of galaxies is to measure the number of massive stars, as they are short-lived and thus only present during the star formation phases of a galactic system. Massive stars radiate most of their energy in the UV, which for galaxies at cosmological distances has been redshifted to the optical part of the spectrum. Optical observations of high redshift star forming galaxies such as the Lyman Break Galaxies (Steidel et al., 1999) and Lyα emitting galaxies (e.g., Hu, 2004), show SFRs between a few and several tens of $M_\odot yr^{-1}$. For comparison, our Milky Way has a SFR $\sim 1\,M_\odot yr^{-1}$. Star formation happens in the presence of dust. Optical and in particular UV light is very sensitive to the presence of dust, as the photons are being absorbed. This extinction heats up the dust, which reradiates the energy in the far-IR (FIR). Consequently, UV/optical observations of the SFR of high redshift galaxies need to be corrected for the dust extinction. Attempts to correct for the dust extinction have been done, and in some cases a factor of $\sim$10 has been estimated (e.g., Meurer et al., 1997, 1999). However, such estimates are very uncertain as there are many unknowns, such as the geometry of the galaxies and the wavelength dependence of the extinction. There are alternative methods for estimating the SFR for galaxies, where the most common ones are to study the FIR emission from dust, supernova remnants through radio observations, and high mass binaries through X-ray observations (e.g., Hughes et al., 1998; Haarsma et al., 2000; Norman et al., 2004).

In the global picture of galaxy formation and evolution, the star formation rate per comoving volume is determined as function of cosmic epoch. This is often referred to as the cosmic star formation history. In Figure 1.2 we have plotted the cosmic star formation history as it is observed through different methods described above. The increase between redshift 0 and 1, is reasonably well-established through multi-wavelength observations (e.g., Lilly et al., 1996; Flores et al., 1999). There are clear indications of a peak between redshift 1 and 2 (Connolly et al., 1997; Smail et al., 2002; Blain et al., 1999b; Knudsen et al., *Chapter 4*). The actual shape at redshift > 2 is not yet agreed upon. The extinction corrected data at redshifts $z \approx 3$ and 4 suggest at very shallow decline (e.g., Steidel et al., 1999), while the data for redshifts ~ 5 and 6 suggests at steeper decline (e.g., Stanway et al., 2004). In the FIR, the SFR density must decline at high redshift to fit the spectral slope of the FIR extregalactic background light (EBL) (Blain et al., 1999b; Knudsen et al., *Chapter 4*).

1.3 Submillimetre cosmology

After it was realised that the FIR extragalactic background light was indeed extragalactic (Puget et al., 1996; Fixsen et al., 1998) and not zodiacal light (Mather et al., 1994), submillimetre cosmology has come to play an important role in the studies of galaxy formation and evolution. While sensitive space-based FIR space observatories are or have been underway, with ground-based observations with SCUBA it has been possible to observe the redshifted Rayleigh-Jeans tail of the FIR spectral energy distribution (SED) of distant galaxies. The class of distant galaxies, which are observable to SCUBA, are ultra-luminous IR galaxies (ULIRGs) with bolometric luminosities $L_{bol} > 10^{12} \, \mathrm{L_\odot}$.

The first results of high redshift observations after the commissioning of SCUBA, were presented by Smail et al., (1997), Barger et al., (1998) and Hughes et al., (1998). In the years to follow, several surveys have been published. It was quickly concluded that this new population of dusty, distant ultra-luminous galaxies make a major contribution to the FIR EBL. In fact, their contribution is so large, that they account for about 30 % of the total energy budget at redshifts ~ 2.5. This makes the submm galaxies (SMGs) an important population, which plays an essential role for our understanding of the processes at earlier epochs.

The actual nature of the SCUBA sources and what type of galaxy they evolve into (that we can see at the current epoch) are still debated. In the local part of the universe, ULIRGs are relative rare objects with space densities in the order of $10^{-8} \, \mathrm{Mpc^{-3}}$, i.e. about 0.1 % of all local galaxies (Saunders et al., 1990; Kim & Sanders, 1998), while the distant SCUBA sources have comoving space densities ~ 1000 times larger (e.g., Scott et al., 2002). Among the local ULIRGs are Arp 220 and Mrk 231. It is likely, but has not yet been confirmed that SCUBA sources are high redshift analogues of local ULIRGs, for which it is thought that the FIR emission is powered by intense star formation triggered by a dramatic merger event (e.g., Genzel et al., 1998). Major mergers and galaxy interactions are probably the only way to reach star formation rates large enough to form the stellar populations in massive elliptical galaxies during $\sim 10^8 \, \mathrm{yr}$. The suggestion that SCUBA sources
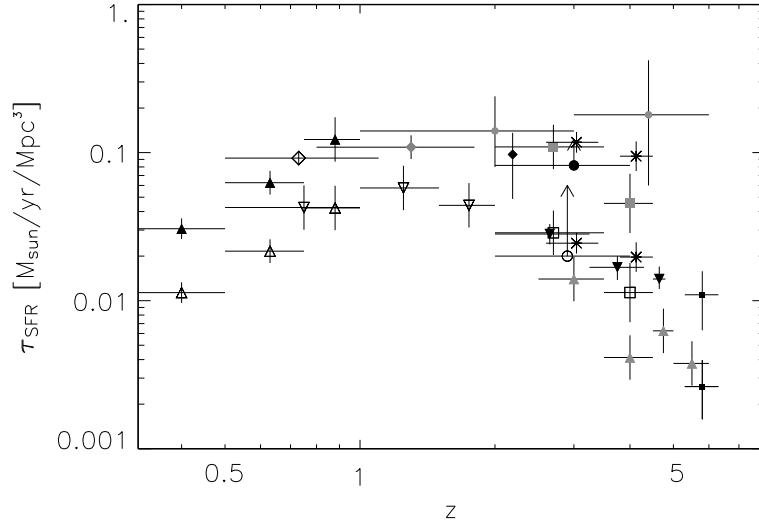
Figure 1.2: *The star formation rate per comoving volume as function of redshift; this is often referred to as the cosmic star formation history. The data points are results from various surveys at UV/optical/IR wavelengths: empty triangles: Lilly et al. (1996); empty, inverse triangles: Connolly et al. (1997); empty squares: Madau et al. (1998); grey squares: Pettini et al. (1998) have extinction corrected the the results from Madau et al.; crosses: Steidel et al. (1999), who additionally estimated an extinction correction of a factor ∼ 5 for their results; filled, inverse triangles: Bouwens et al. (2003); grey triangles: Fontana et al. (2003), data points corrected for dust extinction; small filled squares: Stanway et al. (2004), data points corrected for dust extinction; filled triangles: Flores et al. (1999); empty diamond: Tresse et al. (2002) who have reddening corrected the result; grey diamond: Yan et al. (1999); filled diamond: Moorwood et al. (2000); open circle: Scott et al. (2002); filled circle: Hughes et al. (1998); small grey circles: Barger et al. (2000). The triangles, squares and crosses are UV/optical data, except the filled triangles, which represent ISOCAM 15 μm data (Flores et al., 1999) from the same fields as the data from Lilly et al. (1996). The diamonds represent the Hα observations. The circles represent SCUBA observations, for which redshifts have been assumed. The Scott et al. (2002) result is from the UK 8 mJy survey, where a redshift bin 2-4 has been assumed. The data point is indicated as a lower limit, as the survey only probes the bright sources, while the dominant fraction of SCUBA sources are 5-10 times fainter than that. The data points from Barger et al. (2000) are based on radio-submm photometric redshift for sources with $S_{850} > 6$ mJy, but have been completeness corrected by a factor ∼ 11 to account for the faint sources. The data points from Hughes et al. (1998) are the first results from the SCUBA map of Hubble Deep Field North, also with no redshift information.*

have a similar nature as the local ULIRGs is supported by the redshift distribution of mergers (e.g., Patton et al., 2002) and the space density of local massive elliptical galaxies (e.g., Gardner et al., 1997).

The number counts of the distant dusty galaxies detected with SCUBA, *Infrared Space Observatory* (*ISO*) and others, cannot be reproduced by galaxy models without strong evolution (e.g., Elbaz et al., 1999; Blain et al., 1999b). The evolution is dominated by luminosity evolution with a substantial increase in the luminosity density towards higher redshift. One way for the luminosity density to increase with redshift is by increasing the number of ULIRGs. For a luminosity function that would mean to increase the value of $L_\star$, which is the turn-over point between faint and bright sources. As redshift information for the SCUBA sources is very difficult to obtain, the exact shape of the evolution is difficult to constrain observationally.

The star formation rate of the SCUBA sources can be estimated from their FIR luminosity assuming that the heating of the dust is powered by star formation. The SFRs estimated for SCUBA sources are in the order of 100-1000 $M_\odot yr^{-1}$. Determining the FIR luminosity from the submm flux is done typically by assuming that the SED is described by a blackbody modified by an emissivity function $f_\nu \propto \nu^\beta$, where β takes values typically of 1.5-2. Often only one or few points on the SED are known, and hence the uncertainties on the luminosity are dominated by the uncertainty from not knowing the exact temperature and β. The conversion between SFR and FIR luminosity can be determined from models for star formation, in which an initial mass function is assumed (for a review see e.g., Kennicutt, 1998).

It has been found, that a significant fraction of the bright SCUBA galaxies harbour active galactic nuclei (AGN) (e.g., Alexander et al., 2003; Ivison et al., 2000). Thus star formation is not the only mechanism heating the dust, though it is the dominant heating mechanism (Alexander et al., 2003; Waskett et al., 2003). Many of the local ULIRGs host an AGN, though the connection between starburst and AGN is not fully understood. The empirical relation between the black hole mass and the mass of the host galaxy (Magorrian et al., 1998), shows that there is a close relation between the formation of the stars and the nuclear black hole. It is possible that the massive starburst and the fueling of the AGN in ULIRGs is triggered by a dramatic merging process (Genzel et al., 1998), and it is possible that the ULIRGs are part of a common evolutionary sequence with quasars (Haas et al., 2003).

1.4 Submillimetre observations

The instrument SCUBA is a submm wavelength mapping instrument. Of such instruments, it is the first one with a large number of bolometers. More recently other millimetre mapping instruments have appeared, such as the MAMBO (Max-Planck Millimeter Bolometer) and SIMBA (SEST IMaging Bolometer Array). SCUBA can observe simultaneously 850 μm and 450 μm. The bolometer arrays have 37 elements at 850 μm and 91 elements at 450 μm. Given the diameter of 15 m of the James Clerk Maxwell Telescope (JCMT, where SCUBA is mounted),

the full width at half maximum (FWHM) of the beam at $850\,\mu$m is $15''$ and at $450\,\mu$m is $\sim 7.5''$. To fully sample the beam at both wavelengths, the secondary mirror and the telescope are nodded in a 16-point or 64-point jiggle pattern.

The JCMT is located at $4092\,$m above sea level at Mauna Kea at Hawaii. In the FIR, submm and mm, there are only few open windows in the atmosphere in terms of wavelengths, where it is possible to do astronomical observations. Thus the location at high altitude is crucial for minimising the telluric absorption.

Given the large beam at $850\,\mu$m of $15''$, in deep observations the background noise is caused by both instrumental noise and unresolved faint sources. Using the cumulative surface number density of sources it is possible to determine a flux limit for which the unresolved faint sources will create confusion in the map. This flux limit is known as the *confusion limit*. For the JCMT at $850\,\mu$m the confusion limit is $\sim 2\,$mJy.

The only way to observe fluxes fainter than $2\,$mJy at $850\,\mu$m with SCUBA is to target massive galaxy clusters. The deep gravitational potential wells of the clusters will cause a strong effect of *gravitational lensing*, where both the fluxes of background sources and the region behind the cluster is magnified. Especially the latter plays a very important role in this type of observations: the distance between sources is increased, which makes it possible to separate the sources and thereby detect them individually. In SCUBA observations, this effect is of major importance as it reduces the effective confusion limit to fainter fluxes, and thereby allows for observations of sources with $850\,\mu$m fluxes $< 2\,$mJy.

A unique aspect of submm observations at redshifts $z > 1$ is that the observable flux density for a source of a given FIR luminosity is essentially constant out to redshifts $z \approx 8$. This is the effect of the geometrical dimming being cancelled by the so-called *negative k-correction*, which is the redshifting of the peak of the SED into the observing band. This is illustrated in Figure 1.3. The important consequences of this for SCUBA observations are: (*i*) that observations are volume-limited to that redshift $z \sim 8$; (*ii*) in deeper observations fainter sources are being observed, not more distant sources (in e.g. optical observations this is the opposite, where deep observations mean probing a larger volume). This means that from the measured submm flux estimates cannot be made for the distance, which is why follow-up observations at other wavelengths are crucial.

1.5 Previous far-infrared and submm surveys

The first infrared satellite was *Infrared Astronomical Satellite* (*IRAS*), for which the sensitivity of the instruments allowed for observations of sources typically with redshift < 0.3 and the major extragalactic catalogues published are the PSCz catalogue and the QDOT survey (Saunders et al., 1990, 2000; Lawrence et al., 1999).

The successor to *IRAS* was the Infrared Space Observatory (*ISO*) with which large surveys have been conducted both in the mid-IR with CAM and in the FIR with PHOT. With ISO it was possible to probe luminous IR galaxies ($L_{bol} > 10^{11}L_{\odot}$) to redshifts ~ 1. The extragalactic surveys for star forming galaxies include the European Large Area ISO survey (ELAIS; Oliver et al., 2000; Efstathiou et al., 2000), which was conducted with ISOCAM and ISOPHOT. Furthermore, ISOCAM
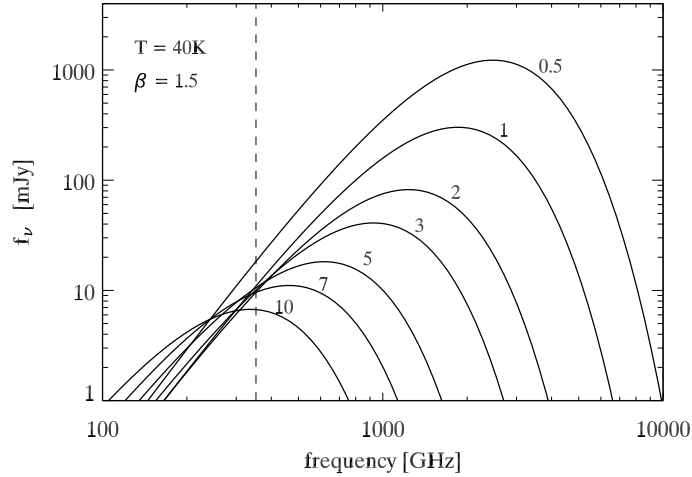
Figure 1.3: *For a given luminosity, the 850 μm flux density is essentially constant between redshift 1 and 8, as the negative k-correction cancels the geometric dimming of the light. We illustrate this by plotting an SED of a blackbody which has been modified with a emissivity function, $\propto \nu^\beta$, for different redshifts (redshift is indicated close to each of the curves). The dashed line indicates where 850 μm (= 353 GHz) is. The SED has been normalised to 10 mJy at 850 μm for redshift $z = 3$, which corresponds to a luminosity is $\sim 4 \times 10^{13}\, L_\odot$, for a cosmology of $H_0 = 70\, km/s/Mpc$, $\Omega_M = 0.3$ and $\Omega_\Lambda = 0.7$.*

surveys include the observations of the HDF (Oliver et al., 2002), the Lockman Hole and the Marano Field (Elbaz et al., 1999), and cluster fields (Altieri et al., 1999 and Metcalfe et al., 2003). The major ISOPHOT surveys are FIRBACK (Puget et al., 1999; Dole et al., 2001) and deep observations of the Lockman Hole (Kawara et al., 2004, 1998).

The published submillimetre surveys are both blank field surveys and lens surveys. The blank field surveys are the Canada-UK Deep SCUBA Survey (CUDSS; Eales et al., 2000; Webb et al., 2003a), which covered parts of the 3h and 14h field of the Canada-France Deep Fields; the UK 8 mJy survey (Scott et al., 2002), which covered parts of the Lockman Hole and the ELAIS N2 fields; the Hawaii Deep Fields (Barger et al., 1999b); and the Hubble Deep Field has been observed extensively (Hughes et al., 1998; Borys et al., 2003; Serjeant et al., 2003). The lens surveys are the UK-SCUBA Lens Survey (Smail et al., 1997, 2002), for which Cowie et al. (2002) obtained deeper data for three of the seven fields, and a shallow cluster survey of eight clusters by Chapman et al. (2002). Additionally, Barnard et al. (2004) have placed upper limits for the number of bright $S_{850} > 50$ mJy.

The sensitive millimetre instrument MAMBO is mounted at the IRAM 30 m telescope. The 1.2 mm surveys for high redshift galaxies are of the cluster field A2125 (Carilli et al., 2001), the NTT Deep Field (Bertoldi et al., 2002; Dannerbauer et al., 2002, 2004) and the large survey of the Lockman Hole and ELAIS N2 (Greve et al., (2004).

1.6 Outline of this thesis

Chapter 2
Source extraction of sources with low signal-to-noise ratios ($S/N > 3$) from maps with structured background is a non-trivial task and it is important to use as much of the available information as possible, such as the size and the shape of the beam. We have explored the mathematically rigorous Mexican Hat Wavelets (MHW) algorithm as a source extraction tool from SCUBA jiggle-maps. This is presented, in Chapter 2 as a case study on the data set of A2218. Extensive simulations have been performed to test the reliability of MHW. We demonstrate that MHW is a powerful tool for our purpose. The results are presented along a with multi-wavelength study of the extracted submm sources.

Chapter 3
The Leiden-SCUBA Lens Survey is the basis of this thesis. This survey is the largest survey of its kind to date. As previously mentioned, it is a lens-survey in which field of massive galaxy clusters have been observed. In Chapter 3, the analysis and resulting catalogue of the survey is presented along with the final number counts. This work adds a substantial contribution to the number of faint submm sources known. As the survey probes both the faint and the bright end, it is the first time that a turn-over in the number counts has been directly detected from a single survey. Based on the number counts the contribution to the background is determined, and almost all of the integrated submm background radiation is resolved. The dominant contribution to the background arises from sources with fluxes between 0.5 and 2.5 mJy.

Chapter 4
The number count is one of the few observables for the submm galaxy population as an ensemble. The number counts can be used for constraining models of the SMG population. In Chapter 4 we present a first analysis of the counts, in which we fit a model for galaxy evolution to the $850\,\mu$m number counts. In the model it is assumed that the $60\,\mu$m *IRAS* luminosity function (Saunders et al., 1990) undergoes a significant luminosity evolution. Using the deep $850\,\mu$m number counts from the Leiden-SCUBA Lens Survey in combination with deep radio counts, we are able to place better constraints on the luminosity evolution. Based on the results, we calculate the predicted star formation rate density and find that it peaks around redshift 1.8-2.

Chapter 5
To understand the nature of the submm sources and determine their redshift, extensive multi-wavelength follow-up observations are needed. Here we present optical and near-infrared (NIR) observations for 10 out of 13 fields. The identifications of SCUBA sources is often hampered by the intrinsic dust obscuration and the high redshift, which means that the bulk of the stellar light from the individual sources is observable in the NIR and not in the optical. For 48 sources, we find that about one third are reliably identified, one third have one or more plausible counterparts and about one third could not be identified with the available data. Most of the sources have been identified with red galaxies which have $I - K > 4$ and/or

9

$J - K > 2.3$. In Chapter 5, we also present spectroscopy for four of the identified galaxies. These do not exhibit Lyα in emission, which is different from the result for radio-identified SMGs with 850 μm flux > 4 mJy (Chapman et al., 2003). We discuss the details of the identification of a multiply-imaged 0.8 mJy SMG in A2218.

Focusing on the MS1054-03 field, which has the deepest ever NIR data for a galaxy cluster, we study the submm emission from the extremely red objects (EROs; $I - K > 4$) and distant red galaxies (DRGs; $J - K > 2.3$). We find that these two populations have average submm fluxes in the order of 1 mJy and contribute to $\approx 20-30\%$ of the integrated submm EBL. Combining this result with the optical/NIR identifications of the SMGs, we find good evidence for a strong relation between the SMG population and ERO/DRG population.

Chapter 6
The brightest source in the Leiden-SCUBA Lens Survey has been securely identified as a type-1 quasar. This is the first submm selected type-1 quasar. The identification and the relevant details were presented in an article (Knudsen et al., 2003), upon which Chapter 6 is based. The quasar appears to have a higher submm flux than optically selected quasars with similar optical properties. A possible explanation for the high submm flux is that the host galaxy is undergoing intense star formation. This is supported by a recent discovery of one of the most massive CO reservoirs known at high redshift.

Chapter 7
In Chapter 7, we summarise the work and main conclusions presented in this thesis. We discuss this in perspective with other aspects concerning the SMGs, which were not discussed in the preceding chapters. We highlight important unanswered questions, which are essential for our understanding of the SMGs and their role for in galaxy formation and evolution.

References

Alexander, D.M., Bauer, F.E., Brandt, W.N., et al., 2003, AJ, 125, 383
Altieri, B. Metcalfe, L., Kneib, J.-P., et al., 1999, A&A, 343, L65
Armand, C., Milliard, B. & Deharveng, J.M., 1994, A&A, 284, 12
Barger, A.J., Cowie, L.L., Sanders, D.B., et al., 1998, Nature, 394, 248
Barger, A.J., Cowie, L.L. & Sanders, D.B., 1999, ApJ, 518, L5
Barger, A.J., Cowie, L.L. & Richards, E.A., 2000, AJ, 199, 2092
Barnard, V.E., Vielva, P., Pierce-Price, D.P.I., et al., 2004, MNRAS, 352, 961
Baugh, C.M., Cole, S., Frenk, C.S. & Lacey, C.G., 1998, ApJ, 498, 504
Bernstein, R.A., 1999, in *The Hy-Redshift Universe*, eds. A.J. Bunker & W.J.M. van Breughel, ASP Conf.Series, Vol. 193, ASP, San Francisco, p. 487
Bernstein, R.A., Freedman, W.L. & Madore, B.F., 2002a, ApJ, 571, 56

Bernstein, R.A., Freedman, W.L. & Madore, B.F., 2002b, ApJ, 571, 107

Bertoldi, F., Menten, K.M., Kreysa, E., Carilli, C.L., Owen, F., 2000, in *JD9: Cold Gas and Dust at High Redshift*, Highlights of Astronomy, Vol. 12, ed. D.J. Wilner, p. 473 (astro-ph/0010553)

Blain, A.W., Kneib, J.-P., Ivison, R.J. & Smail, I., 1999a, ApJ, 512, L87

Blain, A.W., Smail, I., Ivison, R.J. & Kneib, J.-P., 1999b, MNRAS, 302, 632

Borys, C., Chapman, S., Halpern, M. & Scott, D., 2003, MNRAS, 344, 385

Bouwens, B., Broadhurst, T. & Illingworth, G., 2003, ApJ, 593, 640

Carilli, C., Owen, F., Yun, M., et al., 2001, in *Deep millimeter surveys: implications for galaxy formation and evolution*, eds. J.D. Lowenthal & D.H. Hughes, p. 27

Chapman, S.C., Scott, D., Borys C. & Fahlman, G.G., 2002, MNRAS, 330, 92

Chapman, S.C., Blain, A.W., Ivison, R.J. & Smail, I.R., 2003, Nature, 422, 695

Cole, S., Aragon-Salamanca, A., Frenk, C.S., Navarro, J.F. & Zepf, S.E., 1994, MNRAS, 271, 781

Connolly, A.J., Szalay, A.S., Dickinson, M., Subbarao, M.U. & Brunner, R.J., 1997, ApJ, L11

Cowie, L.L., Songaila, A. & Barger, A.M., 1999, ApJ, 118, 603

Cowie, L.L., Barger, A.J. & Kneib, J.-P., 2002, AJ, 123, 2197

Dannerbauer, H., Lehnert, M.D., Lutz, D., et al., 2002, ApJ, 573, 473

Dannerbauer, H., Lehnert, M.D., Lutz, D., et al., 2004, ApJ, 606, 664

Dole, H., Gispert, R., Lagache, G., et al., 2001, A&A, 372, 364

Dole, H., Le Floc'h, E., Perez-Gonzalez, P.G., et al., 2004, ApJS, in press (astro-ph/0406021)

Dwek, E. & Arendt, R.G., 1998, ApJ, 508, L9

Dwek, E. & Krennich, F., 2004, ApJ, submitted (astro-ph/0406565)

Eales, S., Lilly, S., Webb, T., et al., 2000, AJ, 120, 2244

Efstathiou, A., Oliver, S., Rowan-Robinson, M., 2000, MNRAS, 319, 1169

Eggen, O.J., Lynden-Bell, D. & Sandage, A.R., 1962, ApJ, 136, 748

Elbaz, D., Cesarsky, C.J., Fadda, D., et al., 1999, A&A 351, L37

Fazio, G.G., Ashby, M.L.N., Barnby, P., et al., 2004, ApJS, in press (astro-ph/0405595)

Finkbeiner, D.P., Davis, M. & Schlegel, D.J., 2000, ApJ, 544, 81

Fixsen, D.J., Dwek, E., Mather, J.C., Bennett, C.L. & Shafer, R.A., 1998, ApJ, 508, 123

Flores, H., Hammer, F., Thuan, T.X., et al., 1999, ApJ, 517, 148

Fontana, A., Poli, F., Menci, N., et al., 2003, ApJ, 587, 544

Fukugita, M., Hogan, C.J. & Peebles, P.J.E., 1998, ApJ, 503, 518

Gardner, J.P., Sharples, R.M., Frenk, C.S. & Carrasco, B.E., 1997, ApJ, 480, L99

Genzel, R., Lutz, D. & Tacconi, L., 1998, Nature, 395, 859

Greve, T.R., Ivison, R.J., Bertoldi, F., et al., 2004, MNRAS, *submitted* (astro-ph/0405361)

Guiderdoni, B., Hivon, E., Bouchet, F.R. & Maffei, B., 1998, MNRAS, 295, 877

Haas, M., Klaas, U., Müller, S.A.H., et al., 2003, A&A, 402, 87

Haarsma, D.B., Partridge, R.B., Windhorst, R.A. & Richards, E.A., 2000, ApJ, 544, 641

Hauser, M.G., Arendt, R.G. & Kelsall, T., 1998, ApJ, 508, 25

Hauser, M.G. & Dwek, E., 2001, ARA&A, 39, 249

Holland, W.S., Robson, E.I., Gear, W.K., et al, 1999, MNRAS, 303, 659

Hu, E.M., Cowie, L.L., Capak, P., et al., 2004, ApJ, 127, 563

Hughes, D.H., Serjeant, S., Dunlop, J., et al., 1998, Nature, 394, 241

Hubble, E.P., 1926, ApJ, 64, 321

Ivison, R.J., Smail, I., Barger, A.J., et al., 2000, MNRAS, 315, 209

Kauffmann, G., Colberg, J.M., Diaferio, A. & White, S.D.M., 1999, MNRAS, 303, 188

Kawara, K., Sato, Y., Matsuhara, H., et al., 1998, A&A, 336, L9

Kawara, K., Matsuhara, H., Okuda, H., et al., 2004, A&A, 413, 843

Kennicutt, R.C., 1998, ARA&A, 36, 189

Kim, D.-C. & Sanders, D.B., 1998, ApJS, 119, 41

References

Kiss, C., Abraham, P., Klaas, U., Juvela, M. & Lemke, D., 2001, A&A, 380, 388

Knudsen, K.K., van der Werf, P.P. & Jaffe W., 2003, A&A, 411, 343

Lagache, G., Abergel, A., Boulanger, F., Desert, F.-X. & Puget, J.-L., 2000, A&A, 344, 322

Lagache, G., Haffner, L.M., Reynolds, R.J. & Tufte, S.L., 2000, A&A, 354, 247

Lampton, M., Bowyer, S. & Deharveng, J.M., 1990, in *The Galactic and Extragalactic Background Radiation*, eds. S. Bowyer & C. Leinert, Proc. IAU, Vol. 139, Kluwer, Dordrecht, p. 449

Lawrence, A., Rowan-Robinson, M., Ellis, R.S., et al., 1999, MNRAS, 308, 897

Lilly, S.C., Le Fèvre, O., Hammer, F. & Crampton, D., 1996, ApJ, 460, L1

Magorrian, J., Tremaine, S., Richstone, D., et al., 1998, AJ, 115, 2285

Madau, P., Ferguson, H.C., Dickinson, M.E., et al., 1996, MNRAS, 283, 1388

Madau, P., Pozzetti, L. & Dickinson, M., 1998, ApJ, 498, 106

Mather, J.C., Cheng, E.S., Cottingham, D.A., et al., 1994, ApJ, 420, 439

Meurer, G.R., Heckman, T.M., Lehnert, M.D., Leitherer, C. & Lowenthal, J., 1997, AJ, 114, 54

Meurer, G.R., Heckman, T.M. & Calzetti, D., 1999, ApJ, 521, 64

Metcalfe, L., Kneib, J.-P., McBreen, B., et al., 2003, A&A, 407, 791

Moorwood, A.F.M., van der Werf, P.P., Cuby, J.-G. & Oliva, E., 2000, A&A, 362, 9

Moriondo, G., Cimatti, A. & Daddi, E., 2000, A&A, 364, 26

Murthy, J., Hall, D., Earl, M., Henry, R.C. & Holberg, J.B., 1999, ApJ, 522, p. 904

Norman, C., Ptak, A., Hornschemeier, A., et al., 2004, ApJ, 607, 721

Oliver, S., Rowan-Robinson, M., Alexander, D.M., et al., 2000, MNRAS, 316, 749

Oliver, S., Mann, R.G., Carballo, R., et al., 2002, MNRAS, 332, 536

Papovich, C., Dole, H., Egami, E., et al., 2004, ApJS, in press (astro-ph/0406035)

Patton, D.R., Pritchet, C.J., Carlberg, R.G., et al., 2002, 565, 208

Pettini, M., Kellogg, M., Steidel, C.C., et al., 1998, ApJ, 508, 539

Pozzetti, L., Madau, P., Zamorani, G., Ferguson, H. & Bruzual, A., 1998, MNRAS, 298, 1133

Press, W.H. & Schechter, P., 1974, ApJ, 187, 425

Puget, J.-L., Abergel, A., Bernard, J.-P., et al., 1996, A&A, 308, L5

Puget, J.-L., Lagache, G., Clements, D.L., et al., 1999, A&A, 345, 29

Sanders, D.B. & Mirabel, I.F., 1996, ARA&A, 34, 749

Saunders, W., Rowan-Robinson, M., Lawrence, A., et al., 1990, MNRAS, 242, 318

Saunders, W., Sutherland, W.J., Maddox, S.J., et al., 2000, MNRAS, 317, 55

Schlegel, D.J., Finkbeiner, D.P. & Davis, M., 1998, ApJ, 500, 525

Scott, S.E., Fox, M.J., Dunlop, J.S., et al., 2002, MNRAS, 331, 817

Serjeant, S., Dunlop, J.S., Mann, R.G., et al., 2003, MNRAS, 344, 887

Smail, I., Ivison, R.J. & Blain, A.W., 1997, ApJ, 490, L5

Smail, I., Ivison, R.J., Blain, A.W. & Kneib, J.–P., 2002, MNRAS, 331, 495

Soifer, B.T., Neugebauer, G. & Houck, J.R., 1987, ARA&A, 25, 187

Stanev, T. & Franceschini, A., 1998, ApJ, 494, L159

Stanway, E.R., Bunker, A., McMahon, R., et al., 2004, ApJ, 607, 704

Steidel, C.C., Adelberger, K.L., Giavalisco, M., Dickinson, M. & Pettini, M., 1999, ApJ, 519, 1

Toller, G., Tanabe, H. & Weinberg, J.L., 1987, A&A, 188, 24

Tresse, L., Maddox, S.J., Le Fèvre, O. & Cuby, J.-G., 2002, MNRAS, 337, 369

Waskett, T.J., Eales, S.A., Gear, W.K., et al., 2003, MNRAS, 341, 1217

Webb, T.M., Eales, S.A., Lilly, S.J., et al., 2003, ApJ, 587, 41

Wright, E.L. & Johnson, B.D., 2001, ApJ, submitted (astro-ph/0107205)

Yan, L., McCarthy, P.J., Freudling, W., et al., 1999, ApJ, 519, L47

Chapter 2

Point source detection in SCUBA jiggle-maps using Mexican Hat Wavelets: analysis of A2218

K.K. Knudsen, V.E. Barnard, P. Vielva, J.-P. Kneib, P.P. van der Werf, A.W. Blain, R.B. Barrerio, R.J. Ivison, I. Smail, J.A. Peacock

Abstract

Extraction of sources with low signal-to-noise from maps with structured background is a non-trivial task. In this article we study source extraction from submillimetre jiggle-maps from the instrument SCUBA (Submillimetre Common-User Bolometer Array) using the algorithm Mexican Hat Wavelets (MHW), a technique of isotropic wavelets. As a case study we have used a large jiggle map of the galaxy A2218. Through analysis of the data and extensive experiments including Monte Carlo simulations we have tested the performance of MHW as a source extraction tool. We find that it is a powerful tool for reliable extraction of low signal-to-noise from SCUBA jiggle-maps. The importance of being able to extract such sources comes from the demand of studying the faint end of the submillimetre number counts of submm-bright high redshift sources. In the SCUBA map of A2218, nine sources were detected. After correcting for the gravitational lensing, which makes it possible to study objects fainter than the blank field confusion limit, three sources were found to have flux fainter this limit. A multi-wavelength follow-up study including optical, near infrared and 15 μm imaging has been carried out. Three of the sources have been identified as a multiply-imaged background source at redshift $z = 2.516$. One source has been identified with a redshift $z = 1.034$ arc. For seven of the nine sources at least one very or extremely red galaxy is found within the identification search radius.

2.1 Introduction

The arrival of the Submillimetre Common-User Bolometer Array (SCUBA; Holland et al., 1999) on the James Clerk Maxwell Telescope (JCMT) has heralded a new era in galaxy evolution studies. The new populations of submillimetre-bright, high redshift galaxies (Hughes et al., 1998) have been studied in two types of surveys: gravitational lens surveys, where pointings are made in the region of

known cluster lenses in order to detect lensed background galaxies, and in blank field surveys, where no strongly lensing clusters are present and the fields typically are selected to overlap with areas already surveyed at other wavelengths.

The blank field surveys (Barger et al., 1999b; Hughes et al., 1998; Eales et al., 2000; Scott et al., 2002; Serjeant et al., 2003; Webb et al., 2003a) have produced counts at fluxes brighter than $S_{850} \sim 2$ mJy. This limiting flux is caused by the confusion, which for the $15''$ angular resolution of the JCMT at $850\,\mu$m appears to become a problem at about 2 mJy, which has been a limiting factor in the flux depths of these surveys (Blain et al., 1998; Condon, 1974; Hogg 2001; Barger et al., 1999b; Eales et al., 2000).

The cluster gravitational lens surveys (Smail et al., 1997a, 2002; Cowie et al., 2002; Chapman et al., 2002a; Knudsen et al., *Chapter 3*) have the advantage that they suffer less from confusion than blank-field surveys, as the angular magnification reduces the flux limit when confusion becomes a problem, and so these surveys have produced the deepest counts. The actual area surveyed through the lens is smaller than the SCUBA field-of-view, but is spread out as a result of the lensing. SCUBA's $2.3'$ diameter field-of-view is well-matched to the spreading caused by typical gravitational lenses. In this paper we present one of the deepest ever SCUBA maps of a gravitational lens, and apply a new technique for detecting the point sources in the image.

2.1.1 Detection techniques used in other surveys

The noise in SCUBA jiggle maps has a temporal variation and the sources we wish to detect typically have low signal-to-noise ratio (S/N), hence the source extraction algorithm applied to the SCUBA maps must be a robust, well-characterized method. High-redshift point sources typically have extents of a few arcseconds, so that in comparison to SCUBA's beam of $\sim 15''$ at $850\,\mu$m they can be regarded as point sources. A number of techniques have been used for locating point sources in previous SCUBA jiggle-maps.

In their jiggle-maps of the Canada UK Deep SCUBA Survey (CUDSS) fields, Eales et al. (2000) and Webb et al. (2003a) selected sources from a convolved signal-to-noise map, which was constructed by convolving their reduced map with a beam map derived from a calibrator, and dividing by a simulated noise map (see section 2.2.3). An iterative deconvolution (CLEANing) routine was then used for determination of the position and flux of the detected sources.

In the 8-mJy survey (Scott et al., 2002), sources were extracted by a simultaneous maximum-likelihood fit to the flux densities of all probable peak locations, selected purely on the grounds of flux. A template beam map from a calibration observation was centred on every pixel with flux > 3 mJy in a map convolved with a Gaussian filter. The height of each potential source was then increased independently until a minimum was found in the χ^2 statistic between this built-up map and the real map. A similar approach was used in the extended Hubble Deep Field (HDF) and flanking fields source extraction (Serjeant et al., 2003).

In the cluster lens surveys, extraction techniques have tended to be simpler, as these surveys yield smaller fields with fewer sources. The UK-SCUBA Lens Survey group (Smail et al., 1997a, 2002) used SExtractor (Bertin & Arnouts, 1996),

which was primarily developed for use in optical images which have very different noise characteristics to SCUBA maps. In the Hawaiian deep fields, Barger et al. (1999b) simply used a signal-to-noise criterion for their source selection, a technique also used for the original HDF map source extraction (Hughes et al., 1998).

2.1.2 The Mexican Hat Wavelet Technique

Wavelets are a useful tool for many aspects of signal analysis, acting as a band–pass filter on the Fourier Transform of an image. In the resulting wavelet space, structures of certain shape and size are preferentially selected, depending on the definition of the 'mother wavelet' (see section 2.3.1).

In this paper, we use the Mexican Hat Wavelet (MHW, so-called because the mother wavelet is like a sombrero in 3-d space) technique and routines developed by Cayón et al. (2000), Sanz et al. (2001), Vielva et al. (2001a,2001b) and Vielva (2003) for use with anticipated *Planck-Surveyor* data. The MHW will be used in analysis of the *Planck-Surveyor* data to remove contaminating foreground extragalactic point sources and leave the Cosmic Microwave Background (CMB) signal. However in this paper we are interested in the point sources themselves as the end product. The key advantage of the MHW technique is that without needing to characterise the background and noise in an image, Gaussian shaped beams can be picked out from a variety of backgrounds with accurate positions and fluxes. This makes the technique ideal for submillimetre images where sources are significant in size with respect to the field-of-view, and the noise is often relatively high, variable across the field and hard to model accurately.

Other wavelet routines have been suggested for the extraction of point sources (Tenorio et al., 1999), but Sanz et al. (2001) demonstrated that for Gaussian-shaped beams the best wavelet basis to use for a wide range of backgrounds is the Mexican Hat. This was found to be preferable to a straightforward Gaussian filter, which was found to produce a smoothing effect, lowering the amplitudes of detected sources with respect to the noise levels within a map. The MHW has also been used in detecting point sources in X-ray data by Damiani et al. (1997).

This paper is intended to serve as an introduction to the use of the MHW technique in SCUBA jiggle-maps, and so only the results from one cluster image are presented here: A2218. Another paper (Knudsen et al., *Chapter 3*) describes the results of applying the technique to a wider survey of cluster lenses, and another (Barnard et al., 2004) describes a parallel application of the technique to SCUBA scan-maps of Galactic regions in order to determine the extremely bright, $S_{850} \geq 50$ mJy SCUBA galaxy count.

2.2 Observations and data reduction

2.2.1 Observations

We have obtained observations of the cluster of galaxies A2218 at $850\,\mu$m and $450\,\mu$m with SCUBA. The data were obtained during March 1998, August 2000, January 2001 and January 2002. SCUBA is a submillimetre mapping instrument
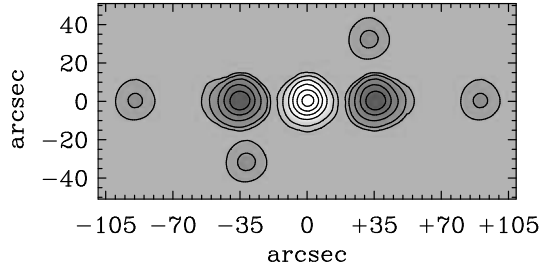
Figure 2.1: *The 850 μm beam map. The contours represent the levels −0.4,−0.3,−0.2, −0.1,−0.03,−0.01,−0.02,0.1,0.3,0.5,0.7,0.9. The data for A2218 were obtained with different chopping configurations. The beam map was constructed by weighting the different chop configurations with observing time. Most of the data were obtained with a chop throw of 35″. The configurations with chop throws of 45″ and 90″ were used for a short time in the observations, which is reflected by the few per cent in the beam map. The negative dips at 35″ have a little tail away from the central peak, which is due to the 45″ chop throw.*

operating at 850 μm and 450 μm simultaneously (Holland et al., 1999). The field–of–view on the sky, which is approximately the same for both arrays, is roughly circular with a diameter of 2.3′. The observations were carried out in jiggle mode with a 64 point jiggle pattern, in order to fully sample the beam at both operating wavelengths. In jiggle map mode, the secondary mirror and the telescope is nodded in a 16-point and 64-point pattern. In order to cover a larger sky area four pointings were made, though with a big overlap region. The primary sky subtraction is done by chopping the secondary mirror. The chop configuration used for most of the time was a chop throw of 35″ with a chopping position angle fixed in right ascension (RA), though larger chop throws and other position angle has also been used for a limited part of the observations (resulting beam is shown in Figure 2.1). As a result of the chopping the beam pattern has a central positive peak with negative sidelobes on each side each with minus half the peak flux. During the observations the pointing was checked every hour by observing nearby bright blazars with known positions. The noise level of the bolometer arrays was checked at least twice during an observing shift, and the atmospheric opacity, τ, was determined with JCMT at 850 μm and 450 μm every two–three hours and supplemented with the $\tau_{225\text{GHz}}$ data from the neighboring Caltech Submillimeter Observatory (CSO). Calibrators with accurately known flux densities were observed every two to three hours. If available, primary calibrators, i.e. planets, preferably Uranus, were observed at least once during an observing shift.

The zenith opacity was $0.15 < \tau_{850\mu\text{m}} < 0.40$. The data were flux calibrated using both primary and secondary calibrators (e.g., Sandell et al., 1994). The uncertainty in the flux calibration is approximately 10 % at 850 μm and approximately 30 % at 450 μm. The total observing time was 39.7 hours at 850 μm and 33.4 hours at 450 μm without overhead, i.e. without time needed for the chopping, jiggle, etc. The total area surveyed is 11.8 arcmin^2 at 850 μm and 9.1 arcmin^2 at 450 μm.

2.2.2 Reduction

The data were reduced using the standard SURF package (Jenness & Lightfoot, 1998). The reduction procedure is described in detail in the catalogue paper for the Leiden-SCUBA Lens Survey (Knudsen et al., in prep. (Chapter 3)). Unless otherwise mentioned the 850 μm maps used in the analysis have been smoothed with a 5″ full width half maximum (FWHM) Gaussian to reduce spatial high frequency noise. Similarly the 450 μm map was smoothed with a 10″ FWHM Gaussian. When smoothing the 450 μm data with a Gaussian with a larger the FWHM than the beam itself, any regular high redshift source will become a point source, similar to the 850 μm, with all the 450 μm flux collected in one beam. After smoothing the maps, the final beam sizes are 15.1″ at 850 μm and 12.5″ at 450 μm. The resulting maps are shown in Figure 2.2. The sensitivity in the final 850 μm map is 0.65 mJy/beam in the deepest part of the map and 1.06 mJy/beam area-weighted, and the sensitivity in the final 450 μm map is 3.2 mJy/beam and 16.0 mJy/beam area-weighted, as determined from the noise simulations described below.

In this paper we concentrate on the 850 μm map. Analysis of 450 μm maps is more difficult because the 450 μm beam pattern is very sensitive to temperature variations on the primary of the JCMT. The beam pattern cannot easily be described by a 2D Gaussian function. Furthermore, both the atmospheric opacity and the uncertainty in the flux calibration are large at 450 μm. This makes observations of faint objects difficult. In the following we only use the 450 μm map to check if any source detected at 850 μm has detectable 450 μm flux.

2.2.3 Construction of noise maps

When a data set is combined and regridded into a map, some areas will be sampled less than the rest of the map. These are the areas along the edges, the areas where the bolometers are either more noisy or data has been excluded, and areas with less integration time outside the overlap between different pointings. It is thus imperative to assess the noise as function of position in the map to be able to make a reliable analysis of the observed flux map.

When data files for the SCUBA jiggle maps have been fully reduced, i.e. all correlated noise has been removed, the noise in each individual bolometer is independent of other bolometers. The sources we are observing are very faint and thus large integration times are necessary in order to reach the needed noise levels for detections. However, the observations are carried out on short time scales on the order of an hour, which are the standard lengths of our observations, thus the data points from the bolometers are dominated by noise rather than signal.

In order to determine the position–dependent noise a Monte Carlo (MC) simulation was used to construct 'empty' (i.e. no source signal present) maps representing the noise component in the real data files. For each original data file, the statistical properties of each bolometer's data set were calculated. Then a simulated data set for each bolometer was created using a Gaussian random number generator with the same properties. This produced an empty map for each original data file, and the entire set of these was reduced and concatenated using SURF in the same manner as the original data files. The resultant single map is thus one
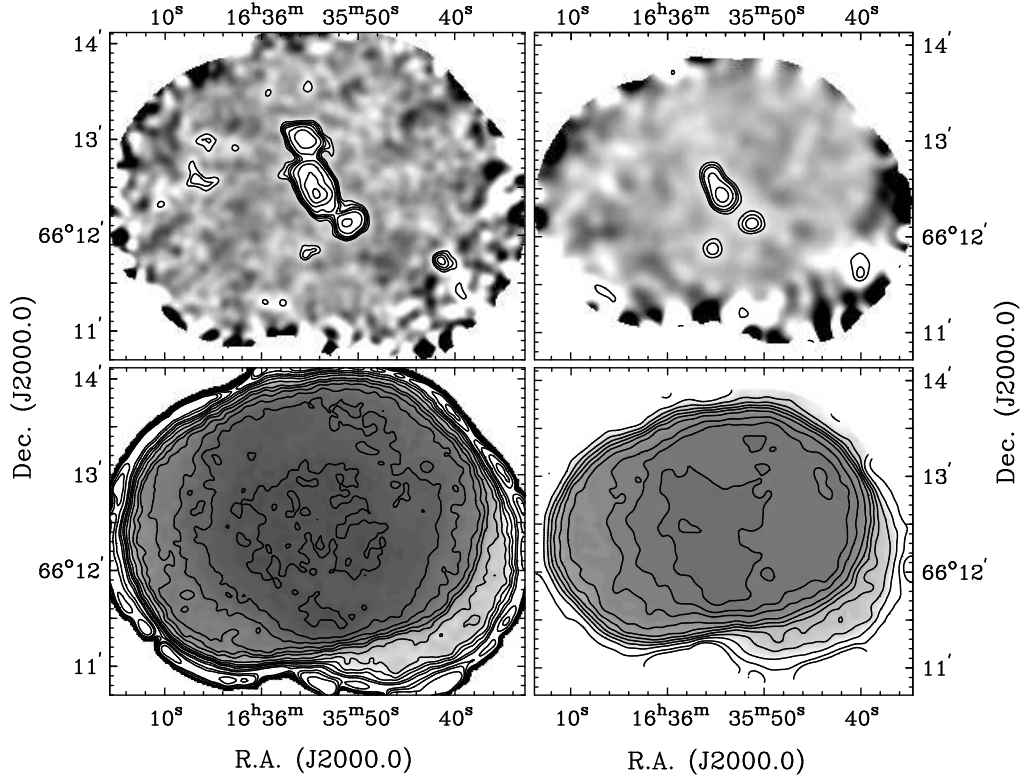
Figure 2.2: *In this mosaic the SCUBA flux maps (top) of A2218 and the corresponding noise maps are shown (bottom). The left side represent the 850 μm maps, and the right side the 450 μm maps.* **Top-left:** *The 850 μm flux map overlayed with 850 μm signal-to-noise contours of $S/N = 3,4,5,6,8,12,18,24$. The map has been cleaned and sources have been restored using the central positive peak of the beam (see Sect. 2.2.4). The map has been smoothed with a two-dimensional Gaussian with width 5″.* **Top-right:** *The 450 μm flux map overlayed with the 450 μm signal-to-noise contours of $S/N = 3,4,5,7,10$. The map has been smoothed with a two-dimensional Gaussian with width 10″.* **Bottom-left:** *The 850 μm noise map. This map represents the position dependent noise after smoothing with 5″. The contours have been overlayed to enhance the contrast and are $\sigma = 0.75,1,1.25,1.5,1.75,2,2.5,3,3.5,4,5,6,9,12,20$ mJy/beam. Darker shades of grey indicate a lower noise. The edges are clearly very noisy and the whole edge region of the map is not included in the analysis.* **Bottom-right:** *The 450 μm noise map. This is the noise map for the data smoothed with 10″. The contours have been overlayed to enhance the contrast and represent $\sigma = 3,4,5,6,8,10,12,15,20,30,60,100$ mJy/beam. Comparing left to right, the slightly smaller field of view at 450 μm is evident.*

realization of the empty map simulation procedure. This process is then repeated about 500 times. Noise maps were constructed from the simulated empty maps by taking all the empty maps and at each pixel calculate the standard deviation. The noise maps at both 850 μm and 450 μm are shown in Fig. 2.2, where it can be seen how the noise is not uniform across the field and how the different effects described above appear.

2.2.4 Deconvolution of beam map

As described in section 2.2.1, the chopping of the secondary mirror on the JCMT introduces a beam pattern with a positive peak and two negative sidelobes. This is undesirable because negative sidelobes can hide sources or bias their fluxes. Also the negative sidelobes contain useful signal that can be used in source detection. Therefore it is useful to deconvolve the beam pattern out. Since we are dealing mostly with isolated point sources the classical CLEAN algorithm (Högbom, 1974) is ideally suited for this purpose. In summary, the classical CLEAN algorithm is an iterative algorithm which searches for the brightest point, which matches the beam pattern, in the final map. The beam pattern is scaled to some fraction of the peak flux and subtracted from the map at that position. The whole process is then repeated in principle until the residual map has an r.m.s. comparable with the noise, though in practice until a given flux limit. All the information about subtracted fluxes and positions (the resultant "delta-functions") can then be used for source detection and restoration with a different beam pattern e.g. the central positive peak of the beam pattern.

In our cleaning algorithm, the selection of the peaks was done in the following way. A beam map was constructed from point source calibration observations. The central, positive peak from a calibration map was used as a template point source and was placed in the middle of the map, while the same peak was inverted and positioned relative to the center according to the chop configuration used for the observations. The negative dips were weighted according to the observing time with the particular chop configuration. The 850 μm beam map is shown in Figure 2.1. During each iteration the (cleaned) data map was convolved with the beam map and divided by the associated convolved noise map. The former was to enhance any present signal in the map and the latter was to ensure that no noise peaks (e.g. along the edges) would be mistaken for signal. The cleaning itself takes place on the unconvolved data map. We found that subtracting 10 % of the flux at each iteration produced acceptable convergence. The cleaning was continued until the residual map contained no pixels brighter than 3 times the r.m.s. noise level. Finally, the data maps were restored on top of the uncleaned residual using only the central positive peak from the beam map. The cleaned 850 μm map, where the sources have been restored using the central positive peak of the beam, is shown in Figure 2.2.

2.3 Mexican Hat Wavelets

2.3.1 Detection parameters: mathematical formalism

A brief summary of the standard mathematics involved in the Mexican Hat wavelets (MHW) transform is given below. Further detail can be found in the original papers describing this work (Cayón et al., 2000; Sanz et al., 2001; Vielva et al., 2001a, 2001b).

The continuous isotropic wavelet transform of a 2-dimensional signal $f(x)$ is

$$w_f(R, \boldsymbol{b}) = \int d^2\boldsymbol{x} \, \frac{1}{R^2} \psi\left(\frac{|\boldsymbol{x} - \boldsymbol{b}|}{R}\right) f(\boldsymbol{x}), \tag{2.1}$$

where $w_f(R, \boldsymbol{b})$ is the wavelet coefficient associated with the scale R at the point $\boldsymbol{b}$. $\psi\left(\frac{|\boldsymbol{x}-\boldsymbol{b}|}{R}\right)$ is known as the 'mother wavelet' which defines the spatial frequencies of interest. The two-dimensional Mexican Hat mother wavelet is given by

$$\psi(x) = \frac{1}{\sqrt{2\pi}} \left[2 - \left(\frac{x}{R}\right)^2\right] e^{-x^2/2R^2}. \tag{2.2}$$

The one-dimensional Mexican Hat function is plotted in Figure 2.3. A Gaussian point source, generated by the convolution of a delta function of amplitude A with a Gaussian telescope beam of FWHM θ, can be described as

$$f(\boldsymbol{x}) = \frac{A}{\Omega} e^{-x^2/2\theta^2}, \tag{2.3}$$

where Ω is the area under the beam. For such an input signal, the wavelet coefficient for a scale R at the position of the source will be

$$\frac{w_f(R, 0)}{R} = 2\sqrt{2\pi}\frac{A}{\Omega}\frac{(R/\theta)^2}{[1 + (R/\theta)^2]^2}. \tag{2.4}$$

The effectiveness of the Mexican Hat Wavelet is revealed through the definition of the *detectability* or detection level of the source. In flux space, the criterion for detection of a source is usually the signal-to-noise of the source, given by

$$D_r = \frac{A/\Omega}{\sigma_n}, \tag{2.5}$$

where σ_n is the flux r.m.s. noise.

In wavelet space, the equivalent parameter for the same point source (as a function of scale R) is defined as

$$D_w(R) = \frac{w_f(R, 0)}{\sigma_{w_n}(R)}, \tag{2.6}$$

where $\sigma_{w_n}(R)$ is the dispersion of the noise field in wavelet space.

Comparing the ratio of these two detectabilities, the amplification, $\mathcal{A}$, due to the transform into wavelet space is
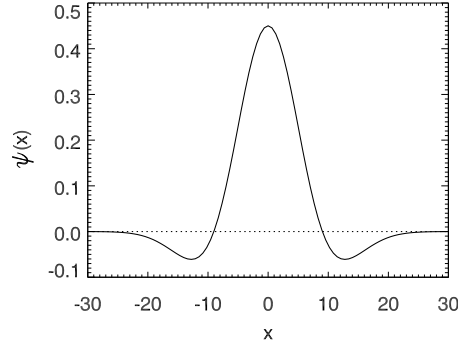
Figure 2.3: *The one-dimensional Mexican Hat function, as equation 2.2; R = 15.*

$$\mathcal{A} = \frac{D_w(R)}{D_r} = 2\sqrt{2\pi}\,\frac{(R/\theta)^2}{[1 + (R/\theta)^2]^2}\,\frac{\sigma_n}{\sigma_{w_n}(R)}. \tag{2.7}$$

This formula demonstrates that, for a suitable scale $R_{\mathrm{opt}} \simeq \theta$, the amplification possible by transforming an image into wavelet space can be very large, because at this scale the dispersion of the general noise field in wavelet space will be lower than in real space. Unless the noise field has Gaussian peaks of the same scale as the point sources (i.e. unless the noise is completely indistinguishable from the real point sources), the noise will always be relatively less amplified.

2.3.2 Detection parameters: results of previous simulations

Point source detection is primarily controlled by setting numerical requirements for two parameters, derived from the above relations. We performed initial, simple simulations to understand the response of the MHW routines to SCUBA jiggle-maps, since these are quite different in several respects to the simulated *Planck* data sets on which the technique was previously tested. The procedure involved selecting sources for the final detection list is as follows:

1. Firstly the optimal scale, R_{opt}, is calculated by the MHW software for each input map. This involves iterating through small changes in the value of R around the point source scale θ until the maximum amplification $\mathcal{A}$ is found for the map. The final value will be dependent upon the measured impact of the noise on varying scales (Vielva et al., 2001b) — noise with a characteristic scale a little larger than θ, for instance, can be most strongly counteracted by an optimal scale R_{opt} slightly smaller than θ.

2. Point source candidates are then selected at positions with wavelet coefficient values $w_f(R_{\mathrm{opt}}) \geq 2\sigma_{w_n}(R_{\mathrm{opt}})$ i.e. $D_w(R_{\mathrm{opt}}) \geq 2$. The value of 2 was suggested by our early simulations as a value which allowed all real sources to pass through to an initial catalogue.

3. For each candidate, the 'experimental' $w_f(R)$ is compared to the theoretical variation expected with R, as a further check on the source's shape. A value

of χ^2 is calculated between the expected and experimental results and the second parametrised requirement is therefore that $\chi^2 \leq 4$, i.e. that the region surrounding the identified peak has the characteristics of a Gaussian point source.

2.3.3 Application of the Mexican Hat Wavelet

Since, as discussed in Section 2.2.3, the noise level in the map varies widely, the input map to the MHW software used was a signal-to-noise map, created by dividing the final, smoothed data map by the final, smoothed noise map. This normalises the input map with respect to the noise. This is especially useful for this technique as the properties of the whole map are used to determine detection parameters, and so high noise values can distort these values unfairly.

Despite this normalisation, detections close to the edge of the map, where the noise levels are at their highest, were considered to still be unreliable and such detections in a 1.5-beam region around the edge are not retained in the final catalogue.

The standard MHW routines used require square input maps. In order to retain as much of the image for point source detection as possible, the signal-to-noise image was reflected outside of its own boundaries to make a larger square, "unfolding out" from the centre to ensure that no discontinuous edges were created. This retains all of the real data area for investigation, but does alter the power spectrum of the map, which is crucial in deciding the optimal scale for detecting point sources. Several reflection techniques were tested but none were able to retain with sufficient accuracy the characteristics of the power spectrum of the original map. Instead, a power spectrum taken from the central square of the original map, which contained noise and sources but no blank pixels, was imposed on the MHW software by hand. The MHW routines create files listing the general properties of the map and of the detected sources.

2.4 Simulations

One of the aims of this paper is to test the performance of Mexican Hat Wavelets as a source detection algorithm on SCUBA jiggle maps. To do so we do controlled detection experiments, where we simulate the maps on which we apply the MHW algorithm. From this simulations we expect to quantify the uncertainty on the position and flux determination for the individual sources, and the completeness as function of flux. Furthermore, these controlled detection experiments can be used for a qualitative understanding of the appearance of a low S/N source on a structured background; this is discussed in Appendix 2.A.

The simulations were performed in the following way. We used the Monte Carlo maps described in section 2.2.3. First to check that these maps really were empty, i.e., that there were no sources present in the maps, we performed MHW source extraction on these maps following the same procedure as for the real data. In a hundred maps we found two sources which have $S/N \sim 3$. We concluded that the MC maps were indeed empty and spurious sources would not interfere with the results of the detection experiments. At the significance levels of the
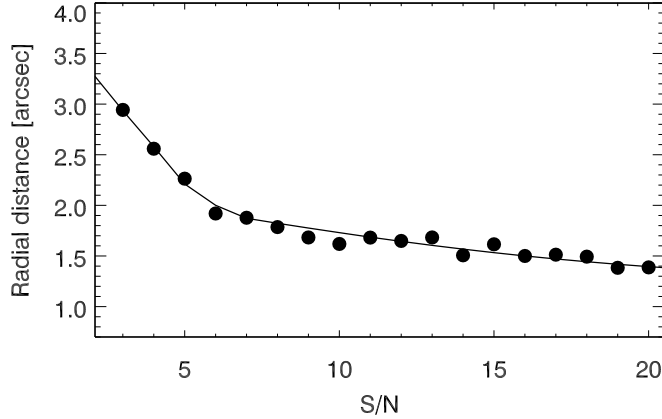
Figure 2.4: *The average radial distance between input and detection position as function of S/N based on the simulations.*
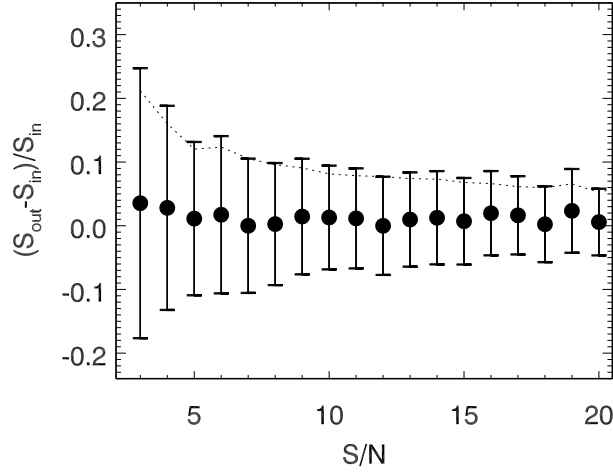
Figure 2.5: *The relative difference between the input and detected flux as function of S/N based on the simulations. The filled dots represent the average in each S/N bin, while the error bars represent the standard deviation in the same bin. The dotted line indicates the standard deviation as function of S/N. The average relative difference is off-set by a couple of percent, indicating a minor over-estimation of the flux in the source extraction.*

sources detected in the real map, the probability of spurious sources is very low as demonstrated by our MC experiments. A detailed analysis of this is performed for the full Leiden-SCUBA Lens Survey (Knudsen et al., *Chapter 3*). Point sources were added on to the MC maps. The template point source used was the central peak of a high signal-to-noise observations of point source calibrator. One point source was added at the time. We used 10 MC maps, and repeated this 400 times
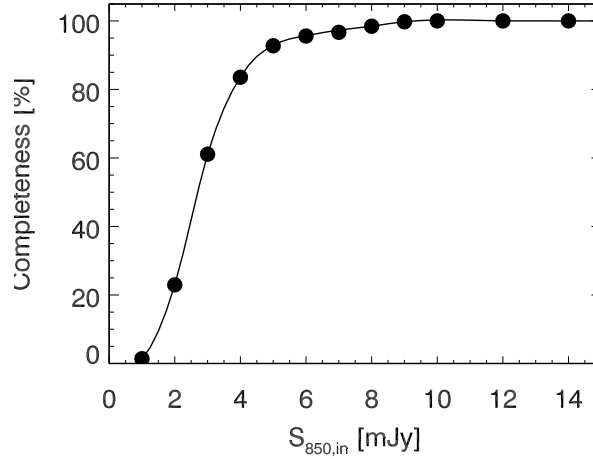
Figure 2.6: *The completeness as function of input flux based on the simulations. The 850 µm is 80 % complete at 3.8 mJy and 50 % complete at 2.7 mJy.*

for each flux step. The position was randomly chosen, with a uniform distribution across the map, so that the whole map area was well sampled. It is important to sample all parts of the mapped area as the sensitivity various across the surveyed area. The flux steps were chosen as $1, 2, 3, ..9, 10, 12, 14, .., 22, 24$ mJy. The results of the MHW source detection experiments were analysed. First we checked if the source was detected, and if so we checked if it was detected with the detection criteria described in section 2.3. The detection position and flux were then compared to the input position and flux. The deviations in position and flux were quantified as function of S/N. Furthermore, the completeness as function of input flux was analysed.

Position: The deviation between input and detection position is given as the radial distance in arcsec. In Figure 2.4 we plot the average positional deviation as function of S/N. We see that the deviation decreases with increasing S/N. The average deviation is 3″ for a $S/N \sim 3$ and 1.5″ for $S/N > 15$. We adopt these as the uncertainty on the determined position introduced by the extraction algorithm. This added in square with the pointing uncertainty of the JMCT gives the error on the determined position.

Flux: The deviation between input and detection flux is given as the difference in mJy. In Figure 2.5 we plot the relative average flux deviation, $(S_{det} - S_{in})/S_{in}$, as function of S/N. We see that the deviation decreases with increasing S/N, and that there is an offset of a few percent. The offset we interpret as a slight average overestimation of the faint sources. We use the relative average deviation as the uncertainty on the determined flux. This error will be added in square with the calibration error from the SCUBA reduction to give the total error on flux density of the individual sources.

Completeness: The completeness as function of input flux is determined from the same set of simulations. The fraction of sources detected at each flux level is calculated. The result is plotted in Figure 2.6. The observations are 80 % complete at 3.8 mJy and 50 % complete at 2.7 mJy.

2.5 Results

The total area of useful data surveyed is 7.7 arcmin^2 (see Sect. 2.3.3). The actual map covers a large area, however, we exclude the outer 1.5 beam wide edge due to larger uncertainties. The result of the source extraction with Mexican Hat wavelets is a list of nine sources detected with $S/N > 3$. Five of these sources have detectable 450 μm emission. The detected sources are listed in Table 2.1 with name, position, flux and uncertainties. The sources are named using the prefix SMM followed by their J2000 coordinates. For the 850 μm parameters we give the S/N in real space, the combined uncertainty of the flux and the uncertainty of the position. For the 450 μm, where no emission is detected, we give 3σ upper limits. The uncertainty on the 450 μm flux is 30%. In Figure 2.7 we show the 850 μm S/N map.

We subtract the sources from the map, using a template for the central beam scaled to the fluxes of the individual sources. We perform source extraction with MHW on the residual image. If there are sources closer than a beam to the other sources, which have remained undetected, then we expect them to show up in the residual map. Four sources are detected with $S/N > 3$. Three of these are directly associated with bright sources and are likely artifacts resulting from an imperfect match of the bright source and the scaled beam subtracted from the map. The fourth source may be real, but too close to the SW edge to be included in the analysis.

2.6 Discussion

2.6.1 Gravitational lensing

As A2218 is a massive galaxy cluster at redshift $z = 0.171$ (Sarazin et al., 1982) it acts like a telescope or magnifying glass of the volume behind it. The gravitational lensing of background sources caused by the gravitational potential magnifies both the brightness of the background sources and the area of the region surveyed. As a result the confusion limit is moved to a fainter flux level, thereby enabling us to reliably study the fainter submm population, which unaided is not accessible with the current telescopes and instrumentation. We exploit the detailed mass model of A2218 (Kneib et al., 1996) updated to include a recently discovered $z = 5.56$ lensed galaxy (Ellis et al., 2001).

To calculate the magnification by the gravitational lensing, the redshift must be known. The redshift is known for four sources in the field, three being a multiply-imaged object at redshift $z = 2.516$ (Kneib et al., 2004) and one being a source at redshift $z = 1.034$ (Kneib et al., 1996). For the sources with unknown redshift we assume $z = 2.5$. By means of ray-tracing, using LENSTOOL (Kneib et al.,

Table 2.1: *Sources detected in the SCUBA maps of A2218. f is flux; S/N is signal-to-noise in real space; σ gives the uncertainties on the flux and position at 850 μm and 450 μm respectively. The positional uncertainty does not include confusion errors, which are $\sim 1.9''$ (see Subsection 2.6.2.*

NAME	RA(J2000.0) h m s	Dec(J2000.0) ° ' "	f_{850} mJy	S/N	σ_{850} mJy	σ_{pos} "	f_{450} mJy	S/N	σ_{450} mJy
SMMJ16357+66117	16 35 41.2	+66 11 44	10.4	7.5	1.4	2.6	53.4	3.5	16.0
SMMJ16358+66121*	16 35 50.9	+66 12 07	8.7	11.5	1.1	2.4	22.9	5.9	6.9
SMMJ16359+66124*	16 35 54.2	+66 12 25	16.1	21.7	1.6	2.3	46.4	12.4	13.9
SMMJ16359+66126*	16 35 55.2	+66 12 38	12.8	16.9	1.5	2.2	31.8	8.3	9.5
SMMJ16359+66118	16 35 55.2	+66 11 50	3.1	3.8	0.7	3.3	17.1	4.7	5.1
SMMJ16359+66130	16 35 55.5	+66 13 00	11.3	15.8	1.3	2.2	< 11.8	...	...
SMMJ16360+66129	16 36 02.6	+66 12 55	2.8	3.5	0.6	3.3	< 14.5	...	...
SMMJ16361+66130	16 36 05.6	+66 12 59	5.2	4.9	0.9	3.1	< 17.4	...	...
SMMJ16361+66126	16 36 06.5	+66 12 34	4.8	4.6	0.8	3.1	< 17.4	...	...

* SMMJ16358+66121, SMMJ16359+66124 and SMMJ16359+66126 have been identified as a multiply-imaged galaxy, which is denoted SMMJ16359+6612 (Kneib et al., 2004).
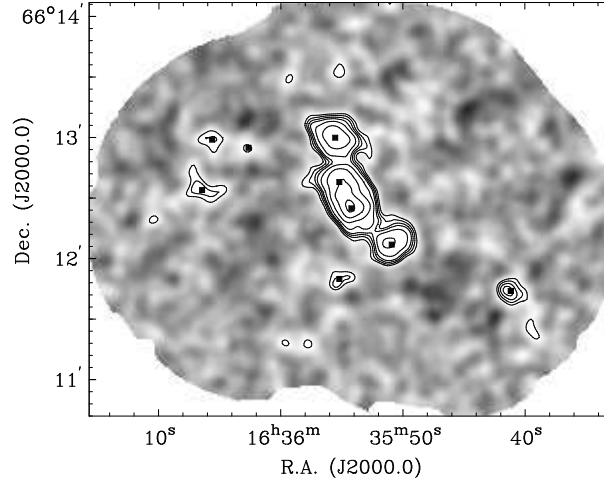
Figure 2.7: *A2218 850 μm S/N map with contours of S/N = 3,4,5,6,8,12,18,24; the boxes indicate where sources have been detected.*

1993), we determine the magnification factor for the individual sources and the observational sensitivity of the field in a source plane at redshift $z = 2.5$.

The area surveyed behind the cluster has been magnified by a factor 2.8 for the whole field, which means that the area in the source is 2.7 arcmin^2. In Figure 2.8 we show the area as function of magnification for source planes at the redshifts $z = 1,1.5,2,2.5,3,4$. About 1.3 arcmin^2 has magnification factors for the flux > 2. Furthermore, in Figure 2.8 we show the area as function of sensitivity both in the image plane and in the source plane, again for sources planes in at different redshifts, $z = 1,1.5,2,2.5,3,4$. The magnification factors of the individual singly lensed sources range between 1.6 and 6.7. For the multiply-imaged source the magnification factors for individual images are 9, 14 and 22, i.e. a total magnification of 45 for the three images combined (Kneib et al., 2004). In Table 2.2 we list the magnification factors and the lensing corrected fluxes for the individual galaxies. Three sources have unlensed fluxes fainter than the blank field confusion limit. A general discussion on the uncertainties of the determined gravitational magnification for SCUBA sources will presented in Knudsen et al. (*Chapter 3*).

2.6.2 Confusion

Understanding the confusion in a map is essential to be able to estimate the relative importance of uncertainties due to blending of sources. As a rule of thumb the confusion limit in imaging is defined as 1 source per 30 beams (e.g., Hogg, 2001). Using the definition by Hogg (2001) of a beam $\Omega_{beam} = \pi(\theta_{FWHM}/2.35)^2$ and $\theta_{FWHM} = 15''$, the number of beams in the survey 850 μm map is 217. This corresponds to 7.3 sources in the field for this field not to be confused according to those definitions. We detect 9 sources in this field, which corresponds to 1/24 sources per beam. We interpret this as the field being slightly confused, and

Table 2.2: *The magnification and lensing corrected 850 µm flux for the sources in A2218.*

NAME	z_{spec}	μ	f_{850}/μ
SMM J16357+66117	...	1.8	5.8
SMM J16359+6612*	2.516	45.0	0.8
SMM J16359+66118	1.034	6.7	0.4
SMM J16359+66130	...	4.1	2.8
SMM J16360+66129	...	2.0	1.7
SMM J16361+66125	...	1.6	2.8
SMM J16361+66130	...	1.8	2.9

* Multiply-imaged source, see Table 2.1.

draw to the readers attention that this potentially can lead to extra errors in the source detection (see e.g. Hogg, 2001, and Eales et al., 2000, for additional details concerning this issue). As discussed in Knudsen et al. (*Chapter 3*), an additional uncertainty on the position of $\sim 1.9''$ should be added to the total positional error for confused fields.

The confusion limit in blank field observations is ~ 2 mJy. Gravitational lensing pushes the confusion limit to fainter fluxes. For a single power law number count distribution of the source density on the sky with fluxes larger than S, $N(>S) \propto S^{-\alpha}$, the confusion limited is reduced by a factor $\sqrt[-\alpha]{A^{(1-\alpha)}}$, where A is the magnification (for details see Knudsen et al., *Chapter 3*). In this simple estimate we take A as the ratio between the area in the image plane and the source plane, which is 2.8 (see previous subsection). In case of the A2218 850 µm, the confusion limit in the source plane based on this simple estimate is ~ 1.1 mJy on average across the whole field. This number would be smaller if we focused only on the area of the map close to the caustics, where the magnification of the background area is much larger. As the area of the source plane various only little with redshift, this number will not change by a lot if we had a assumed a source plane at another redshift. In this field we detect four sources with unlensed fluxes below or just at the blank field confusion limit. These sources would most likely not be detected in blank field surveys and thus not have been accessible to us without the use of gravitational lensing or a larger telescope with sensitive instruments.

2.6.3 Discussion of individual sources

Here follows a discussion of the individual sources. We discuss the SCUBA detection and the identifications of the underlying galaxies. The multi-wavelength data employed for identifying the underlying galaxies, which give rise to the submm emission, includes HST WFPC2 images (Kneib et al., 1996; Smail et al., 1997b) Canada-France-Hawaii Telescope (CFHT) CFH12k data (Smith et al., 2002), William Herschel Telescope (WHT) INGRID data in the J and K bands (Packham et al., 2003), Gemini NIRI data, and a 15 µm ISOCAM map (Metcalfe et al., 2003).
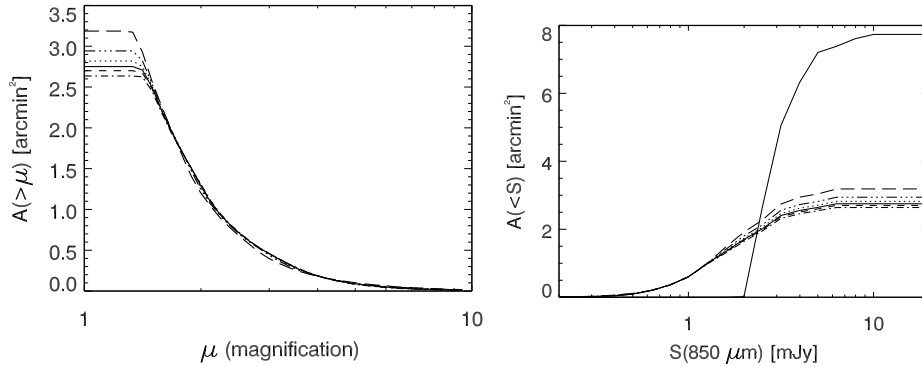
Figure 2.8: Left panel: *The area of the source plane as function of magnification. The different lines represent source planes at different redshifts, $z = 1, 1.5, 2, 2.5, 3, 4$, starting with the lowest redshifts highest in the plot. The difference between the different redshifts is relatively small.* Right panel: *The area of the source plane as function of 1σ sensitivity. The different lines represent source planes at different redshifts (see left panel). The solid line, which is very different from the rest, is the area as function of sensitivity in the image plane. The source plane is about 2.5 times smaller than what we observe in the image plane.*

The limiting magnitudes (5σ within an aperture of $2\,\mathrm{FWHM}$) of the near-IR data are: $K_{lim} = 20.0$ and $J_{lim} = 20.5$ for NIRI, and $K_{lim} = 19.3$ and $J_{lim} = 20.9$ for INGRID. The NIRI data are deeper than the INGRID data, however, the NIR J and K images used here are from a preliminary reduction and the photometric calibration is done relative to the INGRID images. For starforming galaxies, the radio and submm emission is correlated (Condon, 1992), and thus radio data is very useful for the process of identification of SCUBA sources at redshifts less than ~ 3 (depending on the depth of the radio data). No deep radio map is available for A2218. The cluster itself, however, contains strong radio sources (Zwaan et al., 2001), which would complicate the usage of such radio data. Webb et al. (2003b) have demonstrated that the potential of using deep near-infrared (NIR) data combined with optical data for identification is similar to that of using radio data, when applying probability analysis. Postage stamps at the positions of the SCUBA sources have been produced and are presented in Figures 2.9 and 2.10. Photometric information is presented in Table 2.3: Unless otherwise noted, the photometric colours have been measured within an aperture of $2.5''$, and the K band magnitude is the isophotal magnitude determined using SExtractor (Bertin & Arnouts, 1996).

We use a search radius of $8''$, which corresponds to about 2σ uncertainty on the detection positions taking into account that the field is slightly confused. The search radius is comparable to the half width at half maximum of the beam.

SMM J16357+66117
This source has a clear detection at both $850\,\mu m$ and $450\,\mu m$. Adopting the sim-

ple assumption that the Rayleigh-Jeans tail of a modified blackbody spectrum describes the SED, we can use the flux ratio S_{450}/S_{850} as a redshift indicator, although the fact that the temperature T and β is not known creates a large uncertainty. Using temperatures in a range between 30 and 70K and β of 1.5 and 2, the flux ratio S_{450}/S_{850} implies a redshift of $z \sim 1$ or lower. The S_{450}/S_{850} ratio is also similar to that of SMM J16359+66118, which has a spectroscopic redshift close to 1. The NIRI data do not cover this part of the SCUBA map. But the shallower INGRID images do. In the optical and NIR data, there is no obvious counterpart. Close to the detection position, there are two galaxies, which are close to one another. The northern galaxy (labeled a) has a redshift $z = 3.22$ (J.-P. Kneib, private communication) and is therefore unlikely to be the counterpart. None of the two galaxies are detected in the INGRID data, which, if any of the two is the true counterpart, would mean unusual photometric colours of a SCUBA galaxy. The photometric given in Table 2.3 includes aperture photometry in B, R and I. Given its moderate redshift it is possible that one of the two bright galaxies detected close to the edge of the SCUBA beam in the J and K images is the correct identification, however, the large position offset argues against this.

SMM J16359+6612
In the analysis of the gravitational lensing it was found the three sources, SMM J16358+66121, SMM J16359+66124 and SMM J16359+66126, are all images of a multiply-imaged background galaxy (Kneib et al., 2004), and thus they are here discussed together. All three sources have relatively bright fluxes at both $850\,\mu$m and $450\,\mu$m with identical flux ratios within the errors. All three images are coincident with a multiply-imaged detected in optical and near-IR images. The combination of similar colours and the gravitational lensing makes this a secure identification. The underlying galaxy has an irregular morphology with two blue and one red components. Based on spectroscopy with the Keck telescope this source has redshift 2.516. For further, detailed discussion and colour images, please see Kneib et al. (2004). The photometry quoted in Table 2.3 is from Kneib et al. (2004). Identifying a multiply-imaged source in the SCUBA maps is rare and only one other case is known (Borys et al., 2003).

SMM J16359+66118
This source is detected at both $850\,\mu$m and $450\,\mu$m. The flux ratio S_{450}/S_{850} suggests a redshift $z \sim 1$. The fact that it is detected also at $15\,\mu$m in the ISOCAM map is a strong indication that is at relatively moderate redshift. The underlying galaxy is a lensed arc, also known as #289, with redshift $z = 1.034$ (e.g., Kneib et al., 1996). In Kneib et al. (1996) it is discussed that this galaxy is straddling a caustic, with the dominant part of the galaxy not being strongly lensed. Because of the large $850\,\mu$m beam we can not determine from where in the galaxy the emission originates. As a result there is an uncertainty on the magnification factor and hence the correction for the lensing of submm flux of this source. At the position of the SCUBA detection we find a magnification factor of 6.7, while Swinbank et al. (2003) find a luminosity weighted magnification factor of $\mu = 4.92$. #289 has been studied in greater detail with GMOS Swinbank et al. (2003). The photometry
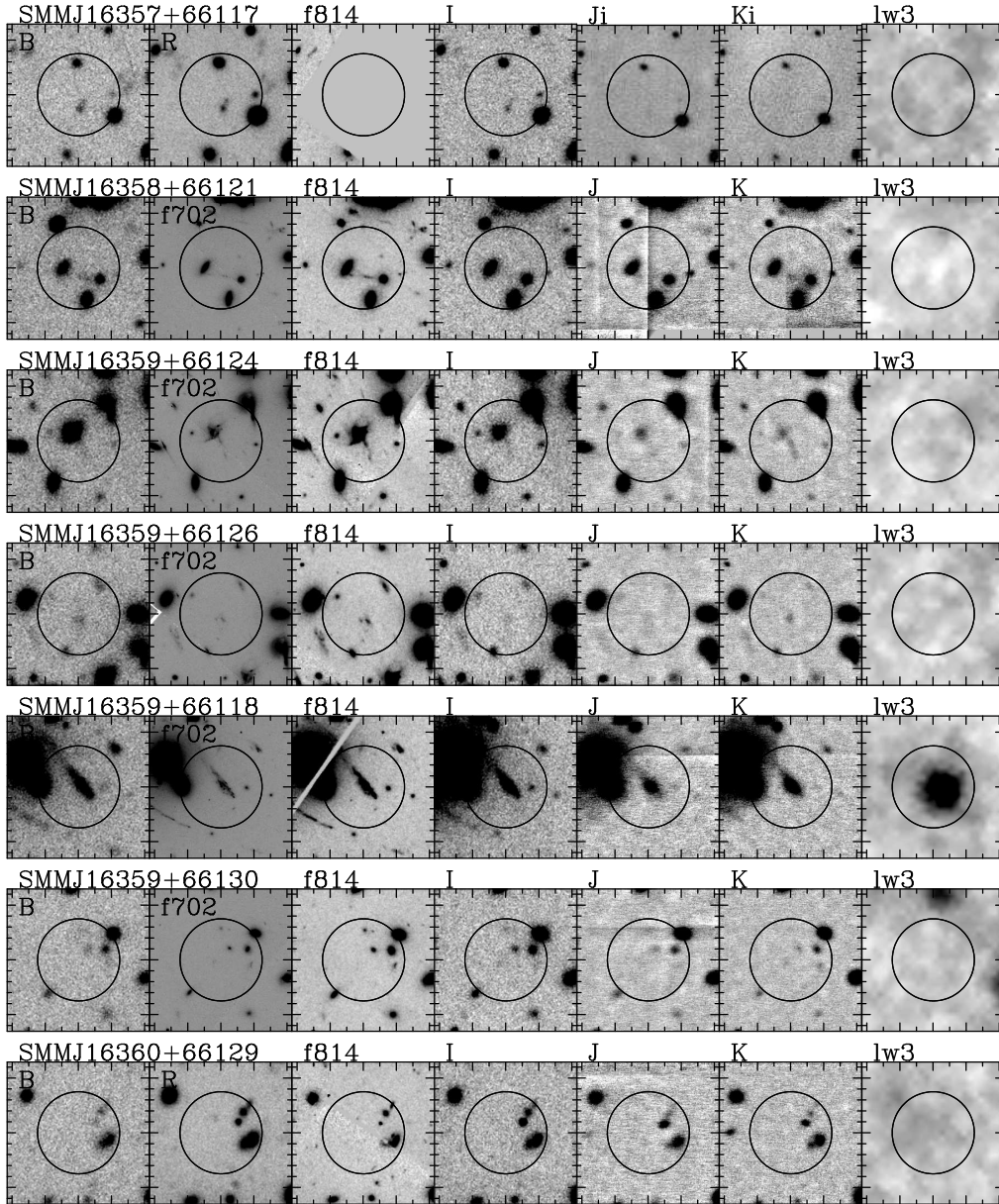
Figure 2.9: *Postage stamp size images of the optical, NIR and 15 μm imaging of seven of the SCUBA galaxies in the field of A2218. Each stamp is 26″×26″; on the horisontal axes the distance between tickmarks is 3″, and on the vertical axes it is 2″. The circle indicates the size of the SCUBA beam and is centered at the detection position. The stamps are labelled with the pass band. B, R and I are from the CFH12k; f702 and f814 are WFPC2 F702W respectively F814W; J and K from NIRI; Ji and Ki are from INGRID; lw3 is 15 μm from ISOCAM. Where the F702W image did not cover the SCUBA field, the R-band image is shown. For details on the individual sources refer to the text.*

given in Table 2.3 is taken from Swinbank et al. (2003).

SMM J16359+66130

SMM J16359+66130 is bright at 850 μm like the triple-imaged SMM J16359+6612 discussed above, however it has no significant detection of 450 μm flux. The flux ratio $S_{450}/S_{850} \leq 1$ suggests that this is a high redshift source with $z > 4$. There is no 15 μm flux at the position. In the optical and near-IR imaging there is no obvious counterpart, though in the I, F814W and K-band images there is a hint of faint emission close to the SCUBA position, which is indicated in Table 2.3.

SMM J16360+66129

This source is close to two other sources (see below, SMM J16361+66126 and SMM J16361+66130). The region of the map with these three source can be considered to be locally crowded or confused, which consequently can increase the uncertainty in the derived positions and fluxes (see Section 2.6.2). In the optical and NIR imaging there is no obvious counterpart, though in the north-western quadrant of the beam (see Figure 2.9), one of the three aligned galaxies appears to have relatively red colours, for which we give the photometry in Table 2.3.

SMM J16361+66130

As mentioned above, the uncertainty on the position of this source might be larger than the formal error due to local confusion. There is no obvious counterpart within the beam, however at the western edge of the beam an extremely red galaxy is present. Given the red colour which is common for many securely identified SCUBA galaxies and the potentially larger uncertainty in the SCUBA detection position, this is a possible identification.

SMM J16361+66126

This source is detected at 850 μm, but not at 450 μm. The flux ratio $S_{450}/S_{850} < 3.6$ suggests that it has a redshift > 2. In the multi–wavelength follow–up, SMM J16361+66126 is coincident with the X-ray emitting ISOCAM detected source #67 (Metcalfe et al., 2003). Its redshift is not known. The presence of X-ray emission together with the detection of 15 μm, which is unusual for $z > 2$ galaxies, suggests an AGN is present in this object. In the optical and NIR images, there are two extremely red objects close to the detection position (indicated with (a) and (b) in Table 2.3).

Summary of identifications

Three sources have been securely identified as a multiply-imaged background sources. One source is securely identified with an ISO-detected redshift 1 lensed arc. Three sources have possibly identified counterparts, which are all extremely red with $I - K > 5$ and $J - K > 2.2$. The probability of a chance superposition of a SCUBA source with very red, K-band bright galaxies is very small (e.g., Knudsen et al., *Chapter 5*). One source has no obvious likely counterpart, though a very faint galaxy could be the counterpart. Lastly, one source has no obvious likely

Table 2.3: *Multi-wavelength information for possible identifications of counterparts for the SCUBA sources. The fluxes given here have not been corrected for the gravitational lensing. Three dots (...) indicate that the source was not detected. A blank space indicates that photometry was not calculated. The errors on J and K represent the detection error, but do not include the uncertainty on the calibration. The first and the last SCUBA source have double entries, since several potential counterparts are present.*

NAME	B − R mag	V − I mag	R − I mag	I − K mag	J − K mag	K mag	7μm μJy	15μm μJy
SMMJ16357+66117 (a)	0.76 ± 0.04		0.23 ± 0.04			I = 24.37 ± 0.02 [1]	< 63	< 150
SMMJ16357+66117 (b)	0.97 ± 0.03		0.63 ± 0.03			I = 23.19 ± 0.02 [1]	< 63	< 150
SMMJ16358+66121*[2]	1.37 ± 0.15	0.30 ± 0.15		3.25 ± 0.1	2.0 ± 0.2	20.5 ± 0.1	< 60	< 150
SMMJ16359+66124*[2]	1.07 ± 0.05	0.30 ± 0.15		3.67 ± 0.1	2.7 ± 0.2	19.5 ± 0.1	< 60	< 150
SMMJ16359+66126*[2]	1.10 ± 0.05	0.45 ± 0.05		3.00 ± 0.1	1.2 ± 0.2	20.2 ± 0.1	< 60	< 150
SMMJ16359+66118[3]	1.13 ± 0.06	1.07 ± 0.06	0.74 ± 0.06	2.47 ± 0.08	1.31 ± 0.08	17.32 ± 0.06	113 ± 19	919 ± 61
SMMJ16359+66130	...		...	2.3 ± 0.4	...	22.0 ± 0.3	< 69	< 162
SMMJ16360+66129	2.67 ± 0.10		1.86 ± 0.03	2.86 ± 0.03	0.83 ± 0.03	19.30 ± 0.02	< 81	< 150
SMMJ16361+66130	...		1.58 ± 0.17	5.58 ± 0.15	2.37 ± 0.08	19.80 ± 0.03	< 81	< 150
SMMJ16361+66126 (a)	2.22 ± 0.18		1.19 ± 0.05	5.70 ± 0.05	2.28 ± 0.03	17.91 ± 0.01	119 ± 19	356 ± 54
SMMJ16361+66126 (b)	2.01 ± 0.16		1.04 ± 0.05	5.17 ± 0.06	2.20 ± 0.04	18.30 ± 0.01	119 ± 19	356 ± 54

* Triple-imaged source, see Table 2.1.
[1] The two galaxies are not detected in the NIR images, therefore the *I* magnitude is given.
[2] Photometry from Kneib et al. (2004).
[3] Photometry from Swinbank et al. (2003).
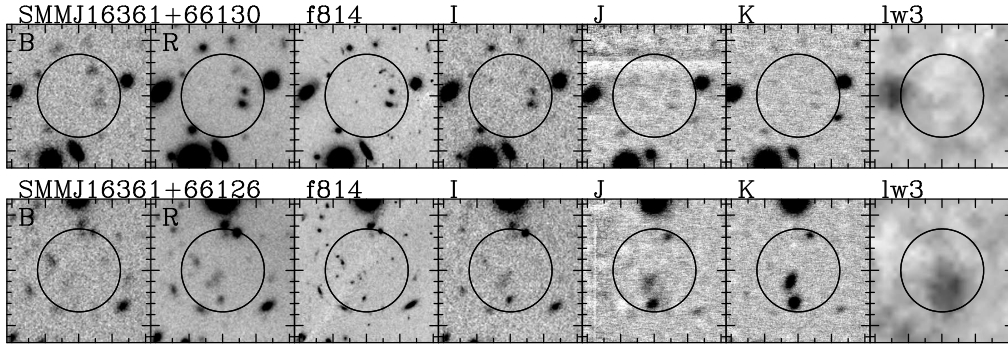
Figure 2.10: *Postage stamp size images of the optical, NIR and 15 μm imaging of the two western most SCUBA sources in the field of A2218. For explanation, see the caption of Figure 2.9. For details on the individual sources, see the text.*

counterpart, but there is some indication of it being at redshift less than one based on the submm colour.

2.7 Conclusions and outloook

We have performed a thorough analysis of the Mexican Hat Wavelets algorithm (MHW) as a source extraction tool applied to SCUBA jiggle-maps. The analysis was done using the deep SCUBA maps of the galaxy cluster A2218, through source extraction with MHW on the real data and through extensive simulations. We found that MHW is a stable method for source extraction at low signal-to-noise ($S/N > 3$). We conclude that MHW is an algorithm suitable for source extraction from SCUBA jiggle maps and is a powerful tool for studying the faint submm sources and thereby the faint end of the submm number counts.

Our conclusions about the MHW being a powerful tool for source extraction is based on a thorough analysis of its performance. In a future paper we will present a systematic comparison of the different methods utilised for source extraction from SCUBA maps.

In the analysis of A2218, nine sources were detected in the 850 μm SCUBA map. Five of these sources were also detected at 450 μm. Correcting for the gravitational lensing by the galaxy cluster, three sources have intrinsic 850 μm fluxes below the blank field confusion limit. The presence of strong gravitational lensing in the observed field is crucial for detection of sources with submm fluxes < 2 mJy. Furthermore, three of the SCUBA sources are identified as being a multiply-imaged background source at redshift $z = 2.516$, which has an unlensed flux of ~ 0.8 mJy. Multi-wavelength follow-up analysis using optical, NIR and ISOCAM is presented for all the sources. One source is identified with an arc at $z = 1.034$. Near seven of the nine sources, including the triple-imaged source, very red or extremely galaxies are present.

2.A Faint sources on structured background

In this appendix we try to visualize the appearance of low signal-to-noise sources on structured background.

The source extraction we are performing is in the low signal-to-noise regime, typically $S/N \sim 3{-}6$. Despite the eye's ability to detect sources, at low S/N the angular structure of the noise fluctuations in a map can influence the eye's perception of the structure of the eye. Here we attempt to illustrate visually with a simple example how a point source can look on different angular noise fluctuations. A number of different cases introduces significant errors in a "by-eye" source extraction and demonstrates the necessity of an algorithm, which uses the knowledge of the shape and size of the beam (point spread function):

1. If a source lands on a noise peak, the source will appear brighter.

2. If a source lands in a noise dip, the source will appear fainter.

3. If a source lands on the shoulder of a noise peak, the source will appear shifted from its true position.

4. If a source lands between a complex structure of noise peaks, the source will not appear as a point source, potentially it will appear as more point sources, though not with the real FWHM of the beam.

In Figure A.1 we have illustrated this with a mosaic of four stamps. Each of the stamps represents S/N of the same area of a field from the Leiden-SCUBA Lens Survey. The top-left stamp is the real data with a source detected at $S/N \sim 5$. The three other stamps are from the same position, but from three different Monte Carlo maps for that particular field, i.e. the statistical properties of the noise is the same, only fluctuations vary (as described in section 2.2.3). A simulated point source has been added at the same position and with the same flux as the MHW detection from the real data (as described in section 2.4). The MHW source detection of the simulated data are essentially identical to the original position. In Figure A.1, the two lower stamps both illustrate how the underlying noise structure can change the appearance of a low S/N source.

In the deep 850 μm SCUBA jiggle-map of the Hubble Deep Field North, the sources HDF850.4 and HDF850.5 are most probable subject to visual influence of the underlying angular noise fluctuations. In the original detection paper (Hughes et al., 1998) presenting the deep jiggle-map of the HDF-N, HDF850.4 and HDF850.5 were listed as two separate sources. The HDF-N jiggle-map has been part of several studies later, of which one is by Serjeant et al. (2003). In Serjeant et al. (2003), the source extraction is done through a simultaneous χ^2 minimisation algorithm for all sources in the field. Their source extraction algorithm does not "deblend"
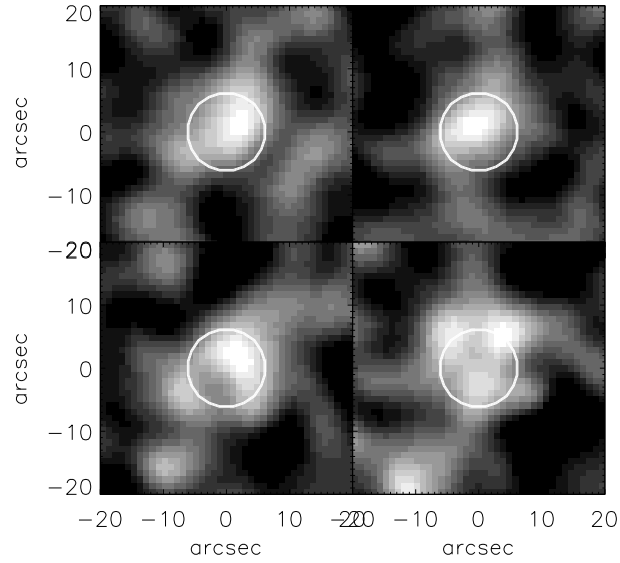
Figure A.1: *Illustration of the appearance of a point source with $S/N \sim 5$ on different angular noise fluctuations (with same statistical properties). The circle indicates the size of the SCUBA beam at 850 μm and is centered at the detection position.*

the two sources, however, the authors state that the combined source is extended and they assume it is a blend of two sources.

We have applied MHW source extraction to the HDF-N jiggle map. We find that HDF850.4 and 5 are one source. If there were two sources present, then after subtracting the first detected source a second source should be detectable in the residual map. Performing MHW source extraction on the residual map, no additional sources were detected around that position, also no insignificant detections. Our interpretation of this result is that there is only a single source, of which the appearance has been affected by the complex structure of the underlying noise fluctuations.

References

Barger, A.J., Cowie, L.L. & Sanders, D.B., 1999, ApJ, 518, L5

Barnard, V.E., Vielva, P., Pierce-Price, D.P.I., et al., 2004, MNRAS, 352, 961

Bertin, E. & Arnouts, S., 1996, A&A, 117, 193

Blain, A.W., 1996, MNRAS, 283, 1340

Blain, A.W., Ivison, R.J. & Smail, I., 1998, MNRAS, 269, L29

Borys, C., Chapman, S., Donahue, M., et al., 2004, MNRAS, 352, 759

Cayón L., Sanz J.L., Barreiro R.B., Martínez-González E., Vielva P., Toffolatti L., Silk J., Diego J.M., Argüeso F., 1981, MNRAS, 315,757

Chapman, S.C., Scott, D., Borys C. & Fahlman, G.G., 2002a, MNRAS, 330, 92

Chapman, S.C., Smail, I., Ivison, R.J. & Blain A.W., 2002b, MNRAS, 335, L17

Condon, J.J., 1974, 188, 279

Condon, J.J., 1992, ARA&A, 30, 575

Cowie, L.L., Barger, A.J. & Kneib, J.-P., 2002, AJ, 123, 2197

Damiani F., Maggio A., Micela G., Sciortino S., 1997, ApJ, 483, 350

Eales, S., Lilly, S., Webb, T., et al., 2000, AJ, 120, 2244

Ellis R., Santos M., Kneib J.-P., Kuijken K., 2001, ApJ, 560, L119

Hogg D.W., 2001, AJ, 121, 1207

Holland, W.S., Robson, E.I., Gear, W.K., et al, 1999, MNRAS, 303, 659

Hughes, D.H., Serjeant, S., Dunlop, J., et al., 1998, Nature, 394, 241

Jenness, T. & Lightfoot, J.F., 1998, *Astronomical Data Analysis Software and Systems VII* , A.S.P.
    Conference Series, Vol. 145, 1998, R. Albrecht, R.N. Hook and H.A. Bushouse, eds.,p.216

Kneib, J.-P., Mellier, Y., Fort, B. & Mathez, G., 1993, A&A, 273, 367

Kneib J.-P., Ellis R., Smail I., Couch W., Sharples R., 1996, ApJ, 471, 643

Kneib, J.-P., van der Werf, P.P., Knudsen, K.K., et al., 2004, MNRAS, 349, 1211

Metcalfe, L., Kneib, J.-P., McBreen, B., et al., 2003, A&A, 407, 791

Packham, C., Thompson, K.L., Zurita, A., et al., 2003, MNRAS, 345, 395

Sandell, G., 1994, MNRAS, 271, 75

Sanz J., Herranz D., Martínez-González E., 2001, ApJ, 552, 484

Sarazin, C.L., Rood, H.J. & Struble, M.F., 1982, A&A, 108, L7

Scott, S.E., Fox, M.J., Dunlop, J.S., et al., 2002, MNRAS, 331, 817

Serjeant S., Dunlop J.S., Mann R.G., et al., 2003, MNRAS, 344, 887

Smail, I., Ivison, R.J. & Blain, A.W., 1997a, ApJ, 490, L5

Smail, I., Ellis, R.S., Dressler, A., 1997b, ApJ, 479, 70

Smail, I., Ivison, R.J., Blain, A.W. & Kneib, J.–P., 2002, MNRAS, 331, 495

Smith, G.P., Smail, I., Kneib, J.-P., et al., 2002, MNRAS, 330, 1

Swinbank A.M., Smith J., Bower R.G., et al., 2003, ApJ, 598, 162

Tenorio L., Jaffe A.H., Hanany, S., Lineweaver, C.H., MNRAS, 310, 823

Vielva P., Barreiro R.B., Hobson M.P., et al., 2001a, MNRAS, 328, 1

Vielva P., Martínez-González E., Cayón L., et al., 2001b, MNRAS, 326, 181

Vielva P., PhD. thesis

Webb, T.M., Eales, S.A., Lilly, S.J., et al., 2003a, ApJ, 587, 41

Webb, T.M., Lilly, S.J., Clements, D.L., et al., 2003b, ApJ, 597, 680

Zwaan, M.A., van Dokkum, P.G. & Verheijen, M.A.W., 2001, Science, 293, 1800

References

Chapter 3

Deep submillimetre mapping of faint, gravitationally lensed sources: the Leiden-SCUBA Lens Survey

K.K. Knudsen, P.P. van der Werf & J.-P. Kneib

Abstract

We have conducted a submillimetre mapping survey of faint, gravitationally lensed sources. In this survey, which is named the Leiden-SCUBA Lens Survey, we have targeted twelve galaxy clusters and one non-lensing blank field. The total area surveyed is $71.5\,\mathrm{arcmin}^2$ in the image plane; correcting for gravitational lensing, the total area surveyed is $40\,\mathrm{arcmin}^2$ in the source plane for a typical source redshift $z \approx 2.5$. The maps of the deepest fields, which are A1689, A2218 and the NTT Deep Field, have reached an image plane depth of 1σ r.m.s. $\sim 0.8\,\mathrm{mJy}$. This survey is the largest survey to date to reach such depths. The source extraction has been performed using the Mexican Hat Wavelets (MHW) algorithm and the results have been analysed through extensive simulations. MHW is a powerful tool for source extraction of low signal-to-noise (> 3) from maps with structured background. In total 58 sources were detected. The gravitational lensing magnification from the galaxy clusters has been calculated and corrected for. The gravitational lensing plays an important role in this survey as it reduces the blank field confusion limit and makes it possible to study the submm population with fluxes below the blank field confusion limit of $< 2\,\mathrm{mJy}$. The lensing corrected fluxes ranges from $0.11\,\mathrm{mJy}$ to $19\,\mathrm{mJy}$. 15 sources have fluxes $< 2\,\mathrm{mJy}$, and of these 11 have sub-mJy fluxes, which triples the number of such sources known. The size and the depth of this survey makes it possible to study the faint and bright end of the number counts together. In the number counts a turn-over is detected and the data is described by a function with a gradual turn-over such as a double power law. For a double power law, the turn-over is at $\sim 6\,\mathrm{mJy}$. This is the first time a turn-over has been detected from a single survey. At $1\,\mathrm{mJy}$ the integrated number count is $\sim 10^4\,\mathrm{deg}^{-2}$, and at $0.5\,\mathrm{mJy}$ it is $\sim 2\times10^4\,\mathrm{deg}^{-2}$. Based on the number counts, essentially all of the $850\,\mu\mathrm{m}$ background emission has been resolved. The dominant contribution to the integrated background arises from sources with fluxes S_{850} between $0.4\,\mathrm{mJy}$ and $2.5\,\mathrm{mJy}$, while the bright sources $S_{850} > 6\,mJy$ contribute only 10%. This means that the bulk of the energy from the submm galaxy population comes from sources with fluxes just below the blank field confusion limit.

3.1 Introduction

The ubiquitous presence of dust throughout the universe and its absorbing properties, which cause obscuration of background sources, have a large influence on our understanding of the processes in the universe. The detection of the far-infrared (FIR) and submillimetre (submm) background radiation with *COBE* (Puget et al., 1996; Fixsen et al., 1998) and the fact that it has a comparable energy density to that of the ultraviolet (UV) and optical background radiation (e.g., Bernstein et al., 2002a, 2002b), indicates that approximately half of the activity in the universe is or has been obscured by dust.

The cosmic star formation history is most often studied through observations of massive short-lived stars, which radiate most of their energy in the UV/optical (e.g. Lilly et al., 1996; Madau et al., 1996). Such observations are, however, very sensitive to the presence of dust. Corrections for the dust extinction of such observations have been attempted (e.g., Meurer et al., 1997, 1999), but the exact values of the results have been debated based on uncertainties in the distribution of dust in galaxies, the extinction curves. and the measured spectral energy distributions (SED). The extinction corrections introduces a large uncertainty especially for measurements at redshift $z > 1$, where optical observations probe the rest-frame UV. As an alternative, the cosmic star formation history can be studied through FIR observations, at which wavelength the heated dust re-radiates the light absorbed from the stars, in the radio by measuring the supernovae remnants, and in the X-ray through high-mass binaries. The current picture of the cosmic star formation history is a steep increase from now to redshifts $z \sim 1-2$ (e.g Lilly et al., 1996; Rowan-Robinson et al., 1997; Haarsma et al., 2000; Norman et al., 2004), after which the star formation rate per comoving volume either stays nearly constant or declines towards higher redshifts (Madau et al., 1996; Meurer et al., 1999; Blain et al., 1999b; Steidel et al., 1999; Hu et al., 2004).

The cosmic star formation history and the star formation rates of the different types of galaxies are crucial observables used for testing the models for galaxy formation and evolution. During the past decades these models have undergone significant development. The models of hierarchical structure formation (e.g., Baugh et al., 1998) so far have proven to be the most successful description of the formation and evolution of galaxies. In that model, the structures are built through assembling of smaller structures and through accretion of smaller galaxies by larger galaxies. This model essentially replaces earlier scenarios where galaxies form at high redshift through a collapse of a single object on a short timescale and undergo a single massive starburst after which they passively evolve (Eggen, Lynden-Bell & Sandage, 1962).

In the hierarchical model, the star formation rates are predicted to be moderate, of a few to few tens $M_\odot yr^{-1}$ (e.g., Baugh et al., 1998; Cole et al., 1994). This is consistent with UV and optical observations of the low- and high-redshift Universe. Broadband and narrowband photometry, studying either the continuum levels or the line emission from the young, massive stellar populations to redshifts $z < 5$, show star formation rates for the individual galaxies in agreement with the hierarchical model and comoving star formation densities > 10 times larger than

observed at the present epoch (e.g., Lilly et al., 1996; Madau et al. 1996; Cowie et al., 1999). The hierarchical model is also supported by the observed merger history, which has a trend similar to that the cosmic star formation history (Patton et al., 2002; Conselice et al., 2003). The observed, moderate star formation rates and the cosmic star formation history can, however, not explain the large number of elliptical galaxies and spheroids harbouring evolved stellar populations at redshift $z \sim 1$ (e.g., Moriondo et al., 2000), which indicates formation at much higher redshift and at star formation rates larger than observed in UV/optical studies.

Very large star formation rates, > 100-1000 have been seen locally. In the *IRAS* FIR all-sky survey galaxies with IR luminosities $> 10^{12}$ $L_{\odot}$ were identified (Soifer, Neugebauer & Houck, 1987). The thermal FIR emission is powered by star formation and active galactic nuclei (AGN) activity. It was found that these extraordinary objects have low space density in the local Universe, $z < 0.3$, and are thus relatively rare (Sanders & Mirabel, 1996).

The first submillimetre mapping instrument SCUBA (Submillimetre Common User Bolometer Array; Holland et al., 1999), which is mounted at the James Clerk Maxwell Telescope (JCMT) at Hawaii, allowed for observations of IR luminous galaxies at high redshift. The first observations at $850\,\mu$m (Smail et al., 1997) showed that these objects are much more common at earlier epochs. Subsequently, a number of surveys have been undertaken to study this population of submm detected galaxies. The blank field surveys include observations of the Hubble Deep Field North (HDF-N) (Hughes et al., 1998, Borys et al., 2003, Serjeant et al., 2003), the Hawaii Deep Fields (Barger et al., 1999b), Canada-UK Deep SCUBA Survey (CUDSS) (Eales et al., 2000, Webb et al., 2003a), and the 8 mJy survey (Scott et al., 2002). In particular the CUDSS and 8 mJy survey have been successful in covering a large area of the sky. However, the blank field surveys are limited by the confusion at 2 mJy at $850\,\mu$m with the 15 m JCMT. To break the blank field confusion limit observing with SCUBA, gravitational lensing must be employed. The UK-SCUBA Lens Survey (Smail et al., 1997, 2002) targeted seven galaxy cluster fields. Three of their fields were observed to larger depth (Cowie, Barger & Kneib, 2002). Another lens survey was performed by Chapman et al. (2002), however, this survey was relatively shallow.

Submillimetre observations of objects at high redshifts, $z > 1$, benefit from the fact that the geometrical dimming of the light is cancelled by the negative k-correction, resulting from the fact that the peak of the SED is shifted toward the observing band. For a given luminosity, the observed submm flux is close to constant between redshift 1 and 8. Consequently, extragalactic submm observations primarily probe the high redshift universe. A further consequence of this situation is that flux-limited samples are also approximately volume-limited. Furthermore, deeper surveys do not probe deeper into the universe, but only sample lower luminosity galaxies. Galaxies in clusters at redshifts $z < 1$ are not expected to be seen with SCUBA, except for sometimes the central cD galaxy (Edge et al., 1999) or an AGN or possibly Sunyaev-Zel'dovich effect.

We here present the Leiden-SCUBA Lens Survey, in which we have targeted twelve galaxy clusters. This is the largest survey so far of gravitationally lensing clusters, and it is the first survey to substantially probe below the blank field con-

fusion limit. This paper presents the observations, the analysis of the data and the resulting catalogue. The analysis involves the mathematically rigorous Mexican Hat wavelets algorithm and Monte Carlo simulations. In following papers, we will use the derived number counts as an observational constraint on models of the submm galaxy population, and we will present multiwavelength follow-up observations.

In Section 3.2 we present the observations and the reduction of the data. The source extraction is discussed in detail in Section 3.3. The issue of confusion is discussed in Section 3.4, and the effect of gravitational lensing is discussed in Section 3.5. The resulting catalogue of the Leiden Deep SCUBA Survey is presented in Section 3.6. Finally, in Section 3.7 we present the number counts for the survey. Throughout the paper we assume $\Omega_m = 0.3$, $\Omega_\Lambda = 0.7$ and $H_0 = 70\,\mathrm{km/s/Mpc}$.

3.2 Observations and reduction

We have obtained observations of a number of clusters of galaxies at $850\,\mu\mathrm{m}$ and $450\,\mu\mathrm{m}$ with the Submillimetre Common User Bolometer Array (SCUBA; Holland et al. 1999), which is mounted on the James Clerk Maxwell Telescope (JCMT) at Mauna Kea, Hawaii. In addition we have obtained similar observations of the NTT Deep Field (Arnouts et al. 1999), which was chosen due to the large, deep data set existing at optical and near-infrared wavelengths. In total our survey contains twelve fields of galaxy clusters and the one blank field covering an area of $71.5\,\mathrm{arcmin}^2$. The parameters for each field are listed in table 3.1.

SCUBA has two arrays of 37 and 91 bolometers optimized for $850\,\mu\mathrm{m}$ respectively $450\,\mu\mathrm{m}$. A dichroic beamsplitter is used for simultaneous observations with both arrays. Both arrays have the bolometers arranged in a hexagonal pattern. Because SCUBA does not have a field rotator, the arrays appear as rotating on the sky. The field–of–view on the sky, which is approximately the same for both arrays, is roughly circular with a diameter of 2.3′. The observations were carried out in jiggle mode with a 64 point jiggle pattern, in order to fully sample the beam at both operating wavelengths. The secondary mirror carries out this jiggle pattern as well as the 7.8 Hz chopping, which is employed for subtraction of the strong sky background. Our observations were performed with a chop throw of 45″ with the chopping position angle fixed in right ascension (RA). As a result the beam pattern has a central positive peak with negative sidelobes on each side, each with minus half the peak value, a pattern which can be used for the detection of at least the brighter sources. During the observations the pointing was checked every hour by observing bright blazars near the targeted fields. The noise level of the arrays was checked at least twice during an observing shift, and the atmospheric opacity, τ, was determined with JCMT at $850\,\mu\mathrm{m}$ and $450\,\mu\mathrm{m}$ every two–three hours and supplemented with the $\tau_{225\mathrm{GHz}}$ data from the neighboring Caltech Submillimetre Observatory (CSO). Calibrators were observed every two to three hours. If available, primary calibrators, i.e. planets, preferably Uranus, were observed at least once during an observing shift. Our observations were supplemented with archival SCUBA data.

The data were reduced using the SURF package (Jenness & Lightfoot 1998). First

Table 3.1: *The observed fields.*

NAME	RA(J2000) h m s	Dec(J2000) ° ′ ″	z_{cl}	t_{int} hours	Ω_{850} arcmin²	σ_{deep}^{850} mJy/Ω_b	σ_{wghtd}^{850} mJy/Ω_b	σ_{deep}^{450} mJy/Ω_b	σ_{wghtd}^{450} mJy/Ω_b
Cl0016+16	00 18 33.2	+16 26 17.8	0.541	7.73(5.46)	4.5	1.33	2.00	9.8	16.5
A478	04 13 25.3	+10 27 54.3	0.0881	7.08	4.3	1.59	2.05	9.1	14.5
A496	04 33 37.8	−13 15 43.0	0.0328	10.4	4.1	1.08	1.47	11.6	17.2
A520	04 54 07.0	+02 55 12.0	0.202	19.6(18.0)	4.3	0.97	1.26	9.2	14.5
MS1054−03	10 56 56.1	−03 36 26.0	0.826	49.2	14.4	0.86	1.49	3.7	10.2
A1689	13 11 17.0	−01 20 29.0	0.181	33.4(32.2)	5.4	0.70	0.97	4.4	9.9
RXJ1347.5−1145	13 47 30.5	−11 45 09.0	0.451	10.5	4.8	2.04	3.06	7.2	24.8
MS1358+62	13 59 50.6	+62 31 05.1	0.328	4.80	4.2	1.39	1.81	7.6	11.2
A2204	16 32 46.9	+05 34 33.0	0.1523	1.60	4.0	3.75	5.20	65.3	87.2
A2218	16 35 54.2	+66 12 37.0	0.171	42.3(35.6)	7.7	0.65	1.06	3.2	16.0
A2219	16 40 20.4	+46 42 59.0	0.225	9.63	4.6	1.10	1.54	6.7	11.8
A2597	23 25 19.8	−12 07 26.4	0.0852	6.76	4.1	1.34	1.77	11.2	17.8
NTT Deep Field	12 05 22.6	−07 44 14.9	–na–	27.1	5.0	0.78	0.97	3.9	6.3

Parameters of the observed fields. The integration time t_{int} is the total integration time, but without overheads (i.e., without the time needed for jiggle, chopping, etc). If the 450 μm exposure time is different from the 850 μm its value is given in parenthesis. The area, Ω_{850}, given is the field covered after removing the noisy edge. σ_{deep} is the lowest noise value in the whole field. σ_{wghtd} is the area-weighted noise level of the field. Ω_b is the beam.

the chop of the secondary mirror was removed, i.e. the off–source measurements were subtracted from the on–source measurements. Then the varying responses of the bolometers were corrected by dividing with the array's flatfield. The extinction correction was performed based on the atmospheric opacity measured both with the JCMT and CSO. The $\tau_{850\mu m}$ and $\tau_{450\mu m}$ was measured a number of times during the night with the JCMT. As the atmospheric opacity may change on shorter timescales, the interpolated τ-values may be somewhat inaccurate. At the CSO on the other hand, the opacity is measured every few minutes at 225 GHz. Using the linear relations between τ_{225GHz} and $\tau_{850\mu m}$ respectively $\tau_{450\mu m}$, deduced by Archibald et al. (2000), it is possible to determine the atmospheric opacity at the time of the observations. The zenith opacity was for most of the time $0.12 < \tau_{850\mu m} < 0.40$. The data were inspected for bad or useless data. For each scan for each bolometer datapoints deviating by more than three sigma, based on the r.m.s. of the individual bolometer, were rejected from further analysis. This statistical exclusion is possible because there are no bright sources present in the data. Furthermore, the data were inspected by eye, and bolometers that were clearly more noisy than other bolometers were flagged and excluded from further analysis. The pointing of each scan was corrected using the pointing observations taken just before and after the observations. The r.m.s. pointing error of the JCMT is typically $2''$. The correlated atmospheric fluctuations still present in the data were subtracted using the pixel–by–pixel median of the 25 least noisy bolometers.

Data taken after January 2002, were affected by a periodic noise of currently unknown origin. For these data, the power spectrum of the individual bolometers showed that some bolometers had a spike around 1/16s (C. Borys, private communication). This spike, however, did not systematically occur in the same bolometers or with the same strength. This effect was corrected for by making a sky subtraction based on the bolometers that were not affected by this, and additionally, the affected bolometers were additionally corrected through multiple-linear regression (T. Webb, private communication). As only a small fraction of the data for the survey was obtained after January 2002, this is relevant mostly for the MS1054-03 data, where the data most affected was the Northern pointing. The correction for the 1/16s spike brought down the noise in the affected data by $\sim 10\,\%$.

The scans were calibrated by multiplying by the flux conversion factors (FCF) determined from the calibration maps. The FCFs are determined from the peak values (or the values corrected for extendedness) of the used calibrators. We estimate the uncertainty in the flux calibration as approximately $10\,\%$ at $850\,\mu m$. At $450\,\mu m$, the calibration uncertainty is about $30\,\%$, because of variations in the beam profile resulting from thermal deformations of the dish. This is in agreement with the canonical calibration uncertainties. The data were despiked by projecting the data on a grid and at each map pixel reject the associated bolometer pixels deviating by more than three sigma. Finally, all the bolometers were weighted based on their measured r.m.s. noise relative to one another and to the whole data set. The data were regridded with $1''$ pixels into a final map. The beam sizes are $\sim 14.3''$ at $850\,\mu m$ respectively $\sim 7.5''$ at $450\,\mu m$. The noisy edge was trimmed by removing the outer 23 pixels; 23 pixels corresponds to one and a half beam. Un-

less otherwise mentioned the maps used in the analysis have been smoothed with a 5″ full width half maximum (FWHM) Gaussian to reduce high spatial frequency noise, resulting in beam sizes of 15.1″ at 850 μm and 9″ at 450 μm.

3.3 Source extraction

The sensitivity in the reduced maps is not uniform across the field. As we are working close to the signal–to–noise limit of these data it is crucial to understand the properties of the noise. Furthermore, the source extraction from maps like the SCUBA maps is a non–trivial task, which must be performed with a robust and well–understood method. Our method of source extraction and its reliability based on simulations are discussed in detail in this section.

3.3.1 Construction of noise maps

When a data set is combined and regridded into a map, some areas will be sampled less than the rest of the map. These are the areas along the edges, the areas where the bolometers are either more noisy or data has been excluded, and areas with less integration time outside the overlap between different pointings (especially for A2218 and MS1054−03). It is thus imperative to assess the noise as function of position in the map to be able to make a reliable analysis of the observed flux map.

In order to determine the position–dependent noise we perform Monte Carlo (MC) simulations to construct 'empty' maps representing the noise component in the real data files. As input to the MC simulations we determine the statistical properties of the fully reduced data files of the SCUBA jiggle maps. In the fully reduced data files all known correlated noise has been removed, hence the noise of the individual bolometers is assumed to be independent of other bolometers. The sources we are observing are very faint, thus the data points from the bolometers are dominated by noise rather than signal.

For each original data file, data was simulated using a Gaussian random number generator with the same statistical properties as the real, fully reduced bolometer data. The simulated data set was reduced and concatenated using SURF in the same manner as the original data files. The result of such a MC realization is an empty map with the same statistical properties as that of the original data. The process is repeated about 500 times resulting in 500 empty maps. By measuring the standard deviation at each pixel in the map across all 500 realizations, the final noise map represents the position–dependent noise in the final data map. This has been performed for all the observed fields at both 850 μm and 450 μm. A noise map at 850 μm is shown in Fig. 3.1, where it can be seen how the noise is not uniform across the field and how the different effects described above appear. The deepest noise level, i.e in the central region, and the area–weighted average noise for each field are listed in Table 3.1.

3.3.2 Deconvolution of beam map

As described in Section 3.2, the chopping of the secondary mirror on the JCMT introduces a beam pattern with a positive peak and two negative sidelobes. This is

45
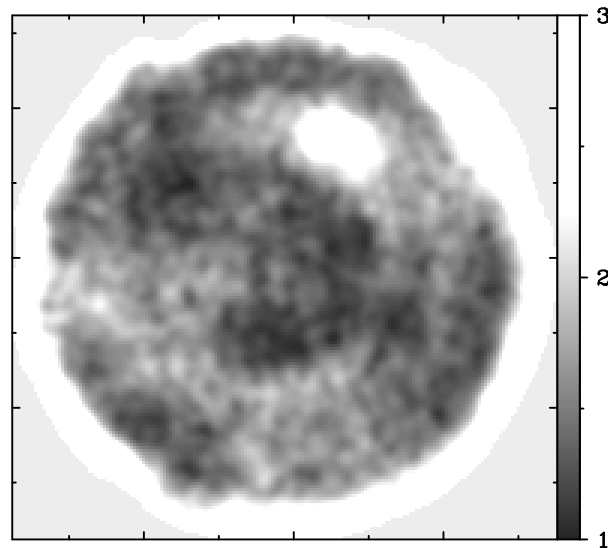
Figure 3.1: *Example of a noisemap, from the A496 field. Because of the low sampling along the edges as the bolometer array appears to be rotating on the sky, the edges have high noise levels. The high-noise region in the upper-right quadrant is due to a "bad" bolometer tracking across there. (Units are mJy/beam.)*

undesirable because negative sidelobes can hide sources or bias their fluxes. Also the negative sidelobes contain useful signal that can be used in source detection. Therefore it is useful to deconvolve the beam pattern out. Since we are dealing mostly with isolated point sources the classical CLEAN algorithm (Högbom, 1974) is ideally suited for this purpose. In our cleaning algorithm, the selection of the peaks was done in the following way. A beam map was constructed from point source calibration observations. During each iteration the (cleaned) data map was convolved with the beam map and divided by the associated convolved noise map. The former was to enhance any present signal in the map and the latter was to ensure that no noise peaks (e.g. along the edges) would be mistaken for signal. The cleaning itself takes place on the unconvolved data map. We found that subtracting 10 % of the flux at each iteration was reasonable. The cleaning was continued till there were no more pixels above 3 sigma in the convolved signal-to-noise map. Finally, the data maps were restored on top of the uncleaned residual using only the central positive peak from the beam map.

3.3.3 Point source detection

Most sources at high redshifts have an angular extent on the sky of less than a few arcseconds. In the 850 μm beam such sources will appear as point sources. To do the point source extraction we choose to use Mexican Hat Wavelets (MHW). MHW is a mathematically rigorous tool for which the performance can be fully understood and quantified. MHW has proven to be a powerful source extraction

technique in both SCUBA jiggle-maps and scan-maps (Barnard et al. 2004, Knudsen et al. *Chapter 2*). Wavelets are mathematical functions used for analysing according to scale. Isotropic wavelets have the advantage that no assumptions about the underlying field need to be made. The beam at $850\,\mu$m is well-described by a 2-dimensional Gaussian, which is best detected with the 'Mexican Hat' wavelets; the 'Mexican Hat' is the second derivative of a Gaussian. The software utilized are programmes written for the *Planck* mission, but modified for application on SCUBA maps. For more details and the application of the programmes on SCUBA maps see Barnard et al. (2004), Cayón et al. (2000) and Knudsen et al. (*Chapter 2*). Here we summarize only the relevant details.

The MHW source extraction is done in the following way. Point source candidates are selected at positions with wavelet coefficient values larger than a given number. For each candidate, the wavelet function is compared to the theoretical variations expected with the scale, as a further check on the source's shape. A χ^2 value is calculated between the expected and the experimental results. If the χ^2 is smaller than a given limit, i.e., that the region surrounding the identified peak has the characteristics of a Gaussian point source of the correct dimensions, the point source is included in the extracted catalogue. In Knudsen et al. (*Chapter 2*) we have performed controlled detection experiments to determine the optimal criteria for the MHW algorithm applied to SCUBA jiggle maps: the wavelet coefficient ≥ 2 and $\chi^2 \leq 4$. These we combine with the $S/N \geq 3$ criterion in the flux map.

In doing the source extraction, the MHW algorithm searches the maps for features at the scale of the beam, features with scales smaller or larger than the beam are not extracted. E.g., in the field RX J1347.5$-$1145 the extended emission presumably due to the Sunyaev-Zel'dovich effect is undetected by MHW point source detection. Also extended sources cannot be detected by changing the χ^2-limit. This of course ensures that all sources detected are point sources.

To check for undetected sources located closer than one beam to a detected source, the detected sources are subtracted from the map. If those are the only point sources present in the map, then MHW finds no sources in the residual map. If any sources are significantly detected in the residual map, those sources are subtracted from the original map and a new MHW detection is done in order to improve the result on the first detection. This is continued iteratively until the output converges. This approach does not resolve extended sources.

3.3.4 Completeness

The completeness, i.e., how large a fraction of sources were detected at a given flux level, was determined through a set of simulations. The simulations were performed as follows: for a given flux level, 400 times a single point source was added onto empty MC maps. The positions were chosen to be random with a uniform distribution, and 10 MC maps were used. This was repeated for different fluxes, where the fluxes were chosen to range from flux levels fainter than the detection threshold of the field to flux levels larger than the brightest source in the field. The fluxes were chosen in steps of 1 to 2 mJy. The source extraction was done using the MHW algorithm with the same constraints as for the real data. Such simulations were performed for each observed field. As the simulations are
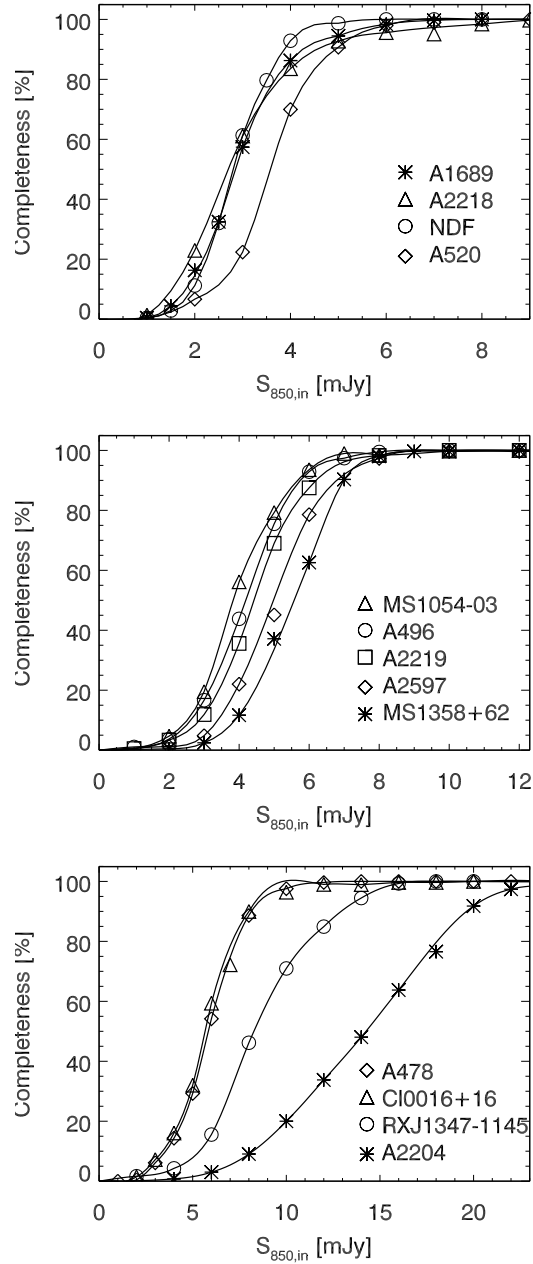
Figure 3.2: *This figure shows the completeness as function of flux for all the surveyed fields. For a better overview the thirteen fields have been plotted in the three panels. The top panel shows the deepest of the fields, while the middle panel shows the medium-deep fields, and the lower panel shows two medium-deep fields, and shallower fields. In the deepest fields the data are 80 % complete at 3.5-4 mJy and 50 % complete at 2.6-2.8 mJy.*

48

performed on the whole field, which has a non-uniform sensitivity, the results we find is an average across each field. In Figure 3.2 we plot the completeness for the individual fields. As is seen in Figure 3.2, the completeness depends on the depth of the observations. For the deepest fields like A1689, A2218 and NTT Deep Field the observations are 80 % complete at a flux level of ~ 3.5-4 mJy and 50 % at ~ 2.6-2.8 mJy. For the other, less deep fields the 80 % completeness is 4.5-7.5 mJy and 50 % at 3.5-5.5 mJy. For A2204, which is a shallow field, the observations are 80 % complete at 18 mJy and 50 % at 14 mJy.

3.3.5 Accuracy of derived parameters

The accuracy of the derived parameters, i.e. the position and the flux, is determined using the simulations described in the previous subsection. Analysing the results of the simulations we can quantify the reliability of the source extraction.

Position: In Fig. 3.3 the difference between input position and detection position, i.e. radial distance, is plotted in bins of S/N (here we use the simulations from A496 as an example). Not surprisingly, the average difference decreases with increasing S/N. The result is similar for all the fields. We use this to quantify the accuracy of the position as it has been determined by the source extraction algorithm and adopt the median deviation in position as function of S/N as the error. We calculate the formal error on the position of the individual sources from this error added in square to the pointing uncertainty of the JCMT. This means that a source detected with $S/N = 3$ has a 1σ error circle of $4''$ around the detected position. For $S/N > 15$ simulations show that the detection position on average deviates no more than an arcsec. Thus the formal error for high S/N is dominated by the pointing uncertainty of the telescope.

Flux: The relative difference between detected flux, S_{out}, and input flux, S_{in}, as function of S/N is shown in Fig. 3.4. The relative difference in flux scatters around zero. A small positive bias of a 2-5 percent is present, i.e., the detected sources appear a bit brighter than they are; this is, however, smaller than the final uncertainties on the flux. Furthermore, we see that the standard deviation of the relative difference decreases with S/N. We use the standard deviation on the relative difference between input and detected flux as measure for the uncertainty in the flux determination by MWH. We do this taking into account the decrease with S/N and thus the uncertainty on the determined flux of a source with $S/N \sim 3$ has a 20 % error, while the determined flux of a source with $S/N \sim 8$ has a 10 % error. In the final catalogue we calculate the formal error of the flux measurement by adding in square this error to the calibration error. For large S/N the uncertainty on the flux from the source extraction is small and the formal error is dominated by the calibration error.

3.3.6 Spurious detections

We have addressed the issue of spurious sources. Source detection was performed on inverted maps to check if any negative sources were detected. We ignore negative sources sitting on a chop throw, which are a known artifacts from the original
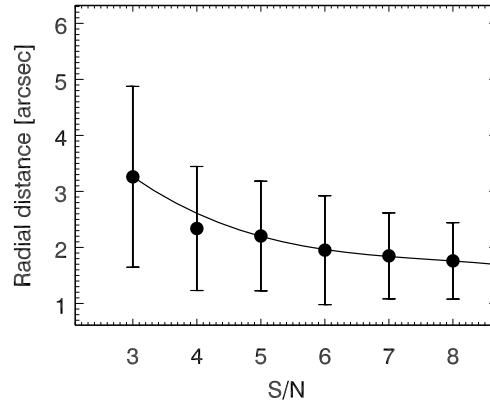
Figure 3.3: *The average radial distance between input position and detection position as function of S/N based on the simulations for the field A496 – the results are similar for all the fields. The simulations have been performed to assess the accuracy of the derived parameters. We adopt this average positional deviation as function of S/N and add it in square to the pointing uncertainty of JCMT to determine the formal error on the position.*

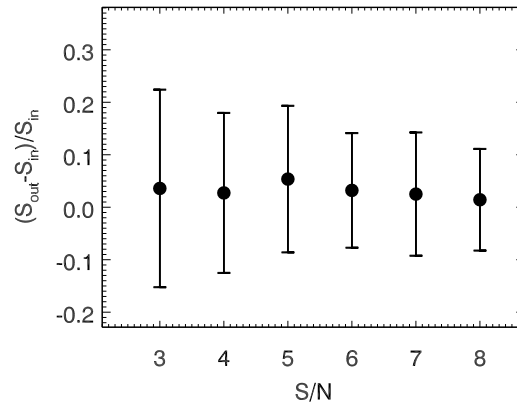**Figure 3.4:** *The relative difference between input flux and detected flux as function of S/N based on the simulations for the field A496 – the results are similar for all the fields. The simulations have been performed to assess the accuracy of the derived parameters. We adopt the standard deviation of the relative difference as a function of S/N to determine the uncertainty of the flux of the sources in the catalogue.*

beam pattern. Furthermore, we ignore the deepest fields, where confusion plays a role. For those fields even a detected negative source can be a real structure in the background. Along the edges many negative sources were detected. As this indicates that many positive spurious sources would be found along the edge, we have decided to trim away the edge at a width of one and a half beam, i.e. 23″. In total we find five negative sources, which is in agreement with Gaussian statistics. Our catalogue thus may contain 5 spurious sources.

Additionally, we have performed source extraction from the Monte Carlo maps (see above) for all the fields. We find that within a hundred maps typically two sources were detected with $S/N \approx 3$, and no sources with $S/N > 3.5$. This demonstrates the reliability of MHW to pick out real sources with $S/N > 3$. With essentially no sources in the pure noise maps, the spurious sources detected in the inverted maps are probably due to the structured background.

3.3.7 The 450 μm maps

The optical depth at 450 μm is five times larger than that at 850 μm. This makes it difficult to reliably calibrate the 450 μm maps, as the data are much more sensitive to any variation in the sky opacity. As opposed to the 850 μm beam pattern, the 450 μm beam pattern is not well-described by a 2-dimensional Gaussian, and for brighter sources Airy rings are very pronounced. In addition, the 450 μm beam pattern is very sensitive to any deformation of the JCMT dish. Such deformations are normally the result of temperature variations. Consequently, the beam pattern change during the night, with changing observing conditions. These effects complicate a reliable source extraction from the 450 μm. Furthermore, the 450 μm beam is much narrower than the 850 μm beam, and more of the calibration sources may appear extended. This has to be taken into account as well and might add to the uncertainty of the 450 μm flux calibration.

We have chosen not to perform deconvolution and MHW source extraction from the 450 μm maps to make a separate 450 μm point source catalogue. Instead we use the maps to determine the 450 μm flux at the 850 μm source positions. That is done in the following way. The S/N map, the flux and the noisemap are used. In a circle with radius 4″ around the 850 μm source position, the maximum S/N value is found. If this value is equal to or greater than 3, the flux value in that pixel is adopted as the S_{450} of the 850 μm source, and the uncertainty, $\sigma_{S_{450}}$, is 30% of that value. If no pixels in that circle fullfil the S/N criteria, an upper limit is given as three times the mean flux value corresponding to the three lowest noise values within the circle. This has been done three times for all the 450 μm maps, namely when the maps have been smoothed with a Gaussian with FWHM of 5″, 10″ and 12.7″. Smoothing with e.g. a 5″ Gaussian reduces the high spatial frequency noise, while smoothing with a 12.7″ Gaussian makes the 450 μm beam equivalent to the 850 μm beam. Furthermore, the smoothing reduces the effect that sources might be slightly extended in the original map due to intrinsic size and point errors. In a couple of cases the S/N criterion is met with one smoothing, but not quite in the other one(s). For the reasons described above, the 450 μm fluxes listed in Table 3.3 should used with caution.

3.4 Confusion

3.4.1 Confusion limit in blank fields

In the background of deep SCUBA maps the instrumental noise and the confusion noise from a fainter submm population are of approximately equal magnitude. We adopt Condon's (1974) formalism and use the same definition for the beam as Hogg (2001): $\Omega_{beam} = \pi(\theta_{FWHM}/2.35)^2$, where θ_{FWHM} is the width of the beam (SCUBA at $850\,\mu$m: $\theta_{FWHM} = 15''$). We adopt the rule of thumb that the number of sources per beam should not exceed one source per 30 beams before the image is considered confused (e.g., Hogg, 2001). The confusion limit is the flux, S_{conf}, at which the number of sources in the map is one source per 30 beams. To estimate the confusion limit, the integrated number counts, $N(> S)$, where $N(> S)$ denotes the number density on the sky of sources brighter than S, are used. For blank fields a single power law suffices to describe the number counts, $N(> S) = N_0 S^{-\alpha}$. For $N(> S) = 1/30\Omega_{beam}$, the confusion limit is $S_{conf} = \sqrt[\alpha]{30\Omega_{beam}N_0}$. If we assume $\alpha = 2.0$ and $N_0 = 13000\,\mathrm{deg}^{-2}$ (based on e.g. Barger et al., 1999b; Borys et al., 2003), for SCUBA $850\,\mu$m blank field observations, the confusion limit is $\sim 2\,$mJy. For an average-sized, trimmed map in our survey of $5\,\mathrm{arcmin}^2$, this number of sources is $n_s = 4.7$. This is close to the average number of sources per field in our survey.

Confusion in the maps affects the position and flux determination. Eales et al. (2000) found in their simulations that in confusion-limited fields 10 % to 20 % of the detected sources would lie outside an error circle of $6''$. Furthermore, they found that the fluxes of the sources were boosted by a median factor of 1.44, albeit with a large scatter. However, as argued by Blain (2001), confusion effects will only appear in SCUBA maps with detection limits of $2\,$mJy or less at $850\,\mu$m; hence our data are relatively unaffected by flux boosting. Hogg (2001) have made general simulations addressing the issue of the errors caused by confusion. Based on Figure 4 of his paper (Hogg, 2001), which gives the position error as function of detected source density where no prior knowledge is used in the source detection, in the Euclidean case, a detected source density of one per 30 beams causes a median position error of 0.25 times half width at half maximum (HWHM). At $850\,\mu$m this corresponds to an additional error in the position of $1.9''$. For crowded fields in our survey where the source density is larger than one per 30 beams, the error in the position caused by the confusion is 4-$5''$.

3.4.2 Confusion limit in lensed fields

For the cluster fields the confusion limit is affected by the gravitational lensing. The gravitational lensing magnifies the region seen behind the cluster, hence the source plane is smaller than the image plane. The number of beams is conserved between the image plane and the source plane, i.e. the size of the beam scales with the magnification. This is why it is at all possible to observe the fainter sources, which have a higher surface density than the brighter sources.

The number counts in the lensed case can be written as $N_{lens} = (N_0/\mu)(S/\mu)^{-\alpha}$ $= N_{blank}\mu^{\alpha-1}$, where μ is the gravitational lensing magnification. The average magnification for a field can be found as the ratio of the area in the image plane
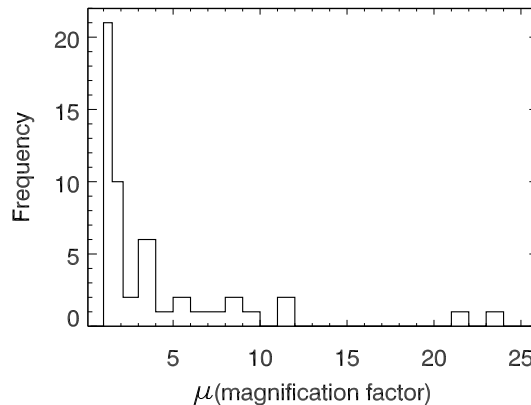
Figure 3.5: *Histogram showing the distribution of the magnification factors. The histogram is binned with $\Delta\mu = 1$, except between 1 and 2, where the bin-size is 0.5.*

and the area in the source plane. The confusion limit in the lensed case can thus be written as $S_{conf} = \sqrt[\alpha]{30\Omega_{beam}N_0\mu^{1-\alpha}}$. As the lensing magnification varies across the field, this simple estimate gives an average across the field, which in some cases means that the estimated lensed confusion limit does not reflect the confusion limit of the highly magnified region close to the caustics. For the most extreme case in our sample, A1689, where the source plane area surveyed is 20 times smaller than the SCUBA field of view, the confusion limit is reduced by a factor 4.5, i.e., $S_{conf} = 0.44$ mJy. The confusion limits for the cluster fields based on this simple calculation are given in Table 3.2. In the simplified estimate of the confusion limit presented here we assumed that the number counts are described by a single power law. There are good indications that the number counts are described by a double power law or another function with a (gradual) turn-over (see Sect. 3.7). Including this in such a calculation will work in a favourable direction and the confusion limit in the source plane will be lower.

3.5 Lensing

Our observations have been assisted by the gravitational lensing caused by the presence of the galaxy clusters in the targeted fields. This has enabled us to observe intrinsically fainter objects which would otherwise not have been detected in the blank fields. The magnification of the light of any background object and the angular extension of the background area in combination with steep number counts, means that the gravitational lensing is of great advantage to our observations: The confusion limit will be pushed to lower flux levels, which means that fainter objects can be detected without suffering confusion.

To quantify the lensing effect we use LENSTOOL (Kneib et al., 1993). The gravitational potential of each galaxy cluster is mapped in a mass model. This mass model describes the distribution of the overall potential of the cluster and to some extent of the individual galaxies. For clusters where the cluster lensing is a less
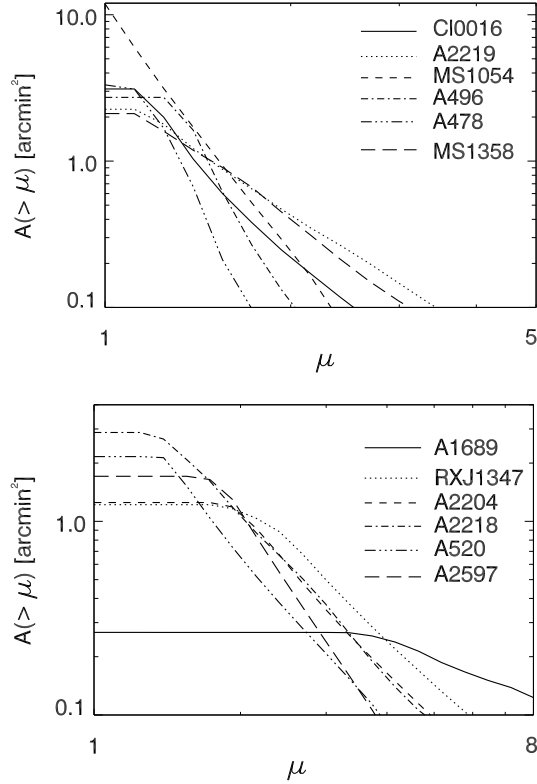
Figure 3.6: *The area as function of magnification for the individual fields. This has been split into two figures for clarity. The top panel shows the fields with relatively less strong lensing effect, while the bottom panel shows those with stronger lensing effect. We have assumed a redshift of $z = 2.5$. Placing the source plane at a different redshift, $z > 1$, would not make a significant difference.*

strong effect only the brightest cluster galaxies are considered in the mass model in addition to the global cluster potential. For clusters where the cluster lensing is a dominant effect many galaxies have been included to map the substructure of the total potential, as individual galaxies might cause extra lensing of the background sources. The lensing correction is done for the individual submm sources and for the sensitivity maps. The latter are needed in the calculation of the number counts.

As the redshift is not yet known for a majority of the objects, we assume a redshift of 2.5 based on the findings from Chapman et al. (2003) for the objects with unknown redshift. Likewise, the sensitivity maps, which gives us the observational sensitivity in the image plane, are traced to a source plane at $z = 2.5$.

The magnification factors of the individual sources range from 1.1 to 23. We have plotted a histogram of the magnification factors in Fig. 3.5. About 40 % of the sources are magnified by factors $\mu > 2$, while 20 % are magnified by $1.5 < \mu < 2$,
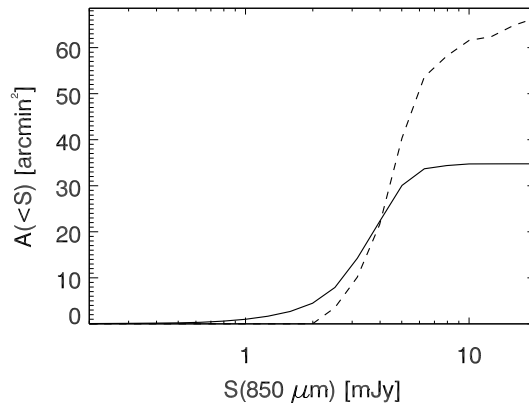
Figure 3.7: *The area as function of 1σ sensitivity for the whole survey. The dashed line represents the area in the image plane, and the solid line represents the area in a source plane at redshift $z = 2.5$. The actual area surveyed in the source plane is a factor two smaller than what we observe in the field of view of SCUBA at $850\,\mu m$. For the twelve cluster fields the total area surveyed of useful data in the image plane is $66.5\,arcmin^2$ and in a source plane at redshift $z = 2.5$ is $35\,arcmin^2$. For comparison the seven cluster fields from the UK-SCUBA Lens Survey are $40\,arcmin^2$ in the image plane and $15\,arcmin^2$ in the source plane (Smail et al., 2002). Likewise, in the deep though small survey by Cowie et al. (2002), the area in the image plane is $18\,arcmin^2$; assuming a reasonable amplification this corresponds to $6\,arcmin^2$ in the source plane.*

and 40 % have relatively low magnification factors $1 < \mu < 1.5$. One multiply-imaged object has been found in A2218, where three images of the same faint object has been detected. This object is described in detail in Kneib et al. (2004). We have plotted the area as function of magnification factor for the individual fields in Figure 3.6, and the area as function of source plane sensitivity for the whole survey Figure 3.7. In Figure 3.6, the two most extreme cases are A1689, where the area surveyed is a factor 20 smaller in the source plane than in the image plane, and MS1054-03, where the average over the large angular area surveyed of the cluster dilutes the strong lensing effect caused by the core of the cluster. The total area observed by our survey in these 13 fields is $71.5\,arcmin^2$. When taking into account the gravitational magnification the area of the cluster fields is reduced to $35\,arcmin^2$ in the source plane. The area of the individual fields as well as the sensitivity in the source plane is listed Table 3.2.

The uncertainties of the corrected fluxes and positions introduced by the lensing are in most cases small. The magnification is generally a monotonic function of the redshift (except in the very central part of a strong lensing cluster), but for source redshifts twice larger than the lens redshift, the amplification is only weakly increasing with redshift. As essentially all the SCUBA sources are expected to be at $z > 1$, this is only a minor effect. However, the position of the source relative to the cluster center and cluster members can play an important role, as the magnification can vary from ~ 2 to ~ 20 for typical background sources. The uncertainty

on the magnification (assuming a known redshift) is directly linked to the uncertainty on the mass model. The closer the object is to the critical line, the higher its magnification will be and the larger the uncertainty on the magnification will be. At most four of the SCUBA sources lie relatively close to critical lines and therefore their magnification factors are subject to larger uncertainties. However, on an ensemble basis, when e.g. deriving the counts in terms of unlensed flux, the error in magnification is compensated by the error in lensed area, thus the change in the unlensed counts due to error in the mass model is of the second order.

Table 3.2: *The area in the source plane at redshift $z = 2.5$, an estimate of the source plane confusion limit (also see subsection 3.4.2), and the area-weighted 1σ sensitivity in the source plane.*

CLUSTER	$\Omega_{s.pl.}$ arcmin^2	S_{conf} mJy/Ω_b	σ^{850}_{wghtd} mJy/Ω_b
Cl0016+16	3.1	1.7	1.48
A478	3.3	1.7	1.65
A496	2.7	1.6	0.98
A520	2.2	1.4	0.78
MS1054$-$03	11.9	1.8	1.17
A1689	0.3	0.4	0.13
RXJ1347.5$-$1145	1.2	1.0	1.06
MS1358+62	2.0	1.3	1.17
A2204	1.3	1.1	2.23
A2218	2.9	1.2	0.50
A2219	2.3	1.4	1.06
A2597	1.7	1.3	0.78

$\Omega_{s.pl}$ is the area of the source plane.
S_{conf} is the flux confusion limit (see subsection 3.4.2).
Ω_b is the area of the beam.
σ^{850}_{wghtd} is the area-weighted 1σ sensitivity in the source plane.

3.6 The catalogue

In the twelve cluster fields we detect 53 sources and in the NTT Deep Field we detect 5 sources. The sources have been named according to their detection (SMM) and their J2000 coordinates. The catalogue of the extracted point sources is given in Table 3.3. The unlensed fluxes and gravitational magnifications are given in Table 3.4. The final maps are shown in Figures 3.8-3.9. The positions of the sources are indicated on the maps. We have detected 15 sources below the blank field confusion limit. Of these, 11 have flux densities < 1 mJy, which *triples the number of known sub-mJy sources* (compare Cowie et al. 2002, Smail et al. 2002). Here follows a description of the individual fields. The references for mass models for the individual clusters are also mentioned.
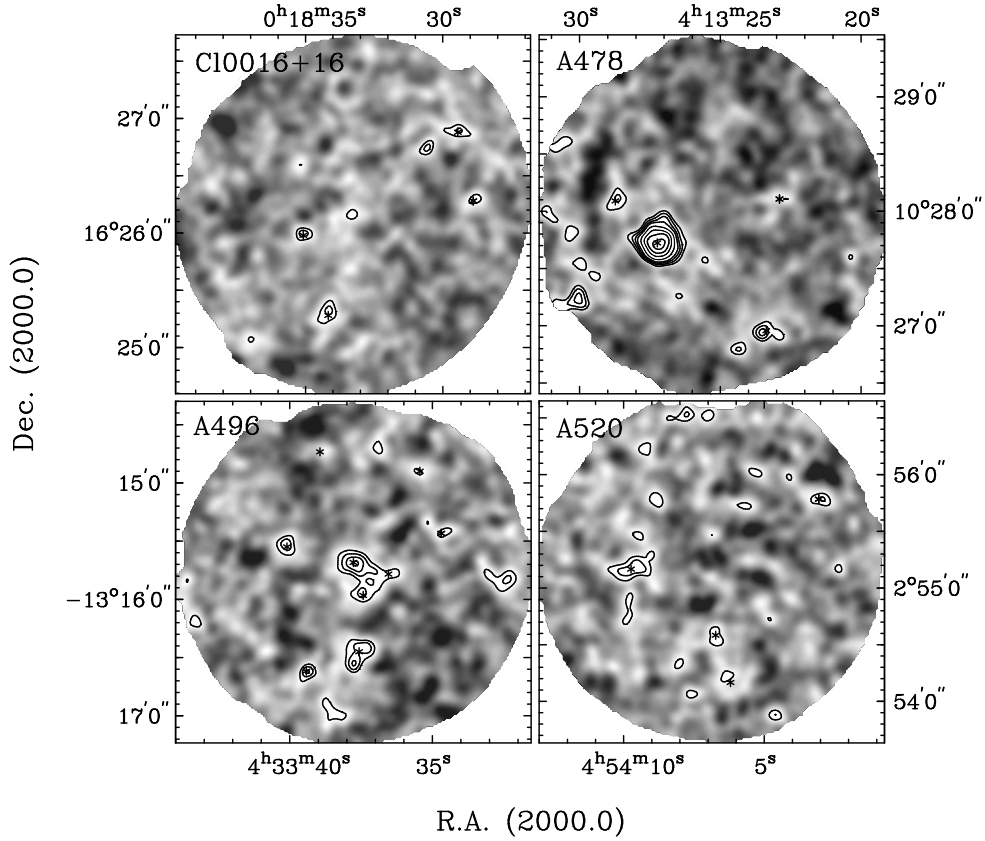
Figure 3.8: *The signal-to-noise (S/N) 850 μm SCUBA maps of the clusters Cl0016+16, A478, A496 and A520. The overlayed contours represent S/N = 3,4,5,6,7, but for A478 the contours represent S/N = 3,4,5,6,8,10,12,14. The stars ⋆ indicate the position of the detected sources.*

Cl0016+16 In this field, four point sources were detected with $3 < S/N < 4$. The magnification factors for the four sources are between 1.2 and 2.2. The corrected flux of the sources are between 2.4 and 5.2 mJy. None of the sources have significant 450 μm flux detections. A shallower SCUBA map of this field is presented in Chapman et al. (2002), where the depths is about a factor two shallower than our map. Within the positional uncertainties the two sources from Chapman et al. are coincident with SMM J00186+16253 and SMM J00186+16260, though we find that the observed fluxes are fainter than in Chapman et al. The mass model is based on the results from Natarajan (private communication) with a substantially more detailed description compared to that of Chapman et al.

A478 This cluster is well-known in cooling-flow studies (e.g., White et al., 1991).

Some of the SCUBA data presented here were obtained by others to study the cooling-flow, however, the cooling-flow has not been detected in the data. Four point sources are detected. With a detected flux of $S_{850} = 25\pm3$ mJy the source SMM J04135+10277 is the brightest source in the survey. This source has been studied in detail and is identified with a quasar at redshift $z = 2.837$ (Knudsen et al. 2001, Knudsen et al. 2003). The three fainter sources have S/N between 3.3 and 4.2. All four sources have magnification factors of 1.2-1.3. The fluxes of the three other sources are 5.6-7.3 mJy. The quasar is the only source in this field with 450 μm flux detection. Close to the SE-edge a fifth bright source is detected, however, as it is less than 1.5 beam from the edge it is not included in the catalogue. The mass model is a simple model, which we constructed based on the published velocity dispersions: the model includes the cluster potential and the potential of the cD galaxy (Allen et al., 1993; Zabludoff et al., 1990).

A496 This is the lowest redshift cluster in the survey. Nine point sources have been detected. Even though this cluster has not been observed to the blank field confusion limit, the large number of source might introduce extra uncertainties on the derived parameters. Three sources towards the center of the field are just 14″ (just smaller than a beam) from one another. One of the central sources, SMM J04336−13157, is coincident with the cD. The two other central sources, SMM J04336−13160 and SMM J04336−13158, are so close (just less than a beam) to the centre of the cD galaxy, that they are likely associated with cD galaxy. The latter of those two sources has a probable detection of 450 μm emission. All three central sources will be excluded from the further analysis in this paper. In Figure 3.8, source SMM J04336−13147 has no $S/N = 3$ contour as it is located in a depression in the background. The six other sources are magnified by factors 1.3-1.4 and have unlensed fluxes of 3-6.3 mJy. This large number of source in a low-z cluster field is surprising. Follow-up observations indicate that they are not cluster members, which might otherwise be expected because of the low redshift of the cluster. Like A478, the lens mass model is a simple model including the cluster potential and the cD galaxy (Peletier et al., 1990; Zabludoff et al., 1990)

A520 The optical center and the X-ray center of A520 is not coincident, and the cluster seems to be undergoing strong dynamical evolution, as the cD galaxy is not located at the center of the X-ray emission (Proust et al., 2000). Our SCUBA map is about 1′ E of the X-ray center (Govoni et al., 2001). Four point sources have been detected with lensing corrected fluxes between 0.7 and 3.4 mJy. The brightest source in the field, SMM J04542+02552, has a possible detection of 450 μm flux. The mass model is based on the general cluster potential (White et al., 1997; Carlberg et al., 1996).

MS1054−03 For this cluster the deepest multi-wavelength data set exists, ranging from radio to X-ray. It is a part of the FIRES-project (Faint IR Extragalactic Survey; Franx et al., 2000, Förster Schreiber et al., *in prep*), which includes the deepest near-IR imaging of a cluster taken with ISAAC at VLT. The area covered with ISAAC and other instruments is about 5′×5′, so we decided to obtain three point-
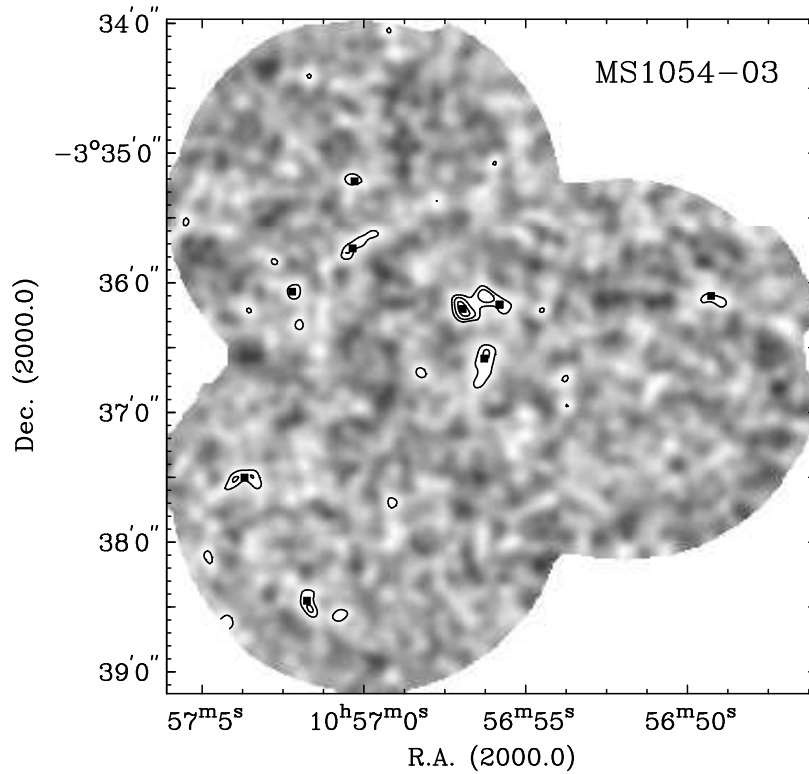
Figure 3.9: *The signal-to-noise 850 μm SCUBA map of the cluster MS1054-03. The overlayed contours represent S/N = 3,4,5,6,7,8. The black boxes indicate the positions of the detected sources. To cover a large area of the existing multi-wavelength data (see text for details), we have obtained three pointings for this field.*

ings to cover a larger area of the field and take advantage of the excellent data available for follow-up studies. The three pointings, which are denoted by S, N and NW, according to the relative position cover a signification part of the FIRES field. The S pointing is centered at the cluster center. We detect nine sources with fluxes between 3.5 and 5.0 mJy. The largest fraction of the sources are located in the N pointing, while the NW pointing is a lot sparser. This suggests a level of clustering of SCUBA sources, though the field is too small for a reliable clustering analysis. Our map is about three times deeper than the shallow map of the area of the S-pointing published by Chapman et al. (2002). They find one source, which is off-set $\sim 25''$ north of SMM J10571−03375 and not at all detected in our much deeper map. The gravitational lensing is not particularly strong for this cluster, which is partly related to the relative high redshift. The mass model is based on the overall cluster potential (Tran et al., 1999; P. van Dokkum, private communication).

A1689 With ~ 34 hours raw integration time for a single pointing and a 1σ r.m.s. ~ 0.7 mJy, this is one of the deepest maps of the survey. A1689 is a cluster known to have an exceptionally large Einstein radius (e.g. King et al., 2002). Because the gravitational lensing is so strong, the area of a source plane at redshift $z = 2.5$ is only 0.3 arcmin^2, i.e. 20 times smaller than area of the image plane or the field of view of SCUBA. We detect nine SCUBA sources, and note that this field might be confused due to the large number of sources. The three central sources are approximately one beam from one another, and the same is the case for two eastern sources. The sources have observed fluxes between 2.6 and 5.4 mJy. When correcting for the gravitational lensing magnification the fluxes are between 0.11 and 1.3 mJy. Two of the sources have large magnification factors of $\mu \sim 20$ suggesting that these sources are very close to critical lines, where the calculation of the magnification factors can become uncertain (see comment in section 3.5). There is a non-negligible chance that some of the sources are multiple images of the same background galaxy – this we will discuss in a future paper. The central source SMM J13115$-$01208 has a probable detection of 450 μm flux. The mass model will be presented in detail in Kneib et al., (*in prep.*).

RX J1347.5$-$1145 This is the most X-ray-luminous cluster known (Allen et al., 2002). In this field we detect one source, SMM J13475$-$11459, which has $S_{850} = 16.2\pm3.1$ mJy and $S_{450} = 98.7\pm29.6$ mJy. The source is strongly lensed and has an unlensed flux of 4.5 mJy. Furthermore, a large, extended source near the cluster center is present. This is the Sunyaev–Zel'dovich effect reported in Komatsu et al. (1999). The mass model is based on Cohen & Kneib (2002).

MS1358+62 This field is relatively poor with only one detection SMM J13600+62312, with $S_{850} = 6.8\pm1.3$ mJy; 4.4 mJy after correcting for the lensing. These data were first obtained to study the strongly lensed, redshift $z = 4.92$ galaxy MS1358+62-G1 (Franx et al., 1997), which however was not detected (van der Werf et al., 2001). We here find a 3σ upper limit for G1 of $S_{850} < 4.8$ mJy. A detailed mass model describes the potential for this cluster (Franx et al., 1997; Santos et al., 2004).

A2204 This field has the shallowest SCUBA observations of the whole survey. One point source, SMM J16327+05349, has been detected at a $S/N = 4.9$ with an observed flux of $S_{850} = 22.2\pm5.7$ mJy making it the second brightest source in the catalogue. This source is lensed by more than a factor 3, resulting in a corrected flux of ~ 7 mJy.

A2218 Together with A1689 and the NTT Deep Field, this field is the deepest data taken for the survey. The data for this field cover an area corresponding to more than two pointings. The data was used as a case study for the source extraction method, the Mexican Hat Wavelets algorithm, applied for this survey (Knudsen et al., *Chapter 2*).

In this field nine sources were detected. The three source, SMM J16358+66121, SMM J16359+66124 and SMM J16359+66126, have been identified as the same, multiply-image source at redshift $z = 2.516$ (Kneib et al., 2004), and is referred
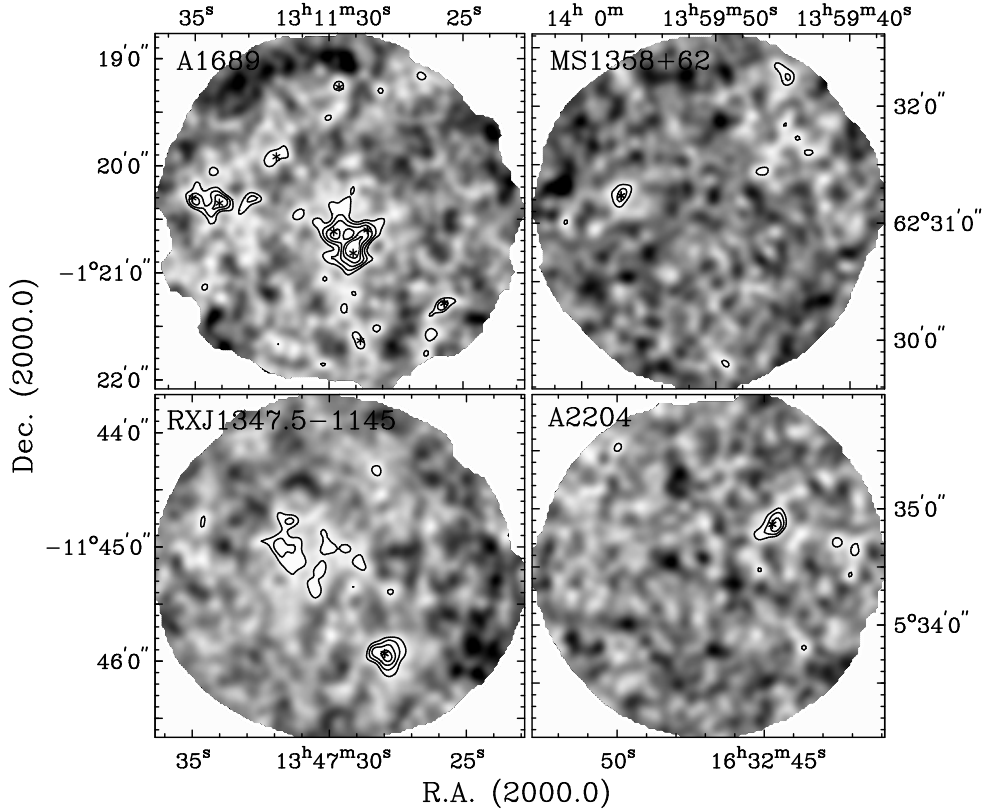
Figure 3.10: *The signal-to-noise (S/N) 850 μm SCUBA maps of the clusters A1689, MS1358+62, RX J1347.5-1145 and A2204. The overlayed contours represent S/N = 3,4,5,6,7,8. The stars ⋆ indicate the positions of the detected sources.*

to as SMM J16359+6612. The source SMM J16359+66118, which is detected both at 850 μm and 450 μm, is coincident with a known galaxy, #289, with redshift $z = 1.034$ (Pelló et al., 1992) and is also detected at 15 μm with ISOCAM (e.g., Metcalfe et al., 2003). The relatively bright source SMM J16357+66117 is detected at both 850 μm and 450 μm. The sources in A2218 have observed fluxes between 2.8 and 16.1 mJy. The lensing corrected fluxes are 0.4–6.1 mJy. The mass model is based on Kneib et al. (1996), Ellis et al. (2001) and Kneib et al. (2004).

A2219 In this field we detect two point sources that both have possible detections of 450 μm flux. This field was also a part of Chapman et al. (2002)'s sample, though their observations are shallower. The source SMM 16403+46440 agrees well with their finding. In Chapman et al. (2002) the source C SMM J16404+4643 has an upper limit at 850 μm, while being detected at 450 μm. We do not get a significant detection of the source, but MHW does suggest a $S/N \sim 1.9$ detection, which corresponds to a flux of ~ 2.3 mJy; the 3σ upper limit is < 3.6 mJy.

61
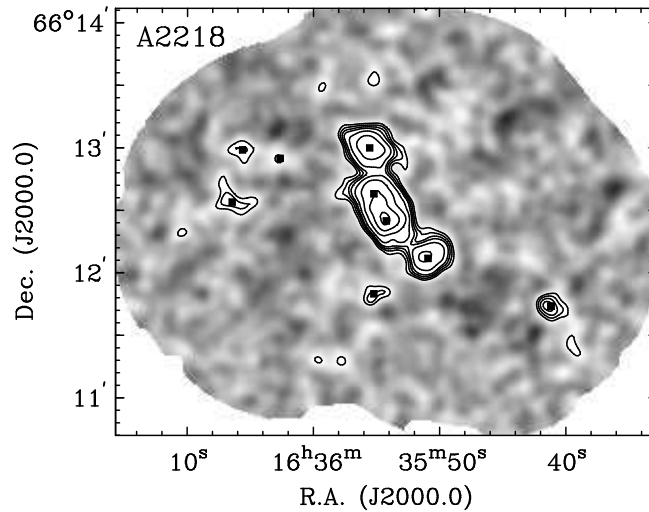
Figure 3.11: *The signal-to-noise 850 μm SCUBA map of the cluster A2218. The over-layed contours represent S/N = 3,4,5,6,8,12,18,24. The black boxes indicate the positions of the detected sources.*

For the source B SMM J16403+46437 MHW suggests a $S/N \sim 2.3$ detection. The source D SMM J16404+4644 is close to the edge by a beam. In our map a positive fluctuation is present, though it does not have the characteristics of a significant 850 μm detection. Furthermore, MHW also finds a $S/N \sim 2.9$ source at $\alpha, \delta =$ 16^{h}40^{m}22^s,+46°42′25″. The mass model is described in Smith et al. (2004).

A2597 In this field, two point sources were detected with $S/N > 3$. The brightest source, SMM J23253−12075, is a 12 mJy source located in the center of the map and is coincident with the cD galaxy of the cluster, which is a well-known AGN (e.g. McNamara et al., 1999). The cD galaxy is excluded from the rest of the analysis in this paper. The other source, SMM 23254−12078, is a 5 mJy source, which also has detected 450 μm flux. The mass model includes both the overall potential of the cluster and that of the cD galaxy (Wu & Xue, 2000; Smith et al., 1990).

NTT Deep Field This field, the blank field of the survey (Arnouts et al., 1999). is one of the deepest fields of the survey. Five sources have been detected with fluxes between 3 and 4 mJy. None of them have detected 450 μm flux. In Figure 3.12, source SMM J12053−07448 has no $S/N = 3$ contour as it is located in a depression in the background. A 1.2 millimeter map of the NTT Deep Field has been obtained with the Max-Planck Millimetre Bolometer (MAMBO) covering a larger area of the NTT Deep Field than the SCUBA map presented here (Dannerbauer et al., 2002, 2004). Considering that 1.2 mm probes a part of the modified blackbody where the flux is fainter compared to the 850 μm, the MAMBO map is a bit shallower than the deep SCUBA map. Two MAMBO sources are covered by the SCUBA map. The

Table 3.3: *Catalogue of source positions, submm fluxes and uncertainties. S is the flux, S/N is the signal-to-noise of the detection in real space, the σ's give the uncertainties in the flux and position. The uncertainties do not take into account possible additional uncertainties due to confusion. For the position, the additional confusion-uncertainty is $\sim 1.9''$ (as described in Section 3.4).*

NAME	RA(2000) h m s	Dec(2000) ° ′ ″	S_{850} mJy	S/N	$\sigma_{S_{850}}$ mJy	$\sigma_{position}$ ″	S_{450} mJy	S/N_{450}	$\sigma_{S_{450}}$ mJy
Cl0016+16									
SMMJ00185+16263	00 18 28.9	+16 26 17	6.5	3.2	2.2	4.0	< 34.2	...	...
SMMJ00185+16269	00 18 29.4	+16 26 53	5.8	3.2	2.0	4.0	< 77.9	...	...
SMMJ00186+16253	00 18 34.2	+16 25 17	7.0	3.9	2.4	4.0	< 56.1	...	...
SMMJ00186+16260	00 18 35.1	+16 25 59	5.3	3.1	1.8	4.0	< 34.2	...	...
A478									
SMMJ04134+10281	04 13 22.9	+10 28 06	6.8	3.3	2.5	3.8	< 35.3	...	...
SMMJ04134+10270	04 13 23.4	+10 26 57	7.9	4.2	2.1	3.1	< 53.9	...	...
SMMJ04135+10277	04 13 27.2	+10 27 43	25.0	14.4	2.8	2.3	55.4	5.3	16.6
SMMJ04135+10281	04 13 28.7	+10 28 05	9.0	3.8	3.3	3.8	< 32.8	...	...
A496									
SMMJ04336−13154	04 33 34.7	−13 15 26	4.7	3.1	1.7	4.1	< 43.6	...	...
SMMJ04336−13149	04 33 35.4	−13 14 54	5.3	3.3	1.9	4.1	< 54.7	...	...
SMMJ04336−13158	04 33 36.5	−13 15 47	4.8	4.0	1.7	3.2	51.1	3.0	15.3
SMMJ04336−13160	04 33 37.4	−13 15 58	4.7	3.8	1.7	4.1	< 42.9	...	...
SMMJ04336−13164	04 33 37.6	−13 16 27	9.0	5.5	1.6	3.0	< 40.3	...	...
SMMJ04336−13157	04 33 37.8	−13 15 41	7.9	5.7	1.4	3.0	< 39.4	...	...
SMMJ04336−13147	04 33 38.9	−13 14 44	4.0	3.1	1.4	4.1	< 67.3	...	...
SMMJ04337−13166	04 33 39.4	−13 16 37	4.8	3.6	1.7	4.1	< 52.1	...	...
SMMJ04337−13156	04 33 40.1	−13 15 33	6.4	5.1	1.1	3.0	< 36.9	...	...
A520									
SMMJ04541+02558	04 54 03.1	+02 55 47	4.7	4.1	1.1	3.3	< 31.9	...	...
SMMJ04541+02542	04 54 06.2	+02 54 10	3.9	3.1	1.4	4.2	< 32.6	...	...
SMMJ04541+02546	04 54 06.7	+02 54 35	4.3	3.1	1.5	4.2	< 37.0	...	...
SMMJ04542+02552	04 54 09.7	+02 55 10	6.0	4.4	1.4	3.3	29.0	2.7	8.7

63

Table 3.3: — *Continued from previous page.*

NAME	RA(2000) h m s	Dec(2000) ° ′ ″	S_{850} mJy	S/N	σ_{S850} mJy	$\sigma_{position}$ ″	S_{450} mJy	S/N$_{450}$	σ_{S450} mJy
MS1054–03									
SMMJ10568–03361	10 56 49.3	–03 36 06	5.0	3.6	1.1	3.3	< 17.6	...	...
SMMJ10569–03362	10 56 55.8	–03 36 10	3.9	3.8	0.9	3.3	25.6	3.4	7.7
SMMJ10569–03366	10 56 56.3	–03 36 35	3.9	3.7	0.9	3.3	< 21.2	...	...
SMMJ10569–03362	10 56 57.0	–03 36 12	4.9	4.8	0.9	2.8	61.7	3.6	18.5
SMMJ10570–03352	10 57 00.3	–03 35 13	3.5	3.2	1.1	3.9	< 20.2	...	...
SMMJ10570–03357	10 57 00.3	–03 35 44	4.4	3.5	1.0	3.3	28.1	3.6	8.4
SMMJ10570–03385	10 57 01.8	–03 38 27	4.7	3.5	1.1	3.3	< 27.9	...	...
SMMJ10570–03361	10 57 02.2	–03 36 04	4.4	3.0	1.4	3.9	< 21.8	...	...
SMMJ10571–03375	10 57 03.7	–03 37 30	4.2	3.3	1.4	3.9	62.7	5.7	18.8
A1689									
SMMJ13114–01213	13 11 25.7	–01 21 17.0	5.0	3.9	1.6	3.3	< 66.4	...	...
SMMJ13115–01206	13 11 28.6	–01 20 36.0	2.6	3.4	0.8	4.3	...	...	...
SMMJ13115–01216	13 11 28.8	–01 21 38.0	3.6	3.3	1.2	4.3	< 32.9	...	...
SMMJ13115–01208	13 11 29.1	–01 20 49.0	4.7	6.0	0.8	2.8	21.4	4.4	6.4
SMMJ13115–01193	13 11 29.6	–01 19 16.0	3.8	4.0	1.2	3.3	< 36.8	...	...
SMMJ13115–01206	13 11 29.8	–01 20 37.0	2.5	3.2	0.8	4.3	< 11.3	...	...
SMMJ13115–01199	13 11 32.0	–01 19 55.0	3.3	3.6	1.0	3.3	< 14.8	...	...
SMMJ13116–01204	13 11 34.1	–01 20 21.0	3.2	4.0	1.0	3.3	< 12.4	...	...
SMMJ13116–01203	13 11 35.1	–01 20 18.0	4.9	4.2	1.6	3.3	< 17.6	...	...
RX J1347.5–1145									
SMMJ13475–11459	13 47 28.0	–11 45 56	15.5	5.67	3.1	3.0	98.7	12.8	29.6
MS1358+62									
SMMJ13600+62312	13 59 57.1	+62 31 14	6.7	4.42	1.3	3.2	< 25.5	...	...
A2204									
SMMJ16327+05349	16 32 44.7	+05 34 52	22.2	4.9	5.7	3.2	< 219.5	...	...

Table 3.3: — *Continued from previous page.*

NAME	RA(2000) h m s	Dec(2000) ° ' "	S_{850} mJy	S/N	$\sigma_{S_{850}}$ mJy	$\sigma_{position}$ "	S_{450} mJy	S/N_{450}	$\sigma_{S_{450}}$ mJy
A2218									
SMMJ16357+66117	16 35 41.2	+66 11 44	10.4	7.5	1.4	2.6	53.4	3.5	16.0
SMMJ16358+66121	16 35 50.9	+66 12 07	8.7	11.5	1.1	2.4	22.9	5.9	6.9
SMMJ16359+66124	16 35 54.2	+66 12 25	16.1	21.7	1.6	2.3	46.4	12.4	13.9
SMMJ16359+66126	16 35 55.2	+66 12 38	12.8	16.9	1.5	2.2	31.8	8.3	9.5
SMMJ16359+66118	16 35 55.2	+66 11 50	3.1	3.8	0.7	3.3	17.1	4.7	5.1
SMMJ16359+66130	16 35 55.5	+66 13 00	11.3	15.8	1.3	2.2	< 11.8	...	...
SMMJ16360+66129	16 36 02.6	+66 12 55	2.8	3.5	0.6	3.3	< 14.5	...	...
SMMJ16361+66130	16 36 05.6	+66 12 59	5.2	4.9	0.9	3.1	< 17.4	...	...
SMMJ16361+66126	16 36 06.5	+66 12 34	4.8	4.6	0.8	3.1	< 17.4	...	...
A2219									
SMMJ16403+46440	16 40 19.5	+46 43 58	10.0	5.8	2.0	2.9	53.4	5.0	16.0
SMMJ16404+46429	16 40 25.5	+46 42 55	5.1	3.1	1.7	3.7	29.4	2.9	8.8
A2597									
SMMJ23253−12075	23 25 19.8	−12 07 27	12.3	7.1	1.8	2.6	< 37.9	...	...
SMMJ23254−12078	23 25 23.4	−12 07 45	5.2	3.2	1.7	4.1	71.2	5.0	21.4
NTT Deep Field									
SMMJ12053−07441	12 05 19.0	−07 44 09	3.8	4.0	0.9	3.3	< 16.0	...	...
SMMJ12053−07448	12 05 20.6	−07 44 48	3.0	3.2	0.8	4.0	< 13.7	...	...
SMMJ12054−07445	12 05 22.1	−07 44 31	3.5	3.9	0.9	3.3	< 14.0	...	...
SMMJ12054−07453	12 05 23.1	−07 45 16	3.4	3.4	0.9	4.0	< 16.7	...	...
SMMJ12054−07452	12 05 25.1	−07 45 12	4.0	4.3	0.9	3.3	< 23.8	...	...
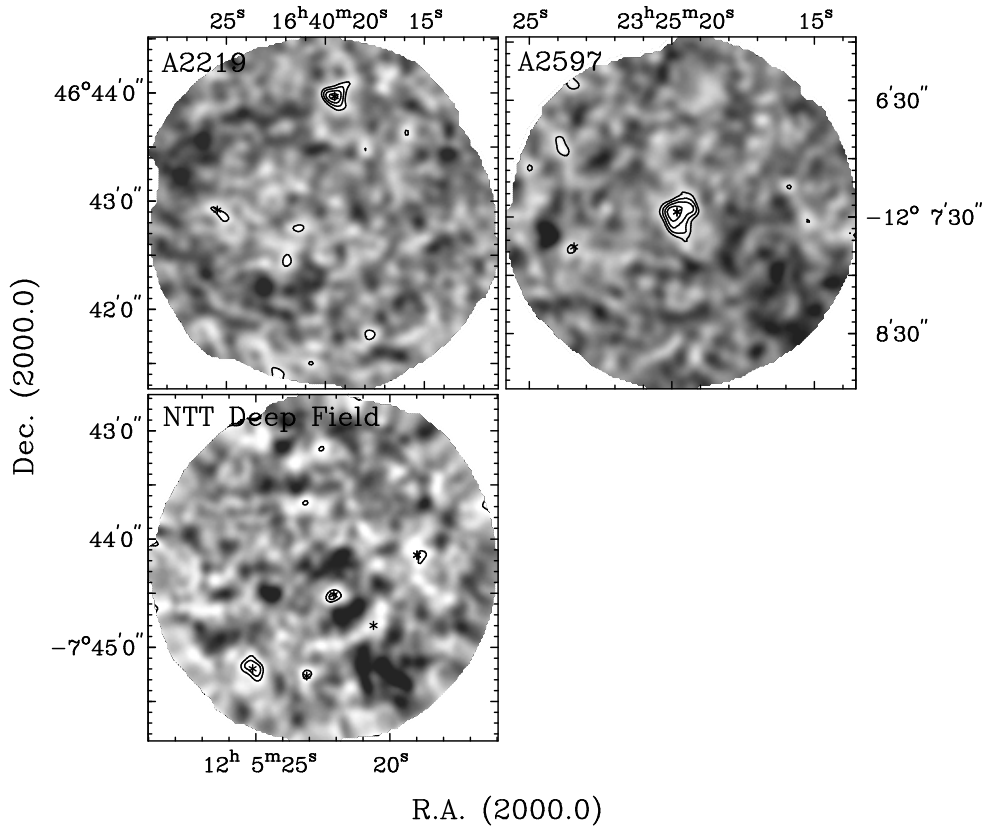
Figure 3.12: *The signal-to-noise (S/N) 850 μm SCUBA maps of the clusters A2219 and A2597 and of the blank field NTT Deep Field. The overlayed contours represent $S/N = 3,4,5,6$. The stars $\star$ indicate the positions of the detected sources.*

source MM J120517−0743.1 is very close to the edge of the SCUBA map, where there are no indications of a source. The source MM J120522−0745.1, which has a radio detection, is only 6″ from the submm source SMM J12054−07453. The radio detection is coincident with the submm source.

3.7 Number counts

The notation $N(>S)$ is typically used for cumulative number counts: the number of sources per unit solid angle brighter than a flux limit S. Calculating the cumulative number counts by counting the number of sources with $>S$ must be done on a map with uniform sensitivity. However, the SCUBA maps do not have uniform sensitivity. This is dealt with in the following way: For a given flux level S, only the surveyed area where $3\sigma < S$ is considered. The $N(>S)$ is then the number of sources with $>S$ within that area divided by the source plane area, $\Omega_{<S}$. The problem of determining number counts for maps of non-uniform sensitivity has

Table 3.4: *Source list with lensing corrected flux and gravitational amplification factor, μ. For sources with unknown redshift, we have assumed a redshift of z = 2.5, which is indicated in italics.*

NAME	z	S_{850} mJy	μ
Cl0016+16			
SMM J00185+16263	*2.5*	5.5	1.2
SMM J00185+16269	*2.5*	4.7	1.2
SMM J00186+16253	*2.5*	5.4	1.3
SMM J00186+16260	*2.5*	2.8	2.0
A478			
SMM J04134+10281	*2.5*	5.6	1.2
SMM J04134+10270	*2.5*	5.8	1.3
SMM J04135+10277	2.837	19.4	1.3
SMM J04135+10281	*2.5*	7.4	1.3
A496			
SMM J04336−13154	*2.5*	3.5	1.4
SMM J04336−13149	*2.5*	4.0	1.4
SMM J04336−13158	0.03	...	0.0
SMM J04336−13160	0.03	...	0.0
SMM J04336−13164	*2.5*	6.0	1.5
SMM J04336−13157	0.03	...	0.0
SMM J04336−13147	*2.5*	2.8	1.4
SMM J04337−13166	*2.5*	3.2	1.4
SMM J04337−13156	*2.5*	4.4	1.5
A520			
SMM J04541+02558	*2.5*	3.1	1.5
SMM J04541+02542	*2.5*	0.7	5.5
SMM J04541+02546	*2.5*	0.9	4.5
SMM J04542+02552	*2.5*	3.4	1.7
MS1054-03			
SMM J10568−03361	*2.5*	4.6	1.1
SMM J10569−03362	*2.5*	3.5	1.1
SMM J10569−03366	*2.5*	4.6	1.1
SMM J10569−03362	*2.5*	4.3	1.1
SMM J10570−03352	*2.5*	3.4	1.1
SMM J10570−03357	*2.5*	4.0	1.1
SMM J10570−03385	*2.5*	3.7	1.3
SMM J10570−03361	2.423	3.9	1.1
SMM J10571−03375	*2.5*	2.6	1.6

NAME	z	S_{850} mJy	μ
A1689			
SMM J13114−01213	*2.5*	1.3	3.9
SMM J13115−01206	*2.5*	0.11	23.6
SMM J13115−01216	*2.5*	0.62	5.8
SMM J13115−01208	*2.5*	0.22	21.6
SMM J13115−01193	*2.5*	0.47	8.1
SMM J13115−01206	*2.5*	0.74	3.3
SMM J13115−01199	*2.5*	0.34	9.7
SMM J13116−01204	*2.5*	0.50	6.5
SMM J13116−01203	*2.5*	1.3	3.8
RX J1347.5-1145			
SMM J13475−11459	*2.5*	5.2	3.0
MS1358+62			
SMM J13600+62312	*2.5*	4.6	1.5
A2204			
SMM J16327+05349	*2.5*	6.4	3.4
A2218			
SMM J16357+66117	*2.5*	6.1	1.7
SMM J16358+66121*	2.515	0.97	9.0
SMM J16359+66124*	2.515	0.73	22
SMM J16359+66126*	2.515	0.91	14
SMM J16359+66118	1.034	0.41	7.6
SMM J16359+66130	*2.5*	2.9	3.4
SMM J16360+66129	*2.5*	1.6	1.8
SMM J16361+66130	*2.5*	3.4	1.5
SMM J16361+66126	*2.5*	3.0	1.6
A2219			
SMM J16403+46440	*2.5*	8.3	1.2
SMM J16404+46429	*2.5*	3.3	1.5
A2597			
SMM J23253−12075	0.08	...	...
SMM J23254−12078	*2.5*	2.5	2.1

⋆ Triple imaged source (Kneib et al., 2004).

also been discussed for the CUDSS (Webb et al., 2003a).

Upper and lower errors are calculated using Poisson statistics weighted by the area, $\Omega_{<S}$. We use the tables for confidence limits on small numbers of events from Gehrels (1986). For the cluster fields we use the fluxes and sensitivity maps corrected for the gravitational lensing, as described in the previous section.

The resulting number counts for the $850\,\mu$m observations are plotted in Figure 3.13. The number counts, $N(>S)$, the number of sources for each data point and the area, $\Omega_{<S}$, are given in Table 3.5. Due to the non-uniform sensitivity across the observed fields, the area $\Omega_{<S}$ varies with S. Consequently, $N(>S)$ is not uniformly decreasing with S, which would otherwise be expected for cumulative number counts determined in fields with uniform sensitivity. We note that even though the area of the circle with diameter $15''$ is $0.049\,\mathrm{arcmin}^2$, and that the counts for $S_{850} < 0.2$ are calculated from an area that appears to be smaller than the beam in the image plane, it should be remembered that the area is in the source plane, which due to the large magnification would appear as a much larger area in the image plane corresponding to many beams.

The number counts are probed to the faintest source in the survey, which has a lensing corrected flux of $0.11\,\mathrm{mJy}$. A tentative analysis of the number counts show that the counts are not well-described by a single power-law function, but are better described by a double power-law:

$$\frac{\mathrm{d}N(>S)}{\mathrm{d}S} = \frac{N_0}{S_0}\left(\left(\frac{S}{S_0}\right)^{\alpha} + \left(\frac{S}{S_0}\right)^{\beta}\right)^{-1}. \tag{3.1}$$

We have performed a simple χ^2-analysis and find $\alpha = 4.0$, $\beta = 2.1$, $S_0 = 6.0\,\mathrm{mJy}$ and $N_0 = 2\times10^3\,\mathrm{deg}^{-2}$; this function has been plotted on top of the number counts in Figure 3.13. The value of S_0 varies between 5 and 8 mJy depending the choice of the exact value of N_0, where the best-fit values are $N_0 = 2.5-1.0\times10^3\,\mathrm{deg}^{-2}$. Likewise also for α and β the values vary between 3.5-4.5 and 1.9-2.3 respectively. This is the first time a turn-over has been detected from a single data set. The value of the turn-over point, S_0, is a bit higher than what has previously been assumed (e.g. Borys et al., 2003).

Using the differential number counts from equation 3.1, we calculate the integrated background light. At $S \sim 0.15\,\mathrm{mJy}$, the integrated background produced by our sources is comparable to the background light detected with COBE (Fixsen et al., 1998). Given that sources with fluxes below 0.1 mJy also contribute to the integrated background, there is a possibility that our counts overpredict the integrated the integrated background somewhat. The overproduction of the background light, which is caused by the shape of the number counts at the faint end, is possibly due to the low number statistics and/or unidentified multiply imaged sources in fields like A1689. The possibility of unidentified multiply imaged sources in the field A1689 is supported by summing up the flux of all sources detected in the different fields and dividing by the area observed, both before and after correcting for the gravitational lensing. This has been done in Table 3.6. Comparison of the resolved flux per observed area for the individual fields indicates how large the contribution to the integrated background light is. It can been seen that for most fields there is a fairly good agreement with before (image plane) and after (source
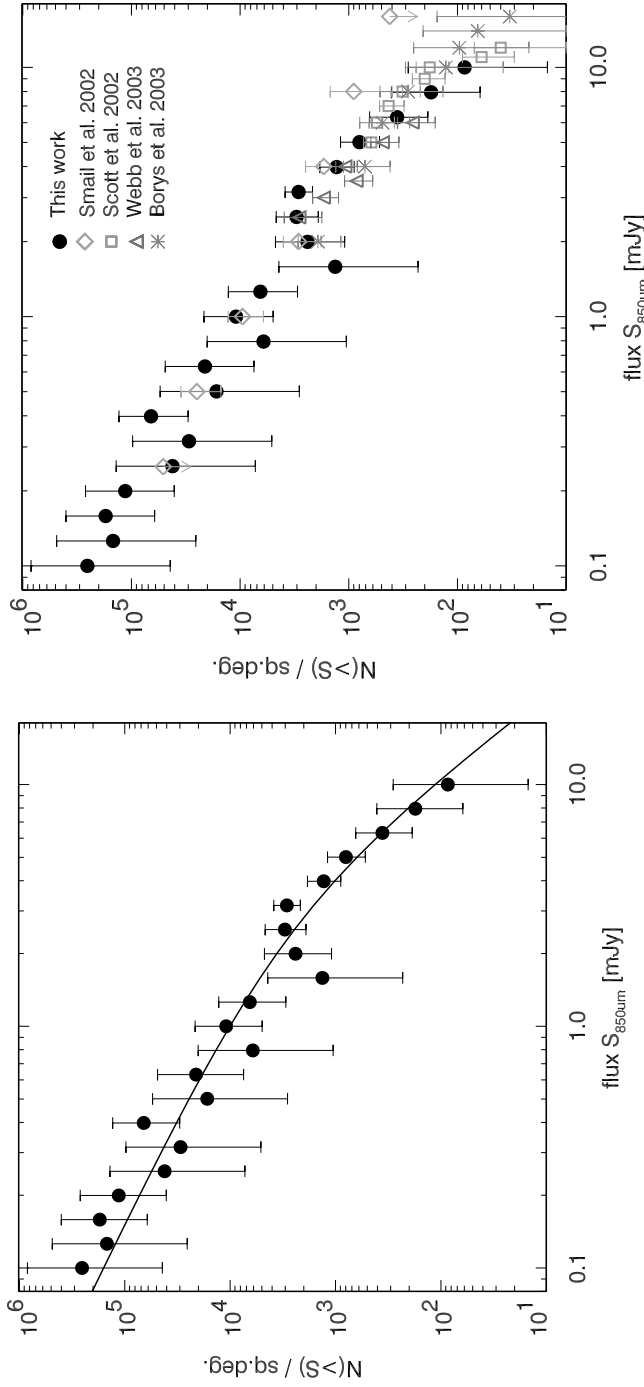
Figure 3.13: *The 850 μm number counts, $N(>S)$, as determined from this work. The number counts are determined based on the data from 12 cluster fields and one blank field. The data from the cluster fields have first been corrected for the gravitational lensing. 11 sources have been detected with sub-mJy sources. This triples the number of such sources known (compare Cowie et al., 2002). A turn-over between the bright and faint end is evident, and the number counts are best described by a function with a turn-over such as a double power-law. On the left panel a double power-law with parameters determined through a simple analysis is plotted on top of the number counts (for details see text). As this survey has almost twice as many fields than previous lensed surveys and also includes blank field observations, we can compare the number counts with those determined in the both lensed surveys and blank field surveys. On the right panel the number counts from four other fields have been plotted together with the number counts from this work. The faint end (i.e., fluxes below the blank field confusion limit) are in good agreement with those of other lensed surveys. The bright end (i.e., fluxes above the blank field confusion) is in good agreement with those of the larger blank field surveys.*

Table 3.5: *The 850 μm number counts.*

S_{850} mJy	$N(>S)$ arcmin^{-2}	N_{src}	$\Omega_{<3\sigma}$ arcmin^2
0.10	$70.6^{+162}_{-58.4}$	1	0.014
0.13	$41.0^{+94.3}_{-33.9}$	1	0.024
0.16	$48.0^{+63.3}_{-31.0}$	2	0.042
0.20	$31.7^{+41.8}_{-20.5}$	2	0.063
0.25	$11.6^{+26.8}_{-9.62}$	1	0.086
0.32	$8.21^{+18.9}_{-6.79}$	1	0.12
0.40	$18.3^{+17.8}_{-9.99}$	3	0.16
0.50	$4.58^{+10.5}_{-3.79}$	1	0.22
0.63	$5.85^{+7.72}_{-3.78}$	2	0.34
0.79	$1.69^{+3.89}_{-1.40}$	1	0.59
1.00	$5.05^{+3.41}_{-2.18}$	5	0.99
1.26	$2.41^{+1.91}_{-1.15}$	4	1.76
1.58	$0.74^{+0.98}_{-0.48}$	2	2.70
2.00	$0.67^{+0.65}_{-0.36}$	3	4.51
2.51	$0.84^{+0.45}_{-0.31}$	7	8.33
3.16	$0.80^{+0.27}_{-0.21}$	15	18.6
3.98	$0.36^{+0.15}_{-0.11}$	10	27.8
5.01	$0.22^{+0.11}_{-0.08}$	8	36.1
6.31	$0.10^{+0.08}_{-0.05}$	4	40.1
7.94	$0.049^{+0.064}_{-0.031}$	2	41.2
10.00	$0.023^{+0.054}_{-0.019}$	1	41.9

plane) correcting for the gravitational lensing, which is expected as the surface brightness is conserved. However, in A1689 the resolved flux per observed area is significantly larger in the source plane than in the image plane. The deviations in the cases of A496 and A2597 are explained by the presence of cD galaxies. Accounting for the effect such as described for A1689 would require more accurate source redshifts. In any case, it would tend to lower the counts at the faint end and would thus make the flattening of the cumulative counts at faint flux levels more pronounced.

Given the differential counts from equation 3.1 the dominant contribution to the integrated background light comes from the sources with fluxes S_{850} between 0.4 mJy and 2.5 mJy with 50 % of the background resolved at 1 mJy. The latter is in reasonable agreement with the results from the UK-SCUBA Lens Survey (Smail et al., 2002). Sources with $S_{850} > 2.5$ mJy contribute ~ 25 % to the integrated back-

Table 3.6: *The total flux resolved per area observed for the individual sources, both as seen in the image plane and as seen in the source plane.*

Field	$\Sigma f_{im}/\Omega_{im}$ mJy/deg^{-2}	$\Sigma f_{src}/\Omega_{src}$ mJy/deg^{-2}
Cl0016+16	19753	21318
A478	41526	41566
A496	45600	31451
A520	15669	13703
MS1054-03	9676	10094
A1689	22287	75260
RXJ1347	11639	15241
MS1358	5773	8193
A2204	20038	18502
A2218	34990	22950
A2219	11743	18628
A2597	15296	5276
NDF	12946	(12946)
Total	19518	17593

ground, of which sources with $S_{850} > S_0$ contribute only $\sim 10\%$. This means that the bulk of the submm energy output from the submm galaxy population arises from sources just fainter than the blank field confusion limit.

3.7.1 Comparison with other surveys

Here we will compare the derived number counts with those determined through other surveys, both lensed surveys and blank field surveys. The number counts from four other studies have been plotted together with the number counts from this work in Figure 3.13.

Lensing surveys: Three other studies of SCUBA observations of cluster fields have been published: The UK-SCUBA Lens Survey, in which seven cluster fields were targeted and number counts were determined to $S_{850} = 0.5$ mJy (e.g. Smail et al., 2002, 1997, Blain et al., 1999a). Cowie et al. (2002) obtained deeper SCUBA observations of three of the fields from the afore-mentioned UK-SCUBA Lens Survey, in which they detected five sub-mJy sources and have studied the number counts to $S_{850} \sim 0.1$ mJy. A shallower cluster survey was performed by Chapman et al. (2002), in which eight clusters were observed with SCUBA. No sub-mJy sources were detected. Here we will focus the comparison on the surveys from Cowie et al. (2002) and Smail et al. (2002). As both those surveys are relatively small in area, a comparison is only interesting where such surveys have their strength, namely at the faint fluxes. Cowie et al. (2002) detects five sub-mJy sources. We detect eleven sub-mJy sources, and thereby triple the number of known sub-mJy sources. Our faint number counts are in good agreement with

those of Cowie et al. and Smail et al.

Blank field surveys: Blank field surveys are surveys with no strongly gravitation-ally lensing clusters present in the surveyed area. Such surveys typically cover much large areas than the lensed surveys, and are limited in flux by the blank field confusion limit ($\sim 2.0\,$mJy). Hence the strength of those surveys lies at brighter fluxes. Several such surveys have been carried out: The Canada-UK Deep SCUBA Survey (CUDSS) (Eales et al., 2000, Webb et al., 2003a), covered 75 arcmin^2 to the blank field confusion limit. The 8mJy-survey (Scott et al.) covered an area of 260 arcmin^2 to a flux limit $> 5\,$mJy/beam. The Hubble Deep Field North (HDF-N) has been surveyed extensively, which has been brought together in the so-called "HDF-N SCUBA supermap" by Borys et al. (2003), which covers 165 arcmin^2 to depths between 0.4 and 6 mJy/beam. Barger et al. (1999b) have surveyed the Hawaii Survey Fields covering an area of 104 arcmin^2 to a flux limit of 8 mJy with a small area of 7.7 arcmin^2 almost to the confusion limit. With minor deviations, there is an overall good agreement between the bright end the number counts of the work presented here and previous work. Though, we do find that the slope of the power-law at the bright end is a bit steeper than previous work ($\alpha \sim 1.9\text{-}2.2$).

3.8 Conclusions and outlook

We have conducted a deep submm survey using SCUBA. We have observed twelve clusters of galaxies and the NTT Deep Field. The total area surveyed is 71.5 arcmin^2 in the image plane. For the cluster fields the total area in the source plane is 35 arcmin^2. This is the largest deep submm lens survey of its type to date. The gravitational lensing reduces the confusion limit allowing for observations of sources with $S_{850} < 2\,$mJy. The data have been analysed using Monte Carlo simulations to quantify the noise properties, Mexican Hat Wavelets have been used for source extraction and simulations were performed to quantify the error of the analysis.

- In total 58 sources have been detected, of which 15 have flux densities below the blank field confusion limit. Four of these 58 sources are associated to cluster cD galaxies. Three sources in the field of A2218 are multiple images of the same galaxy.

- Our survey for the first time substantially probes the sub-mJy population. The number of sub-mJy sources is 11, which triples the number of such sources.

- The integrated number counts are probed to 0.10 mJy. The integrated number counts cannot be described by a single power law, but have to be described by a double power law or another function with a turn-over. Describing the differential counts by a double power law function we find that the turn-over is $\sim 6\,$mJy. This is the first time a turn-over in the number counts has been directly detected from a single data set. At 1 mJy the number counts are $\sim 10^4\,$deg^{-2} and at 0.5 mJy they are $\sim 2 \times 10^4\,$deg^{-2}, based on derived differential counts.

- Another key result is that essentially all of the integrated submm background is resolved. At 1 mJy 50 % of the background is resolved, and at 0.4 mJy

75 % is resolved. The dominant contribution to the background comes from sources with fluxes S_{850} between 0.4 mJy and 2.5 mJy, while the bright sources with fluxes $S_{850} > 6$ mJy contribute only 10 %. This means that the bulk of the energy comes from submm galaxies with fluxes just below the blank field confusion limit.

The information about the submm number count distribution and the contribution to the integrated background radiation has been derived using the number counts as observed from our survey. Ideally to improve statistics, the number counts should be calculated from all the data available from all surveys performed to date. The optimal way of doing that is to reduce and analyse all the data consistently applying the same reduction and source extraction algorithms. Considering the large number of data available, that is a rather large task.

The submm number count distribution is the observable for the submm galaxy population as a whole. The counts are used for constraining models of the submm galaxy population. Blank field surveys probe $S_{850} > 2$ mJy, for which the number counts can be approximately described by a single power law function. Including the data at $S_{850} < 1$ mJy is important to study the turn-over, as a turn-over provides an extra constraint on the models describing the submm galaxy population and their evolution. Detailed analysis of the number counts and modelling of implications for our understanding the submm population, especially the sub-mJy submm population, will be presented in a future paper (Knudsen et al., *Chapter 4*). Furthermore, the nature of the submm galaxy population can only be studied through extensive multi-wavelength follow-up observations. In a future paper we will present such a study with identification of about half of the sources from the Leiden-SCUBA Lens Survey (Knudsen et al., *Chapter 5*).

References

Archibald, E.N., Wagg, J.W. & Jenness, T., 2000, SCD System Note 2.2, http://www.jach.hawaii.edu/JACdocs/JCMT/SCD/SN/002.2/

Allen, S.W., Fabian, A.C., Johnstone, R.M., et al., 1993, MNRAS, 262, 910

Allen, S.W., Schmidt, R.W. & Fabian, A.C., 2002, MNRAS, 335, 256

Arnouts, S., D'Odorico, S., Christiani, S. et al, 1999., A&A, 341, 641

Barger, A.J., Cowie, L.L. & Sanders, D.B., 1999, ApJ, 518, L5

Barnard, V.E., Vielva, P., Pierce-Price, D.P.I., et al., 2004, MNRAS, 352, 961

Baugh, C.M., Cole, S., Frenk, C.S. & Lacey, C.G., 1998, ApJ, 498, 504

Bernstein, R.A., Freedman, W.L. & Madore, B.F., 2002a, ApJ, 571, 56

Bernstein, R.A., Freedman, W.L. & Madore, B.F., 2002b, ApJ, 571, 107

Blain, A.W., Ivison, R.J. & Smail, I., 1998, MNRAS, 296, L29

Blain, A.W., Kneib, J.-P., Ivison, R.J. & Smail, I., 1999a, ApJ, 512, L87

References

Blain, A.W., Smail, I., Ivison, R.J. & Kneib, J.-P., 1999b, MNRAS, 302, 632

Blain, A.W., 2001, in *Deep Fields* , eds. S. Christiani, A. Renzini & R.E. Williams, Springer (Berlin), p.129

Borys, C., Chapman, S., Halpern, M. & Scott, D., 2003, MNRAS, 344, 385

Carlberg, R.G., Yee, H.K.C., Ellingson, E., et al., 1996, ApJ, 462, 32

Chapman, S.C., Scott, D., Borys C. & Fahlman, G.G., 2002, MNRAS, 330, 92

Chapman, S.C., Blain, A.W., Ivison, R.J. & Smail, I.R., 2003, Nature, 422, 695

Cohen, J.G. & Kneib, J.-P., 2002, ApJ, 573, 5241

Cole, S., Aragon-Salamanca, A., Frenk, C.S., Navarro, J.F. & Zepf, S.E., 1994, MNRAS, 271, 781

Conselice, C.J., Bershady, M.A., Dickinson, M. & Papovich, C., 2003, AJ, 126, 1183

Cowie, L.L., Songaila, A. & Barger, A.M., 1999, ApJ, 118, 603

Cowie, L.L., Barger, A.J. & Kneib, J.-P., 2002, AJ, 123, 2197

Crawford, D.F., Jauncey, D.L. & Murdoch H.S., 1970, ApJ, 162, 405

Condon, J.J., 1974, 188, 279

Dannerbauer, H., Lehnert, M.D., Lutz, D., et al., 2002, ApJ, 573, 473

Dannerbauer, H., Lehnert, M.D., Lutz, D., et al., 2004, ApJ, 606, 664

Eales, S., Lilly, S., Webb, T., et al., 2000, AJ, 120, 2244

Edge, A.C., Ivison, R.J., Smail, I., Blain, A.W. & Kneib, J.-P., 1999, MNRAS, 306, 599

Eggen, O.J., Lynden-Bell, D. & Sandage, A.R., 1962, ApJ, 136, 748

Elbaz, D., Cesarsky, C.J., Chanial P., et al., 2002, A&A 384, 848

Ellis, R., Santos, M.R., Kneib, J.-P. & Kuijken, K., 2001, ApJL, 560, 119

Fixsen, D.J., Dwek, E., Mather, J.C., Bennett, C.L. & Shafer, R.A., 1998, ApJ, 508, 123

Franx, M., Illingworth, G.D., Kelson, D.D., van Dokkum, P.G., Tran, K.V., 1997, ApJ, 486, L75

Franx, M., Moorwood, A., Rix, H.-W., et al., 2000, Msngr, 99, 20

Gehrels, N., 1986, ApJ, 303, 336

Genzel, R., Baker, A.J., Tacconi, L.J., et al., 2003, ApJ, 584, 633

Govoni, F., Feretti, L., Giovannini, G., et al., 2001, A&A, 376, 803

Haarsma, D.B., Partridge, R.B., Windhorst, R.A. & Richards, E.A., 2000, ApJ, 544, 641

Hogg, D.W., 2001, AJ, 121, 1207

Holland, W.S., Robson, E.I., Gear, W.K., et al, 1999, MNRAS, 303, 659

Hu, E.M., Cowie, L.L., Capak, P., et al., 2004, ApJ, 127, 563

Hughes, D.H., Serjeant, S., Dunlop, J., et al., 1998, Nature, 394, 241

Högbom, J.A., 1974, A&AS, 15, 417–426

Jenness, T. & Lightfoot, J.F., 1998, *Astronomical Data Analysis Software and Systems VII* , A.S.P. Conference Series, Vol. 145, 1998, R. Albrecht, R.N. Hook and H.A. Bushouse, eds.,p.216

King, L.J., Clowe, D.I. & Schneider, P., 2002, A&A, 383, 118

Kneib, J.-P., Mellier, Y., Fort, B. & Mathez, G., 1993, A&A, 273, 367

Kneib, J.-P., Ellis, R.S., Smail, I., Couch W.J. & Sharples R.M., 1996, ApJ, 471, 643

Kneib, J.-P., van der Werf, P.P., Knudsen, K.K., et al., 2004, MNRAS, 349, 1211

Knudsen, K.K., van der Werf, P.P. & Jaffe W., 2001, in *Deep Millimeter Surveys: Implications for Galaxy Formation and Evolution* , eds. J.D. Lowenthal & D.H. Hughes (Singapore: World Scientific), p.168

Knudsen, K.K., van der Werf, P.P. & Jaffe W., 2003, A&A, 411, 343

Komatsu, E., Kitayama, T., Suto, Y., et al, 1999, ApJ, 516, L1

Lilly, S.C., Le Fèvre, O., Hammer, F. & Crampton, D., 1996, ApJ, 460, L1

Madau, P., Ferguson, H.C., Dickinson, M.E., et al., 1996, MNRAS, 283, 1388

McNamara, B.R., Jannuzi. B.T., Sarazin, C.L., Elston, R. & Wise, M., 1999, ApJ, 518, 167

Metcalfe, L., Kneib, J.-P., McBreen, B., et al., 2003, A&A, 407, 791

Meurer, G.R., Heckman, T.M., Lehnert, M.D., Leitherer, C. & Lowenthal, J., 1997, AJ, 114, 54

Meurer, G.R., Heckman, T.M. & Calzetti, D., 1999, ApJ, 521, 64

Moriondo, G., Cimatti, A. & Daddi, E., 2000, A&A, 364, 26

Norman, C., Ptak, A., Hornschemeier, A., et al., 2004, ApJ, 607, 721

Patton, D.R., Pritchet, C.J., Carlberg, R.G., et al., 2002, ApJ, 565, 208

Peletier, R.F., Davies, R.L., Illingworth, G.D., Davis, L.E. & Cawson, M., 1990, AJ, 100, 1091

Pelló, R., Le Borgne, J.F., Sanahuja, B., Mathez, G. & Fort, B., 1992, A&A, 266, 6

Proust, D., Cuevas, H., Capelato, H.V., et al., 2000, A&A, 355, 443

Puget, J.-L., Abergel, A., Bernard, J.-P., et al., 1996, A&A, 308, L5

Rowan-Robinson, M., Mann, R.G., Oliver, S.J., et al., 1997, MNRAS, 289, 490

Sanders, D.B. & Mirabel, I.F., 1996, ARA&A, 34, 749

Santos, M.R., Ellis, R.S., Kneib, J.-P., Richard, J. & Kuijken, K., 2004, ApJ, 606, 683

Serjeant, S., Dunlop, J.S., Mann, R.G., et al., 2003, MNRAS, 344, 887

Scott, S.E., Fox, M.J., Dunlop, J.S., et al., 2002, MNRAS, 331, 817

Smail, I., Ivison, R.J. & Blain, A.W., 1997, ApJ, 490, L5

Smail, I., Ivison, R.J., Blain, A.W. & Kneib, J.–P., 2002, MNRAS, 331, 495

Smith, E.P., Heckman, T.M. & Illingworth, G.D., 1990, ApJ, 356, 399

Smith, G.P., Kneib, J.-P., Smail, I., et al., 2004, astro-ph/0403588

Soifer, B.T., Neugebauer, G. & Houck, J.R., 1987, ARA&A, 25, 187

Steidel, C.C., Adelberger, K.L., Giavalisco, M., Dickinson, M. & Pettini, M., 1999, ApJ, 519, 1

Tran, K.-V.H., Kelson D.D., van Dokkum, P., et al., 1999, ApJ, 522, 39

van der Werf, P.P., Knudsen, K.K., Labbé, I., Franx, M., 2001, in "Deep millimeter surveys: implications for galaxy formation and evolution", eds. J.D. Lowenthal & D.H. Hughes., p.103

van Dokkum, P., Franx, M., Förster Schreiber, N., et al., ApJ, in press, (astro-ph/0404471)

Webb, T.M., Eales, S.A., Lilly, S.J., et al., 2003, ApJ, 587, 41

White, D.A., Fabian, A.C., Johnstone, R.M., Mushotzky, R.F. & Arnaud, K.A., 1991, MNRAS, 252, 72

White, D.A., Jones, C. & Forman, W., 1997, MNRAS, 292, 419

Wu, X.-P. & Xue, Y.-J., 2000, ApJ, 542, 578

Zabludoff, A.I., Huchra, J.P. & Geller, M.J., 1990, ApJS, 74, 1

References

Chapter 4

The evolution of the integrated star formation rate of dusty galaxies from deep submillimetre number counts

K.K. Knudsen, A.W. Blain & P.P. van der Werf

Abstract

In this Chapter we present the results of a first analysis of fitting models of galaxy evolution to the $850\,\mu$m number counts from the Leiden-SCUBA Lens Survey. The model used in the first analysis uses the $60\,\mu$m IRAS luminosity function and assumes that it undergoes luminosity evolution. The luminosity evolution is described by a function $g(z) = (1+z)^{(3/2)}\mathrm{sech}(b\ln(1+z)-c)\cosh c$, where the best-fit values for the parameters are determined here as $b = 2.04\pm0.1$ and $c = 1.7\pm0.08$. The additional quality of the submm data here allows the typical temperature describing the spectral energy distribution to be treated as a free parameter, with the best fit value of $T = 37\pm2.5$ K. While the result is not differing significantly from previous fits, the new deep $850\,\mu$m in combination with similar information at other wavelengths allows for a better constraint on the parameters. Based on the model, we calculate the predicted star formation rate density. It is a factor 2-10 higher than the results from optical and ultraviolet surveys. The peak of the predicted activity is at redshift ≈ 2, and the decline for redshift $z > 3$ can be approximated by $\propto (1+z)^\gamma$ with $\gamma \sim -3.5\pm0.5$.

4.1 Introduction

The $850\,\mu$m number counts can be used as constraints on evolutionary models for the submillimetre galaxies (SMGs). Here we present a first analysis of the number counts from the Leiden-SCUBA Lens Survey. These number counts probe for the first time both the faint and the bright end in the same survey. We fit a simple model to the the afore-mentioned number counts and number counts from other far-infrared (FIR) wavelengths and radio emission. The model assumes that the $60\,\mu$m *IRAS* luminosity function (Saunders et al., 1990) undergoes luminosity evolution. While this is not a physical model, it does mimic aspects of models based on e.g. hierarchical galaxy formation (e.g., Smail et al., 2002; Blain et al., 2002).

In Section 4.2 we summarise the deep 850 μm number counts from the Leiden-SCUBA Lens Survey. Fitting the counts with the model of luminosity evolution of the luminosity function is present in Section 4.3. Finally, we briefly discuss the results in Section 4.4 and summarize in Section 4.5.

Throughout the paper we assume $\Omega_m = 0.3$, $\Omega_\Lambda = 0.7$ and $H_0 = 70$ km/s/Mpc.

4.2 Deep 850 μm number counts

In the Leiden-SCUBA Lens Survey, twelve massive galaxy clusters were observed, taking advantage of the strong gravitational lensing of the background sources (Knudsen et al., *Chapter 3*). Through such observations it is possible to observe sources with fluxes fainter than the blank field confusion limit, ~ 2 mJy at 850 μm with the 15 m James Clerk Maxwell Telescope. Additionally the blank field NTT Deep Field was observed. The total area covered is 71 arcmin^2 in the image plane. For the cluster fields, assuming a redshift $z = 2.5$, the area in the source plane is 35 arcmin^2. In total 58 sources were detected. Of these, 4 were associated with central cD galaxies in the clusters and excluded from the analysis. The gravitational lensing magnification was calculated using the LENSTOOL software (Kneib et al., 1993). The sources have lensing-corrected fluxes between 0.1 and 19 mJy. It is first time that number counts have been reliably probed in this flux range in a single survey. This has not previously been possible, as blank field observations cannot probe the counts below < 2 mJy (e.g., Webb et al., 2003a; Scott et al., 2002; Borys et al., 2003), and previous lens surveys have covered a smaller area and could therefore not probe the bright end reliably (Smail et al., 2002; Cowie et al., 2002).

The number counts can be described by a double power-law. A simple χ^2 analysis performed in Knudsen et al. (see Chapter 3), suggests a change of slope in the cumulative 850 μm counts at ~ 6 mJy. The source density at >1 mJy is $\sim 10^4$ deg^{-2} and at > 0.5 mJy $\sim 2 \times 10^4$ $^{-2}$. Based on these counts, the contribution to the integrated submm extragalactic background light (EBL; Fixsen et al., 1998; Puget et al., 1996) can be determined, where sources with $S_{850} > 6$ mJy contribute with 10 %, while the dominant contribution arises from sources with 0.5-2 mJy.

In the Leiden-SCUBA Lens Survey in total 15 sources with $S_{850} < 2$ mJy are detected, of which 11 have $S_{850} < 1$ mJy. This triples the number sub-mJy sources known. It should be mentioned, that of these possibly two or three are different images of a multiply-imaged galaxy in A1689. If that is the case, the number of sub-mJy sources will be smaller by that number and the change of slope in the cumulative counts will be even more pronounced. It is in any case a substantial contribution to the known sample of such sources. Therefore it is interesting to use the new information to re-visit models previously used for the SMG population (e.g., Blain et al., 1999b; Smail et al., 2002).

4.3 Fitting the counts with models of galaxy evolution

Already with the first results from SCUBA and from other infrared wavelengths surveys from *ISO* and *IRAS*, it was realised that the number counts could only be

reproduced if evolution was included in models for the observed populations (for a review see Blain et al., 2002). It was found that the evolution had to be dominated by luminosity evolution. One possible explanation of such an evolution is a change of the star formation efficiency with redshift. Pure density evolution cannot dominate the evolution included in models, as it would overproduce the EBL because of the large contribution of faint sources, when fixing the bright end of the luminosity function with observed SCUBA counts (density and luminosity evolution is illustrated in Figure 4.1).

Our counts of the distant dusty galaxies described above provide the most comprehensive results for submm-selected galaxies available so far. While fully compatible with other determinations (as summarized by Greve et al. 2004), the results have been obtained from a uniform survey covering two decades of flux and thus do not need to be supplemented with the count results from other surveys. They are also the deepest counts available, comparable to the results from a smaller survey by Cowie et al. (2002). The counts at the bright end are consistent with the counts from blank field surveys (Webb et al., 2003a; Scott et al., 2002). At brighter flux densities limits to the density of sources on the sky (Barnard et al., 2004) provide confirmation of a steep rise in the counts at flux densities fainter than about 500 mJy, and demonstrate consistency with the results.

There is only partial redshift information available for the galaxies. It is reasonable to expect that their redshift distribution follows the form determined by Chapman et al. (2003 and *in prep.*) from optical spectroscopy, but it is not yet certain. We do not include redshift information in our comparison with models, but note that the models are consistent with this redshift distribution.

In order to demonstrate the power of the counts derived here for constraining the past history of galaxy evolution, we update a previous approach, using the model described by Blain et al. (1999a, 2002). The model assumes that the low-redshift 60 μm *IRAS* luminosity function luminosity undergoes luminosity evolution and is fitted to the various count results at submm and *ISO* wavelengths. It is a well constrained model without unnecessary features and details. Note that the additional quality of the submm data presented here allows the typical temperature that describes the SED of the galaxies to be treated as a free parameter rather than being fixed by *IRAS* and 175 μm *ISO* results as in Blain et al. (1999a). New results from *Spitzer* are relevant for this model, but affect the form of the SED at shorter wavelengths without changing the fitted parameters.

4.3.1 Luminosity function model

The 60 μm *IRAS* luminosity function, i.e., the total number sources within a given logarithmic luminosity interval is:

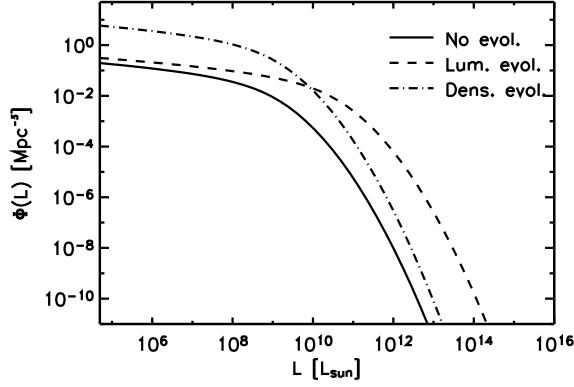$$\Phi(L) = \int_{L_{min}}^{L_{max}} \phi(L) \mathrm{d} \log L \, , \tag{4.1}$$

Figure 4.1: *The 60 μm IRAS luminosity function (LF) as published by Saunders et al. (1990). For illustration of how luminosity evolution and density evolution affects the LF, we have also plotted LF with luminosity evolution (dashed line) and density evolution (dashed-dot line). Including luminosity evolution, the relative number of luminous sources increases, while including density evolution the relative number of low-luminosity sources increases.*

where $\phi(L)$ is the density function in units of $\mathrm{Mpc}^{-3}\,\mathrm{dex}^{-1}$ and can be described by a the function:

$$\phi(L) = C\left(\frac{L}{L_\star}\right)^{1-\alpha} \exp\left(\frac{-1}{2\sigma^2}\log^2\left(1 - \frac{L}{L_\star}\right)\right). \tag{4.2}$$

$L_\star$ is the turn-over point of the function. Based on an extensive analysis Saunders et al. (1990) present the following values for all the parameters

$$
\begin{aligned}
C &= (2.6 \pm 0.8) \times 10^{-2}h^3\mathrm{Mpc}^{-3} \\
\alpha &= 1.09 \pm 0.12 \\
\sigma &= 0.724 \pm 0.031 \\
L_\star &= 10^{8.47\pm0.23}h^{-2}\mathrm{L}_\odot
\end{aligned}
$$

for a cosmology with $H_0 = 66\,\mathrm{km/s/Mpc}$, $\Omega_m = 1$ and $\Omega_\Lambda = 0$. The luminosity function is shown in Figure 4.1 together with an indication of the effects of luminosity evolution and density evolution. This functional form was found by Saunders et al. (1990) to provide a better fit than the conventional Schechter function. The principal difference is a shallower slope at the bright end.

The functional form of the 60 μm *IRAS* luminosity function (Saunders et al., 1990) is assumed to undergo luminosity evolution, which must dominate over density evolution (Blain et al., 1999a). The form of evolution $\Phi'(L, z) = \Phi[L/g(z), 0]$ is assumed to be

$$g(z) = (1 + z)^{3/2}\mathrm{sech}^2[b\ln(1 + z) - c]\cosh^2 c. \tag{4.3}$$

This form is the analytical solution in a model describing the evolution of the star formation efficiency in merging galaxies, which takes into account the merger
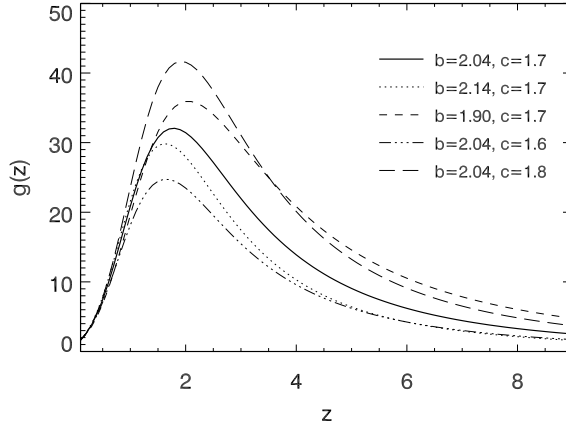
Figure 4.2: *The evolution function, $g(z)$, as given in equation 4.3. Here plotted for five different sets of (b, c). The solid line is $b = 2.04$ and $c = 1.7$, which are the best-fit parameters found in the analysis presented in this paper.*

rate of dark matter haloes and assumptions about the effects of the evolution of both the density of gas and the metallicity (Jameson 1999; Smail et al., 2002). For illustration purposes, the function is plotted in Figure 4.2. The parameters b and c can be varied to describe a wide range of different forms of evolution of the luminosity density of the Universe. The most important other parameter in the model is the dust temperature that defines the (single) spectral energy distribution (SED) of the galaxies.

We assume that the FIR SED of the sources is well-described by a modified blackbody, where the emissivity function of dust $\epsilon_\nu \propto \nu^\beta$ has a value of $\beta = 1.5$, affecting the Rayleigh-Jeans tail, and Wien tail is substituted with a power law SED $f_\nu \propto \nu^{-\alpha}$ (for details on this, see e.g., Blain et al. (2003, 1999b)). If the value of β is different, or there is a more complex mix of different temperatures of cool dust grains present in the galaxies, then the derived value of the temperature of the modified blackbody SED, T, will require modification to better represent the physical temperature of the dust present. Note, however, that the dust temperatures (and masses) derived from sparse photometry of faint galaxies should never be overinterpreted as a physical property of the dust in the interstellar medium. The temperature can be either kept as a fixed parametre in the model or it can fitted, as it the case here. The best-fit value of T should be thought of as a fitting parameter used to characterise the SED.

Based on a range of available data the values of the parameters T, b and c that are compatible with the data are determined. We use the following observational data: counts at $850\,\mu$m from the Leiden-SCUBA Lens Survey, limits to the brighter $850\,\mu$m count from Barnard et al. (2004), the count at $1200\,\mu$m from Greve et al. (2004), the $450\,\mu$m count from SCUBA surveys (Smail et al., 2002), the $175\,\mu$m count of *ISO* galaxies (Juvela et al., 2000), and the faintest counts in the 8.4-GHz radio band (Fomalont et al., 2002).
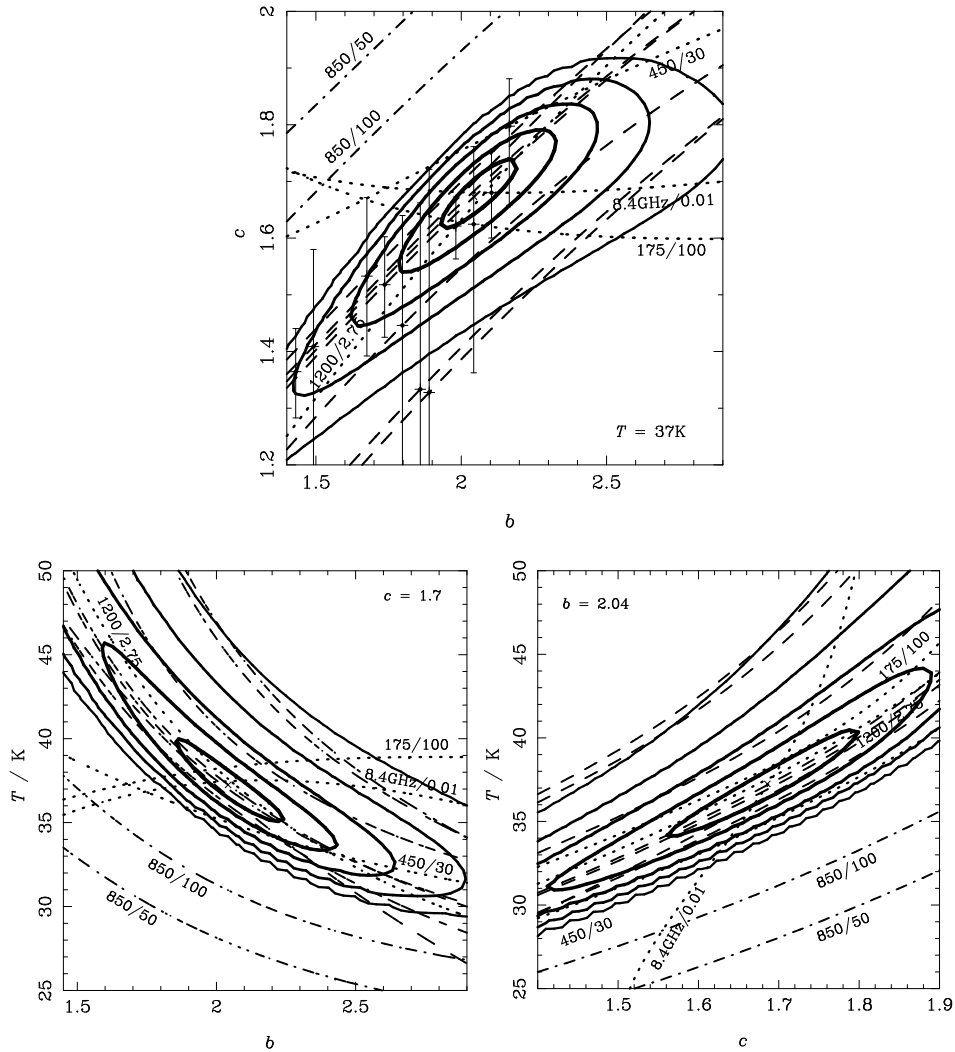
Figure 4.3: *The probability as a function of pairs of fitted parameters, at the most probable value of the other. The thick solid contours show $N\sigma$ contours away from the best fit values combining all the data. The extent of the probability contours for each marked wavelength/flux density pair are represented approximately by the size of the error bar shown on each line. The dashed lines show the results coming from the counts presented here, representing $S_{850} = 0.1, 0.25, 0.5, 1.0, 2.5, 5$ and 10 mJy. In the b vs. c plot (going up on the left-hand vertical axis): 0.25, 0.5, 10, 2.5, 5, 0.1 and 1 mJy; in the T vs. c plot (going up on the right-and vertical axis): 1, 0.1, 5, 2.5, 10, 0.5 and 0.25 mJy; in the T vs. b plot (going up on the left-hand vertical axis): same. The dot–dashed lines represent 2-σ upper limits from Barnard et al. (2004) at 50 μm and 100 μm. The permitted region of parameter space given these constraints is compatible with the maximum probability. The dotted lines represent results obtained at other wavelengths, indicated by wavelength/depth in mJy.*
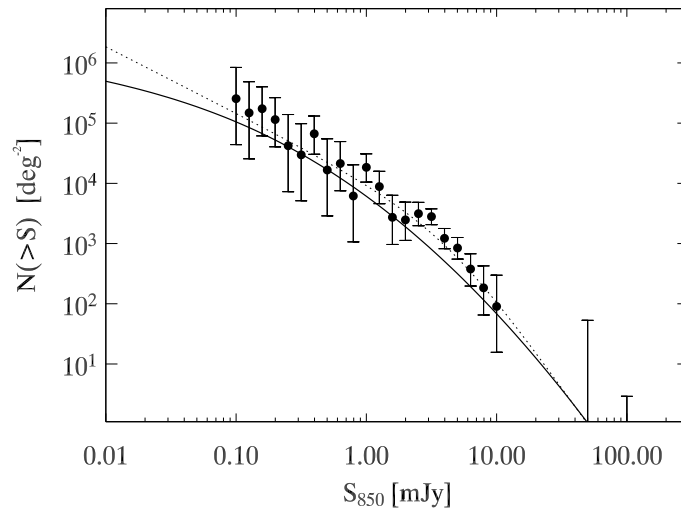
Figure 4.4: *The 850 μm number counts with the predicted counts from the model using the best-fit values — shown by the solid line. The dotted line shows the result of the chi^2 fitting analysis from Knudsen et al. (Chapter 3). Additionally, the two upper limits at 50 mJy and 100 mJy from Barnard et al. (2004) are also indicated.*

The likelihood plots in Figure 4.3 show the probability of fitting the data with the three-parameter model, slicing through the most probable value of the third parameter as listed on the frame. The results of the fits give $b = 2.04\pm0.1$, $c = 1.7\pm0.08$ and $T = 37\pm2.5$ K. The 850 μm number counts as predicted from this model using the best-fit values are shown in Figure 4.4.

Note that the accuracy of the constraints obtained are due predominantly to the 850 μm counts and the radio count. The additional constraints on the fit by including counts data from the other submm, mm and FIR data points (i.e., not the 850 μm points) is relatively weak, as they constrain the fitting parameters parallel with the 850 μm counts. This means that using other high quality data sampled at other parts of the FIR SED, does not give much extra information than can already be derived from very accurate counts at a An accurate redshift distribution of the detected sources remains essential to confirm the results absolutely.

In previous work, the lack of such detailed count data meant that the shape of the submm/far-IR background radiation spectrum was also used to constrain the parameters. Now this is unnecessary: the addition of background data provides no effective additional constraint – the region of permitted parameter space from the background is extremely large as compared with the contours in the likelihood plots shown in Figure 4.3.

4.4 Discussion

The best fitting parameters and their errors provide an ensemble of tracks for the evolution of the luminosity density of dusty galaxies as a function of redshift. We

convert the luminosity density into a star formation rate (SFR) density, using the conversion value from Thronson & Telesco (1986), which assumes a Salpeter initial mass function (IMF) for a burst of OBA stars averaged over 2×10^6 yr:

$$SFR = 2.1 \times 10^{-10} \left(\frac{L_{FIR}}{L_\odot} \right) M_\odot / \text{yr} \ . \tag{4.1}$$

The proportionality factor between the luminosity and SFR is uncertain by a factor ≈ 3, where the main source of uncertainty is caused by the IMF, the time-scale of the burst and the fraction of ultraviolet (UV) and optical light being absorbed by dust (e.g., Scoville & Young, 1983; Thronson & Telesco, 1986; Rowan-Robinson et al., 1997). We plot the SFR density as function redshift in Figure 4.5.

There is a clear peak in the predicted level of activity at $z \approx 1.8$-2. The resulting comoving star formation rate density is a factor of 3-10 higher than the optically-derived results, which have not been corrected for dust extinction, and about factor 2 higher than the extinction corrected results at redshifts 3-4 and factor 4-10 higher than those at redshifts 5-6. For the Hα results, which have not been reddening corrected (Yan et al., 1999; Moorwood et al., 2000) the discrepancy is closer to a factor 2. The predicted level of activity for redshifts $z < 1$ is in good agreement with the ISOCAM results from Flores et al. (1999). Direct comparison with star formation rates derived from SCUBA observations is difficult as the redshift information is very limited. It is worth notesing that the shape of the curve for the star formation rate density as function of redshift, as shown in Figure 4.5, turns over instead of flattening at high redshift. For redshift $z > 3$, the curve can be approximated with the function $\propto (1 + z)^\gamma$, where $\gamma \sim -3.5 \pm 0.5$. The function $g(z)$ in Eq. 4.3 would allow for a flattening at high redshift if the right parameter set (b, c) was chosen. That, however, does not fit the currently available multi-wavelength number counts data. The decrease of the predicted level of activity at high redshift is similar to the trend seen for the high redshift, extinction corrected UV/optical data. The resulting turn-down is consistent with the slope of the background radiation and the redshift distribution of radio-identified SCUBA sources (Chapman et al., 2003), even though we have not used this information in the fitting process.

4.5 Summary

We have fitted a simple model for galaxy evolution to the deep $850\,\mu$m number counts from the Leiden-SCUBA Lens Survey and deep radio number counts and other FIR number counts. The strongest constraints on the fit were provided by the $850\,\mu$m counts and the deep radio counts. The results of this first analysis demonstrate the strength of the deep $850\,\mu$m data. Based on the results from the fit to the model, we predict the level of star formation rate density for different redshifts, where the activity peaks around redshift 1.8-2. At redshift $z > 3$, the decline of the activity can be approximated by $\propto (1 + z)^\gamma$ with $\gamma \sim -3.5 \pm 0.5$. The star formation rate density is about a factor 2-10 higher than the values measured in UV/optical surveys, but in reasonable agreement with those from IR and submillimetre surveys.
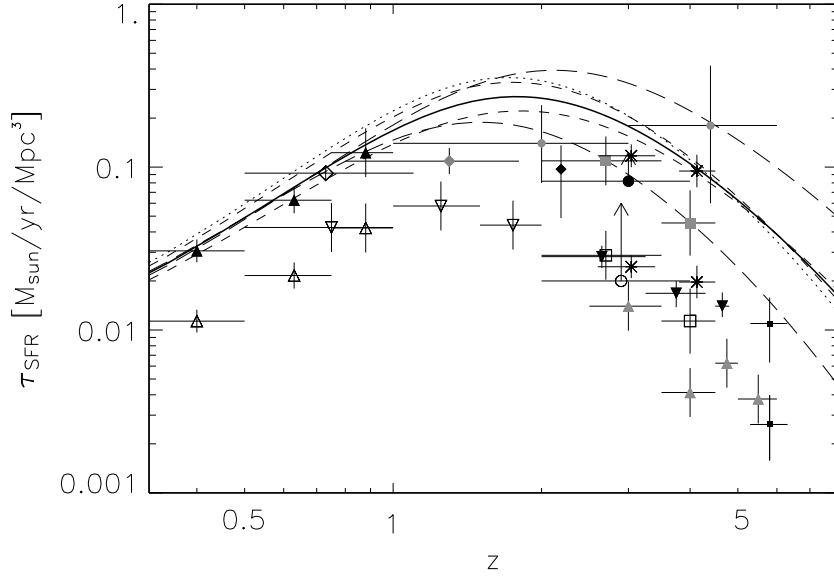
Figure 4.5: *The star formation rate density as function of redshift: The thick solid line indicates the SFR density for the best-fit parameters using the model of luminosity evolution of the 60 µm IRAS luminosity function, where b = 2.04 and c = 1.7 for Eq. 4.3. The short-dashed lines represent (b, c) = (2.14,1.8) and (1.94,1.6), while the long-dashed lines represents (b, c) = (1.94,1.8) and (2.14,1.6). The dotted line indicates the result from Smail et al. (2002), where (b, c) = (2.2,1.84). The relative vertical normalization of the curves depends on the assumed IMF and the fraction of active galactic nuclei. The data points are results from various surveys at UV/optical/IR wavelengths: empty triangles: Lilly et al. (1996); empty, inverse triangles: Connolly et al. (1997); empty squares: Madau et al. (1998); grey squares: Pettini et al. (1998) have extinction corrected the the results from Madau et al.; crosses: Steidel et al. (1999), who additionally estimated an extinction correction of a factor ∼ 5 for their results; filled, inverse triangles: Bouwens et al. (2003); grey triangles: Fontana et al. (2003), data points corrected for dust extinction; small filled squares: Stanway et al. (2004), data points corrected for dust extinction; filled triangles: Flores et al. (1999); empty diamond: Tresse et al. (2002) who have reddening corrected the result; grey diamond: Yan et al. (1999); filled diamond: Moorwood et al. (2000); open circle: Scott et al. (2002); filled circle: Hughes et al. (1998); small grey circles: Barger et al. (2000). The triangles, squares and crosses are UV/optical data, except the filled triangles, which represent ISOCAM 15 µm data (Flores et al., 1999) from the same fields as the data from Lilly et al. (1996). The diamonds represent the Hα observations. The circles represent SCUBA observations, for which redshifts have been assumed. The Scott et al. (2002) result is from the UK 8 mJy survey, where a redshift bin 2-4 has been assumed. The data point is indicated as a lower limit, as the survey only probes the bright sources, while the dominant fraction of SCUBA sources are 5-10 times fainter than that. The data points from Barger et al. (2000) are based on radio-submm photometric redshift for sources with $S_{850} > 6$ mJy, but have been completeness corrected by a factor ∼ 11 to account for the faint sources. The data points from Hughes et al. (1998) are the first results from the SCUBA map of Hubble Deep Field North, also with no redshift information.*

References

References

Barger, A.J., Cowie, L.L. & Richards, E.A., 2000, AJ, 199, 2092

Barnard, V.E., Vielva, P., Pierce-Price, D.P.I., et al., 2004, MNRAS, 352, 961

Blain, A.W., Kneib, J.-P., Ivison, R.J. & Smail, I., 1999a, ApJ, 512, L87

Blain, A.W., Smail, I., Ivison, R.J. & Kneib, J.-P., 1999b, MNRAS, 302, 632

Blain, A.W., Jameson, A., Smail, I., et al., 1999c, MNRAS, 309, 715

Blain, A.W., Smail, I., Ivison, R.J., Kneib, J.-P. & Frayer, D.T., 2002, Physics Reports, 369, 111

Blain, A.W., Barnard, V.E. & Chapman, S.C., 2003, MNRAS, 338, 733

Borys, C., Chapman, S., Halpern, M. & Scott, D., 2003, MNRAS, 344, 385

Bouwens, B., Broadhurst, T. & Illingworth, G., 2003, ApJ, 593, 640

Chapman, S.C., Blain, A.W., Ivison, R.J. & Smail, I.R., 2003, Nature, 422, 695

Connolly, A.J., Szalay, A.S., Dickinson, M., Subbarao, M.U. & Brunner, R.J., 1997, ApJ, L11

Cowie, L.L., Barger, A.J. & Kneib, J.-P., 2002, AJ, 123, 2197

Fixsen, D.J., Dwek, E., Mather, J.C., Bennett, C.L. & Shafer, R.A., 1998, ApJ, 508, 123

Flores, H., Hammer, F., Thuan, T.X., et al., 1999, ApJ, 517, 148

Fomalont, E.B., Kellermann, K.I., Partridge, R.B., Windhorst, R.A. & Richards, E.A., 2002, AJ, 123, 2402

Fontana, A., Poli, F., Menci, N., et al., 2003, ApJ, 587, 544

Greve, T.R., Ivison, R.J., Bertoldi, F., et al., 2004, MNRAS, *submitted* (astro-ph/0405361)

Hughes, D.H., Serjeant, S., Dunlop, J., et al., 1998, Nature, 394, 241

Jameson, A., 1999, Ph.D. thesis, Cambridge University

Juvela, M., Mattila, K. & Lemke, D., 2000, A&A, 360, 813

Kneib, J.-P., Mellier, Y., Fort, B. & Mathez, G., 1993, A&A, 273, 367

Lilly, S.C., Le Fèvre, O., Hammer, F. & Crampton, D., 1996, ApJ, 460, L1

Madau, P., Pozzetti, L. & Dickinson, M., 1998, ApJ, 498, 106

Moorwood, A.F.M., van der Werf, P.P., Cuby, J.-G. & Oliva, E., 2000, A&A, 362, 9

Pettini, M., Kellogg, M., Steidel, C.C., et al., 1998, ApJ, 508, 539

Puget, J.-L., Abergel, A., Bernard, J.-P., et al., 1996, A&A, 308, L5

Rowan-Robinson, M., Mann, R.G., Oliver, S.J., et al., 1997, MNRAS, 289, 490

Saunders, W., Rowan-Robinson, M., Lawrence, A., et al., 1990, MNRAS, 242, 318

Scoville, N.Z. & Young, J.S., 1983, ApJ, 265, 148

Scott, S.E., Fox, M.J., Dunlop, J.S., et al., 2002, MNRAS, 331, 817

Smail, I., Ivison, R.J., Blain, A.W. & Kneib, J.–P., 2002, MNRAS, 331, 495

Stanway, E.R., Bunker, A., McMahon, R., et al., 2004, ApJ, 607, 704

Steidel, C.C., Adelberger, K.L., Giavalisco, M., Dickinson, M. & Pettini, M., 1999, ApJ, 519, 1

Thronson, H.A. & Telesco, C.M., 1986, ApJ, 311, 98

Tresse, L., Maddox, S.J., Le Fèvre, O. & Cuby, J.-G., 2002, MNRAS, 337, 369

Webb, T.M., Eales, S.A., Lilly, S.J., et al., 2003, ApJ, 587, 41

Yan, L., McCarthy, P.J., Freudling, W., et al., 1999, ApJ, 519, L47

Chapter 5

Host galaxies of faint submillimetre sources: the Leiden-SCUBA Lens Survey

K.K. Knudsen, P.P. van der Werf et al.

Abstract

We present optical and near infrared identifications of the underlying host galaxies of faint submillimetre (submm) sources in the Leiden-SCUBA Lens Survey. For 48 submm sources, 30 % are identified with a high degree of certainy, while 35 % have one or more possible candidate counterparts and 35 % have no obvious counterpart. Of the secure and candidate identifications 85 % are very or extremely red. Spectroscopy is presented for two securely identified sources with z = 2.423 and z = 2.515 and for one probable identifications with z ∼ 2.6. None of these four show Lyα in emission, as opposed the majority of radio-selected bright $S_{850} > 5$ mJy submm sources.

We discuss in depth the identification of a multiply-imaged 0.8 mJy source, which is located in a small group of galaxies. Understanding $S_{850} \sim 1$ mJy population is of great importance as these are the sources giving rise to the dominant fraction of the integrated submm extragalactic background light (EBL).

We perform a statistical analysis of the submm emission from the extremely red galaxies (EROs; I − K > 4) and distant red galaxies (DRGs; J − K > 2.3) using the very deep data from the field MS1054−03. We find a error-weighted average S_{850} flux of 0.83±0.17 mJy for the EROs and 1.1±0.21 mJy for the DRGs, and that their contribution to the submm EBL is 27-39 % and 22-31 % respectively. The results of the identifications of the individual SCUBA sources and the statistical detection of the EROs and DRGs, are strong signs of an important link between the SCUBA sources and high redshift red galaxies.

5.1 Introduction

With the advent of the first bolometer mapping instrument at submillimetre (submm) wavelengths SCUBA (Submillimetre Common-User Bolometer Array, mounted at the James Clerk Maxwell Telescope (JCMT); Holland et al., 1999) a

---

Also includes results from J.-P. Kneib et al., 2004, MNRAS, 349, 1211 and P. van Dokkum et al., 2004, ApJ, 611, 703

new population of galaxies was detected (Hughes et al., 1998). The submm galaxies (SMGs) have far-infrared (FIR) luminosities of $L_{FIR} > 10^{12} L_{\odot}$, which classifies them as Ultra Luminous Infrared Galaxies (ULIRGs). While ULIRGs locally are rare objects, their comoving number density at high redshift as detected with SCUBA, is more than ten times larger. SMGs with submm fluxes $S_{850} > 0.5$ mJy are the dominant contributors to the integrated submm extragalactic background light (e.g., Blain 1999; Knudsen et al., *Chapter 3*), and are thus believed to play an important role in the formation of galaxies, in particular the massive galaxies.

The nature of the SMGs has become an important subject of study since their discovery. Among the quantities of interest is the redshift, line diagnostics to distinguish between star formation and accretion activity, and the spectral energy distribution (SED). Based on such knowledge it is possible to study the SMG population as a whole and determine the cosmic star formation history of this population of galaxies.

To determine the nature of the SMGs, the underlying galaxy giving rise to the submm emission must be identified. This is, however, complicated by the several factors: the negative k-correction, the large beam of the JCMT at $850\,\mu$m is $15''$, and dust obscuration of the ultraviolet (UV) and optical light from the underlying galaxy. The negative k-correction at $850\,\mu$m is of great advantage for submm observations, as it allows for observations to very high redshift $z \sim 8$. It is, however, unique to the submm regime, and thus observations at other wavelengths with the current instrumentation do not probe the same volume as the submm observations. Thus, if very distant sources exist and are detected with SCUBA, they might be missed in the follow-up observations. The large beam of the JCMT, implies that several objects can be present near the position and a detailed analysis must be done to select the underlying galaxy. Finally, as the submm emission observed is thermal emission from dust, which has been heated by star formation activity, the stellar population the SMG will be obscured by dust and thus may be difficult to detect.

Observations at many wavelengths are needed to elucidate the nature of the galaxies. Radio observations will allow for a better determination of the position of the source, and also allow for an estimate of the redshift (e.g., Blain 1999; Carilli & Yun, 1999). The higher redshift sources, however, will not be detected in the radio because of the large positive k-correction. X-ray observations have been used for assessing the contribution of active galactic nuclei to heating the dust (e.g., Alexander et al., 2003). If the underlying galaxy has been identified, spectroscopy can be done. Optical and near infrared (NIR) observations allow for the detailed spectral analysis from which accurate redshifts can be determined. The importance of NIR and radio observations was realised after mis-identification when using only optical observations. In an early study by Smail et al. (1998), identifications were obtained from deep HST imaging, which was followed up with spectroscopic observations by Barger et al. (1999a). However, follow-up studies with radio observations and NIR imaging led to improved identifications (Smail et al., 2000; Frayer et al., 2000). Identifications from several surveys (Webb et al., 2003b; Smail et al., 2002; Chapman et al., 2003; Fox et al., 2002) have found that a signification fraction of the SMGs are identified with extremely red objects, i.e.,

galaxies with photometric colour $I - K > 4$. In a yet unpublished study Chapman and collaborators have made use of the Keck Telescope and obtained spectra for ~ 80 SMGs, which have radio counterparts. While such a study is major progress for understanding the SMGs, selecting SMGs with radio counterparts limits the sample to the galaxies at $z < 3$ and to the brighter SMG population (i.e. $S_{850} > 5$ mJy). However, SMGs with submm fluxes between 0.5 and 2 mJy, provide the dominant contribution to the integrated submm extragalactic background light (EBL), and thus such sources should be studied.

We have undertaken the Leiden-SCUBA Lens Survey in which twelve massive galaxy clusters have been observed. The blank field confusion limit of the JCMT at 850 μm is ~ 2 mJy. Thus to study the dominant population gravitational lensing must be used to probe fainter than 2 mJy. This is done by observing fields of strongly lensing clusters. In addition to the cluster fields, we have obtained deep data for the NTT Deep Field. The SCUBA observations, analysis and the resulting catalogue has been presented in a previous paper (Knudsen et al., *Chapters 2+3*). The catalogue includes in total 58 sources. These sources have, after correcting for the gravitational lensing, 850 μm fluxes between 0.1 and 19 mJy. The aim of the present paper is to present the multiwavelength observations for these sources with an emphasis on NIR and optical imaging. Additionally, we present optical and NIR spectroscopy for six candidate counterparts. One of the securely identified sources in A2218 is a multiply-imaged ~ 1 mJy galaxy. The identification is discussed in detail. The question of the connection between SMGs and other high redshift galaxy populations is addressed in a statistical analysis of the submm emission from very red galaxies. We do this for the field MS1054$-$03, which has the deepest NIR data currently available for a cluster field.

In Section 5.2 the NIR and optical imaging is presented. The identifications are presented in Section 5.3, which includes a discussion of the individual objects. In Section 5.4 spectroscopic observations are presented. Section 5.5 is an in depth analysis and discussion of a unique identification of a ~ 1 mJy multiply imaged source. In Section 5.6, a statistical analysis of the submm emission from extremely red galaxies is presented. A general discussion on the identified counterparts is done in Section 5.7, and conclusions are given in Section 5.8.

Throughout the paper we assume $\Omega_m = 0.3$, $\Omega_\Lambda = 0.7$ and $H_0 = 70$ km/s/Mpc.

5.2 Imaging

NIR and optical imaging has been used to identify candidate counterparts for the SCUBA sources. Some of the imaging, especially the NIR imaging, were obtained through programmes designed for this project. The rest has been obtained from archives, collaborators and the literature. In this section, we present the imaging data.

5.2.1 Near-infrared imaging

We have obtained deep Ks band imaging with ISAAC at the ESO VLT for the fields Cl0016+16, A496, A520, RX J1347.5-1145, A1689 and A2204 through our VLT programmes 67.A-0095 and 68.A-0097. The observations, which were obtained in

service mode, were done with the following set-up: The Detector Integration Time (DIT) was 10 seconds, the number of DITs (NDIT) was six per exposure. Each Observing Block (OB) consisted of 25 or 30 exposures. The pixel scale is $0.148''$ per pixel. The images were dithered, i.e. each of the exposures were off-set by a few arcseconds in different directions. For each cluster field eight OBs were obtained, which corresponds to 3.6 hours of raw integration time per field. The data were reduced using the reduction software ECLIPSE[1]. The exposures were reduced in groups of the OB. The following steps were taking in the reduction: bias subtraction, flat fielding, flagging bad pixels and sky subtraction. Some of the exposures suffer from the so-called odd-even effect, which is a difference in the flux level between odd and even columns on the detector. The affected data were corrected for this effect. The exposures were registered using a cross-correlation and stacked. Finally, the stacked images from the individual OBs were cross-correlated and stacked. In the case of A1689 and Cl0016+16, the seeing of one combined OB image was much larger than for the other OB images. The OB images with very large seeing were not included in the final combined images as they did not improve the depth of the final image. Consequently the total integration time for A1689 and Cl0016+16 is 3.15 hours. The final images are $\sim 2.8' \times 2.8'$, which is sufficiently large to cover single SCUBA pointings. The data were photometrically calibrated using the standard stars obtained during the observations. The calibration was checked with the 2MASS Point Source Catalogue[2]. The seeing was determined from the point sources in the fields and was found to be 0.5-0.7$''$ (Table 5.1).

The field MS1054$-$03 is one of the two fields observed for the Faint InfraRed Extragalactic Survey (FIRES; Franx et al., 2000) for which some of the deepest ever NIR images have been obtained. MS1054$-$03 has been covered in four pointings with ISAAC with approximately 32 hours in total for each of the filters J, H and Ks. The data and the analysis are presented in a paper by Förster Schreiber et al. (*in prep*).

An H-band image of A478 was obtained with the UKIRT Imaging SpecTrometer (UIST) (Ian Smail, private communication). The image was calibrated using the 2MASS Point Source Catalogue.

The field A2218 been used as a case study for the Mexican Hat wavelets algorithm as a source extraction tool (Knudsen et al., *Chapter 2*). In that paper, multiwavelength observations were also presented, which included NIR J and K band imaging from the Isaac Newton Group Red Imaging Device (INGRID, mounted at the William Herschel Telescope, La Palma) and the Near InfraRed Imager and spectrograph (NIRI, mounted at Gemini-North, Hawaii). The INGRID images are presented in Packham et al. (2003) . NIRI images are based on a preliminary reduction (J. Peacock, private communication). The photometric calibration of the NIRI images was done using the calibrated INGRID images and compared to the 2MASS Point Source Catalogue. The NIRI K image is deeper than the INGRID K band image, while the INGRID J band image is deeper than the NIRI J band image. The INGRID images cover a larger area than the NIRI data.

The NTT Deep Field (Arnouts et al., 1999) has been observed with SOFI (Moor-

---

[1]http://www.eso.org/eclipse
[2]http://vizier.u-strasbg.fr/viz-bin/VizieR?-source=II/246

Table 5.1: *Summary of the near IR imaging.*

Field	Instrument	Filter	$\mathrm{mag}_{\mathrm{lim}}$	FWHM
Cl0016+16	ISAAC	Ks	21.0	0.6″
A478	UIST	H	19.7	0.69″
A496	ISAAC	Ks	20.5	0.7″
A520	ISAAC	Ks	21.0	0.7″
MS1054−03	ISAAC	Js	25.3	0.48″
	ISAAC	H	24.4	0.46″
	ISAAC	Ks	23.8	0.52″
A1689	ISAAC	Ks	21.0	0.5″
RX J1347−1145	ISAAC	Js	21.3	0.56″
	ISAAC	H	20.8	0.6″
	ISAAC	Ks	21.0	0.52″
A2204	ISAAC	Ks	21.0	0.6″
A2218	NIRI	J	20.5	0.95″
	NIRI	K	20.0	0.8″
	INGRID	J	20.9	0.75″
	INGRID	K	19.3	0.75″
NTT Deep Field	SOFI	J	22.9	0.75″
	SOFI	Ks	21.2	0.75″

wood et al., 1998) at the ESO New Technology Telescope. The field was observed both in J and Ks. The total area surveyed is $\sim 20\,\mathrm{arcmin}^2$, and the total observing time was 4.3 hours in J and 10.4 hours in Ks.

In Table 5.1 we list the limiting magnitude and the seeing for each of the fields. The limiting magnitude is calculated as 5σ from the background within in an aperture of diameter 2 FWHM (Full Width at Half Maximum).

For the fields MS1358+62 and A2597 we have no NIR imaging.

5.2.2 Optical imaging

A summary of the optical data with limiting magnitudes and seeing is given in Table 5.2. Limiting magnitudes have been calculated as 5σ from the background within an aperture of diameter 2 FWHM.

As a part of VLT programme 63.O-0087, FORS1 I-band images were obtained for A478 (4×15 minutes) and A496 (3×15 min). The data were reduced using standard reduction procedures for optical CCD imaging: the individual frames were bias-subtracted using a two-dimensional master-bias off-set to the over-scan region, and subsequently flat fielded using a master flatfield, which was constructed from twilight sky flats. The frames were stacked and the astrometry of the final images was calculated using the US Naval Observatory USNO-A Catalogue. The photometry was calibrated using the standard star field PG0231+051 (Landolt, 1992).

Table 5.2: *Summary of the optical imaging.*

Field	Instrument	Filter	mag$_{lim}$	FWHM
Cl0016+16	WFPC2	F555W	25.7	0.2″
	WFPC2	F814W	25.1	0.2″
A478	FORS1	I	23.0	0.94″
A496	FORS1	I	22.9	0.9″
MS1054−03	FORS1	U	26.6	0.69″
	FORS1	B	27.9	0.57″
	FORS1	V	27.0	0.65″
	WFPC2	F606W	28.1	0.21″
	WFPC2	F814W	27.1	0.22″
A1689	WFPC2	F555W	27.2	0.2″
	WFPC2	F814W	24.5	0.2″
	EMMI	V	24.4	1.0″
	EMMI	I	22.6	1.0″
RX J1347−1145	FORS1	B	25.7	0.78″
	FORS1	V	24.7	0.72″
	FORS1	R	25.6	0.8″
	FORS1	I	24.2	0.65″
A2204	FORS1	V	23.7	0.88″
	FORS1	R	23.6	0.86″
	FORS1	I	23.0	0.8″
A2218	CFH12k	B	24.4	0.8″
	CFH12k	R	23.9	0.8″
	CFH12k	I	22.4	0.8″
	WFPC2	F702W	25.9	0.2″
	WFPC2	F814W	27.0	0.2″
NTT Deep Field	SUSI	B	27.0	0.90″
	SUSI	V	26.5	0.83″
	SUSI	r	26.0	0.83″
	SUSI	I	26.0	0.70″

Cl0016+16: WFPC2 images in the passbands F555W and F814W have been published by Smail et al. (1997a). The total exposure time is 3.5 hours in F555W and 4.7 hours in F814W.

MS1054−03: As mentioned in the previous subsection, MS1054−03 is part of the FIRES project (Franx et al., 2000; Förster Schreiber et al., *in prep.*). Deep FORS1 images are available for UBV (for details see Förster Schreiber et al., *in prep.*). Furthermore, WFPC2 images are available in F606W and F814W (for details see van Dokkum et al., 2000). The data set published for MS1054−03 is the deepest and most comprehensive data set with large wavelength coverage available for a galaxy cluster.

A1689: For this field optical images are available from many telescopes at var-

ious depths. We have limited data used here to WFPC2 images at F555W and F814W and EMMI *V* and *I* images from the NTT Telescope (Taylor et al., 1998).

RX J1347.5-1145 and A2204: These fields have been observed with FORS1 in five filters, $UBVRI$, and three filters, VRI, respectively. The reduced images have kindly been provided by Johan Richard (J. Richard, private communication).

A2218: As mentioned in the previous subsection on the NIR imaging, optical follow-up has been presented for this field in Knudsen et al. (*in prep*; see Chapter 2). *B*, *R* and *I* band images from the CFH12k camera on the Canada-France-Hawaii Telescope (Smith et al., 2002) and HST WFPC2 F702W and F814W images have been used (Kneib et al., 1996; Smail et al., 1997b; J.-P. Kneib, private communication).

The NTT Deep Field data was obtained with the SUSI camera on the NTT telescope (Arnouts et al., 1999). Data were obtained in four passbands, *B*, *V*, *r* and *I*. The total exposure time was 14, 6.5, 6.5 and 4.5 hours respectively. The images cover an area of 2.3′×2.3′. For details on the limiting magnitudes and seeing, see Table 5.2.

A520: No deep optical data exists for the area covered by the SCUBA map.

MS1358+62 and A2597: As there are no deep NIR data available for this field, we have chosen not to focus on optical data.

In Table 5.3 we have summarized the correction for the Galactic extinction for all the fields. The Galactic extinction is derived from the recent dust maps by Schlegel, Finkbeiner & Davis (1998). All the fields are out of the Galactic plane. A478 still suffers significant extinction, which is taken into account in the analysis.

Table 5.3: *Galactic extinction for the individual fields, measured by $E(B-V)$ (Schlegel et al., 1998) at the galactic coordinates (l,b).*

Field	l [°]	b [°]	$E(B-V)$ [mag]
Cl0016+16	111.6	-45.7	0.058
A478	182.4	-28.3	0.522
A496	209.6	-36.5	0.135
A520	195.8	-24.3	0.044
MS1054−03	256.5	48.7	0.035
A1689	313.2	61.1	0.025
RXJ1347.5−1145	324.0	48.8	0.062
MS1358+62	109.9	52.9	0.023
A2204	21.1	33.2	0.097
A2218	97.7	38.1	0.025
A2219	72.6	41.5	0.024
A2597	65.3	-64.9	0.030
NTT Deep Field	283.6	53.4	0.038

5.3 Identifications

Here we present the identifications of the underlying galaxies giving rise to the submm emission detected with SCUBA using NIR and optical imaging. Where available we also use data from other wavelengths, such as mid-IR (with ISO-CAM) and radio (VLA). Before a discussion of the individual sources, we first describe the source extraction and how the sources are labeled as cluster or field sources and their likelihood as a counterpart is estimated.

5.3.1 Source extraction

The source extraction from the optical and NIR imaging was performed using SExtractor (Bertin & Arnouts, 1996). The detection of the sources was done in a combined image, where both optical and NIR had been added. This increases the signal-to-noise ratio of the individual objects. Additionally, it means that the detected galaxies are on the same grid and the colours can be determined directly. The flux was measured in apertures of 2 FWHM. For MS1054−03 we use the catalogue available from the thorough analysis and careful source extraction from Förster Schreiber et al. (*in prep*). For the NTT Deep Field we use the catalogue available from Fontana et al. (2000). In the resulting tables with the individual galaxies, the galaxies from MS1054−03 and NDF are listed by their catalogue numbers as given in the published catalogues. For the fields, the galaxies are given the identification numbers that they have been assigned in our own catalogues.

5.3.2 Likelihood estimates

Estimating likelihoods: We searched counterparts within a radius of the SCUBA position. The search radius used is $8''$, which is twice the 1σ positional uncertainty of the detection position of the SCUBA sources. The search radius is comparable to the $850\,\mu m$ beam radius. In a few cases the search radius is expanded to $10''$ as potential counterparts might be found. For the galaxies found within the search radius of the SCUBA sources, we estimate a likelihood for each of them being a possible candidate counterpart. As the surface density of SCUBA sources is low compared to that of optically and NIR detected galaxies, they can be considered rare objects. Considering the vast amounts of dust present in the galaxies, which emit the detected SCUBA emission, it is not unreasonable to expect the sources to exhibit red colours. That is in fact the case for most of the identified SCUBA sources (e.g. Smail et al., 2002; Webb et al., 2003b). We use the colour information from the I and K, and J where available. Galaxies with $I - K > 4$ are also known as extremely red objects (EROs). Using $I - K > 4$ galaxies with redshifts typically $z > 1$ are selected and these galaxies are either starburst galaxies or quiescent ellipticals (e.g., Pozzetti & Mannucci, 2000; Cimatti et al., 1999). Galaxies with $J - K > 2.3$ are known as distant red galaxies (DRGs). Using $J - K > 2.3$ galaxies with redshift $z > 2$ are selected (e.g. van Dokkum et al., 2004), again either being dust reddened star forming galaxies or quiescent ellipticals, where the Balmer-break falls between the J and K. A majority of the securely identified SMGs have counterparts that have similar colours as the EROs and DRGs. We assign a likelihood

to the different galaxies within the search radius by measuring how rare it is based on its K magnitude and its $I - K$ (and where available $J - K$) colour. Including the K magnitude information is important, as faint galaxies are more numerous, there is a larger probability of chance coincidences for faint counterparts. The likelihood estimates are determined in the following way. We use the images of MS1054−03, as those images are the deepest, cover a larger area than the other images used for this project, and have undergone the most thorough analysis. For each galaxy, we determine the number of galaxies found within a search radius at 20000 random positions in the MS1054−03 field that have $(I - K) \geq (I - K)_{gal}$ and $K \leq K_{gal}$ where sub-script gal denotes the galaxy in question. The number detections divided by 20000, p, is then a direct measure for the chance of a random detection of an object of that colour and magnitude. Similarly, if deep J-band photometry is available, we repeat the calculation for $(I - K) \geq (I - K)_{gal}$, $(J - K) \geq (J - K)_{gal}$ and $K \leq K_{gal}$. When doing this for the low redshift clusters, we remove the galaxies from the red cluster sequence from the MS1054−03 data. The smaller p, the more unlikely is a chance coincidence of finding such a galaxy within the search radius of a SCUBA source. An identification with a common object (faint, normal colours) is much more likely to be a chance superposition. The results of this is listed in Tables 5.4-5.11 along with the optical and NIR photometry of the galaxies.

Labeling cluster members: Within the search radius of a SCUBA source, there will in almost all the cases be more than one source. As most of the fields we have studied are galaxy cluster fields, cluster members will also be present nearby the SCUBA sources. The galaxies, which can be clearly identified as being members of the clusters, are elliptical galaxies. In a colour-magnitude diagram, the cluster ellipticals can be identified by locating the red cluster sequence. This can be done using two filter bands, such as I and K, though including more filter bands will add in additional information and prevent the selection of field galaxies. We flag the cluster members near SCUBA source using the red cluster sequence, as such galaxies are quiescent, i.e. not undergoing intense star formation, and thus rather unlikely to be the underlying galaxy of a SCUBA source. One could argue that submm emission could be synchrotron emission from a central massive black hole in the centres of the cluster members, however, signs of this would be expected to be found at other wavelengths, e.g. in the radio or possibly in the optical spectra. Such cases have, however, not been found previously. The only cluster members known to be detected with SCUBA is a sub-sample of central cD galaxies (this work and Smail et al., 2002).

5.3.3 Discussion of the individual fields

Here follows a discussion of the individual fields. The cluster sources are discussed before the NTT Deep Field. The fields and the sources are presented in order of increasing right ascension. The results are summarized in Tables 5.4-5.11. The photometry has not been corrected for lensing. For a discussion on the lensing, see Chapter 3. Postage stamp sized optical and NIR images at the positions of the individual sources are shown in the Figures 5.1-5.11.

SMMJ00185+16263

SMMJ00185+16269

SMMJ00186+16253

SMMJ00186+16260
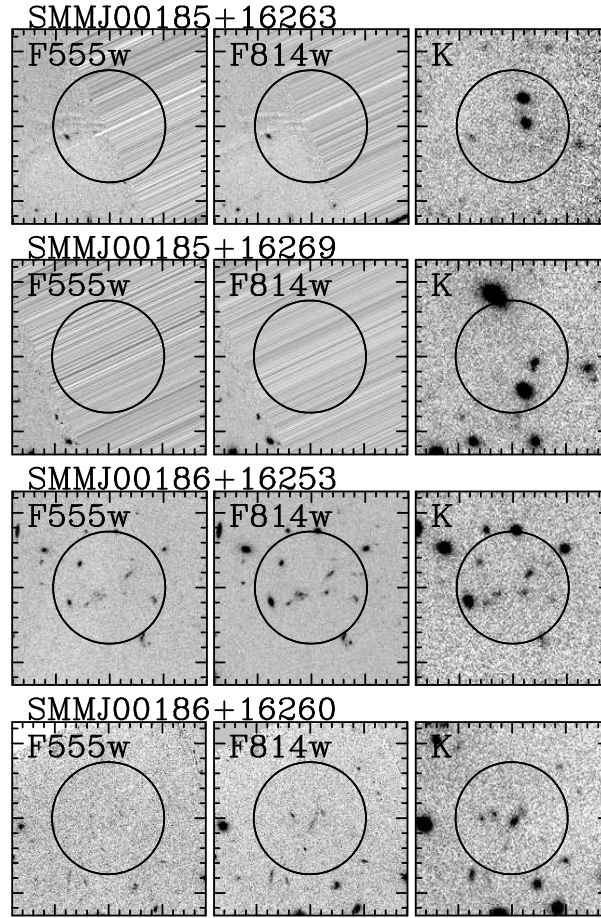
Figure 5.1: *Mosaic of the F555W, F814W and Ks postage stamp sized images around the SCUBA sources in Cl0016+16. Each sub-image is 26″×26″ and is centered on the SCUBA source. The tick marks on the horizontal axis are distanced 1.5″, while the tick marks on the vertical axes are 2″. The circle indicates the size of the 850 μm JCMT beam.*

<u>*Cl0016+16*</u> Of the four sources detected in the field Cl0016+16, two are within the WFPC2 field of view. Photometry is summarised in Table 5.4 and postage stamp sized sub-images are shown in Figure 5.1.

SMM J00185+16263: This source is not covered by the WFPC2 images. Three galaxies were detected in the K band image.

SMM J00185+16269: This source is not covered by the WFPC2 images. Three galaxies were detected in the K band image.

SMM J00186+16253: Within a search radius of $8''$ there are eight galaxies of which three fall on the red cluster sequence. Most of the galaxies only have marginal detections. There is no obvious candidate counterpart for this source.

Table 5.4: *Candidate counterparts for the SCUBA sources in the Cl0016+16. cl indicates whether the galaxy falls on the red cluster sequence (1 = cluster member). p indicates the likelihood of finding a galaxy with $I-K$ and K or redder and brighter at random positions (see Subsection 5.3.2).*

ID	dist	$d\alpha$	$d\delta$	$V-I$	$I-K$	K	σ_K	cl	p
	['']	['']	['']	[mag]	[mag]	[mag]	[mag]		
SMM J00185+16263									
276	4.19	1.82	3.78	...	...	18.50	0.14	0	...
284	1.48	1.42	0.43	...	...	19.43	0.21	0	...
291	6.20	-5.75	-2.30	...	...	21.15	0.47	0	...
SMM J00185+16269									
177	0.82	-0.17	-0.80	...	...	20.15	0.29	0	...
184	7.42	-7.26	-1.54	...	...	20.48	0.34	0	...
189	4.75	1.23	-4.59	...	...	19.14	0.18	0	...
SMM J00186+16253									
415	7.62	-0.55	7.60	2.53	2.75	19.00	0.17	1	0.151
428	5.50	4.34	3.37	1.16	1.55	21.37	0.52	0	0.505
430	2.88	-2.25	1.79	1.14	2.70	20.88	0.41	0	0.327
434	1.77	-1.65	-0.65	2.23	2.48	21.34	0.51	1	0.411
436	2.16	1.97	-0.89	1.70	1.92	21.40	0.52	0	0.493
437	6.11	5.83	-1.85	2.59	2.84	19.05	0.18	1	0.144
441	4.10	3.53	-2.09	1.68	2.68	21.49	0.55	0	0.379
457	7.79	-3.91	-6.74	1.11	2.07	21.21	0.48	0	0.465
SMM J00186+16260									
330	1.86	1.77	0.55	2.59	2.21	21.43	0.53	0	0.468
331	0.96	-0.90	-0.35	1.26	3.30	20.36	0.32	0	0.137
333	3.45	3.45	-0.02	0.39	3.89	21.68	0.60	0	0.087

Table 5.5: *Candidate counterparts for the SCUBA source in A478. p indicates the likelihood of finding a galaxy with $I-H$ and I or H or redder and brighter at random positions (see Subsection 5.3.2).*

ID	dist	$d\alpha$	$d\delta$	I	σ_I	H	σ_H	p
	['']	['']	['']	[mag]	[mag]	[mag]	[mag]	
SMM J04134+10281								
890	2.01	0.52	1.94	23.61	0.36	< 20.3	...	0.304
SMM J04134+10270								
263	6.13	5.92	-1.61	18.44	0.03	16.96	0.03	< 0.001
SMM J04135+10277								
433	1.46	1.30	-0.67	20.41	0.09	20.01	0.15	0.008
SMM J04135+10281								
21	5.04	-4.82	-1.47	< 23.6	...	19.74	0.12	0.053

SMM J00186+16260: Three galaxies were detected within radius $4''$ from the source position. Two of them have $I - K > 3$ and are plausible counterparts.

A478

Besides I and H images, there are ISOCAM and ISOPHOT observations for this field. Only the source SMM J04135+10277 is detected in the ISOCAM data. Furthermore, there are VLA observations (M. Yun, private communication), in which the only source detected is SMM J04135+10277. The I and H photometry is summarised in Table 5.5 and postage-stamp sized I and H sub-images centered on the SCUBA source positions are shown in Figure 5.2.

SMM J04134+10281: Within the beam of the this source, no galaxies have been detected. There is a hint of a signal in the I-band image $2''$ from the position of the SCUBA source.

SMM J04134+10270: Within the beam of this source, one galaxy has been detected. A spectrum of it shows that it is a quiescent elliptical galaxy at the reshift of the cluster. Elliptical galaxies are known not to harbour vast reservoirs of dust. If this elliptical was to be the underlying galaxy, the submm emission would be synchrotron emission from an AGN. There is, however, no sign of such in the radio data or in the optical spectrum.

SMM J04135+10277: SMM J04135+10277 has been securely identified with a quasar at redshift $z = 2.84$, which has been reported in Knudsen et al. (2003). The SCUBA source, which is the brightest in the Leiden-SCUBA Lens Survey, is coincident with a point source in the optical images. Follow-up spectroscopy revealed a type-1 quasar characterized by broad emission lines, power law continuum and Lyman-forest absorption blue of the Lyα line. In the low-resolution spectrum the Lyα line appears to be absorbed at some level, however the resolution is not sufficient to say anything conclusive. The FIR luminosity is $(2.9 \pm 0.5) \times 10^{13}\,\mathrm{L_\odot}$, which suggests a large star formation rate in the host galaxy. A large SFR is supported by more recent CO observations, which revealed one of the most massive CO reservoirs at high redshift (Hainline et al., 2004). The quasar has also been detected with Chandra in the 2-10 keV band with an X-ray flux of $1.7 \times 10^{-14}\,\mathrm{erg/cm^2/s}$ (R. Mushotzky, private communication).

SMM J04135+10281: Within the beam of SMM J04135+10281 there is only one candidate counterpart, which is a red galaxy not visible in the I-band image but detectable in the H-image with $H = 19.4\,\mathrm{mag}$ (after correcting for Galaxtic extinction). There are no other galaxies visible in the I and H band image around this SCUBA source.

A496

The optical and NIR imaging accessible for this field is limited to a 45 minutes I-band image and the K-band image obtained for this project. The central cD galaxy and some of the surrounding cluster members are very bright, which has resulted in that they are saturated in the I-band image. The presence of the cD galaxy complicates the identification of the sources, as its extent and brightness increases the background. Some sources might be either associated with the cD galaxy or
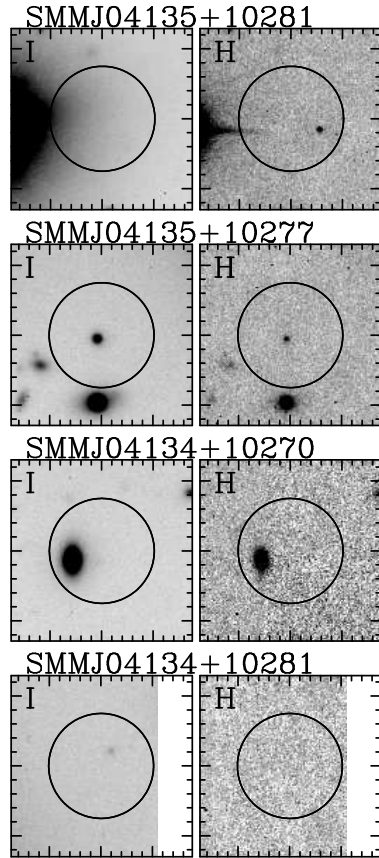
SMMJ04135+10281

SMMJ04135+10277

SMMJ04134+10270

SMMJ04134+10281

Figure 5.2: *Mosaic of the IH images around the SCUBA sources in A478. Each sub-image is $26'' \times 26''$ and is centered on the SCUBA source. The tick marks on the horizontal axis are distanced $1.5''$, while the tick marks on the vertical axes are $2''$. The circle indicates the size of the $850 \, \mu m$ JCMT beam.*

they might be individual galaxies in the foreground or background hidden by the cD galaxy. The cluster is the lowest redshift cluster of the sample, $z = 0.033$. It is also one of the richest SCUBA maps of the survey with nine sources detected. As the redshift of the cluster is relatively low, the volume probed behind the cluster is relatively large compared to the other cluster fields of this survey. For the same reason, the region observed of the cluster itself is only the central part. This means that we detect a limited number of cluster members. Given that the brightest are saturated in the I-band image, it has not been possible to detect the red cluster sequence in a colour-magnitude ($I - K$,K) diagram and through that label the cluster members. Only few of the sources have candidate counterparts. Considering the low redshift of the cluster and the large number of submm sources, it could be hypothesised that in this case we are also detecting cluster members (besides the central cD galaxy). That can, however, not be confirmed, with the small number of sources that have candidate counterparts. If the sources are indeed related to activity in the cluster, they could also be associated with the cooling flow of the cluster. Such findings have not previously been reported in the literature and seem fairly unlikely, as the positions of the SCUBA sources are not coincident with features seen in cooling flow studies such as cold fronts (e.g. Rupke & White,

Table 5.6: *Candidate counterparts for SCUBA sources in A496. p indicates the likelihood of finding a galaxy with $I - K$ and K or redder and brighter at random positions (see Subsection 5.3.2).*

ID	dist ['']	$d\alpha$ ['']	$d\delta$ ['']	$I - K$ [mag]	I [mag]	σ_I [mag]	K [mag]	σ_K [mag]	p
SMM J04336−13154									
153	9.21	-7.55	-5.28	1.73	23.18	0.25	21.45	0.54	0.510
154	6.46	4.11	-4.98	< 2.58	23.58	0.30	< 21.0	...	0.642
160	8.77	5.05	-7.17	< 2.66	23.66	0.31	< 21.0	...	0.696
226	8.11	2.74	7.64	1.17	22.41	0.17	21.24	0.49	0.497
265	9.70	-9.33	2.66	2.41	22.03	0.14	19.62	0.23	0.260
SMM J04336−13149									
no sources detected									
SMM J04336−13158									
associated with the cD									
SMM J04336−13160									
associated with the cD									
SMM J04336−13164									
227	9.96	-3.35	9.38	1.16	21.02	0.09	19.86	0.26	0.329
228	8.81	2.04	8.57	2.29	20.51	0.07	18.22	0.12	0.121
229	6.89	-1.24	6.78	4.72	25.08	0.64	20.36	0.32	0.027
230	6.23	-1.51	6.04	< 2.63	23.63	0.30	< 21.0	...	0.559
234	9.91	8.67	4.81	3.65	22.39	0.17	18.74	0.15	0.041
255	6.61	-5.90	-2.98	2.23	23.19	0.25	20.97	0.43	0.424
258	2.45	-0.33	2.42	2.94	23.76	0.32	20.82	0.40	0.265
260	5.25	0.76	-5.19	3.29	24.02	0.37	20.73	0.38	0.159
SMM J04336−13157									
Coincident with the centre of the cD galaxy.									
SMM J04336−13147									
169	0.89	0.33	0.83	< 2.88	23.88	0.34	< 21.0	...	0.628
213	4.71	-3.21	-3.44	< 2.32	23.32	0.26	< 21.0	...	0.637
218	6.78	1.24	6.66	< 2.28	23.28	0.26	< 21.0	...	0.646
SMM J04337−13166									
249	7.14	-5.13	4.97	1.31	21.71	0.12	20.40	0.33	0.402
SMM J04337−13156									
no sources detected									

2003). Here follows a discussion of the individual sources. Photometry is given in Table 5.6 and images in Figure 5.3.

SMM J04336−13154: Five galaxies have been detected within a search radius of $10''$. Two are detected only in the I-band image. The other three are faint, with the brightest source also being the reddest with $I - K \sim 2.4$. There is no obvious candidate counterpart for this source.

SMM J04336−13149: No sources were detected in the I and K band images.

SMM J04336−13158: This source is only $\sim 15''$ from the centre of the cD galaxy. If it is not associated with the cD galaxy, identifying the underlying galaxy will be
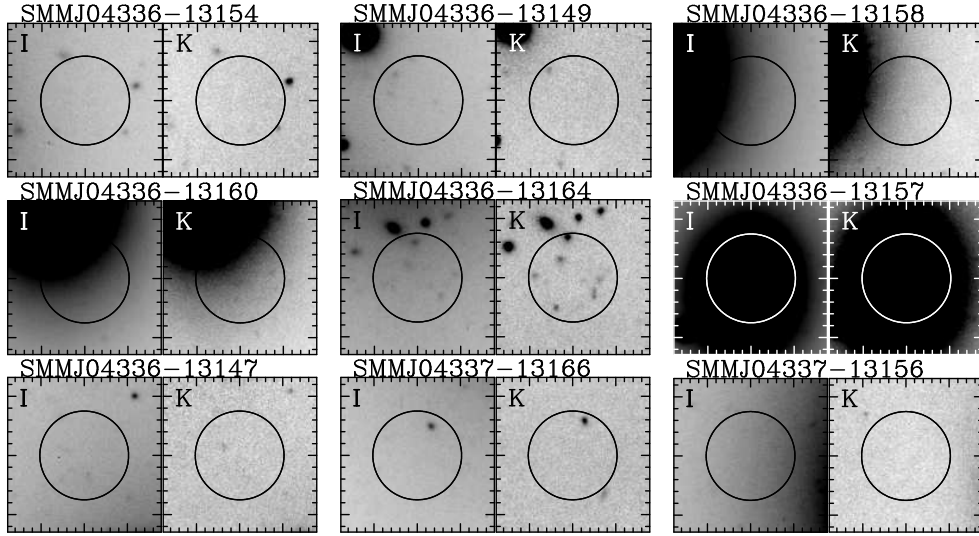
Figure 5.3: *Mosaic of the IK images around the SCUBA sources in A496. Each sub-image is $26'' \times 26''$ and is centered on the SCUBA source. The tick marks on the horizontal axis are distanced $1.5''$, while the tick marks on the vertical axes are $2''$. The circle indicates the size of the $850\,\mu m$ JCMT beam.*

essentially impossible due to the presence of the cD.

SMM J04336−13160: As the previous source, this source is only $\sim 15''$ from the centre of the cD galaxy. If it is not associated with the cD galaxy, identifying the underlying galaxy will be essentially impossible due to the presence of the cD.

SMM J04336−13164: Within a search radius of $10''$ of the source position, there is one galaxy with $I - K > 4$, and two galaxies with $I - K \sim$ 3.3-3.7. This is the only SCUBA source in this field for which several possible counterparts have been found.

SMM J04336−13157: Coincident with the centre of the cD galaxy of the cluster, thus it is most probably submm emission from the nucleus. This is similar to results from Smail et al. (2002) who also detected submm emission from two cD galaxies in their survey.

SMM J04336−13147: Three sources have been detected in the I-band image within a beam. None of these galaxies are detected in the K-band image.

SMM J04337−13166: One galaxy has been detected within a beam from the source, however, it does not exhibit any characteristics that could make it a likely counterpart.

SMM J04337−13156: No sources were detected in the I and K band images.

A520

There is only deep K-band imaging available for area covered by the SCUBA map. Postage stamp sized sub-images centred on the positions of the SCUBA sources are shown in Figure 5.4. As we only have the K band information, we can-
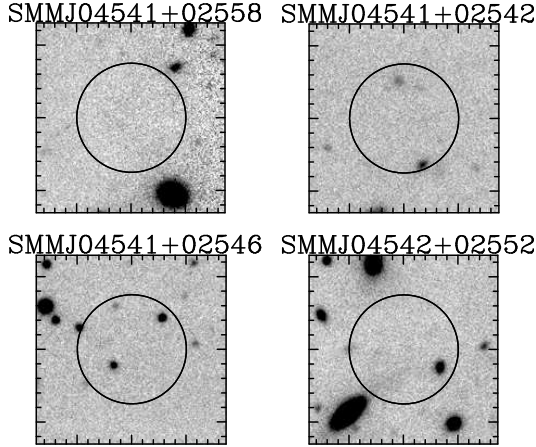
SMMJ04541+02558 SMMJ04541+02542

SMMJ04541+02546 SMMJ04542+02552

Figure 5.4: *Mosaic of the K images around the SCUBA sources in A520. Each sub-image is $26''\times26''$ and is centered on the SCUBA source. The tick marks on the horizontal axis are distanced $1.5''$, while the tick marks on the vertical axes are $2''$. The circle indicates the size of the $850\,\mu m$ JCMT beam.*

not make a satisfactory analysis of possible candidate counterparts for the A520 SCUBA sources, and hence we will not discuss the individual sources.

MS1054−03
A deep radio map at 5 GHz has been published by Best et al. (2002). The map has a rms noise of $5.3\pm0.1\,\mu$Jy. We use the 5 GHz radio detections together with the optical and NIR images to search for counterparts. We do not calculate a probability for chance superpositions between the SCUBA sources and radio sources, in the same way as is done for the optical/NIR detected galaxies. We do, however, note that radio emission from a submm detected star forming galaxies is expected (Condon, 1992), though the radio detection is limited at high redshift due to the positive k-correction at radio wavelengths. The radio also provides an mean of estimating the redshift, which we do by using the 5 GHz flux to estimate the 1.4 GHz flux, assuming a power law spectrum, $S_\nu \propto \nu^\alpha$ with a slope α of -0.8 (Condon, 1992). The ratio between the $850\,\mu$m flux and the 1.4 GHz flux has been demonstrated in previous studies to be useful as a redshift indicator (Blain, 1999; Carilly & Yun, 1999), though the uncertainties remain large, in the order $\Delta z \sim 0.5$. The optical and NIR photometry for the sources within the search radii of the SCUBA source positions are given in Table 5.7, and the postage stamp sized sub-images centred on the SCUBA source positions are shown in Figures 5.5 and 5.6.

SMM J10568−03361: Within a search radius of $8''$ from SMM J10568−03361 two galaxies are found. The galaxy 1370 is only detected in the J, H and K bands. It has $K = 22.38\pm0.07$ and $J - K = 4.6$. The values of p_1 and p_2 highlight the rarity of detection of such an object. There is no radio emission detected at that position, which suggests a redshift $z > 3$. The photometric redshift $3.14^{+1.18}_{-0.24}$ is in agreement with the indication from the radio-submm flux ratio. The other galaxy is faint and does not exhibit unusually red colours. 1370 is most probably the counterpart.

SMM J10569−033610: The detection position of SMM J10569−03362 is between the two radio sources C10 and C11 (Best et al., 2002). The submm source might
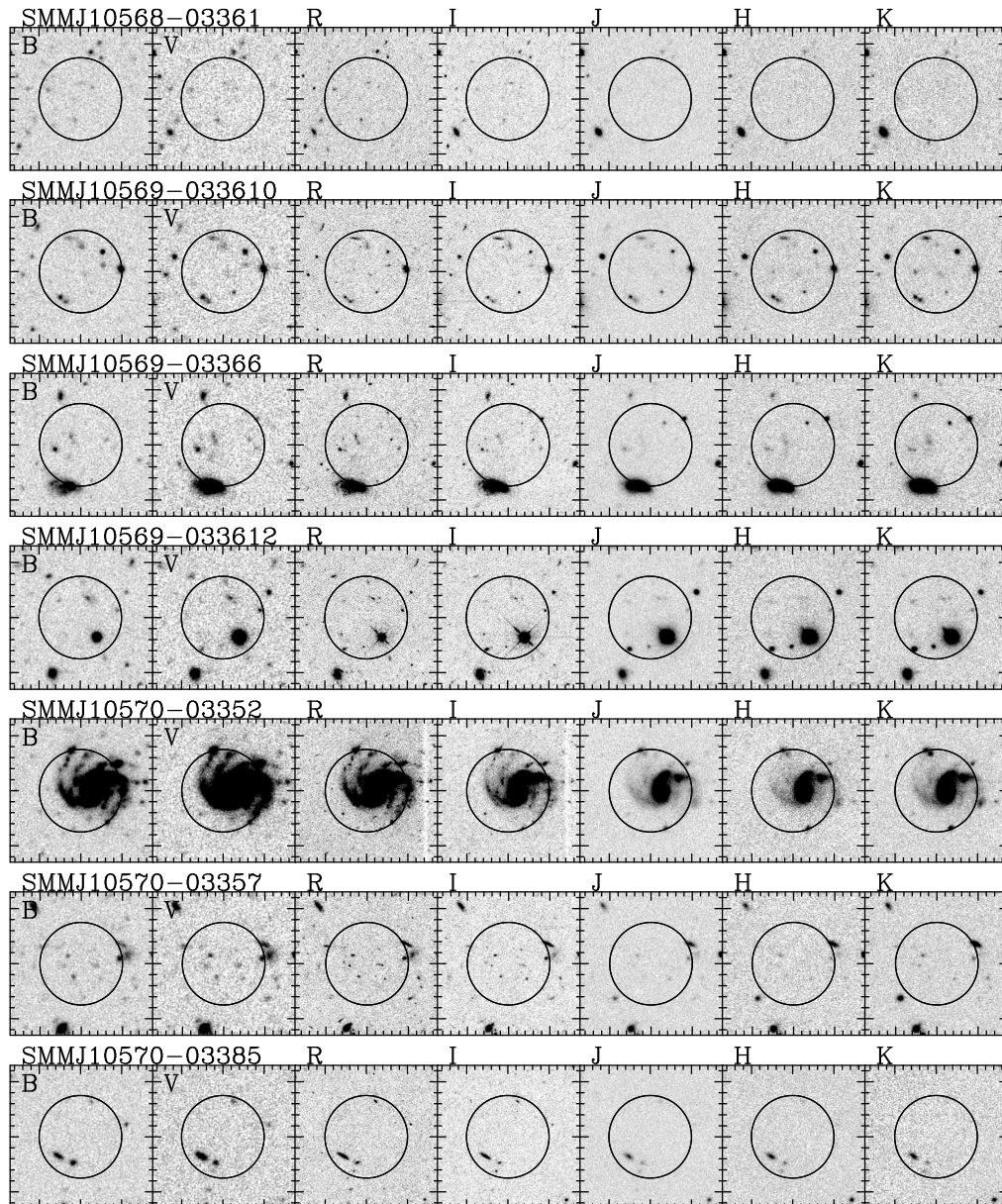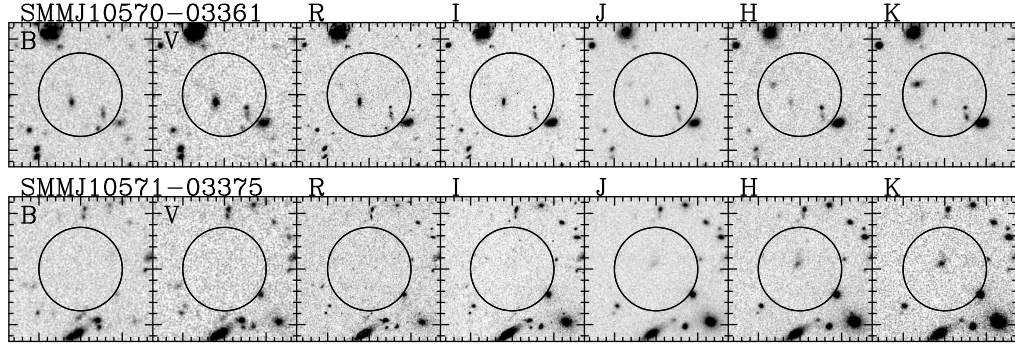
102

Figure 5.5: *Mosaic of the $BVRIJHK$ images around the SCUBA sources in MS1054-03. Each sub-image is $26'' \times 26''$ and is centered on the SCUBA source. The tick marks on the horizontal axis are distanced $1.5''$, while the tick marks on the vertical axes are $2''$. The circle indicates the size of the 850 μm JCMT beam.*

Figure 5.6: *Mosaic of the BVRIJHK images around the SCUBA sources in MS1054-03. Each sub-image is 26″×26″ and is centered on the SCUBA source. The tick marks on the horizontal axis are distanced 1.5″, while the tick marks on the vertical axes are 2″. The circle indicates the size of the 850 μm JCMT beam.*

only be associated with one of the two radio sources, however, it could also be blended submm emission from both radio sources. The two radio sources have similar flux densities. Based on the empirical flux-ratio–redshift relation, assuming that the submm emission is associated with one of the two radio sources, a photometric redshift is ~ 2-2.5. Within a search radius of 8″ there are nine galaxies in the optical and NIR data. The galaxy 1335 is extremely red with $I - K = 6.17$ and $J - K = 2.67$. It is not detected in the optical bands except I. This very red colour is very rare, which makes it unlikely to be a chance coincidence. The galaxy 1333 is an ERO with $I - K = 4.28$. With its red $J - K = 1.99$, the galaxy is fairly un-common, though with $p_1 = 0.077$ and $p_2 = 0.018$ not as rare as 1335. The galaxy 1356 is red, though not extremely red, and has been studied in a paper about DRGs (van Dokkum et al., 2004). 1356 habours an AGN and is coincident with the radio source C11. A $p_2 = 0.02$ also makes this a possible candidate. The galaxy 1294 is coincident with the radio source C10 and does have a red $I - K = 3.38$ colour, but does not exhibit extraordinary rare colours or magnitudes and is found at the edge of the beam of SMMJ10569−033610. All four galaxies, 1335, 1333, 1356 and 1294 have photometric redshifts comparable to the estimate from the submm-radio flux ratio. One of the galaxies 1335, 1333 and 1356 is most likely the counterpart, though the galaxy 1294 could possibly also be a candidate.

SMM J10569−03366: There is no radio emission detected at the position of SMMJ10569−03366, which suggests a redshift > 3, assuming the radio-submm-flux-ratio relation with redshift. Within the search radius of 8″ there are ten objects. Two of these have colours matching the red cluster sequence, and are hence labelled as cluster members. Galaxy 1033 is bright, which brings p_1 and p_2 down. The galaxy has a spectroscopic redshift of $z = 0.458$, which is not in agreement with the radio-submm flux ratio redshift indication, hence this galaxy is unlikely to be the counterpart. Three galaxies exhibit red colours, namely 1172, 1100 and 1182. 1172 is an ERO with $I - K = 4.57$ with $z_{ph} = 1.14^{+0.22}_{-0.06}$. 1100 is close to the DRG criterion with $J - K = 2.19$ and has a $z_{ph} = 2.88^{+0.08}_{-0.08}$. 1182 has ex-

tremely red colours, however, it has very faint JHK-band magnitudes. It has a $z_{ph} = 3.44^{+0.24}_{-0.60}$ and is at the edge of the search radius. Given the radio data 1100 or 1182 is the most likely counterpart.

SMM J10569−033612: The source SMM J10569−033612 is nearby one of the bright stars (ID=1192) in the field, though the star is unlikely to be the source of the submm emission. A couple of arcseconds from the SCUBA detection is an unidentified radio source, C9 (Best et al., 2002). Best et al. report that the position of the source is coincident with one of the diffraction spikes of the star in the optical WFPC2 images, which potentially might be hampering the identification of the underlying source. In the NIR images there is an indication of a source at that position, though it blends with the star and thus in the source extraction is not separable. Within the search radius there are several galaxies, of which three are located on the red cluster sequence. None of the galaxies within the search radius exhibit extraordinarily red colours, though the galaxy 1265 does have $I - K = 3.66$ and $J - K = 1.8$, and is the one with the least likelihood of being a chance coincidence with the SCUBA source at $p_2 \sim 3.5\%$ level. For SMM J10569−033612 there is no obvious candidate counterpart, though 1265 would be a possibility just as the unidentified counterpart of the radio source C9 would be.

SMM J10570−03352: The SCUBA source position is only a couple arcseconds from the extended radio source C15, which at 5 GHz has an integrated flux of 230 μJy. Within the search radius of the SCUBA source, there is a redshift $z = 0.25$ spiral galaxy, which C15 has been identified with (Best et al., 2002), and other galaxies. The number of galaxies listed in Table 5.7 exceeds the number of galaxies actually present near the SCUBA source, as some of these optical/NIR source are components of the spiral galaxy. We investigate whether the spiral galaxy could be the counterpart by comparing the radio and submm emission in two different ways. Using the empirical relation between redshift and radio-submm flux density ratio (Blain, 1999; Carilli & Yun, 1999) we find the following: We assume that the radio emission is non-thermal with a slope of -0.8 (Condon, 1992; see above, page 102) and calculate a 1.4 GHz flux density, $S_{1.4} = 600 \, \mu$Jy. For redshift 0.25, the radio and submm flux must be approximately the same to obey the empirical flux-ratio–redshift relation. That is, however, not the case, as the detected submm flux is almost six times larger, namely, $S_{850} = 3.4$ mJy. This would then suggest that the SCUBA emission originates in one of the surrounding red galaxies. Using the formalism from Condon (1992), the radio emission suggests a star formation rate of $8.6 \, M_{\odot} \text{yr}^{-1}$. Assuming that the FIR emission is well-described by a modified blackbody spectrum with $T = 40$ K and $\beta = 1.5$, which is the FIR SED typically assumed for SCUBA sources (e.g., Blain et al., 1999b), an object at redshift $z = 0.25$ has an SFR of $\sim 11 \, M_{\odot} \text{yr}^{-1}$. The temperature and β are large uncertainties in this type of calculation. The reasonable agreement in the SFRs determined from the radio emission respectively the submm emission, supports that the SCUBA source is the spiral galaxy. However, if the spiral is the counterpart it does not follow the FIR/radio correlation as normally observed for spirals, as the temperature would be too "hot". Among the red galaxies within the search radius, the reddest galaxy is 1614 with $I - K = 3.41$, which, however, falls on the red cluster sequence. Another red object is detected north of the spiral galaxy next to the end

of a spiral arm. This red galaxy is in the catalogue from Förster Schreiber et al. (*in prep*) considered to be a part of the spiral galaxy in the galaxy component 1630. Here we have assumed that the red object is a separate galaxy. The results of aperture photometry for $IJHK$ is given in Table 5.7, where the object is denoted as 1630A. 1630A is extremely red with $I - K = 5.25$ and $J - K = 2.69$. Provided that this object indeed is not a part of the spiral galaxy, this is the most likely counterpart.

SMM J10570−03357: Within a search radius of $8''$ from SMM J10570−03357 seven galaxies have been detected. None of them show exceptional colours. Increasing the search radius to $10''$, three additional sources have been detected. Of these galaxies, galaxy 1459 has $I - K = 5$, which makes it very unlikely to be a chance coincedence. The galaxy has a spectroscopic redshift $z = 2.081$. It is the only obvious candidate counterpart. The only argument against it is the distance from the SCUBA detection position. No radio sources have been detected closeby.

SMM J10570−03385: Within a search radius of $8''$ of SMM J10570−03385 four galaxies have been detected. Three of them have photometric (and spectroscopic) redshifts lower than the cluster. One is possibly a cluster member. None of the four stand out as likely counterparts. No radio sources have been detected closey.

SMM J10570−03361: The source SMM J10570−03361 does not have a radio detection, which would indicate a redshift > 3 (see above); it should be kept in mind that the radio-submm flux ratio as redshift indicator has large uncertainties. Within a search radius of $8''$ five galaxies are present. One of these, galaxy 1383 is an ERO and DRG with $I - K = 5.23$ and $J - K = 2.91$. This galaxy is very unlikely to be a chance coincidence and is thus probably the counterpart. A spectroscopic redshift $z = 2.423$ has been published (van Dokkum et al., 2004). Based on NIR spectroscopy, including a detection of the $H\alpha$ emission line, a star formation rate has been estimated to $400\,\mathrm{M}_\odot\mathrm{yr}^{-1}$, which is in good agreement with the SCUBA data, which suggests a star formation rate of $\sim 500\,\mathrm{M}_\odot\mathrm{yr}^{-1}$. 1383 has recently been detected in CO with Plateau de Bure (P. Papadopoulos, private communatication). The other galaxies within the search radius all have low photometric redshifts and colours that are not extraordinarily red, so given that the 1383 is the galaxy with indication of the most vigorous star formation rates, we identify it as being the counterpart.

SMM J10571−03375: Centered just North of SMM J10571−03375, there is a diffuse extended radio source, C4 (Best et al., 2002), which also covers the position of the SCUBA source. The source has not been identified and could possibly be related to another closeby radio source, C5. Within the search radius of $8''$ five galaxies are detected. Two of these fall on the red cluster sequence, and the other are fainter than $K > 23.3$ and do not have extraordinarily red photometric colours. The source, 723, which is less than an arcsecond from the SCUBA position, has extremely red colours with $I - K = 5.37$ and $J - K = 2.47$. 723 is not visible in the any of the optical bands, but can only be seen in the NIR bands. It has an photometric redshift of $z_p = 1.88^{+0.12}_{-0.02}$. Given that the distance between 723 and SMM J10571−03375 is so small and the very red colour of the galaxy, this is most propably the counterpart.[3]

---

[3]A true-colour VIK image of this source can be found at the back of this thesis.

Table 5.7: *Candidate counterparts for the SCUBA source in MS1054−03. cl indicates whether the galaxy falls on the red cluster sequence (1 = cluster member). p_1 indicates the likelihood of finding a galaxy with $I − K$ and K or redder and brighter at random positions (see Subsection 5.3.2). p_2 indicates the same, though also includes $J − K$.*

ID	dist ["]	dα ["]	dδ ["]	z_{spec}	z_{phot}	B−V [mag]	V−R [mag]	R−I [mag]	I−K [mag]	J−K [mag]	H−K [mag]	K [mag]	σ_K [mag]	cl	p_1	p_2
SMMJ10568−03361																
1340	4.27	1.63	-3.95	...	$2.96^{+0.06}_{-0.14}$	1.01	-0.19	0.76	2.60	1.86	0.44	23.84	0.12	0	0.564	0.163
1370	7.32	7.32	0.14	...	$3.14^{+1.10}_{-0.24}$	...	...	...	...	4.60	1.81	22.38	0.07	0	< 0.001	< 0.001
SMMJ10569−033610																
1280	6.24	4.10	-4.71	...	$1.28^{+0.36}_{-0.82}$	0.45	0.28	0.94	3.09	1.44	0.65	20.10	0.02	0	0.216	0.153
1294	6.17	3.33	-5.19	...	$2.00^{+0.16}_{-0.72}$	0.54	0.18	0.86	3.38	1.77	0.77	21.33	0.02	0	0.188	0.067
1313	4.05	-1.48	-3.77	...	$0.12^{+0.72}_{-0.02}$	2.17	0.50	1.34	1.83	0.69	0.17	22.24	0.05	0	0.626	0.560
1318	6.81	-6.80	0.43	...	$0.70^{+0.00}_{-0.08}$	0.69	0.41	1.35	2.43	1.41	0.71	19.14	0.01	0	0.243	0.178
1333	0.70	-0.40	-0.57	...	$2.14^{+0.14}_{-0.96}$	0.61	0.02	0.14	4.28	1.99	0.71	22.23	0.06	0	0.077	0.018
1335	4.17	4.17	-0.17	...	$1.98^{+0.28}_{-0.08}$	...	...	-0.20	6.17	2.67	1.04	21.69	0.04	0	0.010	0.001
1356	4.95	-3.45	3.54	2.427	$2.40^{+0.48}_{-0.10}$	0.53	0.25	0.77	3.40	2.15	0.94	19.87	0.01	0	0.125	0.021
1368	6.31	2.19	5.92	...	$0.78^{+0.08}_{-0.20}$	0.64	0.36	1.26	2.94	1.50	0.74	20.38	0.02	0	0.275	0.183
1376	4.79	0.25	4.78	...	$0.80^{+0.06}_{-0.06}$	0.25	0.29	1.37	1.85	0.98	0.47	22.62	0.08	0	0.653	0.573
SMMJ10569−03366																
1033	7.81	2.31	-7.46	0.458	$0.40^{+0.04}_{-0.04}$	1.36	0.55	1.34	2.81	1.53	0.75	16.02	0.00	0	0.019	0.012
1100	1.88	1.77	0.64	...	$2.88^{+0.08}_{-0.08}$	0.85	0.18	0.73	3.48	2.19	0.97	20.24	0.03	0	0.124	0.019
1141	5.18	5.13	-0.75	...	$0.14^{+2.76}_{-0.98}$	0.61	0.09	0.63	2.55	1.38	0.61	21.38	0.04	0	0.456	0.342
1146	4.50	4.41	-0.89	...	$3.14^{+0.46}_{-0.02}$	0.95	0.43	0.79	3.17	1.93	1.05	22.47	0.05	1	0.321	0.084
1158	4.17	-4.05	1.00	...	$3.04^{+0.14}_{-2.78}$	0.59	0.45	0.74	2.20	1.65	0.97	23.92	0.13	0	0.658	0.329
1167	7.34	-5.60	4.74	...	$0.72^{+0.06}_{-0.94}$	1.77	0.84	2.21	3.32	1.77	0.86	19.50	0.01	1	0.127	0.046
1172	4.45	-2.02	3.96	...	$1.14^{+0.22}_{-0.06}$	...	0.67	1.54	4.57	1.79	0.83	20.90	0.03	0	0.047	0.016
1182	7.96	-7.00	3.80	...	$3.44^{+0.24}_{-0.60}$	...	1.07	-1.89	6.36	2.93	1.79	24.06	0.14	0	0.011	< 0.001
1186	7.91	6.75	4.13	...	$0.42^{+3.62}_{-0.20}$	1.67	0.43	1.08	2.26	1.40	0.94	23.86	0.12	0	0.647	0.476
1208	7.01	-3.38	6.15	...	$0.56^{+0.08}_{-0.10}$	0.84	0.32	0.96	2.25	1.31	0.87	24.87	0.20	0	0.661	0.525

107

Table 5.7: — *Continued*

ID	dist ["]	dα ["]	dδ ["]	z_{spec}	z_{phot}	B−V [mag]	V−R [mag]	R−I [mag]	I−K [mag]	J−K [mag]	H−K [mag]	K [mag]	σ_K [mag]	cl	p1	p2
SMM J10569−033612																
1263	7.08	4.28	-5.64	…	$0.62^{+0.02}_{-0.02}$	1.75	0.72	1.94	3.15	1.66	0.79	19.42	0.01	1	0.162	0.080
1265	5.24	0.76	-5.18	…	$2.14^{+0.08}_{-0.06}$	1.66	0.60	1.17	3.66	1.80	0.54	20.22	0.02	0	0.105	0.035
1298	5.68	4.86	-2.94	…	$4.26^{+0.10}_{-0.12}$	2.90	0.82	1.08	2.55	1.68	1.17	22.72	0.07	1	0.550	0.253
1332	6.35	-6.20	1.34	…	$3.64^{+0.02}_{-3.40}$	1.22	0.27	0.77	2.30	1.59	0.55	21.99	0.05	0	0.554	0.319
1349	5.44	4.60	2.91	…	$1.20^{+0.26}_{-0.28}$	0.12	0.55	1.07	3.44	1.79	0.78	22.31	0.05	0	0.204	0.071
1351	3.59	-0.90	3.48	…	$0.12^{+2.70}_{-0.02}$	0.54	-0.01	0.71	2.43	1.28	0.57	22.08	0.06	0	0.549	0.441
1354	4.01	-1.97	3.49	…	$1.60^{+0.04}_{-0.30}$	0.12	0.51	0.59	3.04	1.36	0.65	23.28	0.09	1	0.383	0.292
SMM J10570−03352																
1527	1.58	-1.52	0.44	0.250	$0.20^{+0.16}_{-0.02}$	0.95	0.16	0.72	2.10	1.18	0.62	15.66	0.00	0	0.020	0.017
1596	7.88	-7.61	-2.06	…	$0.22^{+0.06}_{-0.02}$	0.85	0.09	0.56	2.46	1.27	0.73	19.19	0.02	0	0.249	0.201
1614	7.05	-2.23	-6.68	…	$0.74^{+0.06}_{-0.06}$	1.39	0.81	1.79	3.41	1.71	0.85	20.03	0.02	1	0.131	0.056
1625	6.99	-6.99	-0.08	…	$0.24^{+0.08}_{-0.04}$	0.79	0.13	0.53	1.65	1.03	0.61	19.47	0.02	0	0.330	0.288
1630	7.14	1.78	6.91	0.250	$0.30^{+0.02}_{-0.06}$	0.91	0.22	0.59	2.34	1.36	0.78	18.71	0.02	0	0.198	0.152
1630A	7.10	1.75	6.88	…	-	-	-	-	5.25	2.69	1.36	19.56	0.02	0	0.011	0.001
1640	6.11	4.54	-4.08	…	$0.46^{+0.04}_{-0.38}$	0.99	0.39	0.97	2.05	1.14	0.61	23.31	0.09	0	0.659	0.563
1647	5.18	-4.63	2.32	…	$0.24^{+0.06}_{-0.06}$	0.60	0.13	0.55	1.75	1.08	0.60	18.32	0.01	0	0.172	0.149
1656	7.82	-6.07	4.93	…	$2.50^{+0.00}_{-2.48}$	0.44	0.19	0.35	1.55	0.98	0.65	20.16	0.03	0	0.416	0.365
SMM J10570−03357																
1459	9.24	6.79	-6.27	2.081	$1.74^{+0.08}_{-0.26}$	0.30	0.22	1.75	5.00	2.21	1.08	19.62	0.01	0	0.043	0.009
1478	9.40	-9.04	-2.59	…	$3.62^{+0.06}_{-0.02}$	1.15	0.58	0.61	2.73	1.94	0.82	22.24	0.05	0	0.617	0.228
1493	4.12	-3.04	-2.78	…	$0.70^{+0.06}_{-0.54}$	1.02	0.04	1.45	2.31	1.07	0.69	23.34	0.08	0	0.625	0.543
1498	2.84	1.61	-2.34	…	$0.76^{+0.06}_{-0.74}$	0.33	0.16	0.91	1.73	1.34	0.57	25.64	0.23	0	0.715	0.555
1500	7.72	-6.85	3.54	…	$0.68^{+0.04}_{-0.24}$	0.81	0.45	1.15	3.10	1.76	0.87	18.93	0.01	0	0.131	0.050
1510	3.38	3.36	-0.33	…	$3.38^{+0.08}_{-0.08}$	0.94	0.45	0.25	2.90	1.74	1.75	23.08	0.08	0	0.437	0.171
1512	6.61	-6.53	0.98	…	$0.60^{+0.20}_{-0.08}$	0.42	0.34	0.79	1.88	1.04	0.67	21.50	0.04	0	0.555	0.483
1517	3.10	2.69	1.53	…	$3.62^{+0.04}_{-0.06}$	1.13	0.32	0.70	2.47	1.67	0.72	21.98	0.04	0	0.520	0.248
1520	7.93	-7.76	1.64	…	$0.08^{+3.32}_{-0.10}$	0.70	0.14	0.58	1.72	0.88	0.48	22.57	0.07	0	0.662	0.587
1525	8.05	7.41	3.14	…	$3.44^{+0.02}_{-0.04}$	0.97	0.44	0.55	2.26	1.97	1.26	22.67	0.07	0	0.732	0.255

Table 5.7: — *Continued*

ID	dist ['']	dα ['']	dδ ['']	z_{spec}	z_{phot}	B − V [mag]	V − R [mag]	R − I [mag]	I − K [mag]	J − K [mag]	H − K [mag]	K [mag]	σ_K [mag]	cl	p_1	p_2
SMMJ10570−03385																
254	6.67	2.37	-6.23	...	$0.56^{+0.06}_{-0.04}$	1.22	0.28	1.67	2.54	1.53	0.65	22.13	0.06	1	0.517	0.328
255	5.56	4.31	-3.52	0.373	$0.40^{+0.04}_{-0.04}$	1.11	0.30	0.87	2.35	1.41	0.70	19.73	0.02	0	0.325	0.238
259	5.05	1.80	-4.72	...	$1.46^{+0.16}_{-0.18}$	0.19	0.08	0.68	2.42	1.13	0.60	21.64	0.05	0	0.508	0.435
311	6.51	-1.53	6.33	...	$0.20^{+0.02}_{-0.06}$	0.94	0.37	0.71	1.78	0.97	0.74	23.53	0.13	0	0.690	0.607
SMMJ10570−03361																
1329	5.57	-3.87	-4.01	...	$0.80^{+0.20}_{-0.20}$	0.46	0.33	1.28	2.92	1.49	0.83	20.40	0.02	0	0.286	0.193
1338	6.87	-2.93	-6.21	...	$0.94^{+0.00}_{-0.00}$	0.02	0.31	1.03	1.85	1.00	0.82	24.03	0.12	0	0.695	0.609
1359	2.32	1.89	-1.35	...	$0.16^{+0.02}_{-0.02}$	1.11	0.25	0.75	1.69	0.93	0.44	21.05	0.03	0	0.522	0.461
1360	4.29	-3.60	-2.33	0.000	$0.22^{+0.24}_{-0.02}$	1.36	0.37	1.69	2.03	0.73	0.28	20.77	0.02	0	0.481	0.429
1383	5.27	4.93	1.87	2.423	$2.26^{+0.38}_{-0.04}$	1.09	0.22	0.86	5.23	2.91	1.27	19.72	0.02	0	0.014	0.001
SMMJ10571−03375																
619	7.82	-6.30	-4.64	0.821	$0.64^{+0.02}_{-0.04}$	1.79	0.75	1.94	3.10	1.61	0.75	18.28	0.01	1	0.088	0.048
723	1.39	0.62	1.24	...	$1.88^{+0.02}_{-0.06}$	...	...	< 3.23	5.37	2.47	0.97	19.61	0.02	0	0.011	0.001
766	7.84	-7.65	1.74	...	$0.56^{+4.78}_{-0.00}$	1.46	1.29	1.96	2.91	1.43	0.69	21.09	0.04	1	0.337	0.241
777	5.30	4.91	1.99	...	$4.76^{+0.34}_{-0.24}$	...	...	2.05	2.57	2.05	1.14	25.37	0.30	0	0.590	0.117
778	7.45	7.00	2.55	...	$0.58^{+0.94}_{-0.12}$	4.71	0.58	1.55	3.16	1.50	0.66	23.35	0.12	0	0.339	0.226
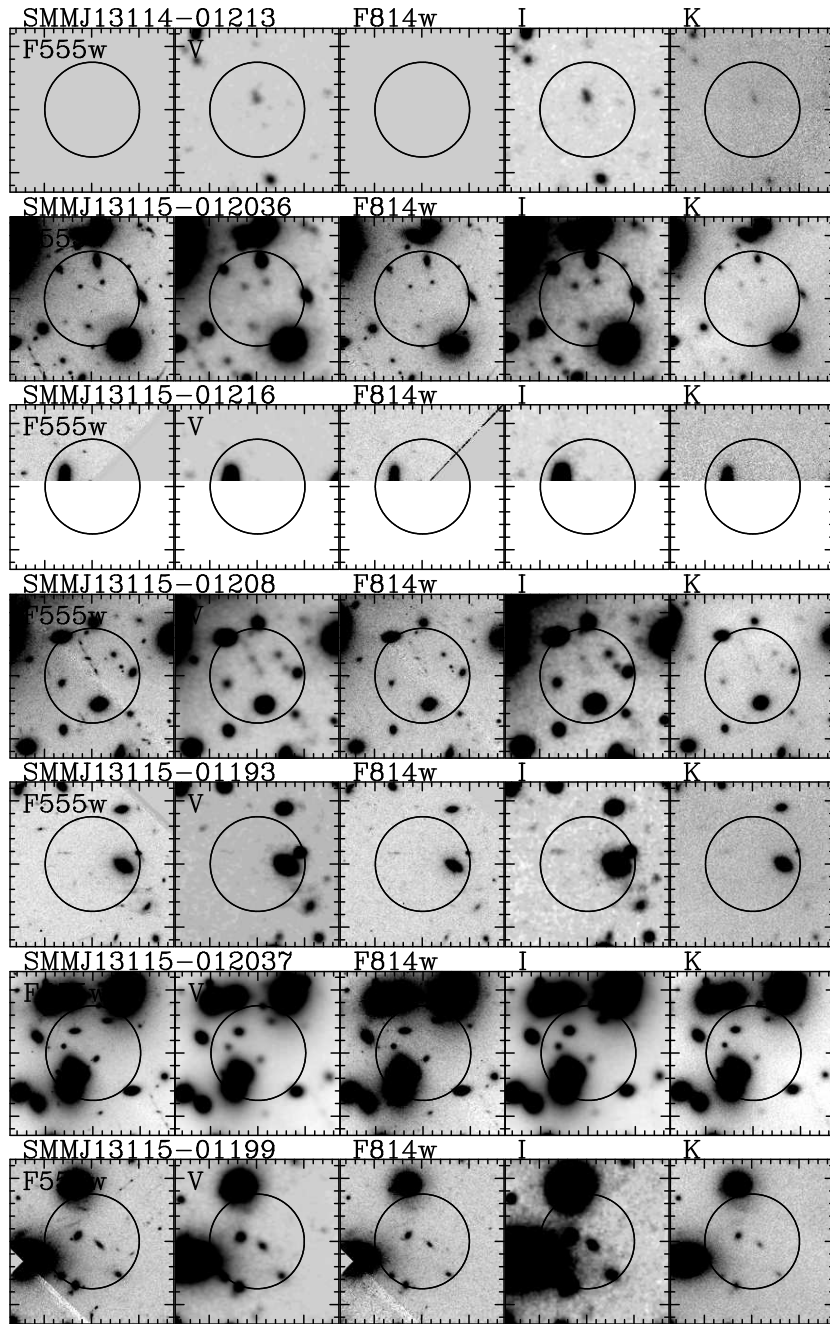
Figure 5.7: *Mosaic of the F555W, V, F814W, I, K images around the SCUBA sources in A1689 Each sub-image is 26″×26″ and is centered on the SCUBA source. The tick marks on the horizontal axis are distanced 1.5″, while the tick marks on the vertical axes are 2″. The circle indicates the size of the 850 μm JCMT beam.*

A1689

The WFPC2 images do not cover the entire area of the SCUBA map. The EMMI images do; however, the resolution is five times lower, which makes it difficult to see details. Within the search radii for the individual SCUBA sources, mostly cluster members are found. For about half, however, there are also faint lensed arcs. Deep ISOCAM observations exists for this (Fadda et al., 2000; Duc et al., 2002). There is, however, no overlap between the ISOCAM sources and the SCUBA sources. Photometry is given in Table 5.8 and images centred on the SCUBA positions are shown in Figures 5.7 and 5.8.

SMM J13114−01213: This is one of the SCUBA sources not covered by the WFPC2 images. Four galaxies are found within the search radius. The brightest one is a cluster member. The other three are not detected in the K-band and are faint in the optical. There are no obvious candidate counterparts for this source.

SMM J13115−012036: This source is very close to the centre of the cluster. Within the search radius of $8''$ nine galaxies are detected. Six of these are most likely cluster members. Galaxy 666 is a lensed arc, which is only detected in the F555W and F814W images. This is a possible candidate counterpart.

SMM J13115−01216: This source is on the edge of the K-band image.

SMM J13115−01208: This source has the brightest observed submm flux in the field. Within in the search radius, there are a large number of cluster members and three lensed arcs. One of the arcs is the radial arc, for which spectroscopy has been obtained and presented in Section 5.4. One of the arcs is most likely the counterpart. The radial arc appears to be a galaxy with at least two components, which could suggest that it is interacting. The other two lensed arcs could be counter-images of other submm detected arcs.

SMM J13115−01193: At least two arcs are detected within the search radius for this source along with cluster members. Possibly one of the arcs is the underlying counterpart.

SMM J13115−012037: This source is the third of the submm sources detected near the centre of the cluster. Within the search radius only cluster members have been detected. Possibly arcs are present, however, obscured by the light from the bright central cluster members.

SMM J13115−01199: Within the search radius of this source, more than two arcs are detected. One of the arcs, galaxy 237, is detected all through to K. It has an extremely red colour of $I - K = 4$. This is possibly the counterpart.

SMM J13116−01204: This source is on the edge of the WFPC2 images. Within the search radius, there are two arcs (also detected in the WFPC2 images). They are red with $I - K \sim 3.8$. Possibly one of them is the counterpart. Furthermore, there are cluster members, and at the edge of the beam there is a bright star.

SMM J13116−01203: This source is not covered by the WFPC2 images. There is one, very faint, red object. The level of significance of the detection is however small. None of the other sources detected are extraordinary and are unlikely candidate counterparts.

Table 5.8: *Candidate counterparts for the SCUBA source in A1689. V_{555} is the isophot magnitude in the F555W-band. cl indicates whether the galaxy falls on the red cluster sequence (1 = cluster member). p indicates the likelihood of finding a galaxy with $I - K$ and K or redder and brighter at random positions (see Subsection 5.3.2).*

ID	dist ["]	$d\alpha$ ["]	$d\delta$ ["]	V_{555} [mag]	$\sigma_{V_{555}}$ [mag]	$V - I$ [mag]	$I - K$ [mag]	K [mag]	σ_K [mag]	cl	p
SMM J13114-01213											
206	1.82	-0.18	1.81	24.26[1]	0.04	1.36	2.31	20.59	0.40	1	0.287
978	1.96	-1.95	0.24	26.90[1]	0.13	0.1	3.6	23.20	1.41	0	0.135
1018	5.12	-5.04	0.92	26.63[1]	0.11	1.56	2.42	22.65	1.06	0	0.444
1041	2.78	-1.20	-2.50	26.34[1]	0.10	0.37	2.17	23.80	1.95	0	0.545
SMM J13115-012036											
489	6.08	-0.79	6.03	21.16	0.01	1.09	2.06	18.93	0.18	1	0.135
464	3.08	-1.62	2.62	23.96	0.04	1.3	-1.22	24.46	2.87	1	0.637
764	2.69	1.86	1.94	24.13	0.05	1.34	0.31	22.98	1.25	1	0.585
476	6.94	5.14	4.66	21.84	0.02	1.4	2.19	19.77	0.27	1	0.210
644	7.85	-7.85	0.39	21.51	0.01	1.12	2.43	19.54	0.24	1	0.169
647	4.41	0.49	-4.38	23.07	0.03	1.25	1.77	22.00	0.77	1	0.489
666	1.64	-0.72	1.48	26.39	0.15	1.32	< 3.78	> 22.00	...	0	...
686	2.00	0.09	-2.00	27.39	0.23	2.33	< 3.07	> 22.00	...	0	...
693	5.56	4.20	-3.64	25.86	0.11	0.88	< 3.3	> 22.00	...	0	...
SMM J13115-01216											
No interesting sources..											
SMM J13115-01208											
712	4.74	-3.40	3.29	23.69	0.04	1.33	1.56	21.48	0.60	1	0.438
657	4.76	-4.56	1.36	24.57	0.06	1.42	1.9	21.42	0.59	1	0.413
643	6.43	-6.41	0.49	22.16	0.02	1.36	2.44	19.37	0.22	1	0.153
470	0.88	-0.59	0.64	24.77	0.06	0.38	2.97	21.94	0.75	0	0.211
611	5.20	1.74	4.89	24.58	0.06	0.57	< 3.15	> 22.00	...	0	...
848	4.95	4.81	-1.18	22.01	0.02	1.31	2.12	20.53	0.38	1	0.299
756	4.66	-1.10	-4.53	19.84	0.01	1.54	2.81	16.27	0.05	1	0.017
469	2.77	0.69	2.68	24.39	0.05	0.54	< 2.25	> 22.00	...	1	...
477	7.77	4.90	6.04	20.13	0.01	1.28	2.61	17.53	0.10	1	0.043
482	6.83	0.88	6.77	24.43	0.05	1.29	< 1.61	> 22.00	...	0	...
658	4.82	-4.78	0.64	26.02	0.11	1.4	1.72	22.87	1.19	1	0.570
761	6.15	0.93	-6.08	26.93	0.19	1.12	1.79	23.98	2.16	0	0.610
774	6.93	1.48	-6.77	24.79	0.07	0.89	2.51	22.51	0.99	0	0.393
817	3.38	-2.17	2.60	26.54	0.15	-0.55	< 5.09	> 22.00	...	0	...
SMM J13115-01193											
192	4.46	4.11	1.75	25.87	0.11	2.03	2.74	21.60	0.64	0	0.263
189	7.37	-7.17	1.72	22.03	0.02	1.01	1.46	19.83	0.28	1	0.254
190	4.94	-4.94	-0.27	19.69	0.01	1.52	2.85	16.21	0.05	1	0.015
185	3.08	-2.24	-2.11	26.38	0.15	0.07	4.58	22.11	0.81	0	0.042
186	7.59	-6.32	-4.20	23.85	0.05	0.91	3.14	21.74	0.68	0	0.179
187	6.63	-5.88	-3.07	26.35	0.14	1.1	2.98	22.45	0.96	0	0.235
200	6.60	6.60	-0.29	27.17	0.21	0.98	< 4.71	> 22.00	...	0	...
205	1.52	0.22	-1.51	26.48	0.15	0.7	2.56	23.34	1.52	0	0.417
211	4.07	2.74	-3.00	26.54	0.16	1.28	2.99	22.47	0.97	0	0.235

[1] *V* aperture magnitude from the EMMI *V*-band image.

Continues on next page

Table 5.8: — *Continued*

ID	dist ["]	$d\alpha$ ["]	$d\delta$ ["]	V_{555} [mag]	$\sigma_{V_{555}}$ [mag]	$V - I$ [mag]	$I - K$ [mag]	K [mag]	σ_K [mag]	cl	p
SMM J13115-012037											
491	1.07	-0.50	-0.95	22.11	0.02	1.12	2.56	19.62	0.25	1	0.157
496	4.49	2.80	3.51	20.65	0.01	1.46	2.68	18.01	0.12	1	0.057
490	4.68	4.56	1.05	21.87	0.02	1.44	2.43	18.94	0.18	1	0.120
552	5.60	-2.30	5.11	21.60	0.01	1.35	3.08	18.68	0.16	1	0.058
568	6.26	5.51	-2.96	22.21	0.02	1.52	2.99	18.42	0.14	1	0.058
148	6.52	3.71	-5.37	18.14	0.00	1.55	3.11	15.55	0.04	1	0.006
510	3.77	2.53	-2.79	18.85	0.00	1.55	3.1	16.25	0.05	1	0.012
546	7.57	-0.91	7.52	21.74	0.01	1.48	2.88	18.21	0.13	1	0.047
SMM J13115-01199											
237	4.07	3.15	2.58	23.18	0.03	1.01	4.00	20.89	0.46	0	0.055
536	2.46	2.32	0.81	21.82	0.02	1.39	2.52	19.28	0.21	1	0.131
354	7.44	2.55	-6.99	21.27	0.02	1.33	2.72	19.37	0.22	1	0.119
224	1.26	-1.13	-0.55	22.84	0.03	1.26	2.1	20.38	0.36	1	0.283
349	7.27	4.83	-5.43	22.28	0.02	1.36	2.9	19.59	0.25	1	0.106
387	6.69	-4.20	-5.20	23.34	0.03	1.32	2.12	20.50	0.38	1	0.292
225	6.43	-3.86	-5.14	22.08	0.02	1.28	2.33	20.61	0.40	1	0.285
372	6.62	-5.58	3.56	26.91	0.19	0.11	< 4.72	> 22.00	...	0	...
386	3.03	-2.83	1.08	28.03	0.31	< 1.52	...	> 22.00	...	0	...
403	4.22	-4.01	-1.32	25.82	0.11	1.6	< 2.66	> 22.00	...	0	...
404	6.56	-6.25	-1.99	25.62	0.10	0.66	< 3.23	> 22.00	...	0	...
SMM J13116-01204											
683	6.12	-6.05	0.93	24.86	0.09	0.89	3.82	21.16	0.52	0	0.076
457	7.23	-7.20	0.66	27.23	0.25	1.22	3.84	21.63	0.64	0	0.079
681	3.53	-0.97	3.40	27.06[1]	0.14	1.52	2.15	23.39	1.56	0	0.534
687	0.38	0.36	0.12	25.80[1]	0.07	0.76	3.66	21.38	0.57	0	0.094
688	3.55	3.50	-0.59	24.94[1]	0.05	1.19	2.01	21.74	0.68	0	0.431
689	6.51	4.88	-4.30	25.05[1]	0.05	0.72	2.32	22.01	0.78	0	0.414
690	7.28	0.69	-7.25	17.67[1]	0.00	0.01	3.73	13.93	0.02	0	< 0.001
SMM 13116-01203											
639	6.89	0.15	6.89	27.03[1]	0.14	1.6	3.16	22.27	0.88	0	0.191
442	6.56	-6.25	1.98	27.04[1]	0.14	0.98	4.48	21.58	0.63	0	0.043
677	1.96	-1.88	0.56	24.70[1]	0.04	1.26	2.95	20.49	0.38	1	0.144
693	3.58	-0.33	-3.57	26.91[1]	0.13	1.15	3.2	22.56	1.02	0	0.192
440	4.33	3.99	1.67	22.96[1]	0.02	1.26	2.58	19.12	0.20	1	0.111
469	6.71	1.26	-6.59	25.14[1]	0.05	0.83	0.78	23.53	1.67	0	0.610

[1] V aperture magnitude from the EMMI V-band image.

RX J1347.5−1145

SMM J13475−11459: Within the beam of SMM J13475−11459 eight galaxies have been detected. Three of these, 448, 451 and 453, are cluster members. The galaxies 477 and 450 have blue photometric colours. Galaxy 450, which is the brigher of the two, is known to be a foreground galaxy at $z = 0.101$ (Cohen & Kneib, 2002). The galaxies 449, 452 and 485 have extremely red colours, $I - K > 4$ and $R - K > 5.3$. 449 and 452 have similar colours and appear the images to be two component of the same strongly lensed galaxy (an arc). As the arc is detected in all passbands, it has a redshift $z < 2.5$. 485 is not detected in B, V and R, which suggests that the galaxy is either extremely reddened by dust extinction or at very high redshift
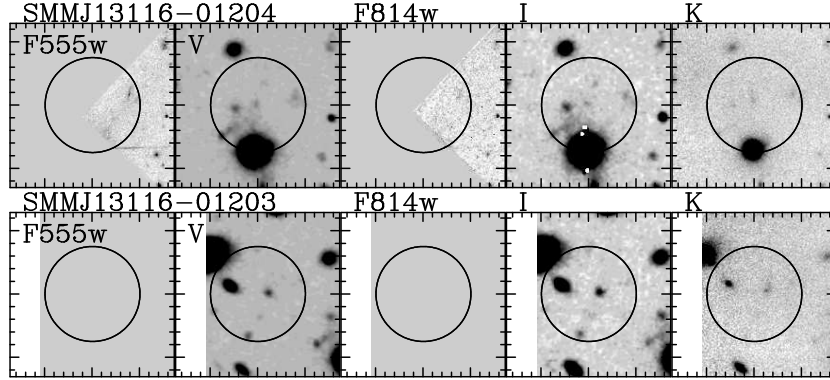
Figure 5.8: *Mosaic of the F555W, V, F814W, I, K images around the SCUBA sources in A1689 Each sub-image is 26″×26″ and is centered on the SCUBA source. The tick marks on the horizontal axis are distanced 1.5″, while the tick marks on the vertical axes are 2″. The circle indicates the size of the 850 μm JCMT beam.*
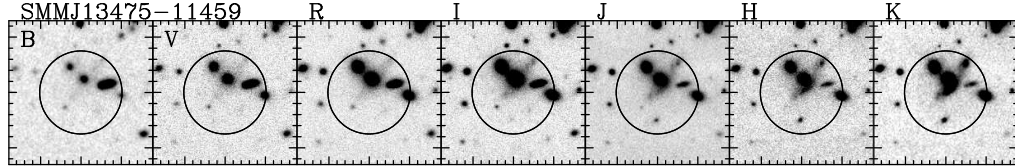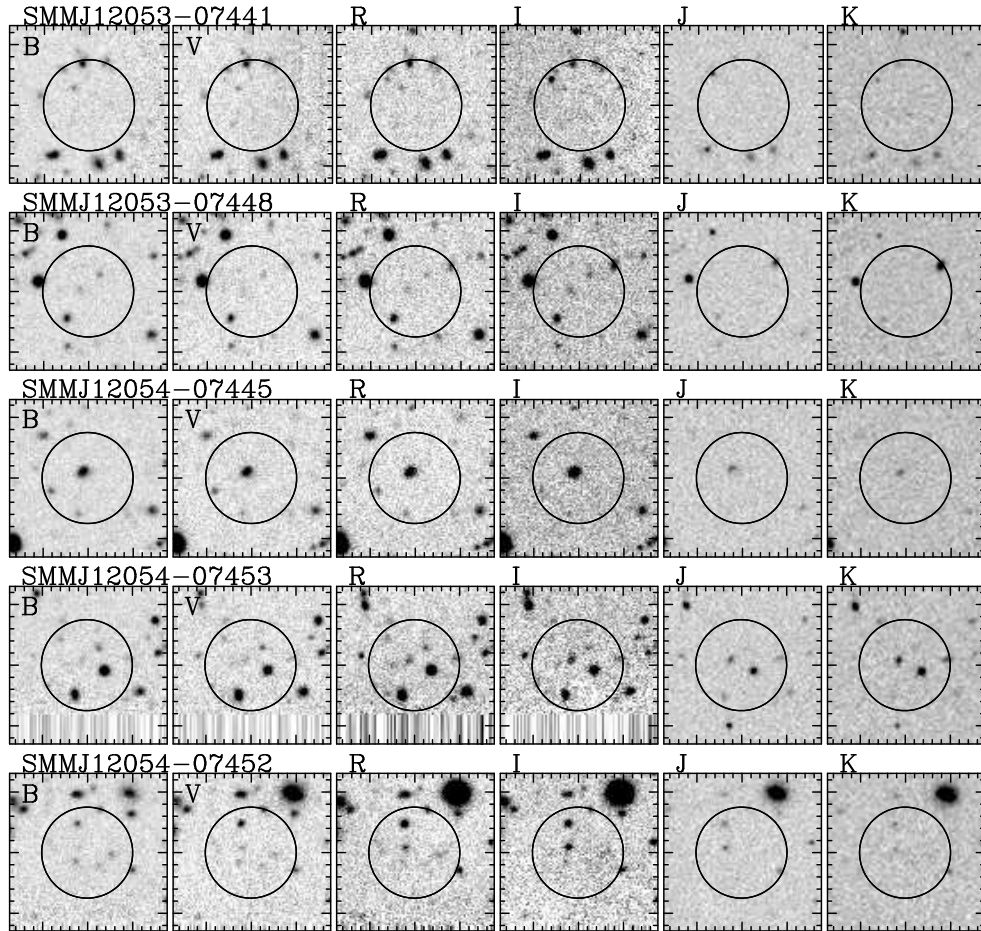

Figure 5.9: *Mosaic of the BVRIJHK images around the SCUBA source in RXJ1347-1145. Each sub-image is 26″×26″ and is centered on the SCUBA source. The tick marks on the horizontal axis are distanced 1.5″, while the tick marks on the vertical axes are 2″. The circle indicates the size of the 850 μm JCMT beam.*

$z \sim 5-5.5$. Photometry is given in Table 5.9 and images are shown in Figure 5.9.

A2204

SMM J16327+05349: A2204 has the shallowest SCUBA map in this survey, and SMM J16327+05349 is the only source detected in the field. Within the search radius size of $8''$, two galaxies have been found, 188 and 212 with very red colours. Galaxy 188 is a lensed arc detected in all passbands from B to K. It has red photometric colours suggesting dust reddening. Galaxy 212 is more compact galaxy, which drops out in the V band and is only marginally detected R, while being detected clearly in the NIR images. Like 188, 212 has the colour of an ERO. Both galaxies are possible counterparts of the SCUBA source. Photometry is given in Table 5.10 and images are shown in Figure 5.10.

A2218

This field has been discussed in a previous paper (Knudsen et al., *Chapter 2*). Please refer to that paper for details. Here we give a brief summary of the over-

Table 5.9: *Candidate counterparts for the SCUBA source in RXJ1347-1145. cl indicates whether the galaxy falls on the red cluster sequence (1 = cluster member). p_1 indicates the likelihood of finding a galaxy with $I - K$ and K or redder and brighter at random positions (see Subsection 5.3.2). p_2 indicates the same, though also includes $J - K$.*

ID	dist ["]	$d\alpha$ ["]	$d\delta$ ["]	$B-V$ [mag]	$V-R$ [mag]	$R-I$ [mag]	$I-K$ [mag]	$J-K$ [mag]	$H-K$ [mag]	K [mag]	σ_K [mag]	cl	p_1	p_2
SMMJ13475−11459														
448	6.21	-6.19	-0.59	1.83	0.19	1.89	3.51	1.63	0.60	17.73	0.02	1	0.021	0.010
449	5.73	-2.51	5.15	0.59	-0.20	1.96	4.77	2.27	0.97	19.33	0.04	0	0.016	0.002
450	3.85	-3.57	1.44	0.51	-0.78	1.44	2.01	0.90	0.17	19.97	0.06	0	0.324	0.279
451	5.46	2.97	4.58	1.78	0.19	1.89	3.56	1.66	0.62	17.15	0.02	1	0.012	0.005
452	0.53	0.30	0.44	1.11	0.17	1.72	4.70	2.21	0.96	19.42	0.05	0	0.018	0.002
453	2.40	0.46	2.36	1.52	0.11	1.85	3.55	1.66	0.63	17.14	0.02	1	0.012	0.005
477	4.63	3.79	-2.66	0.64	-0.50	1.40	2.11	0.89	0.51	22.59	0.26	0	0.571	0.495
485	5.14	1.16	-5.01	68.57	...	...	6.37	2.18	0.74	19.94	0.06	0	0.002	< 0.001

Table 5.10: *Candidate counterparts for the SCUBA source in A2204. p_1 indicates the likelihood of finding a galaxy with $I - K$ and K or redder and brighter at random positions (see Subsection 5.3.2). p_2 indicates the same, though also includes $R - K$.*

ID	dist ["]	$d\alpha$ ["]	$d\delta$ ["]	$V-R$ [mag]	$R-I$ [mag]	$I-K$ [mag]	K [mag]	σ_K [mag]	p_1	p_2
SMMJ16327+05349										
188	2.50	2.16	-1.26	0.53	0.56	4.01	18.72	0.05	0.022	0.016
212	7.33	-5.36	-4.99	...	> 0.30	4.95	19.36	0.18	0.012	< 0.001
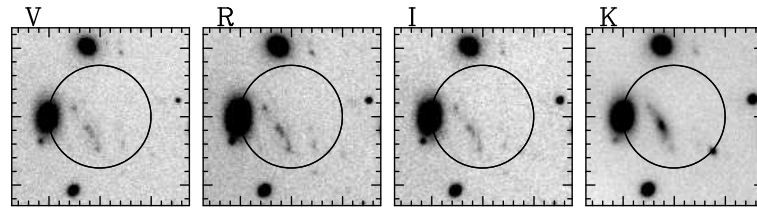
Figure 5.10: *Mosaic of the $VRIKs$ images around the SCUBA source in A2204. Each sub-image is $26'' \times 26''$ and is centered on the SCUBA source. The tick marks on the horizontal axis are distanced $1.5''$, while the tick marks on the vertical axes are $2''$. The circle indicates the size of the $850\,\mu m$ JCMT beam.*

all results. Optical and NIR imaging is available for the field along with deep ISOCAM data (Metcalfe et al., 2003). Of the SCUBA sources in the field, four have been securely identified, three have possible candidate counterparts, and two have no plausible candidate counterparts.

Securely identified: SMM J16359+66118 is a redshift $z = 1.034$ arc also detected with ISOCAM (e.g. Kneib et al., 1996; Swinbank et al., 2003). SMM J16359+6612 is a triple imaged galaxy at redshift 2.515. The galaxy is strongly lensed with a total magnification factor of 45 for all three images. The unlensed flux is $0.8\,\text{mJy}$. This galaxy is a unique opportunity to study the $\sim 1\,\text{mJy}$ SMG population, which is the population thought to be the dominant contributor to the integrated $850\,\mu m$ EBL (Blain et al., 1999a; Knudsen et al., *Chapter 3*). The galaxy has been studied in detail (Kneib et al., 2004; Sheth et al., *submitted*) and will be discussed later in this Chapter (Section 5.5).

A2597

This field has not been studied in greater detail with optical and NIR follow-up observations, hence it will not be discussed in detail. We do, however, note that the source SMM J23253−12075 is identified with the central cD of A2597, which is known to harbour an AGN (e.g., McNamara et al., 1999).

NTT Deep Field

A 1.2 millimetre map of the NTT Deep Field has been obtained with the Max-Planck Millimetre Bolometer (MAMBO) (Dannerbauer et al., 2004). In the same paper, Dannerbauer et al. also presented a VLA radio map. Optical and NIR photometry is given in Table 5.11 and postage stamp sized sub-images centered at the position of the sources are given in Figure 5.11.

SMM J12053−07441: Within a search radius of $8''$ of the detection position five galaxies are detected. None of them, however, appear as likely candidate counterparts.

SMM J12053−07448: Within the beam of SMM J12053−07448, there are four galaxies, of which one, galaxy 120, is extremely red. With $I - K = 4.28$ and $J - K = 2.26$, the estimated photometric redshift of 0.85 can be considered low. Two of the other galaxies detected within the beam were not detected in K and J, while

Figure 5.11: *Mosaic of the $BVRIJK$ images around the SCUBA sources in NDF. Each sub-image is $26'' \times 26''$ and is centered on the SCUBA source. The tick marks on the horizontal axis are distanced $1.5''$, while the tick marks on the vertical axes are $2''$. The circle indicates the size of the 850 μm JCMT beam.*

Table 5.11: *Candidate counterparts for the SCUBA source in the NDF. p_1 indicates the likelihood of finding a galaxy with $I - K$ and K or redder and brighter at random positions (see Subsection 5.3.2). p_2 indicates the same, though also includes $J - K$.*

ID	dist ["]	$\Delta\alpha$ ["]	$\Delta\delta$ ["]	z_{ph}	$B-V$ [mag]	$V-R$ [mag]	$R-I$ [mag]	$I-K$ [mag]	$J-K$ [mag]	K [mag]	p_1	p_2
SMM J12053–07441												
33	7.48	6.83	-3.05	4.32	< 0.77	1.62	0.73	< 2.68	...	> 22.15	0.635	...
37	7.63	2.93	-7.04	0.80	0.25	0.49	0.54	1.63	0.56	22.29	0.602	0.530
53	7.08	-0.97	-7.01	2.39	0.34	0.35	0.26	2.27	1.86	21.30	0.446	0.118
73	7.11	-4.12	-5.79	0.10	0.47	0.26	0.14	< 2.60	< 1.58	> 22.15	0.609	0.525
77	4.50	-3.22	3.15	0.70	1.15	0.50	0.90	< 2.95	...	> 22.15	0.694	...
SMM J12053–07448												
120	7.25	5.86	-4.27	0.85	1.40	1.13	1.17	4.28	2.26	18.93	0.022	0.003
145	3.38	1.96	-2.76	1.03	-0.32	0.66	0.99	< 2.47	...	> 22.15	0.696	...
155	1.35	-1.34	-0.14	0.84	0.12	0.77	0.91	< 2.20	...	> 22.15	0.627	...
156	5.74	-3.59	4.47	0.73	0.28	0.66	0.59	1.47	0.99	21.61	0.531	0.455
SMM J12054–07445												
222	1.13	-0.60	-0.96	0.82	0.35	0.53	0.83	1.83	1.01	20.31	0.382	0.328
265	6.38	-6.00	2.15	2.86	0.39	0.20	-0.13	< 2.77	< 1.60	> 22.15	0.696	0.614
SMM J12054–07453												
267	7.24	7.15	-1.09	1.15	0.34	1.15	0.36	4.18	1.92	20.11	0.045	0.011
284	3.47	1.90	-2.90	1.22	0.13	0.49	0.34	2.85	1.69	21.63	0.337	0.140
347	5.27	-2.00	4.88	0.16	0.64	0.47	0.08	1.31	0.82	21.46	0.517	0.452
368	1.28	-0.95	-0.87	1.25	0.60	1.20	0.85	3.85	1.73	19.80	0.054	0.020
SMM J12054–07452												
424	7.86	7.33	2.84	0.74	0.46	0.72	0.54	2.72	1.43	20.86	0.321	0.217
444	7.35	2.08	-7.05	3.29	0.88	0.25	0.10	< 2.27	> 1.31	> 22.15	0.634	0.558
464	1.76	-1.52	-0.89	4.75	1.77	1.31	1.29	1.68	0.54	21.57	0.525	0.462
465	5.03	-1.67	-4.74	0.44	0.94	0.97	0.38	1.97	0.96	21.03	0.456	0.393
469	4.04	4.03	0.34	1.16	0.19	0.51	0.49	2.76	> 2.00	21.89	0.381	0.009

galaxy 156 do not exhibit very colours. Hence galaxy 120 is the mostly likely candidate counterpart for this source.

SMM J12054−07445: Within the beam there are two galaxies. Galaxy 265 is very faint, while galaxy 222 is moderately bright, though not extraordinarily red by colour. Even though it does not exhibit very red colours, we judge this could be a possible identification.

SMM J12054−07453: Within the beam of SMM J12054−07453 four galaxies are detected. Galaxy 267 is an ERO with $I − K = 4.18$, while galaxy 368 has $I − K = 3.85$. Galaxy 368 is only 1.3″ from the SCUBA detection position, from which we judge it to be the candidate counterpart. SMM J12054−07453 is the only SCUBA source close to the MAMBO detected millimetre source MM J120522−0745.1. It is 6″ from MM J120522−0745.1, which has a radio detection. The radio detection is coincident with the submm source.

SMM J12054−07452: Within a search radius of 8″ five galaxies are detected. Four of them are not likely to be a counterpart. Galaxy 469, however, is not detected in J, which means that it has $J − K > 2.0$, which could indicate a break in the spectrum. This is then the most likely counterpart.

5.4 Spectroscopy

5.4.1 Optical VLT spectroscopy

Optical spectroscopy was obtained using FORS1 in April–July 2003 in service mode for the programme 71.A-0606(B) for the fields A1689 and RX J1347−1145. The data were obtained in Multi-Object-Spectroscopy (MOS) mode. The grism GRIS_150I+17 was used. The width of the slits was 1″, which at 720 nm gives a spectral resolution of 260. Overlap of the second spectral order may affect the wavelength region longwards of 650 nm, but was in the present case found not to affect the spectra. For each field, we obtained 12 exposures of 1225 seconds (≈ 20 min) distributed over six observing blocks, i.e. in total four hours raw observing time. The seeing was between 0.4″ and 0.83″ with an average of 0.6″ for both fields. For A1689 the field was rotated $−30°$ so the slits were aligned with a radial arc near the cluster center. For RXJ1347 the field was rotated $40°$ so the slits were aligned with the arc associated with SMM 13475−11459. The data were bias-subtracted and flatfielded. Wavelength calibration was achieved using exposures of a HgCdHeAr lamp. Observations of the standard stars CD−32°9927, LTT7379 and EG247 (Hamuy et al., 1992, 1994) were used for the correction for telluric absorption and the flux calibration. According to the DIRBE/FIRAS maps (Schegel et al., 1998) the Galactic extinction for A1689 and RXJ13474−1145 is small, $E(B − V) = 0.025$ mag respectively $E(B − V) = 0.062$ mag and thus not corrected for. At wavelengths < 350 nm and > 780 nm, the noise is very high. We trim off these parts of the spectra.

The two sources we targeted in A1689 were candidate counterparts for SMMJ13115 −01199 and SMM J13115−01208. The source we targeted in RXJ1347−1145 was the candidate counterpart for SMM J13475−11459.
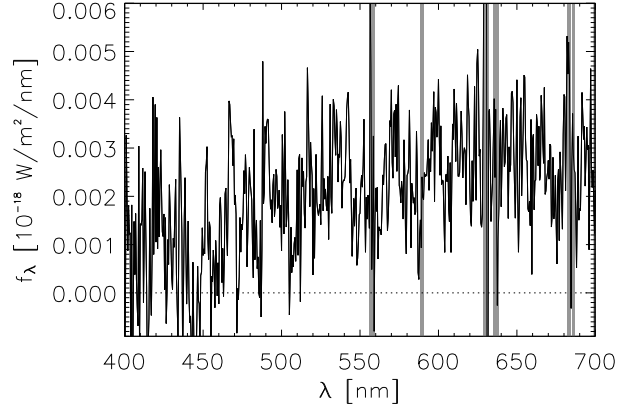
Figure 5.12: *Optical spectrum of the radial arc in A1689. The shaded areas indicate the position on bright skylines.*

SMM J13115−01199:   We obtained a spectrum for a galaxy at α, $\delta(2000)$ = $13^h11^m32.1^s$, $-01°19'55''$. The spectrum, however, shows that it is a quiescent elliptical with no sign of nuclear activity at the redshift of the cluster. Thus we conclude that this is not the underlying galaxy.

SMM J13115−01208: We have identified a radial arc at the position of this SCUBA source. The arc has two main components, which are mirrored on either side of a cluster member. The SW component was well-positioned in the slit, while the NE component was on the edge of the slit. Consequently there is less signal in the spectrum of the NE component, which also means that the integrated flux density for the whole arc is underestimated possibly by a factor two. A combined spectrum for the two components is shown in Figure 5.12. Around wavelengths ~ 450 nm there is possibly an absorption line. The spectrum does have qualitative similarities with spectra for sources in the field A2218 (see later this Section and Figure 5.14), which strongly suggests that the feature around ~ 450 nm is a Lyα absorption line. To verify this, other absorption lines must be identified. However, the signal-to-noise ratio of the spectrum does not allow for that. The possible Lyα absorption suggests a redshift of $z \sim 2.6$. If it is not a Lyα absorption line, then there are no other obvious features in the spectrum, such as Lyα emission or absorption or breaks in the continuum, which gives an upper limit for the redshift of 2.3.

SMM 13475−11459: The continuum is just barely detected. There is not enough signal in the spectrum for a reliable determination of the shape of the continuum or the identification of any lines. The lack of a strong Lyα emission line suggests that the galaxy has a redshift less than 2.3.

120

5.4.2 Keck spectroscopy

Additionally, Keck spectroscopy has been obtained for SMM J10570−03361 and SMM J10569−033610 in the MS1054−03 field and SMM J16359+6612 in the A2218 field. The spectroscopy has been presented in Kneib et al. (2004) and van Dokkum et al. (2004). Here we summarize the results.

Van Dokkum et al. (2004) obtained deep NIR spectroscopy of five DRGs in the field MS1054−03. Two of these are covered by the SCUBA map. The galaxy M-1383 has been identified as the underlying galaxy for SMM J10570−03361, while M-1356 is one of three probable candidate counterparts for SMM J10569−033610. The data were acquired for the K-band region of the NIR spectrum using NIR-SPEC at Keck II (McLean et al., 1998). Both emission lines and continuum are detected. The spectra for M-1383 and M-1356 are shown in Figure 5.13. For details on the observations, reduction and analysis of the data, see van Dokkum et al. (2004).

SMM J10570−03361: In the K-band Hα and [NII] is detected. This implies a redshift of $z = 2.423$, which is consistent with the photometric redshift in van Dokkum et al. (2003) and similar to two other galaxies in the same field.

   The galaxy has been studied in detail with respect to star formation rate and mass. Based on the Hα and the stellar SED, an extinction corrected star formation rate is $\sim 400 \, M_\odot / yr$ assuming a constant star formation rate, which is comparable to the SFR from the FIR luminosity (subsection 5.3.3). There are strong indications that the galaxy is metal rich with a metallicity comparable to the Solar abundance. The stellar mass implied by SED fits is substantial: $\sim 3.5 \times 10^{11} \, M_\odot$. The line width measured for both Hα and [NII] are $\sigma = 153 \pm 20 \, km/s$. The line broadening can be caused by regular rotation in a disk, random motions or non-gravitational effects. Rix et al. (1997) derive an empirically motivated transformation from observed line width to rotation velocity in a disk; applying their relation $\sigma \approx 0.6 V_c$ gives a rotation velocity of $255 \, km/s$. The kinematics are thus in qualitative agreement with the high mass inferred for the stars.

SMM J10569−033610: The rest-frame UV spectrum of M-1356 indicates the presence of an AGN (van Dokkum et al., 2003), with characteristics of Broad Absorption Line QSOs. The UV spectrum shows strong Nitrogen lines indicating a high metallicity. The K-band spectrum shows fairly broad Hα + [NII] emission with FWHM $\sim 2500 \, km/s$. This galaxy is not a Chandra source, consistent with the BAL nature of its active nucleus (e.g. Green & Mathur, 1996). It should be noted, that this galaxy originally was selected with a DRG criterion, however, subsequent revised photometry shows that the galaxy has $J - K = 2.13$.

   The fact that M-1356 harbours an AGN complicates the analysis of the star formation history, mass estimates etc. Estimates from SED fits give a star formation rate in the order of $100 \, M_\odot / yr$ and a stellar mass in the order of $10^{11} \, M_\odot$.

SMM J16359+6612: Deep multi-slit spectroscopy with the Low Resolution Imaging Spectrograph (LRIS; Oke et al., 1995), mounted on the Keck Telescope, was
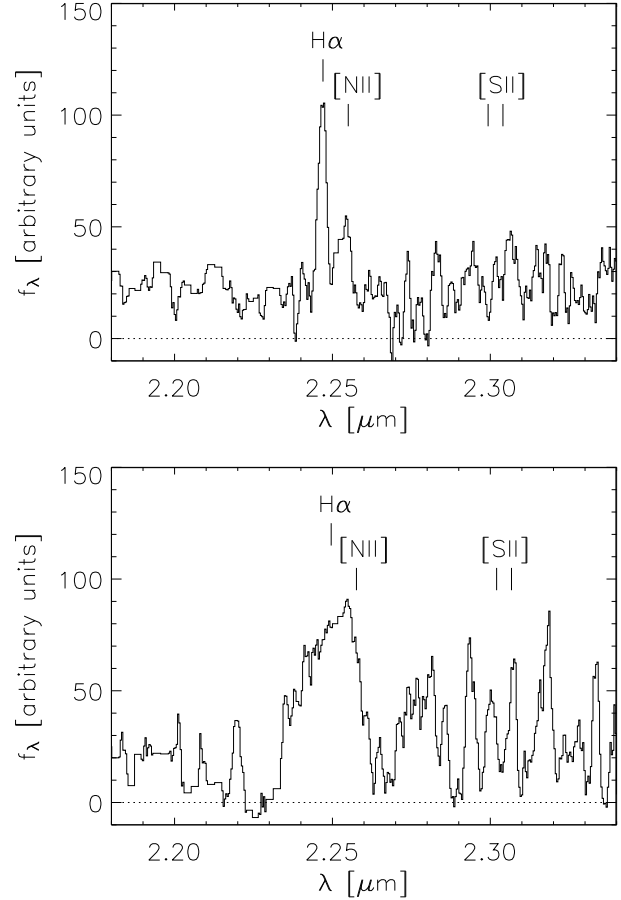
Figure 5.13: *NIR K-band spectra of M1383 and M1356 from the field MS1054−03. The spectra have been smoothed with a 5-pixel (∼ 20 Å) tophat. Top panel: M-1383 which is the identified counterpart for SMM J10570−03661. Bottom panel: M-1356, which is one of the probable candidate counterparts for SMM J10569−033610. M-1356 harbours an AGN, as is also evident from the broad emission lines.*

obtained with the aim to determine the redshift of the triple-imaged source SMM J16359+6612 in the field of A2218. Data were obtained for the Northern image, SMM J16359+66126, and for two other background galaxies in the field, namely #468 and #273. #468 is the counter image of the $z = 2.515$ arc #384 (Ebbels et al., 1996; see also Le Borgne et al., 1992). For details on the acquisition and the reduction of the spectra, see Kneib et al. (2004).

The spectra of all three galaxies show strong Ly-α absorption and numerous metal lines (Fig. 5.14). The derived redshift for SMM J16359+66126 is 2.515±0.001 based on the strongest interstellar absorption lines: OIλ1302.17Å and CIIλ1334.5Å as well as CIVλ1548.19 and 1550.77 in absorption. Likewise, the derived redshift

for #468 is $z = 2.515\pm0.001$ and 2.514 ± 0.001 for #273. All three galaxies are thus within $100\,\mathrm{km\,s^{-1}}$ of each other in the rest frame (ignoring uncertainties due to possible velocity offsets in the UV lines we use). Figure 5.14, shows the UV spectra of all three galaxies.

NIR spectroscopy in the K-band was obtained for the two counterpart images of SMM J16359+66126 and SMM J16359+66124, using the NIR spectrograph NIR-SPEC on Keck II (McLean et al., 1998). For details on the acquisition and the reduction of the spectra, see Kneib et al. (2004).

The flux-calibrated spectrum (Fig. 5.14) reveals three emission lines identified as Hα and the two weaker flanking [N$\textsc{ii}$] lines. The Hα line extends over 2.2″ for SMM J16359+66126 and 5.1″ for SMM J16359+66124, which compares well with their optical size. There are hints in SMM J16359+66126 for a more compact distribution of [N$\textsc{ii}$] emission. The Hα line is centered on 2.30755μm placing the submm galaxy at a redshift of $z = 2.5165\pm0.0015$, indicating that the UV interstellar lines used to derive a redshift in the optical are blue-shifted by $\sim100\,\mathrm{km\,s^{-1}}$ with respect to the systemic velocity of the galaxy. The rest-frame width of the Hα line corresponds to $\sim280\pm60\,\mathrm{km\,s^{-1}}$, and there is a hint of coherent velocity structure in the spectrum of SMM J16359+66124, with a velocity shift of about $220\pm60\,\mathrm{km\,s^{-1}}$ over an angular distance of 2.6 arcsec ($\sim1.5\,\mathrm{kpc}$ in the source plane). The fact that we do not see such structure in the SMM J16359+66126 image is due to only component α was in the NIRSPEC slit. Hence, this velocity shift could argue that the complex optical/NIR morphology of this source is best explained by a strong dust absorption in a rotating disc structure or better by a merger.

The total Hα line flux for the combined spectra of SMM J16359+66126 and SMM J16359+66124 is $f_{H\alpha} = 2.7\times10^{-20}\,\mathrm{W\,m^{-2}}$, with a ratio of 2.3 between their respective Hα flux densities. This corresponds to a an Hα luminosity $L_{\mathrm{H}\alpha} = 3.7\times10^{8}\,\mathrm{L_\odot}$, or a (unlensed) star-formation rate of $11\,\mathrm{M_\odot\,yr^{-1}}$. The narrow width of the Hα emission line and the observed ratio of N$\textsc{ii}$/Hα (0.3 ± 0.1) suggest that the emission is dominated by star formation, with little evidence for a strong AGN.

5.5 SMM J16359+6612: Identification of multiply-imaged faint SCUBA source

As described in Chapter 2 and Kneib et al. (2004), the source SMM J16359+6612 in A2218 has been identified with as a multiply-imaged galaxy, with the three images being SMM J16358+66121, SMM J16359+66124 and SMM J16359+66126. Spectroscopy was present in the previous section. Here follows an analysis and discussion of SMM J16359+6612.

The occurrence of a submm source falling within the caustic lines of a massive foreground gravitational lens provides unique constraints on the properties of this faint submm galaxy. Using the cluster mass model we estimate that the background galaxy is gravitationally amplified by a factor of 45 (integrated across all three images), indicating that the intrinsic $850\,\mu$m flux density of this galaxy would be 0.8 mJy in the absence of gravitational amplification, while in the optical and NIR the galaxy would have magnitudes $I_{814} = 26.1$ and $K_s = 22.8$. The
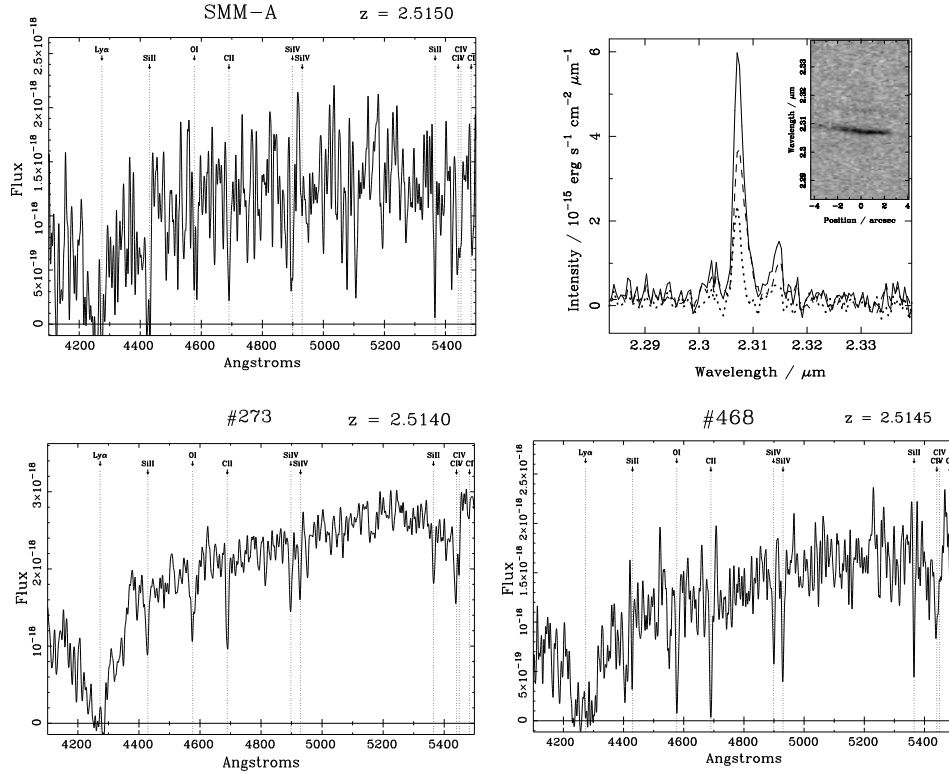
Figure 5.14: *Spectroscopic identification of the three z ≈ 2.515 galaxies behind A2218 from the LRIS spectra: top left: SMM J16359+66126, bottom left: #273 and bottom right: #468. Note the similar UV fluxes of the three galaxies, even though they have very different submm luminosities, and by implication very different total SFRs. The three spectra have been rebinned to the same spectral resolution of 2Å and the wavelength scale is in the observed frame. The flux is given in units of erg/s/cm²/Å. Top right: Keck/NIRSPEC K-band spectrum of SMM J16359+66126 (dotted), SMM J16359+66124 (dashed) and the sum of SMM J16359+66126 and SMM J16359+66124 (solid) showing the redshifted Hα and N\textsc{ii} emission lines. The inset shows the 2-d region of the spectrum around the Hα line in SMM J16359+66124, demonstrating the extended spatial morphology of the emission line and the presence of a gravitationally amplified velocity gradient within this image.*
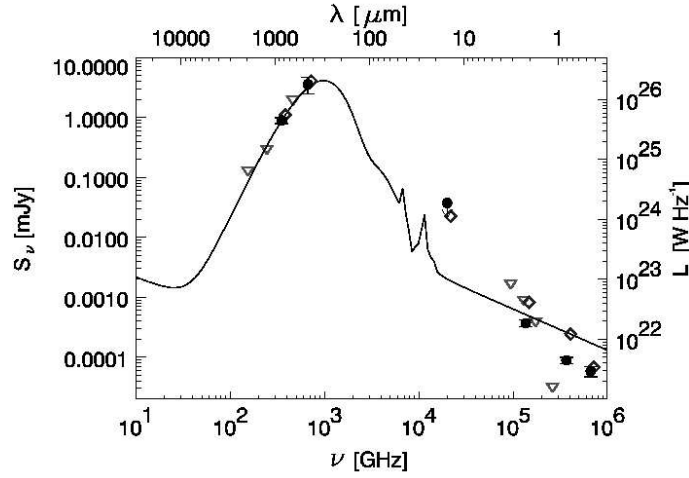
Figure 5.15: *The observed Spectral Energy Distribution (SED) of the multiply-imaged submm galaxy SMM J16359+6612 (solid points with error bars) compared to Arp 220 (solid line, composite spectrum from Anantharamaiah et al. (2000), Klaas et al. (1997), Lisenfeld et al. (2000) and Surace et al. (2000)) which is 1.5 times more luminuous in the FIR, as well as the well-studied submm galaxy SMM J02399−0136 (diamonds, at $z = 2.8$, Ivison et al. (1998)) which is 10 times more luminuous in the FIR, and the ERO HR10 (open triangles, at redshift $z = 1.44$, Dey et al. (1999)), which is 7 times more luminuous in the FIR. All SEDs are redshifted to match that of SMM J16359+6612 and scaled so they have a similar far-infrared luminosity. Notice the relatively large variation of L_{FIR}/L_{opt} between the different galaxies.*

galaxy therefore represents a serendipitously positioned example of the submm galaxy population at flux levels of $\sim 1\,mJy$, the population which produces the bulk of the submm background (Blain et al., 1999a). This provides an unique opportunity to compare the properties of this low-luminosity submm galaxy with those of more luminous, submm galaxies studied in brighter, blank-field surveys (e.g. Ivison et al., 2002; Chapman et al., 2003).

In our assumed cosmology the FIR luminosity of SMM J16359+6612 is $1.0 \times 10^{12}\,L_{\odot}$, roughly 1.5 times fainter than Arp 220, close to the border-line between luminous infrared galaxies and ultraluminous infrared galaxies (ULIRGs). The star formation rate derived from the far-infrared luminosity is about $500\,M_{\odot}\,yr^{-1}$. Figure 5.15 compares the restframe (lens-corrected) SED of the SMM J16359+6612 to the SEDs of Arp 220, the well-studied $z = 2.8$ submm galaxy SMM J02399−0136 and the redshift $z = 1.44$ ERO HR10 (Dey et al., 1999), which is also detected at submm wavelengths. The L_{FIR}/L_{opt} ratio is higher than that seen for Arp 220, suggesting it is more obscured, and similar to the high-redshift, but much more luminous, SMM J02399−0136 (Ivison et al., 1998).

In Figure 5.16 imaging of the triple-imaged source is shown. The Figure is a greyscale reproduction of a colour mosaic presented in Kneib et al. (2004). In

the HST optical and ground-based NIR imaging the morphology is evident: The galaxy consists of three components, here labeled α, β and γ. α and β appear blue, while γ appears to be red. In the images of SMM J16359+66124 and SMM J16358 +66121 γ is the central part.

At $z = 2.515$ the spatial sampling of the *HST* images, corresponds to ~ 0.1 kpc, taking into account the gravitational magnification. Thus the colour gradient within the background galaxy is on 1–2 kpc scales – similar to the obscured region in nuclear starbursts in ultraluminous infrared galaxies at the present-day. A constraint on the size of the submm emission region is obtained by subtracting point sources from the 850 and 450 μm maps. This procedure leaves no detectable residual of extended emission, indicating that to our measurement accuracy we are dealing with point sources. The tightest constraint is obtained at 450 μm where we find that the intrinsic extent of the emission is less than $4''$, which corresponds to ~ 8 kpc. There is thus no indication for a highly extended obscured starburst in this relatively low-luminosity submm galaxy.

The precise redshift we have measured for SMM J16359+6612 (see previous Section) enables us to identify that this galaxy lies at an identical redshift to that of #273 and the #384/#468 system. Using the lens model we estimate that SMM J16359+6612 lies between the #384/#468 and #273 galaxies in the source plane, and all three galaxies are less than 130 kpc apart. If these galaxies were not magnified by the cluster lens, all three galaxies would appear within a radius of $8''$. Moreover, we can place a limit of $\lesssim 100$ km s^{-1} on the possible velocity offset between these three galaxies. They are thus all part of a single group and it is likely that they are interacting, which may explain the activity we detect in the submm waveband. The strong clustering of the submm galaxies with UV-bright populations highlights the opportunity for measuring the distances to submm galaxies from the redshifts of less-obscured companions, as well as the possible confusion which may arise when trying to relate UV- and submm-selected populations, in the absence of precise positions from radio counterparts.

SMM J16359+6612 has much redder colour in $(V - I)$ and $(I - K)$ than the two other nearby UV-selected galaxies, confirming the dustier nature of this galaxy. If we compare the unlensed star formation rate (SFR) for this three systems, we find based on their UV continuum that: SMM J16359+6612: 6 M$_\odot$ yr^{-1} (although certainly underestimated due to dust extinction) #468: 14 M$_\odot$ yr^{-1} and #273: 4 M$_\odot$ yr^{-1}. For SMM J16359+6612 we can compare the three estimates of its amplification-corrected star formation rate: 6 M$_\odot$ yr^{-1} from its dust-corrected UV luminosity, 11 M$_\odot$ yr^{-1} from the Hα flux (uncorrected for extinction or aperture losses) and 500 M$_\odot$ yr^{-1} based on the far-infrared emission. Applying the median extinction correction derived for mid-IR selected luminous infrared galaxies at $z \sim 0.7$ by Flores et al. (2004), $A_{H\alpha} \sim 2.1$, and a modest correction for slit losses would increase the Hα-derived star formation rate by a factor of $\sim 10\times$. These results suggest the vast majority of the young stars in this galaxy are obscured by dust and are undetectable in the restframe far-UV. Although it is $10\times$ less luminous than the typical submm-selected galaxy studied in blank-field surveys, this system shares the same extreme levels of obscuration seen in the more luminous galaxies, rather than the more modest dust obscuration infered for the somewhat less luminous
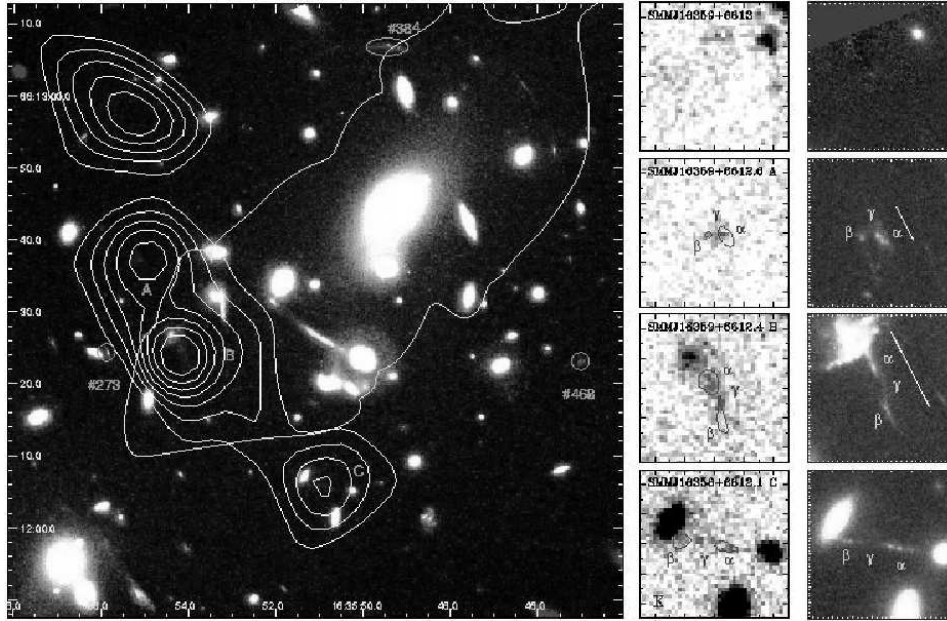
Figure 5.16: *(Left) (This is the greyscale version of the true-colour image presented in Kneib et al., 2004.) A true-colour image of the core of A 2218 composed from the HST F450W (blue), HST F814W (green) and WHT/INGRID K_s (red) images. The 850 μm submm image from SCUBA is overlayed as white contours at flux densities of 2.5, 3.3, 5.0, 6.6, 8.3, 10 mJy beam^{-1}. The three images of the multiply-imaged submm galaxy are annotated as A, B and C. We also identify the 2 other galaxies at $z \sim 2.5$, namely the single-image #273 and the fold-image #384 and its counter-image #468. The yellow line shows the critical line at $z = 2.515$. (Right) Panel of $10'' \times 10''$ images showing the IN-GRID K_s-band (left column) and HST true colour image from F450W/F606W/F814W (right column) of the four submm sources in the core of A 2218. The resolution of these frames is $\sim 0.75''$ and $\sim 0.15''$ respectively. The K-band panels are centered on the submm source, and the colour HST panels are centered on the identified optical counterpart. The contours on the K_s frames show the morphologies of the galaxy in the F814W pass-band at the resolution of the K_s-band frame. Note how each of the submm sources, SMM J16359+66126, SMM J16359+66124 and SMM J16358+66121, comprises a NIR source (γ) which is bracketed by two features in the F814W image (α and β). The morphological and photometric similarity of these three objects suggests that they are all images of the same background source. For SMM J16359+66126 and SMM J16359+66124 we have indicated in their HST true colour image the extent of the Hα line observed in the NIRSPEC data (white segments). Note that there is a very faint red counterpart for the SMM J16359+66130 in the F814W image that does not appear in the K-band data, and that all the bright galaxies near SMM J16359+66124 and SMM J16358+66121 are spectroscopically confirmed cluster members (SMM J16359+66124 is next to a star forming galaxy, and SMM J16358+66121 is next to three elliptical galaxies). In all the images North is up and East is to the left.*

UV-selected galaxies at these redshifts. We also note that the Hα line width and velocity structure, if they reflect the dynamics of the galaxy, suggest that this system is more massive for its UV luminosity than typical UV-selected galaxies at this epoch (Erb et al., 2003).

SMM J16359+6612 has recently been detected in CO (Sheth et al., 2004). The CO (J=3-2) fluxes are 1.2, 3.5 and 1.6 Jy km/s for the three components, i.e. in total 6.3 Jy km/s, which after correcting for the lensing corresponds to a molecular gas mass of 2×10^{10} M$_\odot$ (assuming a Galactic CO-H$_2$ conversion factor).

5.6 Connection between SMGs and other high-*z* populations

Studying the connection between SMGs and other galaxy populations, is done not only through the identification of the underlying galaxies (see previous sections), but also through determining the submm emission from defined classes of galaxies such as the Lyman Break Galaxies (LBGs) and EROs. When the SMGs were first discovered, the relation between these and other star forming galaxies at high redshifts became a subject of study. Attention was given to the connection between SMGs and LBGs. The conclusions in general have been that the contribution of LBGs to the 850 μm EBL and the overlap with securely identified SMG counterparts is limited (Chapman et al., 2000; Webb et al., 2003b), thus they are not the dominant population giving rise to the SMG population. More recent studies point in the direction of a significant contribution to the SMG population from galaxies with red photometric colours. Given the very deep data from the field MS1054−03 we have performed a statistical analysis to study the overlap between the SMG population and EROs and DRGs. In the following we first summarize the results on the LBG-SMG studies and subsequently present the work on the connection between the SMGs and EROs/DRGs.

5.6.1 Submillimetre – Lyman Break Galaxy connection

In a study Chapman et al. (2000) obtained SCUBA photometry for 16 $z \approx 3$ LBG galaxies. Of these, only one galaxy, Westphal-MMD11 (W-MMD11), was detected at 850 μm with a flux of 850 μm = 5.5±1.4. W-MMD11 has a red photometric colour of $R - K \sim 4.6$ mag. At a 1σ sensitivity of ~ 0.5 mJy none of the others were detected. Chapman et al. (2000) estimate that the $z \approx 3$ LBG population contributes 0.2 % to the 850 μm EBL, and argues that a larger contribution from $z \sim 4$ LBGs should not be expected.

Webb et al. (2003b) did a study for three different LBG samples in the CUDSS fields; two are a samples from the Canada-France Deep Field (CFDF; Foucaud et al., 2003) and one is from C. Steidel and collaborators. They find a $\sim 2\sigma$ detection for the CFDF samples, while the result for the Steidel et al. sample is identical to zero. Upper limits to the contribution to the 850 μm EBL are given: for the CFDF samples, which cover a redshift range of $2.9 < z < 3.5$, upper limits are 2.8-3.2 %, while for the Steidel et al. sample, which cover a redshift range of $2.4 < z < 3.4$, the upper limit to the contribution is 5.1 %. Webb et al. (2003b) also estimated an upper limit including LBGs at redshifts $1 < z < 5$, assuming that the LBGs

have a constant comoving number density in that range, and found that the total contribution to the 850 μm is less than 20 %.

Based on the deep jiggle map from the Hubble Deep Field (Hughes et al., 1998), Peacock et al. (2000) made a statistical analysis of the contribution of optically selected starburst galaxies at high redshift. Peacock et al. (2000) constructed synthetic maps through assuming a value of the dust emission based on the UV flux for the high-z starburst galaxies and using that to generate a map with the same resolution as SCUBA 850 μm maps and compare the angular structure. They find an average detection of 0.2 mJy assuming a UV star formation rate of $1\,M_\odot\mathrm{yr}^{-1}$ and estimate that this population of galaxies contributes at least 25 % of the 850 μm EBL. This result is on the higher side, compared to the works of Chapman et al. (2000) and Webb et al. (2003b). That is not unexpected, as the optically selected high-z starbursts satisfy a broader selection criterion, which selected more galaxies than the LBG criterion.

While there can be no doubt that some submillimetre emission arises from the LBG population, the studies mentioned above clearly show that the LBG population is not the dominant underlying population giving rise to the SCUBA detected SMG population or the dominant contributor to the submm EBL. A small number of LBGs have been detected individually in the submm, of which W-MMD11 is probably the best known. There is some suggestion that these LBGs have very or extremely red colours. Shapley et al. (2001) found in a detailed optical and NIR study of $z \sim 3$ LBGs, that the LBGs, which are intrinsically more luminous appear to be more dusty. They find that there is a strong correlation between extinction and the age of the star formation episode with the younger galaxies being more dusty and having much higher star formation rates.

5.6.2 Submillimetre – red galaxy connection

A majority of the securely identified SMGs have very red counterparts. That leads to the question, what is the submm emission from very red galaxies, and what is their contribution to the 850 μm EBL. The question has been addressed in two previous works, by Wehner et al. (2002) and Webb et al. (2004), who studied EROs with $I - K > 4$ and $R - K > 5.3$. In Wehner et al. (2002), three cluster fields from the UK-SCUBA Lens Survey were used. Their analysis included K observations to a depth of 21.25 mag (21.6 mag after correcting for gravitational lensing). They find that EROs contribute to about half of the 850 μm EBL. In Webb et al. (2004), the CUDSS fields were studied using K-band imaging to a depth of 20.7 μm. They find that EROs, contribute with about 10% to the 850 μm EBL.

We here address the same question, using the data from the field MS1054-03. The data is the deepest NIR taken for a cluster field, with a depth of $K_{lim} =$ 23.8 mag. We here do a statistical study of the emission from both EROs selected to have $I - K > 4$ and DRGs with $J - K > 2.3$. Though there is a big overlap between the EROs and DRGs, the main difference in selection criterion is that the DRGs have been tuned to select galaxies at redshift $z > 2$, that are either dust reddened starforming galaxies or where the Balmer-break falls between the J and K.

The statistical measurement of the submm emission from EROs and DRGs is

done by measuring the value in the 850 μm map at the position of each of the galaxies. As the sensitivity is not uniform across the field, we determine the weighted mean, weighted by the uncertainty at the position. We only consider the galaxies present in the area covered by the SCUBA map. Webb et al. (2004) discussed a possible bias due to confusion. If two or more EROs are within the 850 μm beam from one another, emission might be counted twice. This can be corrected for by estimating the flux contribution from each of the close-by EROs to the flux measured at the given position. Webb et al. (2004) have demonstrated that correcting for this confusion of sources can make a significant difference between an uncorrected and corrected result by up to 20 %. We find that this effects our measurements by $\sim 2-10\%$, Furthermore, we know that for five of the SMGs in the field EROs and DRGs are the most likely identification; seven EROs and four DRGs. We calculate the mean 850 μm flux, both including and excluding those objects. Results are given in Table 5.12. We use the weighted mean and standard deviation. The weighted mean compared to the unweighted mean only changes the result by a few percent, which means that the result is not dominated by a few measurements with high weight. We study three different cases, $I - K > 4$, $J - K > 2.3$ and these two in combination. In each case we find a detection which is more than 4σ. We find that the average 850 μm flux of the DRGs is 1.10±0.21 mJy and is larger than that of the EROs at 0.83±0.17 mJy. The mean flux is even larger for the overlapping population of EROs and DRGs, with a mean 850 μm flux of 1.27±0.31 mJy. We also calculate the mean flux for the EROs that do not overlap with the DRGs: The mean flux is 0.76±0.20 mJy. Excluding the EROs and DRGs which have been identified with bright SMGs, the mean 850 μm flux is reduced by 20-37 % to ~ 0.8 mJy. For the EROs and the DRGs the detection is still above 3σ, but for the ERO+DRG population, the mean flux is comparable to the ERO and DRGs apart, but the number of sources is too small to bring down the uncertainty on the mean. Likewise, the mean flux for the ERO population not overlapping with the DRGs goes down to 0.5 mJy with a 2.5σ detection. While avoiding bright SMGs does make a difference in the result, removing the two brightest and two faintest points from the statistics makes a difference of no more than a ±3 %. We note that the completeness of the imaging data might introduce some uncertainties.

To test the reliability of the detection of the mean 850 μm flux from the EROs and DRGs, Monte Carlo simulations were performed by dropping SMGs at random positions in the field and repeat the statistical measurements. The MC simulations were repeated 10000 times. As with the real data, the MC measurements were corrected for the confusion of two or more sources within the distance of a beam from each other. The positions of the five SMGs with EROs/DRGs being the most likely counterpart were not removed. The area of five beams is about $\sim 1.4\%$ of the total area of the map. This might bias the MC towards a larger possibility for getting a signal at random positions. For 45-50 random positions on the map, the weighted mean is 0.13±0.17 mJy, with 2.4 % chance for getting a $> 3\sigma$ detection at random positions, 0.2 % chance for getting a $> 4\sigma$ detection, and 0.02 % chance for a $> 5\sigma$ detection. A similar result is seen for 20-30 and for 10-20 random positions. Thus we conclude that the detected mean 850 μm flux per ERO/DRG is a real

Table 5.12: *Results of the statistical analysis of 850 μm emission from EROs and DRGs.*

Criterion	N	Mean S_{850} [mJy]	Stand.dev. [mJy]	Contribution to EBL [Jy / deg^2]	Relative Contribution F98	P96
$J - K > 2.3$	32	1.10	0.21	9.6	21.9%	31.1%
Same excl. DRGs with bright SMGs	28	0.84	0.23	6.1	14.0%	19.8%
$I - K > 4$	52	0.83	0.17	12.1	27.5%	39.0%
Same excl. EROs with bright SMGs	45	0.66	0.18	8.5	19.4%	27.6%
$I - K > 4, J - K > 2.3$	15	1.27	0.31	5.2	11.8%	16.7%
Same, excl. ERO+DRGs with bright SMGs	11	0.80	0.35	2.5	5.6%	7.9%
$I - K > 4, J - K < 2.3$	37	0.76	0.20	7.7	17.6%	25.0%
Same, excl. ERO-DRGs with bright SMGs	34	0.53	0.21	5.5	12.4%	17.6%
$I - K > 4, K < 20.7$	28	0.47	0.23	3.1	7.2%	10.2%
Same, excl. EROs with bright SMGs	25	0.24	0.24	0.9	2.0%	2.9%
$I - K > 4, K < 21.6$	37	0.92	0.20	10.0	22.6%	32.1%
Same, excl. EROs with bright SMGs	33	0.65	0.21	15.0	15.0%	21.3%
$J - K > 2.3, K < 21.7$	14	1.60	0.34	6.3	14.3%	20.2%
Same, excl. DRGs with bright SMGs	11	1.13	0.39	3.6	8.1%	11.5%

Note:- F98 = Fixsen et al. (1998), P96 = Puget et al. (1996).

detection.

For visualisation, postage stamp sized sub-images of $31'' \times 31''$ were created by stacking together sub-images from around the position of each ERO or DRG. Similarly, we did the same for random MC realisations. The images are shown in Figure 5.17. In the final, weighted average, sub-images the appearance of a source is clearly seen, while in the MC sub-images, which have been plotted with the same levels of grayscale, there is no sign of a signal.

The contribution to the $850\,\mu$m EBL, is calculated by summing up the flux at the positions of the EROs and DRGs, and dividing by the area of the field. The integrated flux contributing to the $850\,\mu$m is compared to the values derived from the COBE satellite: 44 Jy/deg^2 (Fixsen et al., 1998) and 31 Jy/deg^2 (Puget et al., 1996; henceforth this is the value given in parentheses). The contributions from the EROs and DRGs are listed in the Table 5.12. We find that the EROs have the largest contribution of 27.5 % (39%), compared to the EBL value from Fixsen et al. (Puget et al.). Even though the EROs have a smaller mean $850\,\mu$m flux, this is not a surprising result, as they have a large surface density. The contribution from the DRGs is 21.9 % (31.1%), which is a bit lower than that of the EROs. The contribution from the ERO-DRG overlapping population is smaller though not negligible, 11.8 % (16.7%). This suggests that the DRG population is brighter than the ERO population at submm wavelengths, however, the larger surface density of the EROs makes the EROs an equally important contributor as the DRGs to the integrated $850\,\mu$m EBL.

For comparison with the works of Wehner et al. (2002) and Webb et al. (2004), we have also determined the mean $850\,\mu$m flux from the EROs including a cut on the K-magnitude chosen to match the depths of their surveys. The result of this is also given in Table 5.12. Applying a magnitude cut of $K < 20.7$ mag, we find a mean flux of 0.47 ± 0.23 mJy and a contribution to the $850\,\mu$m EBL of 7.2 % (10.2%). This is comparable to the results from Webb et al. (2004), who finds a mean flux of 0.40 ± 0.07 for the $I - K > 4$ EROs and contribution to the EBL of 7-11 %. Excluding the EROs identified with SMGs, the mean flux is reduced to 0.24 ± 0.24 mJy, which is also in agreement with Webb et al.'s (2004), that the mean flux is dominated by the EROs associated with SMGs. Applying a magnitude cut of $K < 21.6$ mag, we find a mean flux of 0.92 ± 0.20 mJy and a 22.6 % (33.1%) contribution to the EBL. This is less than that of Wehner et al. (2002), who finds a mean of 1.58 mJy and contribution of 43 % (61%) to the integrated $850\,\mu$m EBL. The large discrepancy is probably due to different issues, one being, that the surface density of EROs in the fields studied by Wehner et al. is very large compared to the surface density of the EROs in the MS1054$-$03 field and also that of the CUDSS fields, because of the cosmic variance.

In Figure 5.18, we have plotted the surface density of the EROs and DRGs. For comparison we have also plotted the surface density from the CUDSS fields (Webb et al., 2004), indicated the surface density for the fields from Wehner et al., and the ERO surface density as found in a study by Roche et al. (2003). The three fields studied by Wehner et al. includes A2390, which appears to have an over-density of EROs. At $K < 21.6$ mag, the surface density averaged across the three fields is 8 ± 1.4 arcmin^{-2}, which is a factor 2 larger than that of the other studies. Exclud-

132
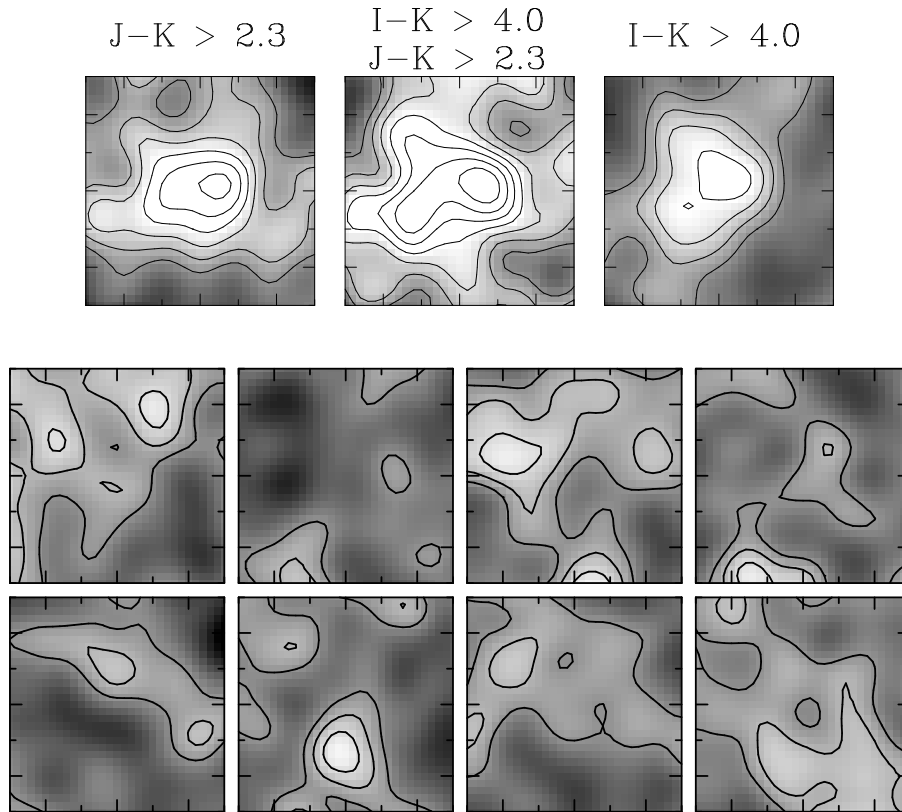
Figure 5.17: *Postage stamp sized sub-images from the statistical stacking analysis of the EROs and DRGs in the field MS1054−03 and the Monte Carlo simulation. The upper panel of three sub-images shows the real data, after stacking 31″×31″ sub-images centered at the position of the EROs and/or DRGs. The images represent a weighted mean. The overlayed contours represent a mean 850 μm flux of 0.0,0.2,..,1.2 mJy. The lower panel of eight sub-images are results from the Monte Carlo simulations stacked at random positions. The sub-images have been treated in the same way as mentioned above, i.e. they are weighted average sub-images. These eight sub-images are purely for illustration purpose to show examples of the results from randomly chosen positions. The levels of the greyscale of sub-images from random positions is the same as that of the ERO/DRG sub-images. Contours are also the same.*
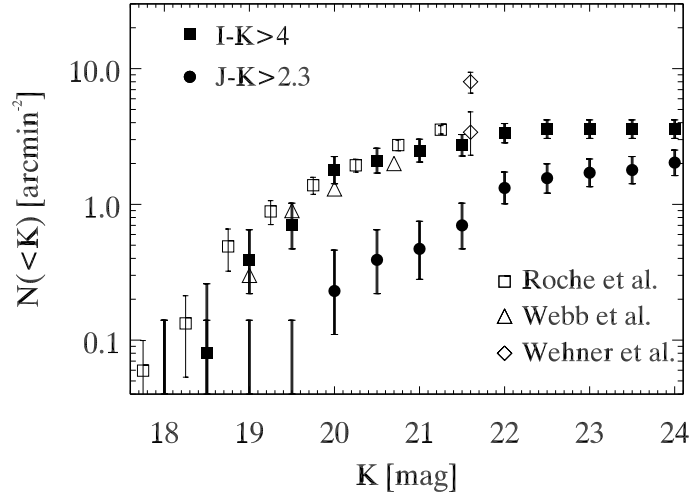
Figure 5.18: *The ERO and DRG surface density as function of K for MS1054−03 for the area, which has been covered by the SCUBA observations. The error bars are based on Poisson statistics (Gehrels, 1986). The surface density determined for the full area covered by the FIRES project for DRGs is 1 arcmin^{-2} at $K < 21$ (Förster Schreiber et al., in prep), where the difference possibly is due to the clustering of the DRG population. For comparison with other ERO projects, the results from Roche et al. (2003) has been plotted (open square). Furthermore, the surface density for the two other projects also studying the submm properties of EROs has been added: triangles represent Webb et al. (2004), where the ERO population was studied to a limiting depth of $K = 20.7$ mag, and diamonds represent Wehner et al. (2002), where the limiting magnitude after correcting for gravitational lensing was $K = 21.6$ mag. For Wehner et al. (2002) the surface density has been plotted including and excluding that of the field A2390, in which an overdensity is present.*

ing A2390, the surface density is $3.4^{+1.4}_{-1.1}$ arcmin^{-2}, which is comparable to other studies. Another issue, why the results from Wehner et al. are higher than that of this study and the one of Webb et al., is related to the surface density: Wehner et al. do not correct the flux of possibly confused sources. As a bright signal might be counted more than once, this will bias the result towards a larger mean flux. Given the large surface density, this can be a problem, as the average separation of the individual EROs will be less, thus increasing the chance for finding two or more EROs within the distance of a beam. Finally, we also determine the mean submm flux for DRGs with $K < 21.7$ for comparison with the work of Förster Schreiber et al. (2004), who analysed this population. Förster Schreiber et al. find that the DRG population is dominated by significantly older, more obscured and more massive stellar populations compared to LBGs at similar redshifts and similar rest-frame V-band luminosities. DRGs with $K < 21.7$ have the highest mean 850 μm flux determined in this analysis with a weighted mean of 1.60±0.34 mJy.

As discussed above for the individual cases and as given in Table 5.12, we

have also calculated the mean flux for each of the cases when excluding the EROs and/or DRGs associated with SMGs. For essentially all the cases, we find that the mean flux goes down, but there is still a signal, except for the case of EROs with $K < 20.7$. This suggest that in the group of bright EROs the submm emission originates from a few sources.

Even though the mean flux and the total contribution to the EBL has been found large in the study by Wehner et al., it is remarkable that all three works, i.e. the present, Webb et al. and Wehner et al., all find a significant detection of $850\,\mu m$ emission from the EROs. The numbers are also considerably larger than those determined for the LBG population, which in combination with the fact that many of the securely identified counterparts have ERO and/or DRG properties, strongly suggests that the EROs and DRGs are intimately linked with a significant fraction of the SMG population.

The dominant contribution to the $850\,\mu m$ EBL arises from SMGs with fluxes $0.5-2$ mJy (Knudsen et al., in prep; Chapter 3). The mean $850\,\mu m$ flux of the EROs and DRGs falls within that flux interval. The surface densities of EROs and DRGs is comparable to that of the number counts for SMGs with $S_{850} \sim 0.5-1$ mJy: The number counts are $N(> 1\mathrm{mJy}) \sim 10^4\,\mathrm{deg}^{-2}$ ($\sim 2.8\,\mathrm{arcmin}^{-2}$) and $N(> 0.7\mathrm{mJy}) \sim 1.5 \times 10^4\,\mathrm{deg}^{-2}$ ($\sim 4.1\,\mathrm{arcmin}^{-2}$), respectively. This suggests that a significant fraction of the $S_{850} = 1 \pm 0.5$ mJy submm sources arises from the ERO and DRG populations.

The fact that the surface density of EROs is larger than that of DRGs is not surprising, as the ERO $I - K > 4$ criterion selects galaxies with $z > 1$ and thereby probe a larger volume that the DRGs, which with the DRG $J - K > 2.3$ criterion selects galaxies with $z > 2$. It is important to notice, that even though the mean $850\,\mu m$ flux of the DRGs is slightly larger than that of the EROs, the larger surface density of the EROs make them a significant contributor to the EBL.

Above we argue that at least the faint submm population, $S_{850} \sim 1$ mJy, is linked with the EROs and/or DRGs. This leads to the expectation that many of the detected SMGs should have EROs and/or DRGs as the underlying galaxy (especially those with $S_{850} < 2$ mJy). The data from the MS1054$-$03 field is the deepest and most comprehensive data set for a galaxy cluster to date. As can be seen in Figure 5.18, the surface density of the EROs flattens for K fainter than ~ 22 mag, while the surface density of DRGs flattens only at much fainter $K > 24$ mag. Consequently, deep K-band imaging, $K_{lim} > 20$ mag, is a necessity to reliably probe the EROs and DRGs, which can may be associated with SMGs.

5.7 Discussion

Here follows a brief discussion of the general results from the identification of the SCUBA sources. Of the 58 sources in the Leiden-SCUBA Lens Survey 48 have been studied with multiwavelength data, especially with optical and NIR imaging. Of the 48, we find 14 (30 %) sources with securely identified counterparts or very high probability identifications. 17 (35 %) sources have one or more likely counterparts, and 17 (35 %) have no likely counterpart. ~ 85 % of the candidate counterparts are very or extremely red. This is in good agreement identifications for other surveys

(Fox et al., 2002; Webb et al., 2003b; Smail et al., 2002). The field MS1054−03 has the best statistics with 5 most probably or securely identified sources and three with multiply possible candidates, while only one has no detected possible counterpart. The field A2218 has four securely identified sources, for which three of these have been identified with a multiply-imaged galaxy. Furthermore, there are one or more candidate counterparts for three, while two have no obvious candidate counterparts. The field NTT Deep Field also has good statistics with one most probable counterpart, three likely and only one with no obvious candidate counterpart. The fields A2204 and RX J13457−1145 each have one SCUBA source for which there are two plausible candidate counterparts per source. Both have an arc and a more compact object within the search radii. The fields Cl0016+16, A478 and A496 have significantly more unidentified sources. The number of identifications is related to the quality of the data. The fact that all but one source in MS1054−03 has one or more candidate counterparts demonstrates the necessity of the deep imaging across multiple passbands, especially NIR.

For four of the securely identified sources, we have spectroscopic redshifts: $z = 2.423$, 2.515, 2.84 and 1.034. The first two are galaxies with no sign of AGN activity, the third is the quasar in A478, and the last is an ISO detected galaxy. Photometric redshifts for other most probable counterparts are essentially all > 2. As the sample of identified counterparts with spectroscopic observations is so limited, it is difficult to draw conclusions. It should be noted, though, that these galaxies appear to be massive systems based on the optical and NIR observations and supported by CO detections.

Chapman et al. (2003) presented identifications and spectra of ten radio-selected submm sources. Eight of these have redshifts, where Lyα is detected in the spectra. For all of them Lyα is detected in emission. Comparing that to our results, based on a small number, the securely identified sources do not have Lyα in emission (except for the quasar SMM J04135+10277). This suggests a difference in the nature between the bright ($S_{850} > 5$ mJy) radio-selected SMGs and the faint ($S_{850} < 5$ mJy) optically/NIR identified galaxies. This highlights the importance in studying both populations in order to determine the nature of the SCUBA sources.

We compare the 850 μm with K and $I - K$ colour for the identified counterparts. This is shown in Figures 5.19 and 5.20, which includes the data for the SMGs with securely identified counterparts and possible candidate counterparts. If more candidate counterparts have been identified, we choose the source with the smallest likelihood of been a chance superposition.

K vs. 850 μm: The submm faint galaxies, $S_{850} < 1$ mJy, typically do not have NIR bright counterparts (i.e., $K > 22.5$ mag). A similar trend is noted by Smail et al. (2002). This is possibly a selection effect due to the exceptionally strong lensing. We do not see a correlation between S_{850} and K, which is in agreement with the results from Webb et al. (2003b) and Smail et al. (2002). We speculate briefly on the interpretation of the lack of an obvious correlation between K and S_{850}. Based on the $K - z$ relation for radio galaxies and a similar work by Serjeant et al. (2003) for SCUBA sources, we assume that the K-magnitudes contain information about the distance to the sources. No correlation between K and S_{850} would then imply that

136
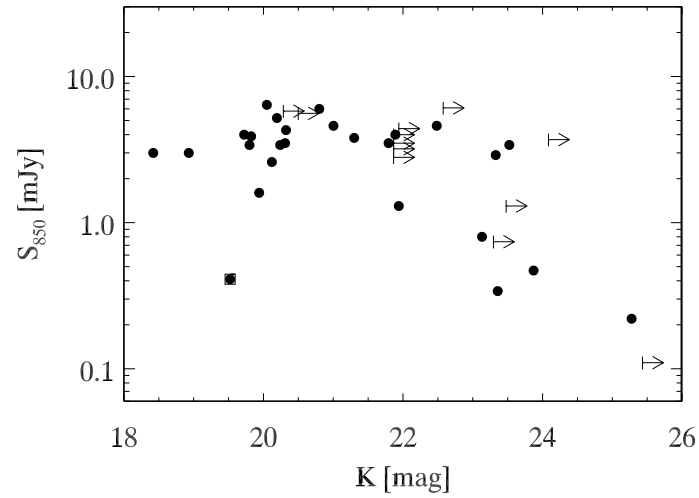
Figure 5.19: *850 μm flux against K for the identified or possibly identified sources. The filled circles indicate the SCUBA sources with K measured. The arrows indicate upper limits for possible identifications and for sources without identifications. The square indicates the $z = 1.034$ source in A2218, which has also been detected with ISOCAM.*
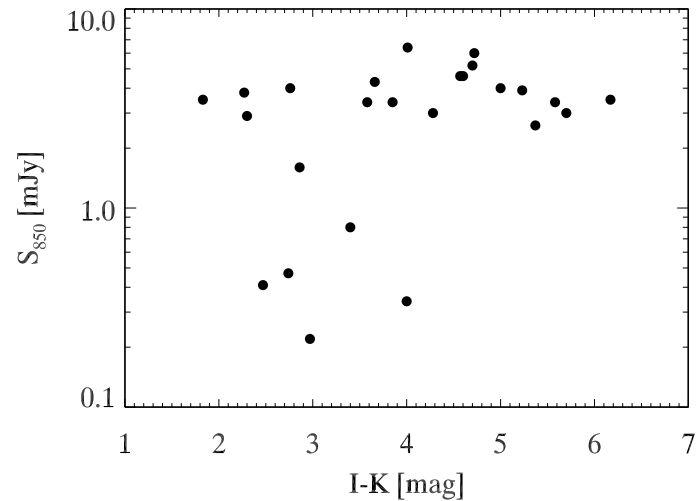
Figure 5.20: *850 μm flux against $I - K$ for the identified or possibly identified sources.*

there is no evolution with time. Given the scatter in the $K - z$ relation, this can only be confirmed when including the redshift information for all the sources. Alternatively, we may assume that the K-magnitude is related to the dust extinction of the underlying galaxies. As K probes the redshifted optical stellar light, if a or large part of the galaxy would be embedded in the dust from where the submm

137

emission originates, an anti-correlation would be expected between K-band flux and S_{850} flux. That is, however, not seen, which could be due to either a large scatter in the properties of the galaxies, the submm emission arising from a localised region of the host galaxy or both. The K-band magnitude could also be used as a measure for the stellar mass, though this in principle needs to be corrected for the redshift, and by assuming it is not affected by dust extinction. In that case, a correlation between K and S_{850} could be expected, if the masses of the individual components would be related to the mass of the whole galaxy, i.e. a large dust mass would be expected for a massive galaxy. Also for such cases, redshift information would be helpful for the interpretation.

$I - K$ vs. 850 μm: There is no correlation between the submm flux and the optical/NIR colour, though there is a hint that the faint submm sources, $S_{850} < 1$ mJy, have bluer candidate counterparts. As this is based on a small number of sources, we cannot say anything conclusive. It could though indicate that at very faint flux levels, we start to detect the LBG population.

5.8 Conclusion

We have presented optical and NIR imaging for 48 SCUBA sources in the Leiden-SCUBA Lens Survey. 14 (30 %) of the sources have been identified with one or more underlying galaxies, 17 (35 %) have one or more possible candidate counterparts and 17 (35 %) have no obvious candidate counterparts. Of the identified sources 85 % of the underlying galaxies have extremely red colours, with $I - K > 4$ and/or $J - K > 2.3$. Spectroscopy is presented for two securely identified counterparts and for one possible counterparts, which all have redshifts between 2 and 3. We find that these galaxies do not show Lyα in emission, which is the opposite of radio-selected submm sources. This suggests a difference between radio-selected $S_{850} > 5$ mJy sources and optically/NIR identified faint submm sources. Additionally, two securely identified counterparts have redshift $z = 1.034$ (ISO source) and $z = 2.84$ (quasar).

Comparing the submm flux and the $I - K$ colour of the sources with candidate counterparts shows no correlation between submm flux and $I - K$. Though, there is a hint that the faint sources, $S_{850} < 1$ mJy, are bluer than the average candidate counterpart.

In a statistical analysis of the submm emission from EROs and DRGs in the MS1054$-$03 field, we find the error-weighted 850μm flux for EROs is 0.83$\pm$0.17mJy and contribute to the submm EBL by 27-39 % and for DRGs is 1.10$\pm$0.21 mJy with a contribution to the submm EBL of 22-31 %. For DRGs with $K < 21.7$ the average flux is higher, 1.60$\pm$0.34 mJy. Removing the EROs and/or DRGs, which are associated with SCUBA sources, the average flux decreases, but is still detected, except for the bright $K < 20.7$ EROs. DRGs and $S_{850} \sim 1$ mJy SCUBA sources have similar surface densities.

Through both the identification of the SCUBA sources and the statistical detected of EROs and DRGs, we find that there are strong signs of an important link between SMGs and distant galaxies with very red colours.

References

Alexander, D.M., Bauer, F.E., Brandt, W.N., et al., 2003, AJ, 125, 383

Anantharamaiah K., Viallefond F., Mohan N., Goss W., Zhao J., 2000, ApJ, 537, 613

Arnouts, S., D'Odorico, S., Christiani, S. et al, 1999., A&A, 341, 641

Barger, A.J., Cowie, L.L., Smail, I., et al., 1999a, AJ, 117, 2656

Barger, A.J., Cowie, L.L. & Sanders, D.B., 1999b, ApJ, 518, L5

Bertin E. & Arnouts S., 1996, A&A 117, 193

Best, P.N., van Dokkum, P.G., Franx, M. & Röttgering, H.J.A., 2002, MNRAS, 330, 17

Blain, A.W., Ivison, R.J. & Smail, I., 1998, MNRAS, 296, L29

Blain, A.W., Kneib, J.-P., Ivison, R.J. & Smail, I., 1999a, ApJ, 512, L87

Blain, A.W., Smail, I., Ivison, R.J. & Kneib, J.-P., 1999b, MNRAS, 302, 632

Blain, A.W., 1999, MNRAS, 309, 955

Borys, C., Chapman, S., Halpern, M. & Scott, D., 2003, MNRAS, 344, 385

Carilli, C.L. & Yun, M.S., 1999, ApJ, 513, L13

Chapman, S.C., Scott, D., Steidel, C.C., et al., 2000, MNRAS, 319, 318

Chapman, S.C., Scott, D., Borys C. & Fahlman, G.G., 2002, MNRAS, 330, 92

Chapman, S.C., Blain, A.W., Ivison, R.J. & Smail, I.R., 2003, Nature, 422, 695

Cimatti, A., Daddi, E., di Serego Alighiere, S., et al., 1999, A&A, 352, L45

Cohen, J.G. & Kneib, J.-P., 2002, ApJ, 573, 5241

Condon, J.J., 1992, ARA&A, 30, 575

Cowie, L.L., Barger, A.J. & Kneib, J.-P., 2002, AJ, 123, 2197

Dey, A., Graham, J.R., Ivison, R.J., et al., 1999, ApJ, 519, 610

Dannerbauer, H., Lehnert, M.D., Lutz, D., et al., 2004, ApJ, 606, 664

Downes, A.J.B., Peacock, J.A., Savage, A. & Carrie, D.R., 1986, MNRAS, 218, 31

Duc, P.-A., Poggianti, B.M., Fadda, D., et al., 2002, A&A, 382, 60

Ebbels T., Le Borgne J.-F., Pello R., et al., 1996, MNRAS, 281, L75

Elbaz, D., Cesarsky, C.J., Chanial P., et al., 2002, A&A 384, 848

Ellis, R.S., Smail, I., Dressler, A., et al., 1997, ApJ, 483, 582

Erb D., Shapley A., Steidel C., et al., 2003, ApJ, 591, 101

Fadda, D., Elbaz, D., Duc, P.-A., et al., 2000, A&A, 361, 827

Fixsen, D.J., Dwek, E., Mather, J.C., Bennett, C.L. & Shafer, R.A., 1998, ApJ, 508, 123

Flores, H., Hammer, F., Elbaz, D., et al., 2004, A&A, 420, L31

Foucaud, S., McCracken, H.J., Le Fèvre, O., et al., 2003, A&A, 409, 835

References

Fontana, A., D'Odorico, S., Polo, F., et al., 2000, AJ, 120, 2206

Förster Schreiber, N.M., van Dokkum, P.G., Franx, M., et al., 2004, ApJ, in press (astro-ph/0408077)

Fox, M.J., Efstathiou, A., Rowan-Robinson, M., et al., 2002, MNRAS, 331, 839

Franx, M., Illingworth, G.D., Kelson, D.D., van Dokkum, P.G., Tran, K.V., 1997, ApJ, 486, L75

Franx, M., Moorwood, A., Rix, H.-W., et al., 2000, Msngr, 99, 20

Frayer, D.T., Smail, I., Ivison, R.J. & Scoville, N.Z., 2000, AJ, 120, 1668

Gehrels, N., 1986, ApJ, 303, 336

Genzel, R., Baker, A.J., Tacconi, L.J., et al., 2003, ApJ, 584, 633

Green, P.J. & Mathur, S., 1996, ApJ, 462, 637

Hainline, L., Scoville, N.Z., 2004, ApJ, 609, 61

Hamuy, M., Walker, A.R., Suntzeff, N.B., et al., 1992, PASP, 104, 533

Hamuy, M., Suntzeff, N.B., Heathcote, S.R., et al., 1994, PASP, 106, 566

Hogg, D.W., 2001, AJ, 121, 1207

Holland, W.S., Robson, E.I., Gear, W.K., et al, 1999, MNRAS, 303, 659

Hughes, D.H., Serjeant, S., Dunlop, J., et al., 1998, Nature, 394, 241

Ivison, R. J., Smail, I., Le Borgne, J.-F., et al., 1998, MNRAS, 298, 583

Ivison, R. J., et al., 2002, MNRAS, 337, 1

Klaas U., Haas M., Heinrichsen I., Schulz B., 1997, A&A, 325, L21

Kneib, J.-P., Mellier, Y., Fort, B. & Mathez, G., 1993, A&A, 273, 367

Kneib, J.-P., Ellis, R.S., Smail, I., Couch W.J. & Sharples R.M., 1996, ApJ, 471, 643

Kneib, J.-P., van der Werf, P.P., Knudsen, K.K., et al., 2004, MNRAS, 349, 1211

Knudsen, K.K., van der Werf, P.P. & Jaffe W., 2003, A&A, 411, 343

Komatsu, E., Kitayama, T., Suto, Y., et al, 1999, ApJ, 516, L1

Landolt, A.U., 1992, AJ 104, 340

LeBorgne J. F., Pello R., Sanahuja B., 1992, A&AS, 95, 87

Lisenfeld U., Isaak K. G., Hills R., 2000, MNRAS, 312, 433

McLean I. S. et al., 1998, SPIE, 3354, 566

McNamara, B.R., Jannuzi. B.T., Sarazin, C.L., Elston, R. & Wise, M., 1999, ApJ, 518, 167

Metcalfe, L., Kneib, J.-P., McBreen, B., et al., 2003, A&A, 407, 791

Moorwood, A., Cuby, J.G. & Lidman, C., 1998, The Messenger, 91, 9

Oke J. B. et al., 1995, PASP, 107, 375

Packham, C., Thompson, K.L., Zurita, A., et al., 2003, MNRAS, 345, 395

Peacock, J.A., Rowan-Robinson, Blain, A.W., et al., 2000, MNRAS, 318, 535

Pozzetti, L. & Mannucci, F., 2000, MNRAD, 317, L17

Puget, J.-L., Abergel, A., Bernard, J.-P., et al., 1996, A&A, 308, L5

Rix, H.-W., Guhathahurta, P., Colless, M. & Ing, K., 1997, MNRAS, 285, 779

Roche, N.D., Dunlop, J. & Almaini, O., 2003, MNRAS, 346, 803

Rupke, R. & White, R.E., 2003, ApJ, 583, L13

Sanders, D.B. & Mirabel, I.F., 1996, ARA&A, 34, 749

Schlegel, D.J., Finkbeiner, D.P. & Davis, M., 1998, ApJ, 500, 525

Serjeant, S., Farrah, D., Geach, J., et al., 2003, MNRAS, 346, L51

Shapley, A.E., Steidel, C.C., Adelberger, K.L., et al., 2001, ApJ, 562, 95

Sheth, K., Blain, A.W., Kneib, J.-P., et al., 2004, *submitted*

Smail, I., Dressler, A., Couch, W.J., et al., 1997a, ApJS, 110, 213

Smail, I., Ellis, R.S., Dressler, A., 1997b, ApJ, 479, 70

Smail, I., Ivison, R.J., Blain, A.W. & Kneib, J.-P., 1998, ApJ, 507, L21

Smail, I., Ivison, R.J., Owen, F.N., Blain, A.W. & Kneib, J.-P., 2000, ApJ, 528, 612

Smail, I., Ivison, R.J., Blain, A.W. & Kneib, J.–P., 2002, MNRAS, 331, 495

Smith, G.P., Smail, I., Kneib, J.-P., et al., 2002, MNRAS, 330, 1

Surace J. A., Sanders D. B., Evans A. S., 2000, ApJ, 529, 170

Swinbank A.M., Smith J., Bower R.G., et al., 2003, ApJ, 598, 162

Taylor, A.N., Dye, S., Broadhurst, T.J., Benitez, N. & van Kempen, E., 1998, ApJ, 501, 539

Trentham, N., Kormendy, J. & Sanders, D.B., 1999, AJ, 117, 2152

van der Werf, P.P., Knudsen, K.K., Labbé, I., Franx, M., 2001, in "Deep millimeter surveys: implications for galaxy formation and evolution", eds. J.D. Lowenthal & D.H. Hughes., p.103

van Dokkum, P.G., Franx, M., Fabricant, D., Illingworth, G.D., Kelson, D.D., 2000, ApJ, 541, 95

van Dokkum, P.G. Förster Schreiber, N.M., Franx, M., et al., 2003, ApJ, 587, L83

van Dokkum, P.G., Franx, M., Förster Schreiber, N.M., et al., 2004, ApJ, 611, 703

Webb, T.M.A., Lilly, S.J., Clements, D.L., et al., 2003a, ApJ, 597, 680

Webb, T.M.A., Eales, S., Foucaud, S., et al., 2003b, ApJ, 582, 6

Webb, T.M.A., Brodwin, M., Eales, S. & Lilly, S.J., 2004, ApJ, 605, 645

Wehner, E.H., Barger, A.J. & Kneib, J.-P., 2002, ApJ, 577, L83

References

142

Chapter 6

A submillimetre selected quasar in the field of Abell 478

K.K. Knudsen, P.P. van der Werf & W. Jaffe

Abstract

We present the discovery of a dusty quasar, SMM J04135+10277, located behind the galaxy cluster Abell 478. The quasar was discovered as the brightest source in a submillimetre survey of high redshift galaxies lensed by foreground rich clusters of galaxies in a project aimed at studying the cosmic star formation history of dusty galaxies. With submillimetre fluxes of S_{850} =25±2.8 mJy and S_{450} = 55±17 mJy this object is one of the brightest submillimetre sources known. Optical imaging revealed a point source with I =19.4±0.1 mag (corrected for galactic extinction). Follow-up optical spectroscopy showed this object to be a quasar at redshift z =2.837±0.003. The quasar was also detected at shorter infrared wavelengths with the Infrared Space Observatory. This object is the first quasar discovered by its submillimetre emission. Given the general lack of overlap between deep submillimetre and X-ray samples, usually interpreted as a low incidence of active nuclei in submillimetre samples, this is an unusual object. Analysis of number counts of quasars and of submillimetre galaxies bears out this suggestion. We compare the properties of SMM J04135+10277 to those of optically selected quasars with submillimetre emission, and argue that the optical faintness results from a large viewing angle with the direction of relativistic beaming, and not from abnormally high extinction. We also find indications that the bulk of the submillimetre flux density is not powered by the quasar nucleus. This conclusion is supported by analysis of the infrared spectral energy distribution. These results are consistent with previous observations that quasars at higher redshift tend to have a more prominent cold dust component, most likely powered by extended star formation in the host galaxy. The temperature for the cold dust component is found be T =29±2 K when assuming β =1.5 for a modified blackbody. The quasar is found to have a total infrared luminosity of $(2.9\pm0.5)\cdot10^{13}$ $L_{\odot}$, dominated by the emission from cool dust.

6.1 Introduction

Major advances in submillimetre (submm) continuum observations came with the Submillimetre Common-User Bolometer Array (SCUBA, Holland et al. 1999), which is mounted at the 15 m James Clerk Maxwell Telescope (JCMT) at Mauna Kea, Hawaii. This dual-channel instrument for the first time allowed sensitive mapping, making it possible to survey larger areas of the sky to greater depths than previously possible at submm wavelengths. This development led to the discovery of a new class of objects of high infrared (IR) luminosity, located at cosmological distances (e.g., Smail et al. 1997). Even though these objects are less common than Lyman-break galaxies at similar redshifts, they would dominate the cosmic star formation rate density at these redshifts, if star formation is indeed the source of their high luminosity (e.g., Blain et al. 1999). Since the importance of these objects was realized, a number of submm surveys have been performed or are in progress (e.g. Smail et al. 2002 ; Eales et al. 1999; Scott et al. 2002; Chapman et al. 2002; Knudsen et al. *Chapter 3*). One of the biggest challenges for those surveys has turned out to be the follow-up observations and the identification of the counterparts causing the submm emission. As a result, the determination of the nature and redshift of these objects has been significantly hampered. While currently more than a hundred submm sources have been detected, less than 20 of these have reliably been identified with sources at other wavelengths, in spite of painstaking attempts. The number of published spectroscopic redshifts is even significantly smaller. The majority of the reliably identified counterparts are very or extremely red objects (e.g., Frayer et al. 2000; Smail et al. 1999); several are also exhibiting active galactic nuclei (AGN) features in their spectra (Ivison et al. 1999). Because of the small number of secure identifications, any new identification adds important information to our understanding of the submm population. A survey with different selection criteria, radio-preselected and submm-detected, has produced 10 spectroscopic redshifts in a sample of 34 sources (Chapman et al. 2003).

We are carrying out an extensive SCUBA survey of a number of galaxy clusters fields, aimed at detecting gravitationally amplified background galaxies: the Leiden-SCUBA Lensed Survey (Knudsen et al. *Chapter 3*). In the course of doing the optical identifications and follow-up of this survey we discovered one of our submm sources to be a previously unknown type-1 quasar (previously reported in Knudsen et al. 2001). While submm surveys of optically selected quasars have been quite successful (Isaak et al. 2002), this object is the first type-1 quasar first discovered by its submm emission. In contrast, type-2 quasars have been detected in small numbers in other submillimetre surveys (e.g. SMM J02399-0136, Vernet & Cimatti 2002), and IRAS-radio-optical quasars have been selected before at a wide range of redshifts (e.g. APM 08279+5255 in Irwin et al. 1998). In this paper we present the observations of the quasar. We discuss unusual properties of the object, its optical spectrum, and its IR spectral energy distribution, and compare the results to optically selected quasars. We adopt an $\Omega_0 = 0.3$ and $\Lambda = 0.7$ cosmology with $H_0 = 70 \, \mathrm{km\,s^{-1} Mpc^{-1}}$.

6.2 Observations and results

6.2.1 Submillimetre data

The SCUBA data of the $z = 0.088$ galaxy cluster Abell 478 have been obtained during five nights in September and December 1997, March 1998 and December 1999. The first data were obtained in a program to study the cooling flow in the cluster itself. In these data a bright point source was detected. Consequently, extra data was obtained to study this object better. The total integration time was 6.6 hours (excluding overheads), recording data at both $850\,\mu$m and $450\,\mu$m simultaneously in jiggle-map mode. The data were obtained mostly under good conditions with $850\,\mu$m zenith atmospheric opacity typically around 0.2. The pointing was checked regularly and was found to be stable. Calibration maps of CRL618 were also obtained. The data were reduced using the SURF (SCUBA User Reduction Facility) and KAPPA software packages (Jenness & Lightfoot 1998). The resulting images have an angular resolution of $15''$ at $850\,\mu$m and $8''$ at $450\,\mu$m.

Source extraction and estimation of the uncertainties were carried out using a method based on Mexican Hat wavelets (Cayón et al. 2000; Barnard et al. 2004; Knudsen et al. *Chapter 2*), which was adopted for the entire Leiden-SCUBA Lensed Survey, and which will be described in a forthcoming publication (Knudsen et al. *Chapter 2*), where the full survey will be presented. This method was adopted because it is mathematically rigorous and its performance on SCUBA jiggle maps can be fully characterized. Monte Carlo simulations have been performed to determine the noise and uncertainties of the derived parameters. The area-weighted noise levels of the maps are 2 mJy at $850\,\mu$m and 14 mJy at $450\,\mu$m.

In the $850\,\mu$m map four sources were detected of which the brightest has a flux of $S_{850} = 25 \pm 2.8$ mJy. This is the only source in the map with detected $450\,\mu$m emission, $S_{450} = 55 \pm 17$ mJy. It was detected with a signal-to-noise of 15, for which the formal positional uncertainty including the pointing uncertainty of the JCMT is $3.2''$. This is the object SMM J04135+10277 for which we are here presenting the follow-up observations. Fluxes and positions are presented in Table 6.1.

6.2.2 Optical identification

For identification and redshift determination of the SCUBA source(s) optical imaging and spectroscopy was obtained with FORS1 at VLT-UT1 (Antu) in Chile, in September 1999. Four 15 min exposures in $I-$band were acquired in photometric conditions. The frames were bias-subtracted, flatfielded and stacked. The resulting image is shown in Figure 6.1 with the SCUBA $850\,\mu$m contours overlayed. The seeing measured in the final image is $0\rlap{.}''9$. The standard star field PG0231+051 (Landolt 1992) was used for the calibration. The source detection and photometry was performed using SExtractor (Bertin & Arnouts 1996). The center of SMM J04135+10277 is coincident with an $I = 20.5 \pm 0.1$ mag point source at $\alpha = 04^{\mathrm{h}}13^{\mathrm{m}}27\rlap{.}^{\mathrm{s}}28$, $\delta = 10°27'40\rlap{.}''4$ (J2000). There are no other apparent candidate counterparts. The optical position is within the error circle of the submm observation. One of the other SCUBA sources (SMM J04134+10270) coincides with a galaxy, which, given its size and magnitude, is a probable cluster member. There are no obvious candidate counterparts for the two other SCUBA

sources. Using the DIRBE/FIRAS maps (Schlegel et al. 1998), a Galactic reddening $E(B - V) \approx 0.52$ mag is derived — a substantial reddening. The corrected I magnitude of the optical counterpart for SMM J04135+10277 is thus 19.4 ± 0.1 mag.

6.2.3 Optical spectroscopy

FORS1 spectroscopy of SCUBA sources in the A478 field was also obtained in September 1999. We used FORS1 in Multi-Object Spectroscopy (MOS) mode to obtain spectra of a number of targets, using grism 150I+17, without order sorting filter. This setup gives a spectral resolution of 260 at 720 nm with the $1''$ slit which we employed. Overlap of the second spectral order may affect the wavelength region longwards of 650 nm, but was in the present case found not to affect the spectra. Two exposures of 1800 sec were obtained in a seeing of $1.3''$. The spectra were bias-subtracted and flatfielded. Wavelength calibration was achieved using exposures of He and Ar lamps. Correction for telluric absorption and flux calibration was carried out using observations of the white dwarf EG274 ($V = 11.03$), which we corrected for photospheric absorption features. The multislit mask included both the bright SCUBA source SMM J04135+10277 and the fainter SCUBA source SMM J04134+10270. The extracted spectra were corrected for galactic foreground absorption using the DIRBE/FIRAS maps.

The optical spectrum of SMM J04135+10277 (Figure 6.2) shows broad emission lines, of which the four most prominent can be identified with Lyα+N V, Si IV+O IV], C IV and C III. In addition the spectrum shows a power-law continuum. All of these features are characteristic of quasars. Bluewards of the Lyα emission line, Lyα forest absorption is seen. We use the C III, C IV and the Si IV+O IV] lines, with the largest weight on the symmetric C III line, to determine the redshift. We find the value $z = 2.837 \pm 0.003$, consistently for the peak value of all three profiles.

The spectrum of SMM J04134+10270 confirms its membership of the A478 cluster. It shows the characteristic spectrum of a quiescent elliptical galaxy with no evidence for nuclear activity. This source will be discussed together with the rest of the survey in Knudsen et al. (*Chapter 5*).

6.2.4 Near-infrared spectroscopy

Since restframe ultraviolet emission lines of quasars can be significantly blueshifted with respect to the systemic velocity (e.g., Carswell et al. 1991), we also attempted to obtain additional redshift information using restframe optical lines. Unfortunately, at $z \approx 2.84$, the brightest lines (Hα, Hβ, [O III] 5007 Å) are all in wavelength regions where the earth atmosphere is opaque. We therefore concentrated on the [O II] 3727 Å line which is redshifted to the blue edge of the H-band window, a region strongly affected by atmospheric absorption lines.

We used ISAAC on VLT-UT1 (Antu) in February 2002, to take H-band spectra of SMM J04135+10277. We used the medium resolution grating with a $1''$ slit to obtain an $R = 3000$ spectrum between 1.41 and 1.49 μm, which should contain the [O II] line for redshifts between 2.78 and 3.00. In addition, we obtained a low-resolution spectrum ($R = 500$) of the entire H-band, in an attempt to detect Hγ, which although intrinsically faint, should at least lie in a clear part of the
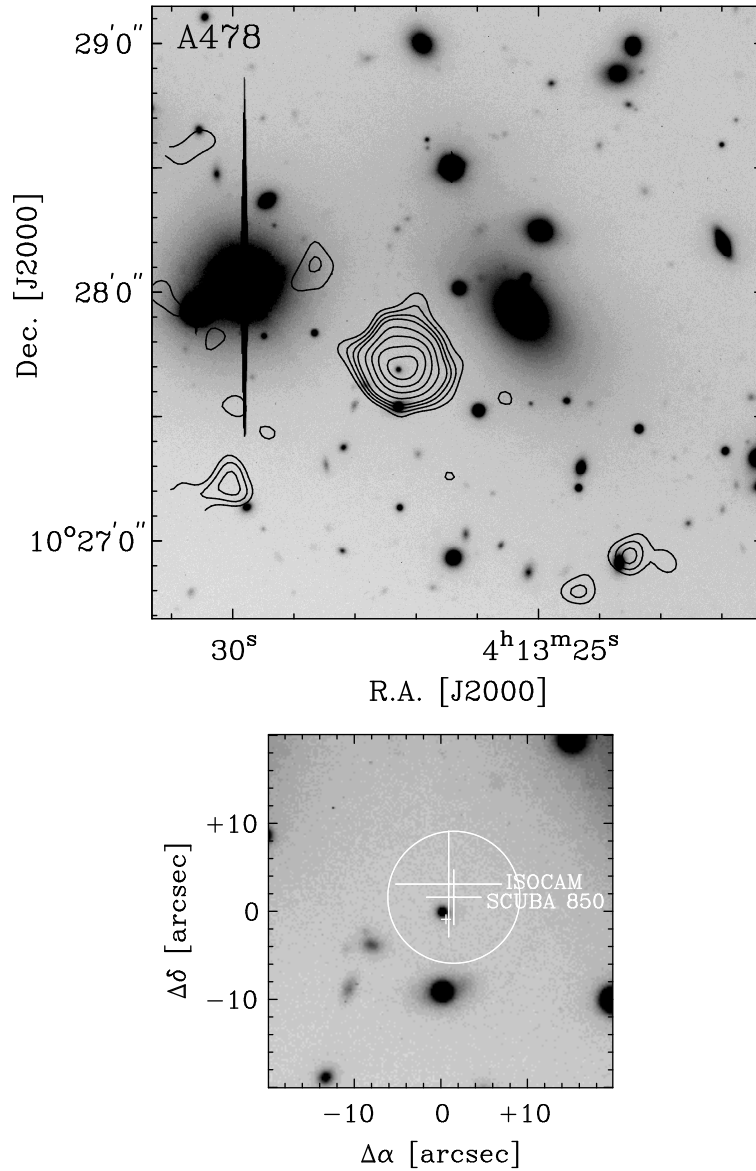
Figure 6.1: Top: *VLT FORS1 I-band image of A478 overlayed with the contours of the SCUBA 850 μm map. The contours represent the 850 μm signal-to-noise ratios of 3,4,5,6,8,10,12,14 − 1σ = 2 mJy.* Bottom: *Zoom in on the quasar. This box is centered on the optical position of the quasar and has a size of 40″×40″. The circle shows the size of the SCUBA 850 μm beam centered on the SCUBA detection. The biggest cross indicates the position in the ISOCAM 14.3 μm map, where the total astrometric uncertainty is 6″. The medium cross indicates the detection position at 850 μm, the positional uncertainty is 3.2″. The smallest cross is the radio position.*

Table 6.1: *Coordinates and fluxes at different wavelengths for SMMJ04135+10277. The fluxes as they are listed here have not been corrected for the gravitational lensing.*

passband	RA(J2000)	Dec(J2000)	f_ν
850μm	04:13:27.2	+10:27:43	$25 \pm 2.8\,$mJy
450μm	04:13:27.2	+10:27:42	$55 \pm 17\,$mJy
180μm			$< 620\,$mJy
14.3μm	04:13:27.24	+10:27:44.5	$470 \pm 80\,$mJy
6.7μm	04:13:27.88	+10:27:43	$200 \pm 30\,$mJy
I	04:13:27.28	+10:27:41.4	$19.4 \pm 0.1\,$mag
$4.86\,$GHz	04:13:27.26	+10:27:40.5	$220 \pm 35\,\mu$Jy
$1.4\,$GHz			$< 750\,\mu$Jy

spectrum. Both spectra were obtained in photometric conditions and in an optical seeing of $0.8''$, by nodding the object along the slit. Total integration time was 44 minutes in both spectra. The individual frames were pairwise subtracted in order to remove the bright OH nightsky lines, flatfielded and coadded. Wavelength calibration was derived from the OH nightsky lines. Correction for telluric absorption and flux calibration were achieved using the B5V star Hip25499 (H=5.62) and the B2V star Hip28142 (H=7.497), corrected for photospheric absorption. Unfortunately, while the continuum of the quasar is clearly detected in both spectra, no emission features are seen. Undoubtedly, this is due to atmospheric absorptions in the region of the redshifted [O II] line, and the faintness of the relevant features in the rest of the H-band spectrum.

6.2.5 ISO data

We also inspected the archive of the Infrared Space Observatory (ISO, Kessler et al. 1996) and extracted observations of A478 using both the mid-infrared camera (CAM, Cesarsky et al. 1996) and the mid/far-infrared photometer (PHOT, Lemke et al. 1996).

The PHOT data were obtained using the P22 raster mode at $180\,\mu$m, with $92''$ pixels, on February 21, 1998. The data were reduced using the PHOT Interactive Analysis (Gabriel et al. 1997). Initial data reduction steps included discarding of corrupted data, non-linearity correction, and deglitching of individual ramps. After fitting all integration ramps with a first order polynomial, further deglitching and data editing, and dark current subtraction, the data were corrected for detector drifts and for vignetting, and calibrated using the internal Fine Calibration Sources. The resulting image shows a $0.62 \pm 0.19\,$Jy source, the centroid of which is however displaced by $46''$ from SMM J04135+10277. This displacement is less than the ISO angular resolution at $180\,\mu$m, but much more than the nominal ISO pointing uncertainty of $2''$. While the centroid of a faint source can be displaced somewhat when placed on top of a highly structured background, in the present case the offset is so large that the $180\,\mu$m detection cannot reliably be associated with the quasar. Hence in the following we label this as an upper limit.

The CAM data were obtained using the LW3 filter (effective wavelength $14.3\,\mu$m) on February 21, 1998, and using the LW2 filter (effective wavelength $6.7\,\mu$m) on March 21, 1998 using the CAM01 raster observing mode with $6''$ pixels. The data were reduced using the CAM Interactive Analysis package (Ott et al. 1997). Processing steps consisted of dark current subtraction, deglitching and correction of transients using the PRETI method (Aussel et al. 1999), which is particularly suited for the detection of faint sources, flatfielding using a flatfield derived from the stacked dataframes, and mosaic construction taking into account the image distortion. This resulted in clear detections of SMM J04135+10277 at $14.3\,\mu$m with a flux density of 0.47 ± 0.08 Jy, and at $6.7\,\mu$m with a flux density of 0.20 ± 0.03 Jy. Positions of these sources are listed in Table 6.1.

6.2.6 CO $J = 3{\rightarrow}2$ emission

In a recent commissioning project of the new COBRA spectrometer on the Owens Vally Radio Observatory, the CO $J = 3{\rightarrow}2$ emission line has been detected from the quasar. This detection confirms the nature of SMM J04135+10277 as a hyper-luminous IR quasar. The redshift implied by the CO line is $z = 2.84$, which is indeed somewhat higher than the optically determined redshift. This result will be discussed in detail in Hainline et al. (in prep).

6.3 Discussion

6.3.1 SMM J04135+10277 and the optical quasar population

Only little is known about the importance of AGNs in the submm population. Most studies comparing X-ray and submm observations conclude that the submm population is powered by star formation rather than AGNs and especially quasars (e.g., Almaini et al. 2003), based on the lack of overlap of X-ray and submm sources in deep studies. This has been confirmed in a study combining very deep *Chandra* observations with SCUBA observations of the HDF-N, where Alexander et al. (2003) found that a significant fraction of bright submm sources ($f_{850\mu\mathrm{m}} > 5$ mJy) harbour an AGN, however, the AGN is not powerful enough to power the submm emission. This makes SMM J04135+10277 a particularly interesting object, since here we have a bright submm source that is unequivocally identified with a type-1 quasar. Given what is known about the abundance of type-1 quasars, is this an ordinary object that we should have expected to find in our survey, or are we dealing with an exceptional case? We here estimate the probability of finding a high redshift submm emitting quasar in our survey. The total area of our survey is 65 arcmin^2 (Knudsen et al., *Chapter 3*). Using the optical spectrum we estimate that the quasar has a B magnitude $B \sim 21.0 - 21.5$ mag. Based on the counts of Kennefick et al. (1997), we find that there is only a 20% probability of finding a quasar with $z > 2.3$ and 16.5 mag $< B < 22$ mag in our survey. Furthermore, the probability that such a quasar is a bright submm source is also less than unity, as shown by Priddey et al. (2002), who did a submm study of optically selected quasars at $1.5 < z < 3$. For the sub-sample of quasars with $z > 2.3$, only 30% of these had detectable submm emission down to 6.8 mJy and all of those are fainter

than SMM J04135+10277. Combining the numbers we estimate only a 6% chance of detecting a submm bright quasar at $z > 2.3$ in our survey, if that quasar was drawn from the population of optically selected quasars.

We also estimate the expected number of bright submm sources in the surveyed area, regardless of their physical nature. According to the number counts from Smail et al. (2002) we should expect to find two sources with $850 \, \mu$m fluxes between 20 and 25 mJy. Our observations (Knudsen et al., in prep.) are in agreement with that number. Comparing this to the small chance of finding a high redshift submm emitting quasar in our survey, this result suggests that the bright part of the submm population does not originate from dusty quasars, and that SMM J04135+10277 is an unusual object.

6.3.2 Optical spectrum

Since SMM J04135+10277 is the first quasar selected based on its submm emission, it is of interest to compare its properties to those of optically selected quasars. Turning first to the optical spectrum, the shapes of the C III, C IV and the Si IV+O IV] lines appear as expected. However, the Ly α+N V emission line has a more unexpected shape. The peak and blue wing appear to be absorbed. Furthermore, the strength of the line relative to the other emission lines is unusually low for a quasar. Since dust is present in this quasar, it is natural to assume that atomic hydrogen will also be present, so that associated absorption may play a role in suppressing the Ly α emission. However, for a more detailed assessment of this effect, a higher resolution spectrum is needed. Comparing the optical spectrum of SMM J04135+10277 to that of quasars selected at other wavelengths (see e.g. Francis et al. (1992) for a composite spectrum), there are no significant differences except for the suppressed Ly α emission.

We note that SMM J04135+10277 belongs to the optically fainter part of the quasar population. Can this be the effect of strong absorption by dust, which would then simultaneously account for the luminous dust emission from SMM J04135+10277? We obtain a measure of the isotropic luminosity of the quasar nucleus using the C IV emission line; obviously, the Ly α line cannot be used since it appears to be absorbed, and the continuum cannot be used because of the effects of relativistic beaming, which cannot reliably be quantified. The observed flux of the C IV line is $1.0 \cdot 10^{-14} \, \text{erg s}^{-1} \, \text{cm}^{-2}$. A comparison sample can be constructed from the optically selected submm emitting quasars studied by Priddey et al. (2002), using the spectra from Hagen et al. (1999). This comparison sample covers redshifts from 2.60 to 2.79 and can therefore be compared directly to SMM J04135+10277. The comparison sample has C IV fluxes from 1.7 to $4.1 \cdot 10^{-14} \, \text{erg s}^{-1} \, \text{cm}^{-2}$, roughly a factor of 3 higher than SMM J04135+10277. The rest-frame *equivalent width* of C IV on the other hand shows the opposite trend: while SMM J04135+10277 has a C IV restframe equivalent width of $\sim 170 \, \text{Å}$, values in the comparison sample are approximately a factor of 10 lower, ranging from 13 to 25 Å. In other words, the quasar continuum is fainter by about a factor of 30 than would be expected for its C IV flux. It is highly unlikely that extinction could account for this, since the quasar continuum and the broad line region should be viewed through approximately the same obscuring column. Further-

more, as Fig. 6.2 shows, the quasar continuum is characterized by a blue power law. The slope of this continuum does not indicate the presence of abnormally large absorption. Therefore a more likely explanation of the optical faintness of this quasar is a large viewing angle away from the direction of relativistic beaming. The beamed flux density is proportional to δ^p with $p \sim 4$, where the Doppler factor $\delta = [\gamma(1 - \beta \cos \theta)]^{-1}$, where β is the bulk velocity in units of the speed of light, and $\gamma = (1 - \beta)^{-1/2}$ is the corresponding Lorentz factor, and θ is the angle away from the beam (Urry & Padovani 1995). Therefore a decrease in δ of a factor 2.3 would be sufficient to produce a factor 30 decrease in the beamed continuum with respect to the lines. The required angle away from the beam cannot be calculated since β is not known. However, as shown by Urry & Padovani (1995), variations in δ of this magnitude are entirely reasonable for angles $\theta < 20°$, provided $\gamma > 2$. This estimate confirms the viability of our suggestion that the optical faintness of the quasar is due to a large viewing angle away from the direction of relativistic beaming, and not to abnormally large extinction. If in fact the optical spectrum is still dominated by the doppler boosted jet then our detection of this one object suggests that a much larger number of yet unidentified sources are similar AGNs viewed from a larger angle to the jet axis. We finally note that it would be interesting to make the same comparison with low-z far-IR detected quasars, addressing also the properties of the dust emission spectrum. This comparison would require spectrophotometry of quasars in the vacuum ultraviolet.

Going further, we can investigate whether the observed submm emission from SMM J04135+10277 is likely powered by the AGN or whether the presence of an additional power source is indicated. In the comparison sample, the observed $850 \, \mu$m fluxes range from 6.8 to 10.0 mJy, increasing monotonically with C IV flux. The three times fainter C IV flux of SMM 04135+10277 thus would suggest an AGN-powered $850 \, \mu$m flux of approximately 3 mJy. The observed flux is almost a factor of 10 higher. This result suggests that the bulk of the submm emission from SMM 04135+10277 is not powered by the AGN but by an additional source of energy, most likely vigorous star formation in the host galaxy. If this interpretation is correct, high resolution imaging of CO lines and dust emission with ALMA should reveal an extended source.

6.3.3 Gravitational magnification

The low redshift ($z = 0.088$) of A478 is far from the optimal lensing redshift ($z \sim 0.2$), and no arcs are detected in the vicinity of the quasar. This suggests that the gravitational magnification is small and that the quasar is not subject to differential lensing, which otherwise would influence the shape of the spectral energy distribution (SED). We calculate the magnification of the quasar using LENSTOOL (Kneib et al. 1993). The cluster is modelled using two components: the overall cluster potential with a core radius $r_c = 250$ kpc and a velocity dispersion $\sigma = 905$ km s^{-1} and the potential of the cD galaxy with $r_c = 2$ kpc and $\sigma = 350$ km s^{-1} (Allen et al. 1993; Zabludoff et al. 1990). We find that the quasar is magnified by a factor of 1.3. Hence, all fluxes should be corrected for this value. In all calculations in the following sections of this paper the fluxes have been corrected for the gravitational lensing.
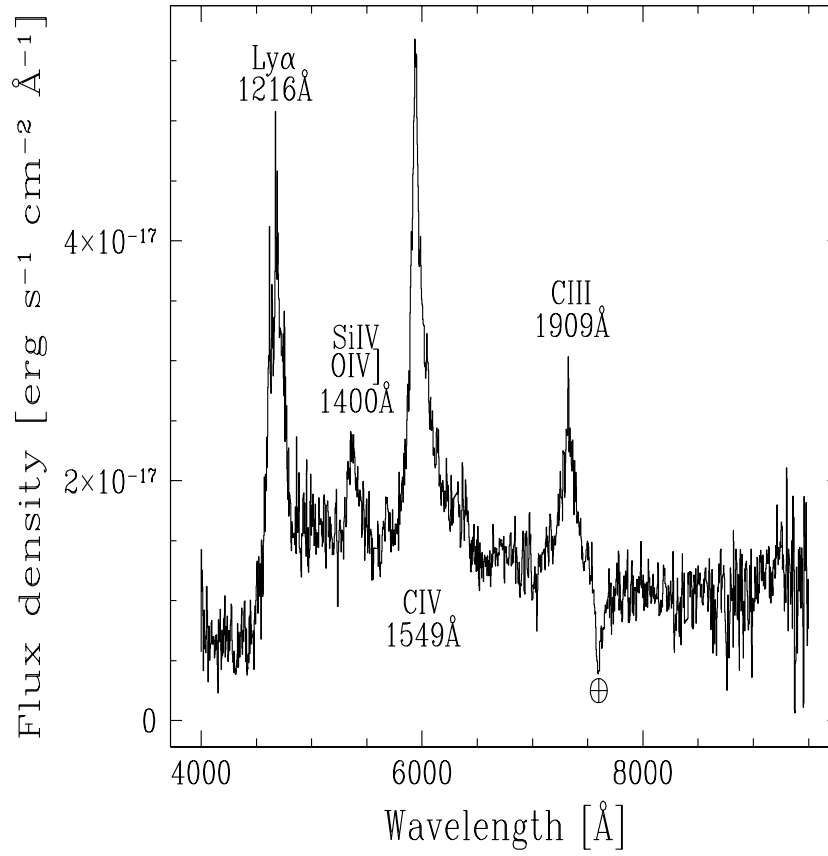
Figure 6.2: *FORS1 spectrum of the SMM J04135+10277. The Earth-symbol indicates a telluric absorption line. The spectrum has been corrected for Galactic extinction.*

6.3.4 Spectral energy distribution

From archival data from the NRAO Very Large Array a radio source near the position of the SMM J04135+10277 was found. The fluxes measured are $S(4.86\,\text{GHz}) = 220 \pm 35\,\mu\text{Jy}$ and $S(1.4\,\text{GHz}) < 750\,\mu\text{Jy}$ (3σ) (M. Yun, private comm.). Based on this low radio flux, it is concluded that the quasar is radio-quiet (according to the radio-power criterion given by Stocke et al. 1992 to divide quasars into radio-loud and radio-quiet types). Hence, the non-thermal contribution to the submm flux is expected to be small and is here neglected.

Combined, we have then six points on the SED and two upper limits, ranging from the radio to the optical regime (see Table 6.1). The SCUBA points and the two ISO points at $14.3\,\mu\text{m}$ and $170\,\mu\text{m}$ are in the rest frame all at wavelengths typical for thermal emission by dust. The ISO $6.7\,\mu\text{m}$ point in rest frame is $1.7\,\mu\text{m}$, which together with the optical point is expected to originate from stellar light, possibly contaminated with non-thermal emission from the AGN. The radio emission is attributed to non-thermal synchrotron emission.

In the following we will focus on the thermal dust emission. Of the thermal emission, the two SCUBA points are most likely due to the cool dust typically described by a modified blackbody, whereas the $14.3\,\mu\text{m}$ point arises from a hot component. The shape of the SED between the cold and hot component seems to be different for different quasars (see e.g. Haas et al. 2000). We have no measurements between $450\,\mu\text{m}$ and $14.3\,\mu\text{m}$, which makes an analysis of the IR SED difficult. We do, however, attempt to make a tentative analysis in which we compare with known objects and also estimate parameters like temperature and luminosity.

We first compare the quasar with other known quasars. Comparing to high-z quasars is not trivial, since the high-z quasars which have well-sampled IR SEDs, are often strongly lensed and their observed SEDs may have suffered differential lensing. We therefore first focus on low-z quasars. Haas et al. (2000) have made a detailed study of the IR SED of Palomar-Green (PG) quasars. The majority of these quasars are at fairly low redshift. We compare to three low-z PG quasars with well-sampled SEDs, PG 0050+124, PG 1206+439 and PG1613+638 (all shown in Fig. 6.3). All three SEDs are redshifted to $z = 2.837$. If the SEDs are scaled to the quasar $850\,\mu\text{m}$ point, the comparison gives the impression of a deficit in the mid/near-IR emission of SMM J04135+10277. Alternatively, inspired by the findings of Archibald et al. (2001) and Page et al. (2001), that the star formation rate observed in AGNs is higher at higher redshift, leading to enhanced long-wavelength emission at higher redshift, we may choose instead to scale the low-z SEDs to the observed $14.3\,\mu\text{m}$ point, i.e., the hot dust emission associated with the AGN. This, not unexpectedly, then suggests an excess in the far-IR-submm emission from SMM J04135+10277. This result corroborates our earlier conclusion that a significant portion of the observed $850\,\mu\text{m}$ emission of SMM J04135+10277 results from extended star formation, and is not powered directly by the AGN. The SED of the strongly lensed $z = 3.87$ quasar APM 08279+5255 (Lewis et al. 1998 and references therein) is also shown in Fig. 6.3. It has also been appropriately shifted and scaled to the $14.3\,\mu\text{m}$ point. In this case the submm/FIR deficit relative to the SMM J04135+10277 is even more pronounced, corroborating the discussion

above.

Given this result, it is also of interest to compare the SED of SMM J04135+10277 to the SEDs of well-studied starburst galaxies. We use the SEDs of the starburst galaxy NGC 253 and the ultraluminous infrared galaxy (ULIRG) NGC 6240 (extracted from the NASA Extragalactic Database), redshifted to $z = 2.837$, for comparison. Scaled to the $850\,\mu$m point, the far-IR/submm range matches quite well, whereas the mid/near-IR emission is much brighter for SMM J04135+10277. This result is expected, as starbursts are known not to have the hot dust component that is characteristic of AGNs, especially quasars (Sanders et al. 1989; Barvainis 1987). Considering that the SED of the quasar is not well-sampled, and that we are looking at only one quasar, no definite conclusions can be drawn about the precise shape of the IR SED and the power source of the dust emission of SMM 04135+10277 in particular, or of the submm-selected quasar population in general. Tentatively, though, these observations support the suggestion that quasars at higher redshift have a high submm and far-IR flux, suggesting a higher star formation rate. To study this in detail, however, observations filling the big gaps in the IR SED are needed. Such data can possibly be obtained with SIRTF.

Finally, we calculate the dust temperature, dust mass, and total luminosity in dust emission of SMM J04135+10277. For the dust emission, we use blackbody emission, modified by the frequency-dependent mass absorption coefficient

$$k_{\mathrm{d}}(\nu_{\mathrm{rest}}) = 1.5\,\mathrm{cm}^2\,\mathrm{g}^{-1} \left(\frac{\nu_{\mathrm{rest}}}{375\,\mathrm{GHz}} \right)^{\beta},\tag{6.1}$$

using the average value from the literature at $800\,\mu$m (see Hughes et al. 1997 for a discussion of the assumptions and uncertainties in this parameter) and assume $\beta = 1.5$. Since the IR SED cannot be fit by a single modified blackbody, we first fit the cold dust component sampled by the SCUBA points. Using only the SCUBA points, we find a temperature $T_{\mathrm{cold}} = 29 \pm 2$ K and a dust mass of $M_{\mathrm{d}} = (1.8 \pm 0.3) \times 10^9$ M$_{\odot}$ for the cold dust component. The total luminosity of a modified blackbody spectrum can be calculated using the following analytical expression:

$$L_{\mathrm{tot}} = 4\pi D_{\mathrm{L}}^2 \frac{S(\nu_{\mathrm{obs}})}{\nu_0^{\beta} B(\nu_0, T)} \frac{2h}{c^2} \left(\frac{kT}{h} \right)^{4+\beta} \Gamma(4 + \beta)\zeta(4 + \beta),\tag{6.2}$$

where h and k are Planck's respectively Boltzmann's constants, D_{L} is the luminosity distance, and the two last factors are the Gamma function and Riemann's zeta function. $S(\nu_{\mathrm{obs}})$ is the flux density at the observing frequency, and ν_0 is the corresponding rest frequency. The total luminosity of the cold component is found to be $(2.4 \pm 0.5) \cdot 10^{13}$ L$_{\odot}$. To estimate the total IR luminosity, we assume a powerlaw between the peak of the modified blackbody curve and the observed $14.3\,\mu$m point. The powerlaw is integrated from $200\,\mu$m (observed frame), where the modified blackbody and the powerlaw balance each other, to $14.3\,\mu$m with the result of $(5.4 \pm 1) \cdot 10^{12}$ L$_{\odot}$. In total the IR luminosity (corrected for gravitational amplification) is then $L_{\mathrm{IR}} = (2.9 \pm 0.5) \cdot 10^{13}$ L$_{\odot}$, dominated by the cold dust component. Using a different method based on the analysis in Blain et al. (2003), where the whole IR SED is fit with a single temperature modified blackbody with
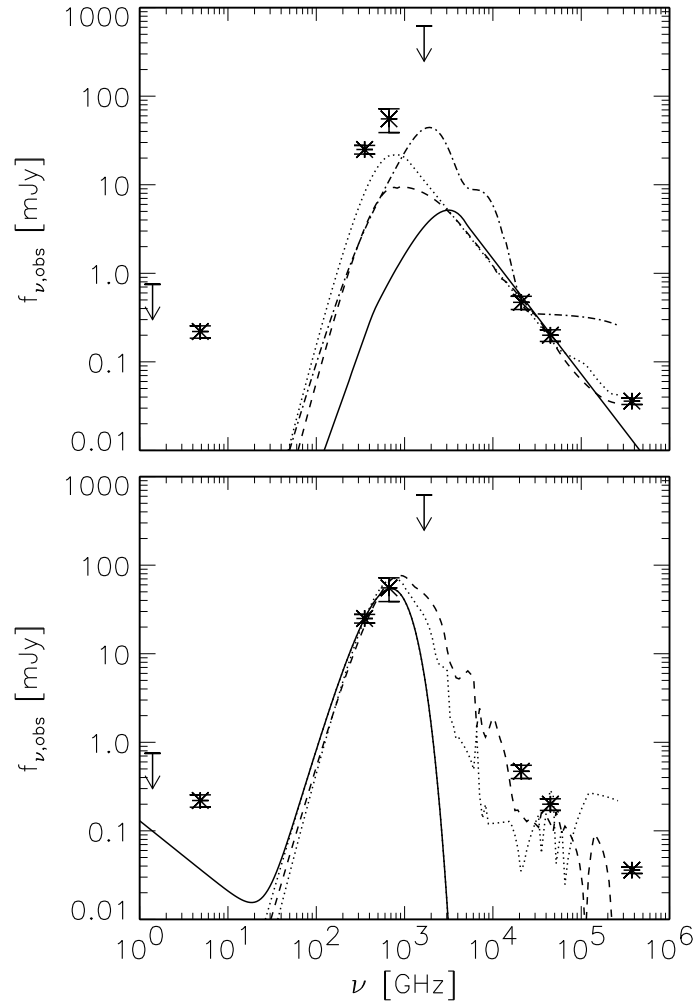
Figure 6.3: *The SED of the quasar SMM J04135+10277 compared to other SEDs. The SED points are given by the asterisks, where the error bars are 1σ, and the upper limits are indicated by arrows. The flux densities as displayed in the figure have not been corrected for the gravitational lensing. As we are primarily interested in the thermal dust emission, the radio points have not been included in the SEDs.* Upper panel: *Comparison to the SEDs of three PG quasars (Haas et al. 2000): PG 0050+124 (z = 0.061; dashed), PG 1206+459 (z = 1.158; dotted), and PG 1613+658 (z = 0.129; dash-dot), and the quasar APM 08279+5255 (z = 3.87; solid; Lewis et al. 1998, Irwin et al. 1998). The four SEDs have been scaled to the observed 14.3 μm flux of SMM J04135+10277, as described in the text.* lower panel: *Comparison to the SEDs of the starburst galaxy NGC 253 (dotted) and the ULIRG NGC 6240 (dashed). Both SEDs have been scaled to the observed 850 μm flux of SMM J04135+10277. The solid line is a regular expected far-IR–radio correlation-based SED line.*
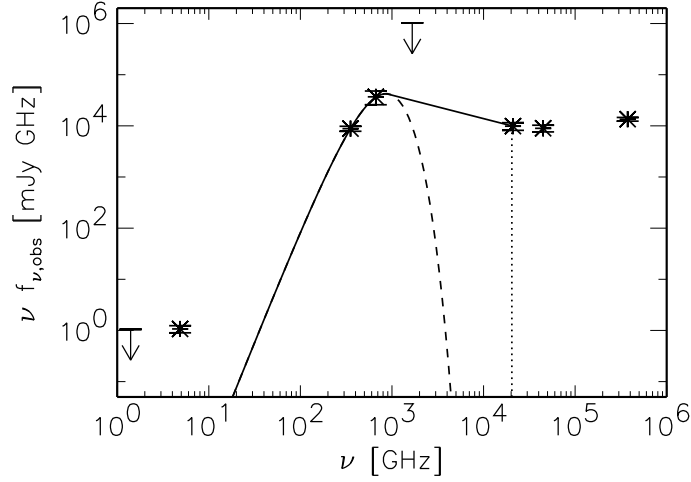
Figure 6.4: *The quasar SED is overlayed with the SED which we have used for calculating the luminosity. The flux as displayed in the figure has not been corrected for the gravitational magnification.*

a powerlaw on the Wien side ranging all the way into the mid-IR, a temperature of 38 K is found and a total IR luminosity of $1.8 \times 10^{13}\, L_\odot$. This gives a higher temperature, though a slightly lower luminosity, compared to the fit above where a cold component was fitted to the two SCUBA points.

The temperature as we find is lower than that found in other high-z quasars such as APM 08279+5255, which has a temperature of $120 - 220\,$K determined for a pure blackbody (Lewis et al. 1998), or BR 1202−0725, which has a dust temperature of $50 - 68\,$K (Leech et al. 2001). Both quasars have luminosities in order of $10^{14-15}\, L_\odot$, thus brighter than SMM J04135+10277, so that higher dust temperatures might be expected. On the other hand, these two quasars are strongly lensed and it is possible that differential lensing distorts the integrated SED and overemphasizes warm dust components.

We finally attempt to compare the radio-submm flux density ratio with the relevant simulations performed by Blain (1999), which are based on the IR-radio correlation observed at low redshift. As we do not have a 1.4 GHz flux density measurement, we estimate it by assuming that the radio SED is a power law, $f \propto \nu^{-\alpha}$, with slope $\alpha = -0.8$ and scale it to the observed flux density at 4.86 GHz. We find $f_{1.4\,\mathrm{GHz}} = 595\,\mu\mathrm{Jy}$ (not corrected for the gravitational lensing). Still assuming $\beta = 1.5$, we use Fig. 4 in Blain (1999) by interpolating between his two models with $T = 20\,$K respectively $T = 40\,$K. For $z = 2.837$ this gives a flux density ratio of between 1.4 GHz and 850 μm of $\sim 3.5 \cdot 10^{-3}$. Therefore, the observed 850 μm flux would imply $f_{1.4\,\mathrm{GHz}} \sim 88\,\mu\mathrm{Jy}$ if the quasar strictly followed the local IR-radio correlation. This number is however a factor $6 - 7$ lower than what we had just estimated based above. This indicates that SMM J04135+10277 has more radio emission (for its IR emission) than e.g., the ULIRG Arp220, which was used

for the template SED in Blain (1999). This result is not surprising, as quasar radio emission is powered by both the synchrotron emission from stellar remnants and the synchrotron emission from the central black hole.

6.4 Conclusions

We have discovered a type-1 quasar behind the cluster of galaxies A478. The quasar, SMM J04135+10277, was discovered by it submm emission. The quasar has a redshift of $z = 2.837$ and is radio quiet. The quasar is optically faint, but has a large submm flux. Using number counts of quasars and of submm sources, we argue that SMM 04135+10277 is an unusual object. It is in any case a remarkable object since there is little overlap between deep submm and X-ray samples, suggesting that the incidence of powerful AGNs among submm galaxies is low. The slope of the rest-frame UV continuum is similar to that of optically selected quasars (Francis et al. 1992) and does not exhibit any signs of extraordinary dust extinction. This leads us to suggest that the line of sight to the quasar nucleus is not abnormally obscured. Analysis of optical continuum, spectral lines and submm emission leads us to conclude that the optical faintness of the quasar results from a large viewing angle from the direction of relativistic beaming, and that a significant amount of the submm flux is not powered by the active nucleus. More likely the cold dust is heated by a high rate of star formation in the environment surrounding the quasar. Comparison of the sparsely sampled IR SED to that of other objects tentatively supports this conclusion. The total IR luminosity is found to be $(2.9 \pm 0.5) \cdot 10^{13} \, \mathrm{L_\odot}$ and is dominated by the emission from cool dust.

References

Alexander, D.M., Bauer, F.E., Brandt, W.N., et al., 2003, AJ, 125, 383

References

Allen, S.W., Fabian, A.C., Johnstone, R.M., et al., 1993, MNRAS, 262, 910
Almaini, O., Scott, S.E., Dunlop, J.S., et al., 2003, MNRAS, 338, 303
Archibald, E.N., Dunlop, J.S., Hughes, D.H., et al., 2001, MNRAS, 323, 417
Aussel, H., Cesarsky, C.J., Elbaz, D., & Starck, J.L., 1999, A&A, 342, 313
Barvainis, R., 1987, ApJ, 320, 537
Bertin, E. & Arnouts, S., 1996, A&A, 117, 193
Blain, A.W., 1999, MNRAS, 309, 955
Blain, A.W., Smail, I., Ivion, R.J., & Kneib, J.-P., 1999, MNRAS, 302, 632
Blain, A.W., Barnard, V.E. & Chapman, S.C., 2003, MNRAS, 338, 733
Carswell, R.F., Mountain, C.M., Robertson, D.J., et al., 1991, ApJ, 381, L5
Cayón, L., Sanz, J.L., Barreiro, R.B., et al., 2000, MNRAS 315, 757
Cesarsky, C., Abergel, A., Agnese, P., et al., 1996, A&A, 315, L32
Chapman, S.C., Scott, D., Borys, C. & Fahlman, G.G., 2002, MNRAS, 330, 92
Chapman, S.C., Blain, A.W., Ivison, R.J. & Smail, I.R., 2003, Nature, 422, 695
Eales, S., Lilly, S., Gear, W., et al., 1999, ApJ 515, 518
Francis, P.J., Hewett, P.C., Foltz, C.B. & Chaffee, F.H., 1992, ApJ 398, 476
Frayer, D.T., Smail I., Ivison R.J. & Scoville N.Z., 2000, AJ, 120, 1668
Gabriel, C., Acosta-Pulido, J., Heinrichsen, I., Morris, H., & Tai, W.-M., 1997, *Astronomical Data Analysis Software and Systems VI*, A.S.P. Conference Series, Vol. 125, 1997, G. Hunt and H.E. Payne, eds., p.108
Hagen, H.-J., Engels, D. & Reimers, D., 1999, A&AS, 134, 483
Haas, M., Müller, S.A.H., Chini, R., et al., 2000, A&A, 354, 453
Holland, W.S., Robson, E.I., Gear, W.K., et al., 1999, MNRAS, 303, 659
Hughes, D.H., Dunlop, J.S. & Rawlings, S., 1997, MNRAS, 289, 766
Irwin, M.J., Ibata, R.A., Lewis, G.F. & Totten, E.J., 1998, ApJ, 505, 529
Isaak, K.G., Priddey, R.S., McMahon, R.G., et al., 2002, MNRAS, 329, 149
Ivison, R., Smail, I., Blain, A., Kneib, J.-P. & Frayer, D., 1999, ApSS, 266, 285
Jenness, T. & Lightfoot, J.F., 1998, *Astronomical Data Analysis Software and Systems VII*, A.S.P. Conference Series, Vol. 145, 1998, R. Albrecht, R.N. Hook and H.A. Bushouse, eds., p.216
Kennefick, J.D., Osmer, P.S., Hall, P.B. & Green, R.F., 1997, AJ, 114, 2269
Kessler, M.F., Steinz, J.A., Anderegg, M.E., et al., 1996, A&A, 315, L27
Kneib, J.-P., Mellier, Y., Fort, B. & Mathez, G., 1993, A&A, 273, 367
Knudsen, K.K., van der Werf, P.P. & Jaffe W., 2001, in "Deep Millimeter Surveys: Implications for Galaxy Formation and Evolution", eds. J.D. Lowenthal and D.H. Hughes, p168 (astro-ph/0009024)
Landolt, A.U., 1992, AJ 104, 340
Leech, K.J., Metcalfe, L. & Altieri, B., 2001, MNRAS, 328, 1125
Lemke, D., Klaas, U., Abolins, J., et al., 1996, A&A, 315, L64.
Lewis, G.F., Chapman, S.C., Ibata, R,A., Irwin, M.J. & Totten, E.J., 1998, ApJL, 505, 1
Ott, S., Abergel, A., Altieri, B., et al., 1997, *Astronomical Data Analysis Software and Systems VI*, A.S.P. Conference Series, Vol. 125, 1997, G. Hunt and H.E. Payne, eds., p.34
Page, M.J., Stevens, J.A., Mittaz, J.P.D. & Carrera, F.J., 2001, Science, 294, 2516
Priddey, R.S., Isaak, K.G., McMahon, R.G. & Omont, A., 2002, astro-ph/0211646
Sanders, D.B., Phinney, E.S., Neugebauer, G., Soifer, B.T. & Matthews, K., 1989, ApJ, 347, 29
Schlegel, D.J., Finkbeiner, D.P. & Davis, M., 1998, ApJ 500, 525
Scott, S.E., Fox, M.J. & Dunlop, J. S., 2002, MNRAS, 331, 817
Smail, I., Ivison, R.J. & Blain, A.W., 1997, ApJ, 490, L5
Smail, I., Ivison, R.J., Kneib, J.-P., et al., 1999, MNRAS, 308, 1061
Smail, I., Ivison, R.H., Blain, A.W. & Kneib, J.-P., 2002, MNRAS, 331, 495

Stocke, J.T., Morris, S.L., Weymann R.J. & Foltz, C.B., 1992, ApJ, 396, 487
Urry, C.M., & Padovani, P., 1995, PASP, 107, 803
Vernet, J. & Cimatti, A., 2001, A&A, 380, 409
Zabludoff, A.I., Huchra, J.P. & Geller, M.J., 1990, ApJS, 74, 1

References

160

Chapter 7

Summary, discussion and outlook

7.1 Summary

In the present thesis we have studied the faint submillimetre (submm) population. We have used the submm mapping instrument SCUBA for observations of strongly lensing galaxy clusters. These massive clusters act as magnifying glasses, because of the deep gravitational potential wells, which allows us to study sources that would otherwise be too faint to be detected with SCUBA. Without gravitational lensing, these observations would be limited to $\sim 2\,\mathrm{mJy}$, which is the blank field confusion limit.

In this survey, the Leiden-SCUBA Lens Survey, we have determined the number counts in the $850\,\mu$m flux range 0.1 to 19 mJy. The survey is constructed to have both regions of strong gravitational lensing and blank field regions. This has allowed us to probe both the bright end and the faint end (divided by the blank field confusion limit) simultaneously. Through that we have for the first time been able to detect the change in slope of the number counts from a single data set. Based on a simple χ^2 analysis, we find that the change of slope happens around $S_{850} \sim 6\,\mathrm{mJy}$. We have used the number counts to determine from which flux interval the dominant contribution to the submillimetre extragalactic background light (EBL) originates. We find that about 50 % of the submm background light comes from SCUBA sources with fluxes between 0.5 and 2.5 mJy.

We fit models of galaxy evolution to the deep $850\,\mu$m number counts from the Leiden-SCUBA Lens Survey. The counts data is supplemented with data from other submm/mm, far-infrared (FIR) and radio surveys, where the strongest constraints come from the $850\,\mu$m data and the radio data. The fits are done *without* using the information about the FIR extragalactic background light or redshift distribution. The model used here assumes that the $60\,\mu$m luminosity function undergoes luminosity evolution. We use the best fit solutions to predict the comoving star formation rates density for different cosmic epochs. We find that the star formation rate density peaks around redshift 1.8-2 and is about a factor 2-5 times larger than that of the observed optical results.

To identify the underlying galaxy giving rise to the submm emission, we have used the optical and near-infrared (NIR) data available for 10 out of 13 fields. The wavelength coverage and depth of the data varies a lot from field to field. For some of the fields we have also used the already available *ISO* and/or radio data.

For 48 SCUBA sources, we securely identify 30 %, we find one or more plausible counterparts for 35 % and are unable to identify any likely counterparts for 35 %. 85% of the identified and possibly identified counterparts have optical/NIR colours fulfilling the Extremely Red Objects (ERO; $I - K > 4$) and/or the Distant Red Galaxies (DRG; $J - K > 2.3$) selection criteria. The spectroscopy presented of four galaxies show no Lyα in emission, which is different from the radio-identified submm bright sources from Chapman et al. (2003).

The optical and NIR data from the field MS1054$-$03 is to date the deepest data obtained for a galaxy cluster. We have obtained three pointings with SCUBA to cover as much as possible of the area. We have used this data to make a statistical analysis of the submm emission from EROs and DRGs. We found that DRGs have an average 850 μm flux of 1.1$\pm$0.3 mJy, and EROs have an average 850 μm flux of 0.8$\pm$0.2 mJy. Their contribution to the submm EBL is 28-39 % for the DRGs and 22-31 % for the EROs. This is substantially larger than the previous results for Lyman Break Galaxies. These results of the submm emission from DRGs and EROs in combination with the results of the identification are strong indications of an important link between these populations.

Among the identifications there are two unusual cases: a multiply imaged source and a quasar.
The multiply-image source, SMM J16359+6612, is a galaxy in the field A2218, for which three images are detected both in the SCUBA map and in the optical/NIR images. The galaxy has an unlensed submm flux of 0.8 mJy and is magnified by a factor 45 in total for all three images. It has a redshift of 2.515, which is the same for two other star forming galaxies in the field. The other galaxies are, however, not detected in the SCUBA map. The three galaxies are less than 130 kpc from each other.
The quasar, SMM J04135+10277, was found in the field of A478. This is the first type-1 quasar selected through submm observations. It is the brightest object in our survey. Comparing its infrared (IR) spectral energy distribution (SED) with that of optically selected quasars, it has a high submm flux, and thus FIR luminosity ($\sim 3\times10^{13}$ L$_\odot$). This suggests very high star formation rates, possibly > 1000 M$_\odot$yr^{-1}. Recent CO observations detect one of the most massive molecular gas reservoirs at high redshift (Hainline et al., 2004), which supports a high SFR.

7.2 Discussion and outlook

The results from this thesis bear directly on our understanding of the nature of the submillimetre galaxies and their relative importance in galaxy formation and evolution. There are still many issues that are highly relevant for further progress on the topic, which we, however, have not touched upon in this thesis. Here we outline some of the most important issues.

Redshift: One of the most important and urgent issues to be settled is the *redshifts distribution* of the submm galaxies (SMGs) — both of the individual sources, which will allow us to study some of the physical properties in greater detail, and of the SMG population as whole. The negative k-correction removes the possibility for extracting redshift information from the $850\,\mu$m flux. Thus the redshift can only be reliably determined through extensive multi-wavelength follow-up observations. Knowledge of the redshift is imperative to allow for CO observations, and determine volume density, spatial clustering, redshift distribution and constraints on evolutionary models. Until recently the number of reliably identified sources was in the order of 20 (Kneib et al., 2004; Knudsen et al., 2003; Smail et al., 2002, 2003; Borys et al., 2004; Webb et al., 2003b; Ivison et al., 1998, 2000, 2002; Ledlow et al., 2002; Dunlop et al., 2004; Frayer et al., 1998, 2003). In a recent paper, Chapman et al. (2003) have published ten redshifts for radio-identified SCUBA sources, and a larger sample is expected to be published in the near future (Chapman et al., *in prep.*). As the counterparts have been identified using radio observations, the SCUBA sources are relatively bright with $S_{850} > 4\,$mJy. These sources might be probing the tip-of-the-iceberg, as the bright sources are not the dominant contributor to the submm EBL (as we have shown in Chapter 3). While this is major progress, another equally important step is to do the same for SCUBA sources with $S_{850} < 4\,$mJy to confirm if their redshift distribution follows that of the bright SCUBA sources.

Clustering: Quantifying the angular and spatial clustering of submillimetre galaxies will give important information about the nature of the sources as a population, how they compare to other populations, and what is their relation to present-day galaxy populations. As first realised by Kaiser (1984), the highest peaks in the density field in the early universe are strongly clustered, in a hierarchical structure formation model. In studies of the local universe, it has been found that luminous $L > L_\star$ galaxies are stronger clustered than less luminous galaxies, and likewise early-type galaxies are stronger clustered than the late-type galaxies (e.g., Willmer et al., 1998, Zehavi et al., 2002). In high redshift studies for Lyman Break Galaxies (LBGs) at $z \sim 3$ and Extremely Red Galaxies (EROs) at $z \sim 1-2$ a clustering signal has been detected (e.g., Giavalisco & Dickinson, 2001; Daddi et al., 2000, 2001). Daddi et al. (2003) found in a recent study that DRGs at redshifts $2-4$ are more strongly clustered than the LBGs in the same redshift range and with similar number densities. For radio galaxies at redshift ~ 1, Overzier et al. (2003) found a clustering signal comparable to that of EROs and local massive elliptical galaxies.

The two largest high-redshift blank field SCUBA surveys conducted till now are the Canada-UK Deep SCUBA Survey (CUDSS; Eales et al., 2000; Webb et al., 2003a) and the UK 8 mJy survey (Scott et al., 2002). The area covered by the CUDSS is about 60 arcmin^2 to a depth of $3\sigma \sim 3\,$mJy, while the 8 mJy survey has covered an area about four times larger to a $3\sigma \sim 7.5\,$mJy. Both Webb et al. (2003a) and Scott et al. (2002) did a clustering analysis of the data, but did not detected a signal, which they assign to the limited area of the survey. Scott et al. noted that a survey of $0.5\,$degree^2 is necessary to reliably determine the strength of the clustering signal at the depth of their survey.

The currently on-going survey, the SCUBA Half Degree Extragalactic Survey (SHADES[1]) has been taylored to study the clustering of the bright $S_{850} > 8$ mJy sources. To study this at fainter submm fluxes, more sensitive instruments are needed. SCUBA-2, which is such an instrument, will be mounted at the JCMT. While its improved sensitivity will allow for clustering studies of the fainter sources, the data obtained with SCUBA-2 will still be limited by the large beam of the JCMT. The Large Millimeter Telescope (LMT[2]), which is under construction in Mexico, will be a 50 m diameter telescope. It will be optimised to millimetre observations, however, during the good observing conditions submm observations will be possible. This will be the largest single-dish mm/submm telescope available. For 850 μm the beam size will be more than a factor three smaller than that of the JCMT, which will allow for clustering studies of the $S_{850} \sim 1$ mJy population, i.e., the submm galaxy population with the dominant contribution to the submm EBL.

Evolutionary sequence: How do we detect a high redshift SMG in the local universe? This question is naturally related to whether SMGs represent a phase of intense star formation in an evolutionary sequence with other galaxies that we see at both high redshift and locally. As has been mentioned in e.g. the Introduction (Chapter 1), the dynamical time scale for the formation of a galaxy is in the order of 10^8 yr, and thus to form the dominant stellar populations of the most massive galaxies, it must have happened at high redshift at prodigious star formation rates. Using the results from the luminosity evolution from the galaxy evolution models fitted to the 850 μm number counts (e.g., Chapter 4), the comoving volume density of SCUBA sources can be estimated and is in the order of $\sim 10^{-5}$ Mpc^{-3} (e.g., Scott et al., 2002) similar to that of the local bright, $L > 3-4 L_\star$ galaxies, which are dominated by the most massive galaxies, (e.g., Bell et al., 2003; Huang et al., 2003; Gardner et al., 1997).

To determine if SMGs are part of an evolutionary sequence, the underlying physics must be understood. In particular, it is important to understand what triggers the massive starburst and what is the relation between starburst and active galactic nuclei (AGN). This must be addressed through studies of both high and low redshift sources. Locally, the ultra-luminous IR galaxies (ULIRGs) appear to be mergers at late stages, where the very high SFRs have been triggered by the merging process (e.g., Genzel et al., 1998). In the famous merger the Antennae Galaxies (NGC 4038/4039; it is not a ULIRG but a nearby merger), the dominant fraction of the energy observed at submm wavelength is emitted from the highly obscured collision zone between the two galaxies (P.P. van der Werf, private communication; Haas et al., 2000; Zhu et al., 2003). While there is strong evidence that the high SFRs in local ULIRGs are triggered by a merging process, this is very difficult to confirm for the high redshift sources. One of the approaches at high redshift is to study the morphology and locate the relative position of the starburst. For this, future high-resolution telescopes are needed, such as the (sub)millimetre-array Atacama Large Millimetre Array (ALMA) for the detection

---

[1]http://www.roe.ac.uk/ifa/shades/
[2]http://www.lmtgtm.org/

of the dust emission and the James Webb Space Telescope (JWST) for detecting the stellar populations.

A significant fraction of the identified SMGs show signs of AGN activity (e.g., Ivison et al., 2000; Alexander et al., 2003). Similarly, in an X-ray study with deep data from *Chandra* on the Hubble Deep Field, Alexander et al. (2003) showed, that almost all of the bright SCUBA sources harbour an AGN (though the AGN would not be powerful enough to be the dominant source of heating of the dust). Likewise, a significant number of high redshift quasars have been found to emit detectable submm emission (e.g., Knudsen et al., 2003 (Chapter 6); Omont et al., 2003; Priddey et al., 2003). The Magorrian relation (Magorrian et al., 1998) predicts an intimate link between the formation and mass of a central supermassive black hole and the mass of its host galaxy. It has been proposed that ULIRGs are the early phases of what could become a quasar (Haas et al., 2003). This is a rather difficult, though very important, question to study through observations. For local ULIRGs it has been found that the mid-IR spectrum provides an important diagnostic, as galaxies with no or little AGN activity exhibit poly-cyclic aromatic hydrocarbon (PAH) features, while the mid-IR spectrum is dominated by a hot dust emission when there is significant on-going AGN activity (e.g., Haas et al., 2003; Klaas et al., 2001; Lutz et al., 1998). To be able to study this in detail at high redshift, the new space observatories, like *Spitzer* and the future *Herschel* will play an important role.

References

Alexander, D.M., Bauer, F.E., Brandt, W.N., et al., 2003, AJ, 125, 383
Bell, E.F., McIntosh, D.H., Katz, N. & Weinberg, M.D., ApJS, 149, 289
Borys, C., Chapman, S., Donahue, M., et al., 2004, MNRAS, 352, 759
Chapman, S.C., Blain, A.W., Ivison, R.J. & Smail, I.R., 2003, Nature, 422, 695
Daddi, E., Cimatti, A., Pozzetti, L., et al., 2000, A&A, 361, 535
Daddi, E., Broadhurst, T., Zamorani, G., et al., 2001, A&A, 376, 825
Daddi, E., Röttgering, H.J.A., Labbé, I., et al., 2003, ApJ, 588, 50
Dunlop, J.S., McLure, R.J., Yamada, T., et al., 2004, MNRAS, 350, 769
Eales, S., Lilly, S., Webb, T., et al., 2000, AJ, 120, 2244
Frayer, D.T., Ivison, R.J., Scoville, N.Z., et al., 1998, ApJ, 506, L7
Frayer, D.T., Armus, L., Scoville, N.Z., et al., 2003, AJ, 126, 73
Gardner, J.P., Sharples, R.M., Frenk, C.S. & Carrasco, B.E., 1997, ApJ, 480, L99
Genzel, R., Lutz, D. & Tacconi, L., 1998, Nature, 395, 859
Giavalisco, M. & Dickinson, M., 2001, ApJ, 550, 177
Haas, M., Klaas, U., Coulson, I., Thommes, E. & Xu, C., 2000, A&A, 356, L83
Haas, M., Klaas, U., Müller, S.A.H., et al., 2003, A&A, 402, 87
Hainline, L., Scoville, N.Z., Yun, M.S., 2004, ApJ, 609, 61
Huang, J.-S., Glazebrook, K., Cowie, L.L. & Tinney, C., 2003, ApJ, 584, 203
Ivison, R.J., Smail, I., Le Borgne, J.-F., et al., 1998, MNRAS, 298, 583
Ivison, R.J., Smail, I., Barger, A.J., et al., 2000, MNRAS, 315, 209
Ivison, R.J., Greve, T.R., Smail, I., 2002, MNRAS, 337, 1
Ledlow, M.J., Smail, I., Owen, F.N., et al., 2002, ApJ, 577, L79
Kaiser, N., 1984, ApJ, 284, L9
Klaas, U., Haas, M., Müller, S.A.H., et al., 2001, A&A, 379, 823

References

Kneib, J.-P., van der Werf, P.P., Knudsen, K.K., et al., 2004, MNRAS, 349, 1211

Knudsen, K.K., van der Werf, P.P. & Jaffe, W., 2003, A&A, 411, 343

Lutz, D., Spoon, H.W.W., Rigopoulou, D., Moorwood, A.F.M. & Genzel, R., 1998, ApJ, 505, L103

Magorrian, J., Tremaine, S., Richstone, D., et al., 1998, AJ, 115, 2285

Omont, A., Beelen, A., Bertoldi, F., et al., 2003, A&A, 398, 857

Overzier, R.A., Röttgering, H.J.A., Rengelink, R.B. & Wilman, R.J., 2003, A&A, 405, 53

Priddey, R.S., Isaak, K.G., McMahon, R. & Omont, A., 2003, MNRAS, 339, 1183

Scott, S.E., Fox, M.J., Dunlop, J.S., et al., 2002, MNRAS, 331, 817

Smail, I., Ivison, R.J., Blain, A.W. & Kneib, J.–P., 2002, MNRAS, 331, 495

Smail, I., Chapman, S.C., Ivison, R.J., et al., 2003, MNRAS, 342, 1185

Webb, T.M., Eales, S.A., Lilly, S.J., et al., 2003a, ApJ, 587, 41

Webb, T.M.A., Lilly, S.J., Clements, D.L., et al., 2003b, ApJ, 597, 680

Willmer, C.N.A., da Costa, L.N. & Pellegrini, P.S., 1998, AJ, 115, 869

Zehavi, I., Blanton, M.R., Frieman, J.A., et al., 2002, ApJ, 571, 172

Zhu, M., Seaquist, E.R. & Kuno, N., 2003, ApJ, 588, 243

Nederlandse samenvatting

Sterrenstelsels

Sterrenstelsels zijn concentraties van materie, bijeengehouden door de zwaartekracht, die een enorme hoeveelheid sterren bevatten. De meeste sterren die 's nachts aan de hemel staan, bevinden zich in ons eigen sterrenstelsel, de Melkweg. Naast sterren, bevatten sterrenstelsels ook grote hoeveelheden gas en stof in verhoudingen die voor ieder type sterrenstelsel anders zijn. Het idee dat ons heelal een grote hoeveelheid sterrenstelsels bevat is nog niet zo oud. Rond 1920 bewees Edwin Hubble dat de afstand tot wat toen nog de Andromeda nevel heette, zo groot was, dat deze nevel een sterrenstelsel moest zijn ver buiten ons eigen stelsel. Vele kleine, nevelige objecten, waarvan men tot dan toe dacht dat ze deel uit maakten van de Melkweg, bleken ieder individuele sterrenstelsels op enorme afstanden. Nu, bijna honderd jaar later, is de studie van de vorming en evolutie van sterrenstelsels een van de belangrijkste onderwerpen van de astronomie. Veel onderzoek is gericht op het verbeteren van ons begrip over hoe structuren, zoals sterrenstelsels, vormen. In 1962 stelden Eggen, Lynden-Bell & Sandage, dat een sterrenstelsel gevormd wordt wanneer een grote hoeveelheid gas onder invloed van de zwaartekracht ineen stort, zodat het merendeel van de sterren in het stelsel in een keer gevormd wordt. Hierna zou er niet al teveel meer gebeuren in het sterrenstelsel, zodat er niet verwacht mag worden dat er gedurende de evolutie van het heelal nog veel activiteit zal zijn. Een andere suggestie werd in 1974 gedaan door Press & Schechter. Zij opperden dat sterrenstelsels hiërarchisch opgebouwd worden, wanneer kleine sterrenstelsels samenklonteren en zo grotere stelsels vormen. Wanneer de kleinere stelsels samengaan, wordt gas in deze stelsels samengeperst, waardoor plotseling op het zelfde moment een grote hoeveelheid sterren gevormd wordt; een zogeheten 'starburst'. In dit model mag er verwacht worden dat er continue activiteit waar te nemen is in sterrenstelsels over de hele geschiedenis van het heelal. De meeste waarnemingen lijken dit laatste scenario te ondersteunen, echter: het lijkt erop dat de vorming en evolutie van sterrenstelsels een combinatie is van beide bovengenoemde scenarios.

Om de vorming en evolutie van sterrenstelsels te bestuderen lijkt het het meest voor de hand liggend om waarnemingen te doen aan de sterren in het stelsel. Sterren stralen het meeste licht uit op optische, ultraviolette en nabij-infrarode golflengten. Het licht op de optische golflengten – het visuele licht – kan waargenomen worden met onze ogen en met gewone telescopen. Voor de andere golflengte gebieden zijn speciale telescopen nodig. Echter, naast het waarnemen van de sterren, is het ook belangrijk de andere componenten van de sterren-

stelsels, zoals het gas en stof, te bestuderen. Deze kunnen waargenomen worden op andere golflengten, zoals bijvoorbeeld die van radio, ver-infrarood en röntgenstraling. In de gebieden waar sterren gevormd worden bevindt zich vaak een grote hoeveelheid stof. Deze interstellaire stofdeeltjes zijn kleine, onregelmatig gevormde gruisjes van koolstof en/of silicaten, met een diameter niet groter dan een miljoenste van een meter. Deze stofdeeltjes spelen een belangrijke rol in het proces van stervorming. Daarnaast, beïnvloedt stof ook het licht dat we van de sterren waarnemen omdat het optische en ultraviolette licht door deze deeltjes geabsorbeerd wordt; dit proces wordt extinctie genoemd. Als gevolg hiervan zien de jonge sterren, normaal blauw, er rood uit, net zoals oude sterren die van zichzelf al rood zijn. De aanwezigheid van stof in sterrenstelsels compliceert dus de interpretatie van de optische waarnemingen. Doordat het stof het sterlicht absorbeert, wordt het stof warmer. Deze warmte wordt uitgestraald op infrarode golflengten. (Dit is een zelfde effect als wanneer op een warme zomerdag de zon een huis heeft bestraald. Na zonsondergang merken we dan, dat de muren nog lange tijd de geabsorbeerde zonnestraling als warmte weer uitzenden.) Infrarood waarnemingen kunnen dus gebruikt worden om het stof te bestuderen. Het merendeel van het infrarood licht uit stervormingsgebieden wordt uitgezonden in het deel van het infrarood spectrum dat het ver-infrarood genoemd wordt. Ver-infrarood straling heeft golflengtes tussen 30-1000 μm (1 μm of 'micrometer' is een miljoenste deel van een meter).

Ongeveer tien jaar geleden realiseerde men zich, dat waarnemingen van ver weg staande sterrenstelsels in het ver-infrarood erg belangrijk zijn. De reden hiervoor is dat het "spectrum van het heelal" (aangetoond in Figuur 1), dat een maat is voor de hoeveelheid energie die gedurende de leeftijd van het heelal is uitgezonden over de hele hemel, aantoonde dat er zich evenveel energie in het (ver-)infrarode deel van het spectrum bevindt als in het hele ultraviolette en optische deel. Zonder in al te veel detail te treden, betekent dit dat de helft van alle activiteit, zoals stervorming, verborgen is achter stof. Dus is het nodig om stof in het verre heelal waar te nemen om een beter begrip te krijgen over de vorming en evolutie van sterrenstelsels.

Waarnemingen op 850 μm

In dit proefschrift worden waarnemingen op 850 μm beschreven. Daar dit net iets minder dan een millimeter is, worden deze waarnemingen ook wel sub-millimeter waarnemingen genoemd. Het doel was het bestuderen van ver weg gelegen sterrenstelsels welke enorme hoeveelheden stof bevatten en waarin intense stervorming gaande is. De waarnemingen werden gedaan met de James Clerk Maxwell Telescope (JCMT; zie de omslag) op Mauna Kea, Hawaii, met het instrument genaamd de Sub-millimetre Common-User Bolometer Array (SCUBA). De JCMT heeft een schotel met een doorsnede van 15 meter. De locatie op 4092 meter boven zeeniveau is niet alleen ideaal geïsoleerd gelegen, maar deze ligging is ook essentieel voor submillimeter waarnemingen, daar waterdamp in de atmosfeer bijna alle ver-infrarood straling absorbeert. Er zijn slechts enkele golflengtes waar de atmosferische absorptie iets minder is, en 850 μm is daar een van. Het instrument SCUBA is het eerste instrument dat daadwerkelijk beelden kan maken van
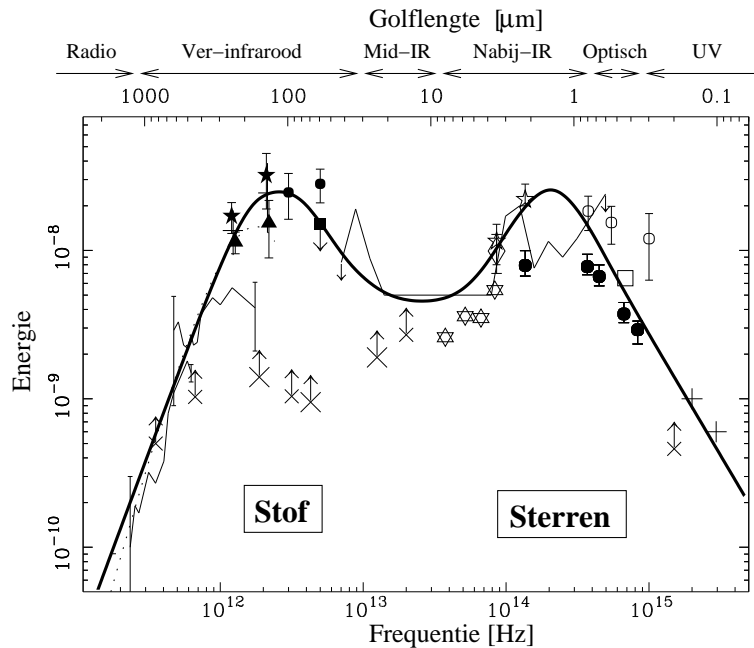
Figuur 1: *"Het spectrum van het heelal". De dikke lijn in deze figuur illustreert de energie-dichtheid van de achtergrondstraling van buiten onze Melkweg, van submillimeter tot ultraviolette golflengtes. Hierbij negeren we de bijdrage van de 'Kosmische Achtergrondstraling' welke een overblijfsel is van de Oerknal. Deze domineert de energie-dichtheid in het niet afgebeelde radio gebied. Voor de afgebeelde golflengtes wordt de straling vooral uitgezonden door stof en sterren. De energie in de straling van het stof (met een maximum op ongeveer 200 µm) is ongeveer gelijk aan die in de straling van de sterren (met een maximum tussen 1 en 2 µm). De symbolen zijn de waarnemingen die over een periode van meer dan 10 jaar door verschillende astronomen en met verschillende instrumenten zijn gedaan. Tevens is in de figuur aangegeven welk golflengte/frequentie gebied bij welke benaming (zoals ver-infrarood) hoort.*

de hemel op de betreffende golflengtes en is geoptimaliseerd voor 850 µm.

SCUBA is in 1997 in gebruik genomen en kort daarna leverde het al nieuwe indrukwekkende resultaten op. Een van de eerste uitkomsten betreffende ver weg gelegen sterrenstelsels is in 1998 gepubliceerd door Hughes en medewerkers. Zij vonden dat, ondanks dat stelsels die helder in het ver-infrarood zijn relatief weinig in het nabije heelal voorkomen, dit soort stelsels ongeveer 1000 keer meer voorkwamen in het vroege heelal. In meerdere aspecten verschillen deze stelsels van onze eigen Melkweg; zo is bijvoorbeeld de hoeveelheid sterren die per jaar in deze stelsels gevormd worden 100-1000 keer groter dan in de Melkweg. Deze veraf gelegen *stoffige sterrenstelsels* worden vaak *submillimeter sterrenstelsels* genoemd, omdat ze voor het eerst in submillimeter golflengtes waargenomen zijn.

Submillimeter waarnemingen van veraf gelegen sterrenstelsels leveren andere
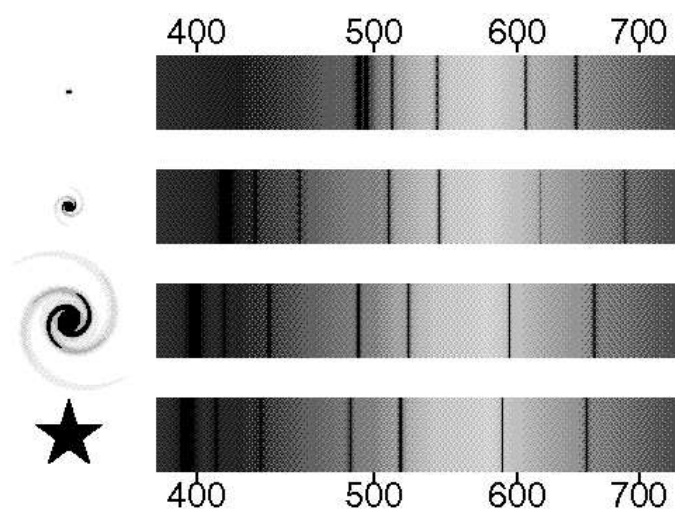
Figuur 2: *Deze figuur Illustreert de Doppler verschuiving van het licht. Onderaan staat een optisch spectrum van een ster die nauwelijks beweegt ten opzichte van de zon. Daarboven staan optische van sterrenstelsel op steeds grotere afstand. Het is duidelijk te zien dat de lijnen in de spectra steeds meer naar rechts en dus hogere, meer rode, golflengtes verschuiven. Door de uitdijing van het heelal bewegen alle sterrenstelsels van elkaar af en zijn alle stelsels dus rood-verschoven. De eenheden van de spectra zijn nanometers, oftewel een miljoenste millimeter.*

resultaten dan de waarnemingen op andere golflengtes. De verre sterrenstelsels zijn makkelijker te zien op submillimeter golflengtes. Omdat het heelal uitdijt, bewegen sterrenstelsels van elkaar vandaan. Een resultaat hiervan is dat de spectra van de stelsels *rood-verschoven* worden door de Doppler verschuiving van het uitgezonden licht (zoals geïllustreerd in Figuur 2). De Doppler verschuiving kennen we van de sirene van een ambulance. Deze klinkt hoger in toon als de ambulance op ons af komt (blauw-verschuiving) en lager in toon als hij van ons weg beweegt (rood-verschuiving). Astronomen meten de afstanden tot veraf gelegen sterrenstelsels in termen van *roodverschuiving*. De sterkte van het licht dat waargenomen wordt van afgelegen bronnen wordt kwadratisch minder als de afstand toeneemt. Dus niet alleen is het licht van veraf gelegen stelsels roder dan de oorspronkelijke kleur, maar het is ook nog eens een stuk zwakker. Echter, een sterrenstelsel is helderder in sommige delen van het spectrum, en het toeval wil, dat voor veraf gelegen stelsels (met een *roodverschuiving* tussen 1 en 8 (figuur 3 geeft een schaal aan)) juist dit helderdere (blauwe) gedeelte zodanig *rood-verschoven* is, dat het precies op submillimeter golflengtes uitkomt. Als gevolg hiervan, compenseert de helderdere straling het feit dat op grote afstanden de waargenomen straling steeds zwakker wordt. Dit betekent dat sterrenstelsels waargenomen op submillimeter golflengtes allemaal ongeveer even helder zijn, ongeacht de afstand (in het betreffende roodverschuivings interval). Dit effect is uniek voor millimeter en submillimeter waarnemingen.
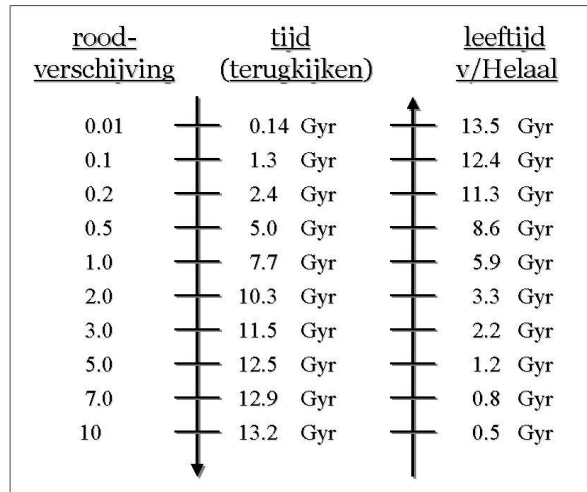
Figuur 3: *Roodverschuiving en afstand: Deze figuur laat een schaal zien waarop af te lezen valt hoe ver terug in de tijd men kijkt voor een bepaalde roodverschuiving (1 Gyr = 1 Miljard jaar). Doordat de lichtsnelheid constant is, doet het licht van verre stelsels er dus vele jaren over om op Aarde aan te komen. We kijken dus effectief terug in de tijd. (De exacte waarden voor afstand en tijd in dit figuur zijn afhankelijk van de kosmologische modellen die ons heelal beschrijven. Hier gebruiken we de meest recente resultaten van kosmologisch onderzoek, waarin de uitdijing van het heelal nog steeds aan het versnellen is).*

Submillimeter sterrenstelsels

Zoals eerder vermeld, worder in submillimeter sterrenstelsels een grote hoeveelheid sterren in korte tijd gevormd. Ze stralen het merendeel van hun licht uit op ver-infrarode golflengtes, wat betekent dat ze ook een grote hoeveelheid stof bevatten. Dit lijkt erop te wijzen dat de dominante bron van energie in deze stelsels gehuld is in stof. De ontdekking van deze soort stelsels heeft tot vele vragen geleid. Ten eerste: Hoe belangrijk zijn ze ten opzichte van andere veraf gelegen stelsels wat betreft hun bijdrage aan de evolutie van het heelal? Dit betekent dat men wil onderzoeken hoeveel energie deze stelsels produceren en hoeveel massa ze bevatten. Ten tweede: Het feit dat ze slechts sporadisch voorkomen in onze directe omgeving, maar veel vaker gezien worden ver weg toen het heelal nog jonger was, betekent dat ze zich ontwikkeld hebben tot een van de soorten stelsels die we in onze omgeving waarnemen — maar welk? Verder wil men weten welk mechanisme teweg brengt dat deze enorme hoeveelheid sterren wordt gevormd. Er zijn nog veel meer van dit soort vragen, en de antwoorden hierop zullen beter inzicht geven in de rol die de submillimeter stelsels spelen gedurende de verdere evolutie van sterrenstelsels.

Al deze vragen worden zowel door middel van observaties als uit theoretisch oogpunt bestudeerd. Empirisch zijn de submillimeter waarnemingen de funda-
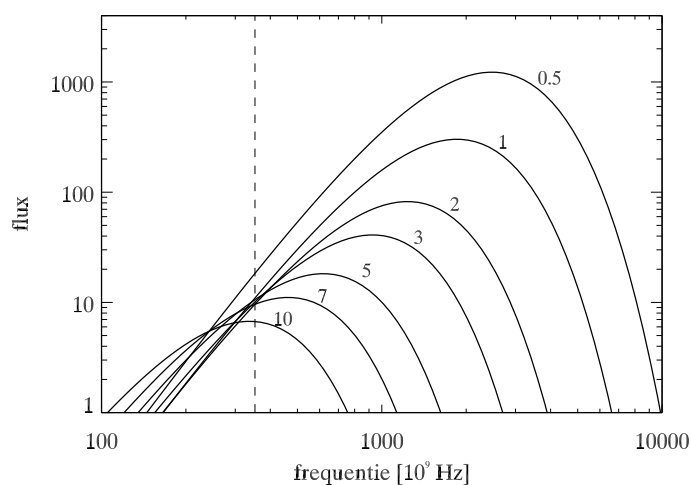
Figuur 4: *Deze figuur illustreerd waarom submillimeter sterrenstelsels tussen roodver-schuiving 1 en 8 ongeveer even helder zijn. Hier afgebeeld is de helderheidsverdeling van een negebootst stelsel voor een roodverschuivingen van 0.5 to 10. We zien dat door de toenemende afstand tot het stelsel de helderheid afneemt, maar dat door her Doppler-effect de helderste piek van de helderheidsverdeling naar links (het infrarood) verschuift. De verticale gestreepte lijn geeft de golflengte van de waarnemingen van 850 µm aan.*

mentele basis voor het ontdekken van submillimeter sterrenstelsels. Gebruik makende van deze waarnemingen kan vastgesteld worden hoeveel van deze stelsels er zijn, hoe helder ze zijn en hoe ze verdeeld zijn over de hemel. Daarnaast moeten de stelsels dan ook op andere golflengtes waargenomen worden om er-achter te komen welk mechanisme het stof opwarmt – is dit stervorming, een actief zwart gat, of iets totaal anders? Verder moet er onderzocht worden hoe-veel gas er zich in deze stelsels bevindt in relatie tot de hoeveelheid stof. Dit is niet gemakkelijk, en wordt meestal gedaan door waarnemingen aan het molecuul CO (koolstof-monoxide). Een ander probleem is het vinden van de sterren in het stelsel, daar dit gedaan moet worden op optische en nabij-infrarood golflengten. Zoals hierboven vermeld, absorbeert stof het licht van de sterren, en als gevolg hiervan kunnen sommige van de submillimeter stelsels niet optisch waargenomen worden. Dit maakt het moeilijk om de roodverschuiving en dus de afstand te bepalen.

De theoretische aspecten van submillimeter stelsels worden behandeld door te proberen de onderliggende fysica van de stelsels beter te doorgronden (bijvoor-beeld door te onderzoeken hoe de hoeveelheid sterren die zich plotseling op een bepaald moment vormen, zoveel groter kan worden) en door algemene simu-laties uit te voeren aan de vorming van structuur in ons heelal. Wat betreft dat laatste, weinig van de modellen hadden het bestaan van submillimeter sterren-stelsels voorspeld en de meeste van de grote kosmologische simulaties hebben nog steeds moeite ze te reproduceren. Ondanks de vrij algemene acceptatie van de belangrijke rol die zij spelen in de vorming van zware sterrenstelsels, zoals die

nu waargenomen worden, is de ware aard van de submillimeter sterrenstelsels nog niet echt begrepen. Een van de redenen voor de grote hoeveelheid stervorming in deze stelsels zou kunnen zijn, dat door het botsen van meerdere grote sterrenstelsels gas in deze stelsels samengeperst wordt en zo een enorme hoeveelheid sterren vormt. Al de onderwerpen die in deze sectie beschreven zijn, zijn cruciaal in de studie van submillimeter stelsels en worden in verschillende projecten behandeld.

De Leiden-SCUBA Lens Survey

Dit proefschrift beschrijft een groot SCUBA project. Dit project, de Leiden-SCUBA Lens Survey, behelst het waarnemen van verschillende velden aan de hemel die groepen van sterrenstelsels bevatten, zogeheten clusters. Sterrenstelsel clusters zijn groepen van sterrenstelsels die zo dicht bij elkaar staan dat ze elkaar door middel van de zwaartekracht beinvloeden. Daar er zich in deze clusters dus erg veel massa bevindt, is de zwaartekracht er erg sterk. Zoals verklaard wordt in Einstein's relativiteits-theorie, is er een verband tussen massa en de zogeheten kromming van de ruimte, en dit heeft belangrijke consequenties voor onze waarnemingen. Onder invloed van de grote massa van een cluster wordt zelfs het pad van licht verbogen, net zoals dit gebeurt in een vergrootglas. Dit fenomeen wordt *gravitationele lensing* genoemd, en stelt ons in staat zwakke, veraf gelegen sterrenstelsels achter de clusters te bestuderen. Eigenlijk kunnen zulke zware clusters dus wel "de natuur's eigen telescoop" genoemd worden. De Leiden-SCUBA Lens Survey is de grootste en meest gevoelige van zijn soort en beslaat tenminste twee keer zoveel oppervlakte aan de hemel als andere gelijksoortige projecten.

Het oplossend vermogen, de resolutie, van een telescoop wordt bepaald door de verhouding tussen de golflengte van de waarnemingen en de diameter van de telescoop, wat voor de SCUBA waarnemingen betekent dat de resolutie van de geproduceerde beelden 15 boogseconden is (1 graad is gelijk aan 60 boogminuten of 3600 boogseconden). Daar de dichtheid van submillimeter stelsels aan de hemel toeneemt naarmate de stelsels zwakker worden, kan op een bepaald moment geen onderscheid meer gemaakt worden tussen verschillende stelsels als gevolg van de resolutie van de beelden. Deze limiet in helderheid wordt ook wel de "confusion limit" (verwarrings limiet) genoemd. Gelukkig is de effectieve resolutie van onze beelden vele malen groter, doordat de als lens fungerende sterrenstelsel cluster, de achtergrond vele malen vergroot. Dit verlaagt de "confusion limit". Kort gezegd, de graviatie lens (de zware cluster) scheidt de achterliggende submillimeter bronnen zodat ze niet samensmelten en dus individueel waargenomen kunnen worden.

De catalogus

Daar het produceren van een catalogus van submillimeter sterrenstelsels aan de basis van dit proefschrift ligt, moeten de details en methodes die gebruikt zijn voor het maken ervan goed begrepen worden.

Veraf gelegen sterrenstelsels zijn aan de hemel een paar boogseconden groot. Zoals hierboven beschreven, is de resolutie van de SCUBA beelden 15 boogsec-

onden, en dus enkele malen groter dan de werkelijke afmetingen van de sterrenstelsels. Dit betekent dat alle veraf gelegen stelsels er hetzelfde uitzien, namelijk als een "blob" op de beelden[3]. Dit betekent dat de informatie die we over de individuele stelsel kunnen verkrijgen beperkt is tot de positie en de 850 μm flux (de flux in een indicatie van de hoeveelheid licht die we van een bron waarnemen). Het identificeren van de verschillende stelsels is niet triviaal en moet erg zorgvuldig gedaan worden. En daar SCUBA het eerste instrument is in zijn soort, en slechts een paar andere vergelijkbare instrumenten later in gebruik zijn genomen, is er geen standaard methode om de waarnemingen te analyseren. Het ontwikkelen van een goede analyse methode is dus een belangrijk onderdeel van alle projecten van deze soort.

In dit proefschrift is ervoor gekozen om een wiskundig beschreven methode te gebruiken die de naam "Mexican Hat Wavelets" draagt (deze methode wordt in hoofdstuk 2 en 3 in detail beschreven). Men kan niet volstaan om simpelweg deze methode te gebruiken, hij moet ook getest worden in controleerbare experimenten. Dit zijn simulaties waar, bijvoorbeeld, waarnemingen gesimuleerd worden, of kunstmatige stelsels toegevoegd worden aan werkelijke waarnemingen. Gebruik makende van deze simulaties kan dan gekwantificeerd worden hoe betrouwbaar de resultaten van de echte analyse zijn. Tijdens deze simulaties zijn tienduizenden kunstmatige sets van waarnemingen geproduceerd.

De uiteindelijke catalogus van de Leiden-SCUBA Lens Survey wordt gepresenteerd in hoofdstuk 3. Het totaal van de waargenomen velden bestaat uit 12 velden van sterrenstelsel clusters en ter vergelijking een veld zonder cluster. Het totaal waargenomen gebied beslaat 71 boogminuten^2 (1 graad^2 is 3600 boogminuten^2, en de hele hemel bestaat uit 41253 graden^2). Zoals eerder vermeld, vergroot de gravitatie lens het gebied achter de cluster, dus in werkelijkheid is het waargenomen gebied (achter clusters) slechts ongeveer de helft, namelijk 35 boogminuten^2. In dit gebied zijn 58 nieuwe submillimeter sterrenstelsels ontdekt. Van deze zijn er 15 die niet waargenomen hadden kunnen worden als er geen gebruik gemaakt was van de gravitatie lenzen. De nieuw waargenomen stelsels in dit project verdrievoudigen het aantal bekende zwakke submillimeter sterrenstelsels.

Uit de catalogus berekenen we het aantal sterrenstelsels van een bepaalde helderheid (flux). Dit is de zogeheten 'number count' (telling), welke een maat is van de hoeveelheid heldere en zwakke submillimeter stelsels over de hele hemel. Gebruik makend van deze telling hebben we bepaald dat de zwakke submillimeter stelsels het grootste aandeel leveren in het totale licht van het "spectrum van het heelal".

Submillimeter sterrenstelsels en modellen voor hun evolutie

In hoofdstuk 4 worden de gegevens uit de Leiden-SCUBA Lens Survey gebruikt om modellen voor de evolutie van sterrenstelsels te verbeteren. De waarnemingen van de Survey worden aangevuld met de nieuwste waarnemingen op andere golflengten, zoals radio en andere ver-infrarood golflengten. Daar in het vroege

---

[3]Een voorbeeld van deze "blobs" is te zien op de omslag van dit proefschrift. Deze is samengesteld uit verschillende van de SCUBA beelden. De vorm van de sterrenstelsels wordt volledig veroorzaakt door de telescoop resolutie.

heelal de submillimeter sterrenstelsels ongeveer 1000 keer vaker voorkomen dan nu, moeten we concluderen dat deze stelsels een significante evolutie ondergaan. Deze evolutie kan op verschillende manieren uitgelegd worden, maar in dit geval is verondersteld dat hij het gevolg is van een grotere hoeveelheid stervorming lang geleden. Dit wordt vaak beschreven als de stervormings-geschiedenis. Gebaseerd op de modellen in hoofdstuk 4, leiden we af dat ongeveer 10 miljoen jaar geleden de grootste hoeveelheid sterren per jaar gevormd werden.

De aard van de submillimeter sterrenstelsels en hun relatie tot andere veraf gelegen stelsels.

Om de aard van de submillimeter stelsels te bestuderen moeten ze op verschillende golflengten waargenomen worden. Hier worden optische en nabij-infrarood waarnemingen gebruikt om de sterren van de stelsels te onderzoeken. Dit betekent dat bepaald moet worden welk sterrenstelsel op een optisch beeld het waargenomen ver-infrarood licht uitzendt. Daar de resolutie van optische beelden beter is, zijn er vaak meerdere stelsels terug te vinden dicht bij de positie van de submillimeter stelsels. Alleen door een gedetailleerde analyse is het mogelijk te bepalen welk van de optisch geïdentificeerde stelsels overeen komt met het onderzochte submillimeter sterrenstelsel. Dit wordt gedaan in hoofdstuk 5 en 6. Waar hoofdstuk 5 gaat over de identificatie van al de sterrenstelsels in de Leiden-SCUBA Lens Survey, gaat hoofdstuk 6 dieper in op de identificatie van een ongewone submillimeter bron. De correcte identificatie van de stelsels is cruciaal om de fysieke processen die in de submillimeter stelsels plaatsvinden te kunnen bestuderen. Een van de eerste gegevens die na identificatie verkregen kan worden is de roodverschuiving ofwel de afstand. Maar er zijn nog vele andere stukjes van de puzzel nodig. Zo kan door optische en nabij-infrarood spectroscopie, en röntgen en radio waarnemingen bepaald worden waardoor het stof verwarmd wordt, of dit alleen gebeurt door stervorming of ook door bijvoorbeeld een zwart gat.

Voor dit proefschrift zijn al de beschikbare optische en nabij-infrarood waarnemingen voor de velden van de survey verzameld. Daarbij zijn voor enkele velden ook radio waarnemingen aanwezig. Het is gelukt om met zekerheid ongeveer een derde van de submillimeter sterrenstelsels te identificeren met stelsels in de andere waarnemingen. Nogmaals een derde van de stelsels heeft een of meer mogelijke identificaties en voor het laatste een derdedeel was geen identificatie mogelijk. Er zijn verschillende redenen waardoor een submillimeter stelsel niet geidentificeerd zou kunnen worden met een stelsel in de andere waarnemingen; het stelsel kan bijvoorbeeld te ver weg zijn om optisch waargenomen te worden, of mogelijk was de kwaliteit van de optische en nabij-infrarode gegevens niet voldoende. Van de stelsels die met zekerheid of grote waarschijnlijkheid geidentificeerd zijn, blijkt dat het merendeel erg rood is in de andere waarnemingen[4]. Dat is niet echt verrassend, daar stof vooral het blauwe licht van sterren absorbeert. Sommige van de stelsels konden alleen worden waargenomen in het nabij-infrarood en niet op optische golflengten. Deze, erg rode, sterrenstelsels worden vaak geclassificeerd in een van de twee soorten stelsels bekend als

---

[4]Voorbeeld op de achterkant van het proefschrift.

'extreem rode sterrenstelsels' en 'veraf gelegen rode sterrenstelsels' (of EROs en DRGs). Deze sterrenstelsels bevinden zich op roodverschuivingen groter dan 1 of 2. Dus een selectie van deze stelsels zal vooral bestaan uit verre sterrenstelsels die ofwel erg oud zijn ofwel veel stof bevatten. Enkele van deze ERO/DRGs zijn in detail bestudeerd en een van de belangrijkste conclusies daarvan is dat ze enorm zwaar zijn. Dit is een belangrijke indicatie dat tenminste sommige submillimeter sterrenstelsels de voorlopers zijn van de oude zware sterrenstelsels die we in de huidige omgeving van onze Melkweg aantreffen.

We kunnen dus vaststellen dat tenminste enkele van de submillimeter sterrenstelsels gerelateerd zijn aan de EROs en DRGs. Om verdere conclusies te kunnen trekken hebben we onderzocht of in omgekeerde zin de meeste EROs/DRGs een connectie hebben met submillimeter stelsels. Dit is gedaan door middel van een statistische analyse van de hoeveelheid submillimeter licht die uitgezonden wordt door de EROs/DRGs. Het resultaat is dat gemiddeld deze stelsels evenveel ver-infrarood licht uitstralen als de zwakke submillimeter stelsels uit de Leiden-SCUBA Lens Survey. Dat is een belangrijke conclusie die, samen met identificatie van de submillimeter stelsels, laat zien dat er een sterk verband bestaat tussen de submillimeter stelsels en EROs/DRGs.

De ongewone identificatie die besproken wordt in hoofdstuk 6, is de ontdekking van een quasar door zijn submillimeter licht. Een quasar is een van het helderste type objecten in het heelal. Het is een massief zwart gat in het centrum van een sterrenstelsel. Het zwarte gat slokt alle materie rondom zich op, en als resultaat daarvan wordt zoveel licht uitgestraald dat het sterrenstelsel zelf volkomen overstraald wordt. Dit licht wordt op alle golflengten uitgezonden, van radio tot aan röntgen. Normaal gesproken worden quasars ontdekt door waarnemingen van hun radio, optische, ultraviolette of röntgen straling. Dit is de eerste keer dat er een ontdekt is door de straling in het submillimeter gebied, waar het een van de allerhelderste verre submillimeter stelsels is. Het submillimeter licht zou door verschillende processen verklaard kunnen worden, maar is meest waarschijnlijk het gevolg van intense stervorming.

Belangrijkste resultaten in dit proefschrift

De Leiden-SCUBA Lens Survey gepresenteerd in dit proefschrift is op het moment de grootste en meest gevoelige submillimeter survey van zwakke veraf gelegen stoffige sterrenstelsels. Met de catalogus die uit dit project is voortgekomen hebben we tegelijkertijd de heldere en zwakke submillimeter stelsels kunnen bestuderen, waardoor we tot de conclusie zijn gekomen dat de zwakke submillimeter stelsels het grootste deel van het licht, waargenomen in stoffige sterrenstelsels, uitzenden. In de studie naar de aard van de submillimeter stelsels hebben we het merendeel kunnen identificeren met "extreem rode veraf gelegen sterrenstelsels" en daardoor kunnen concluderen dat er een verband bestaat tussen deze twee types van sterrenstelsels.

Curriculum Vitae

I was born in Odder in Jutland in Denmark in May 1976. As a child I moved with my parents to different places throughout Denmark. In 1991 I finished elementary school from N. Zahles Seminarieskole, and completed high school 1994 from Høje-Taastrup Amtsgymnasium.

In 1994 I started my studies in physics and astronomy at the University of Copenhagen, where in 1997 I achieved the bachelor's degree, and in January 2000, I completed my studies and achieved the M.Sc. degree. I did my master's thesis under the supervision of Dr. Palle Møller (ESO) on the topic of "Dust in Damped Lyα Absorbers". During my studies, I was involved in the International Association of Physics Students (IAPS) and was chairman for the Astronomical Student Society. I was a summer student twice, once at CERN and once at the Los Alamos National Laboratory, and went observing three times at La Silla and once at La Palma. Additionally, I participated in a Nordic summer school and an international winter school, and spent about one year at ESO (Garching).

In April 2000 I moved to Leiden to do my Ph.D. research at the Sterrewacht Leiden with Dr. Paul van der Werf on faint, distant dusty submillimetre bright galaxies, on a position funded by the Netherlands Organisation for Scientific Research (NWO). The results of this work are described in this thesis. During the last four years, I have been observing multiple times: once at La Palma (W. Herschel Telescope), five times at Hawaii (J.C. Maxwell Telescope). I have attended the NOVA Fall School, and have participated in international meetings and conferences in Greece, USA, UK, Germany and the Netherlands, where I have presented my work. Furthermore, I made multiple working visits to Cambridge (UK), Caltech (CA, USA) and the Joint Astronomy Centre Hilo (Hawaii, USA), and have also given seminars at several institutes. Several of these visits were supported financially by the Leids Kerkhoven-Bosscha Fonds. I was a teaching assistent for the course 'Astronomische Waarneemtechnieken 2', have assisted with the outreach to potential students, and was chairwoman for the Sociale Commissie at the Sterrewacht.

After completing my Ph.D., I will move to Heidelberg to take up a postdoc position at the Max-Planck-Institute for Astronomy in the group of Dr. Fabian Walter.

Curriculum Vitae

Acknowledgements